Transport of Bubbles and Oil Droplets Rising in a Net Co-F1ow through a Rectangular Confinement

by

Hirad Soltani

A thesis submitted in partial fulfillment of the requirements for the degree of

Master of Science

In

Mechanical Engineering

Department of Mechanical Engineering
University of Alberta

This dissertation is dedicated to my parents for their endless support and companionship

Abstract

The passage of air bubbles and oil droplets with net co-flow through a vertical straight rectangular flow channel is investigated experimentally and analytically in this research. A flow channel, varying from 22 mm × 5.84 mm to 3 mm × 5.84 mm (width × thickness) cross-sectional geometry was used in the present experimental investigation. This flow channel allows the passage of bubbles and oil droplets from a region through two parallel plates into a confined rectangular region.

In the rising bubble experiments, the characteristics of bubbles varied from 0.75 mm to 3.2 mm diameter rising in a water/glycerol mixture were captured. Results show that in the parallel plates region, the flow can be described by the available theory. In this region, as bubbles become larger in size, their terminal velocity increase due to the relatively higher buoyancy force (comparing to the smaller bubbles) on the bubbles in the flow and negligible effect of confining geometry on bubble terminal velocity. On entering the rectangular confinement, however, bubbles of relatively large size compared to the rectangular confinement geometry, decelerate to a much lower terminal velocity due to the drag force expressed by the confining walls. A semi-empirical model for determining the bubble terminal velocity in a rectangular geometry is developed to predict this motion. The flow around air bubbles have been investigated using two image processing approaches of PIV and PTV. Because the PTV data was cluttered and the fluid velocity profile cannot be seen, the PTV sparse field was interpolated onto a regular gird. Quantitatively, it was shown that the PIV and interpolated PTV processing results were approximately the same. A theoretical model for streamlines in the flow surrounding bubbles has been developed to be compared against the experimental data. Results showed that the tangential fluid velocity at the bubbles interface matched well with the developed analytical mode.

Flow of an oil droplet in a net fluid co-flow through a vertical rectangular confinement is investigated in this study. Five fluid fluxes were provided to flow along with the droplets through the rectangular confinement and two droplet sizes at each fluid flux were chosen to be investigated. Transparent canola oil was used as the oil droplet and glycerol was chosen to be the working fluid as it allowed the refractive index of both phases to be matched. Similar to the rising bubble experiment, to quantify the velocity vector field, PIV and PTV processing approaches were employed to analyze the displacement of tracer particles in the oil droplet and surrounding fluid. An interesting observation was two counter-rotating vortices on either sides of the rising droplet, because of the mechanical force exerted on the droplet from the surrounding fluid and the confining walls. Results showed that as the fluid flux increased, the counter-rotating vortices became stronger, because of increase in the momentum on the rising droplet. The fluid velocity at the rectangular confinement centerline has been derived from both PIV and PTV processing. It was shown that the fluid velocity at centerline is the maximum magnitude at the droplet center and farther from the droplet center, the centerline velocity decreases.

Preface

This thesis is original work by Hirad Soltani. Material of the thesis has been published in conferences as follows:

1. H. Soltani, DS. Nobes, "Shadowgraph Imaging to Quantify Air Bubble Rising Velocity as Passing Through a Rectangular Flow Cell with a Mini-Slot", Okanagan Fluid Dynamics Meeting, Kelowna, British Columbia, Canada, 2017
2. H. Soltani, R. Sabbagh, DS Nobes, "Quantifying Air Bubble Characteristics Rising Through a Mini-Slot inside a Rectangular Flow Channel Using Shadow Image Velocimetry", 67th Canadian Chemical Engineering Conference, Edmonton, Alberta, Canada, 2017
3. H. Soltani, J. Hadfield, M. Redmond, "Observation of the Flow Behavior for a Rising Droplet in a Mini-Slot", 19th International Conference on Fluid Mechanics, Heat Transfer and Thermodynamics (ICFMHTT), Venice, Italy, 2017
4. H. Soltani, F. Rasimarzabadi, DS. Nobes, "Effect of Bubble Size Passing Through a Rectangular Orifice Using Particle Shadow Velocimetry (PSV)", 2nd Thermal and Fluids Engineering (TFEC) Conference, Las Vegas, USA
5. H. Soltani, J. Hadfield, DS. Nobes, "Developing Quantitative Information From Shadowgraph Images of Air Bubbles Passing Through a Mini-Slot", Second International Symposium on Image based Metrology (ISIMet), Hawaii, USA, 2017
6. H. Soltani, R. Azadi, A. Baldygin and D. S. Nobes, "Developing quantitative information of oil droplets rising through a rectangular confinement", 5th International Conference on Experimental Fluid Mechanics – ICEFM 2018 Munich, Munich, Germany, July 2-4, 2018

The candidate has also been author in other group work as:

7. J. Hadfield, H. Soltani, DS. Nobes, "Application of Plenoptic PTV: A Single-Camera Time-Resolved Three-Dimensional Fluid Flow Measurement Technique", Second International Symposium on Image based Metrology (ISIMet), Hawaii, USA, 2017
8. R. Azadi, H. Soltani, R. Sabbagh, DS. Nobes, "Experimental and Numerical Investigation of bubble dynamics in confined channels", 5th International Conference on Experimental Fluid Mechanics – ICEFM 2018 Munich, Munich, Germany, July 2-4, 2018
9. S. Ansari, R. Sabbagh, H. Soltani and DS. Nobes, "Flow visualization of a droplet penetration through a porous media in SAGD process using μPIV", 5th International Conference on Experimental Fluid Mechanics – ICEFM 2018 Munich, Munich, Germany, July 2-4, 2018
10. R. Sabbagh, H. Soltani., MA. Kazemi and DS. Nobes, "3D Flow measurement using particle tracking velocimetry (PTV) in porous media", 5th International Conference on Experimental Fluid Mechanics – ICEFM 2018 Munich, Munich, Germany, July 2-4, 2018

11. S. Ansari, R. Sabbagh, H. Soltani and DS. Nobes, "Investigating the pressure field of a multi-phase flow in porous media using μ-PTV", 19th International Symposium on Applications of Laser & Imaging Techniques to Fluid Mechanics, Lisbon, Portugal, July 16 – 19, 2018

Chapter 4 and Chapter 5 have been prepared to be submitted to a journal as:

1. H. Soltani, R. Sabbagh, D. S. Nobes, "The Passage of Bubbles Rising Through a Confining Rectangular Geometry", *to be submitted to* Physics of Fluids, 2018
2. H. Soltani, R. Sabbagh, D. S. Nobes, "Theoretical and Experimental Investigation of Fluid Flow around Single Bubbles as Flowing in a Rectangular Confinement", *to be submitted to* Physics of Fluids, 2018

Acknowledgements

It has been a great opportunity for me to do my M.Sc. of mechanical engineering at University of Alberta. I need to thank a number of people who helped me toward completing this degree. I would like to take this opportunity to express my appreciation to professor David S. Nobes as my M.Sc. program supervisor for his wonderful support and training, which helped me to improve my engineering knowledge, writing skills and gain a great deal of experience for my future career.

Special thanks to Jake Hadfield who allowed me to used a couple of his processing codes for PTV processing and data management in MATLAB. Sincere appreciation to Reza Sabbagh who trained me how to develop a semi-empirical model from experimental results and also for his great contribution to the two journal papers that have been prepared to be submitted for publication. Finally yet importantly, I need to thank Shadi Ansari and Yishak Yusuf for all the scientific discussions and their continuous supports.

I gratefully acknowledge financial support from Natural Sciences and Engineering Research Council (NSERC) of Canada, the Alberta Ingenuity Fund, the Canadian Foundation for Innovation (CFI) and RGL Reservoir Management Inc.

Table of Contents

List of Tables

List of Figures

Nomenclature

Symbol	Description
A	Cross-sectional area
a_{xy}	Distance of a bubble center to the nearest plate in xy plane
a_{yz}	Distance of a bubble center to the nearest plate in yz plane
$B_{\bar{x}}$	Bias uncertainty
C_{b-PPR}	Bubble centricity trough PPR
C_{b-RCSR}	Bubble centricity through RCSR
C_d	A parameter dependent on the distance from the center of the rising bubble to the nearest plate
C_{inst}	Instantaneous centricity
C_n	Gegenbauer function
D_h	Hydraulic diameter
D_e	Equivalent diameter
D_e	Instantaneous equivalent diameter of a bubble
D_{max}	Maximum diameter of a bubble/droplet
D_{min}	Minimum diameter of a bubble/droplet
d_p	Diameter of a particle
Eo	Eötvös number
f	Correction factor

F_B	Buoyancy force
F_D	Drag force
F_{D-conf}	Drag force in a confining geometry
$F_{D-plates}$	Drag force on a bubble rising in two parallel plates
F_{D-tube}	Drag force on a bubble rising in a tube
F_g	Gravity force
g	Gravitational constant
l	Length
k_1	Correction factor due to the effect of tube confining walls for a bubble rising in a tube
k_2	Correction factor due to the effect of co-flow for a bubble rising in a tube
k_{conf}	Confining wall factor
$k_{w-plates}$	Wall factor for two parallel plates
Mo	Morton number
p	Pressure
P	Perimeter
Q	Volumetric flow rate
q	Fluid flux: volumetric flow rate over cross-sectional area
q_{PPR}	Fluid flux through PPR
q_{RCSR}	Fluid flux through RCSR
R	Bubble radius
$R_{\bar{x}}$	Random uncertainty
RI	Refractive index

Re	Reynolds number
St	Stokes number
$S_{\bar{x}}$	Standard deviation of mean of a measured parameter, x
S_x	Standard deviation of a measured parameter, x
t	Thickness
U	Fluid velocity in upstream
V	Volume
$\vec{V}$	Velocity field
V_{f-PPR}	Fluid maximum velocity in PPR
V_{f-max}	Maximum fluid velocity
V_r	Radial velocity
V_{rel}	Relative velocity of a particle to the bulk flow
V_{r-inst}	Instantaneous rising velocity of a bubble
V_{t-PPR}	Bubble terminal velocity through PPR
V_{t-RCSR}	Bubble terminal velocity through RCSR
V_{t-conf}	Terminal velocity in a confining geometry
V_{t-inf}	Terminal velocity in an infinite fluid medium
$V_{t-plates}$	Bubble terminal velocity in two parallel plates
V_{t-tube}	Terminal velocity of a bubble rising in a tube
V_x	Horizontal velocity

V_y	Parabolic velocity profile in a rectangular channel
V_y	Vertical velocity
V_{yR}	Fluid velocity at R distance from the centerline
V_{y-tube}	Fluid velocity profile in a tube
V_θ	Tangential velocity
w	Width
x	Widthwise location
∂x_i	The uncertainty in measurement of an i^{th} variable
y	Lengthwise location
Y	A measured value which is a function of n variables
$\frac{\partial Y}{\partial x_i}$	The sensitivity coefficient of parameter Y respecting to each variable

Greek Letters	**Description**
μ_f	Viscosity of the bulk fluid
ρ_f	Density of the bulk fluid
ρ_p	Density of the particle
τ_p	Time response of a particle
$\omega_\emptyset$	Azimuthal vorticity
ω_r	Radial vorticity
ω_θ	Tangential vorticity
$\emptyset$	Azimuthal angle in spherical coordinates

θ	Polar angle
κ	Ratio of the gas viscosity to the bulk fluid velocity
λ	Ratio of bubble equivalent diameter to the diameter of a tube
σ	Surface tension
ψ	Stream function
ω	Vorticity

Abbreviations	**Description**
PIV	Particle image velocimetry
PTV	Particle tracking velocimetry
SAGD	Steam assisted gravity drainage
cSOR	Cumulative steam-oil ratio
PSV	Particle shadow velocimetry
FOV	Field of view
LED	Light-emitting diode
CMOS	Complementary metal-oxide semiconductor
PPR	Parallel plate region
RCSR	Rectangular confinement region
RMSE	Root mean square error
STD	Standard deviation

CHAPTER 1. INTRODUCTION

1.1 Introduction

A fluid flow consisting of more than one phase is known as “multiphase” flow (Brennen 2005). In many technological and biological applications, such as cavitating rotary machines, slurry flows, blood flow and fluidized beds multiphase, flows are involved (Brennen 2005). Multiphase flows could be classified based on the types of their phases as: gas-liquid, gas-solid, solid-liquid and gas-solid-liquid flows (Brennen 2005). A complete body of 0.5 μm to 10 cm size which has a recognizable interface with the medium around that is termed a “particle” which could be fluid (droplets), gas (bubbles) or solid particles (Clift, Grace, and Weber 1978).

The flow associated with fluid and solid particles rising or falling through a stagnant or moving fluid medium has drawn special attention from many engineering systems where this phenomenon plays an important role. Air bubbles rising in a fluid medium are important and practical to many processes such as gas exchange between the atmosphere and oceans (Kanwisher 1963; Woolf and Thorpe 1991), underwater acoustics (Breitz 1989) and the production of aerosols (de Leeuw et al. 2014). They are also used in food and chemical processes (Hassan, Khan, and Rasul 2007) to improve mass and heat transfer (Clift et al. 1978; Hassan et al. 2008). Flotation processes, which are utilized in mineral treatments, are other industries that take the advantage of air bubbles motion. In a floatation process, injection of gas bubbles into a solution is employed so that mineral fines adhere to the bubbles and float to the surface in a foamy form (Okada et al.

1990). The performance of flotation equipment are affected by the time of operation which is influenced by motion, shape and size of air bubbles (Kulkarni and Joshi 2005).

The motion and dispersion of air bubbles in a fluid medium enhances the mass transfer of the bulk fluid, which is the basis of fluid-fluid extraction or the separation of liquid parts of a solution (Clift et al. 1978; Komrakova, Eskin, and Derksen 2013). The terminal velocity and shape of a rising air bubble in a liquid depend on properties of both phases, that include density, viscosity, surface tension, bulk flow rate, impurity, temperature and the dispersed phase size (Baz-Rodríguez, Aguilar-Corona, and Soria 2012; Kulkarni and Joshi 2005; Lighthill 1967; Nickens and Yannitell 1987; Okhotskii 2001; Tomiyama et al. 2002). Predicting the rising velocity and shape of a bubble depends on the flow regime (laminar or turbulent) and the effect of any confining geometry (Shapira and Haber 1988). Therefore, developing a general correlation that covers all different flow regimes and geometry conditions to characterize the bubble characteristics and its motion, such as shape and terminal velocity, is not typically feasible (Kulkarni and Joshi 2005).

An oil-in-water emulsion can undergo coalescence of finer oil droplets forming droplets of a size that need to be considered individually. This occurs in a number of industrial processes and has important consequences at a scale where both body and surface forces are relevant. Hence, understanding of fluid flow behavior as a single oil droplet rises or falls in a fluid medium is a start to further investigate other cases, such as movement of several oil droplets in different geometrical scales.

1.2 Steam assisted gravity drainage (SAGD)

Steam assisted gravity drainage (SAGD) is a thermal oil recovery technique used in Alberta to recover oil in the reservoirs (Al Yousef, AlDaif, and Al Otaibi 2014). Figure 1-1 shows an

overview schematic of the SAGD process. An oil production well is horizontally drilled into oil reservoir a few meters below the steam injection well. Steam is injected to the reservoir to reduce bitumen viscosity allowing it to move toward the production well due to gravity. The low viscosity bitumen passes through a number of rectangular narrow slots in the production well liner to be will be pumped to ground level.

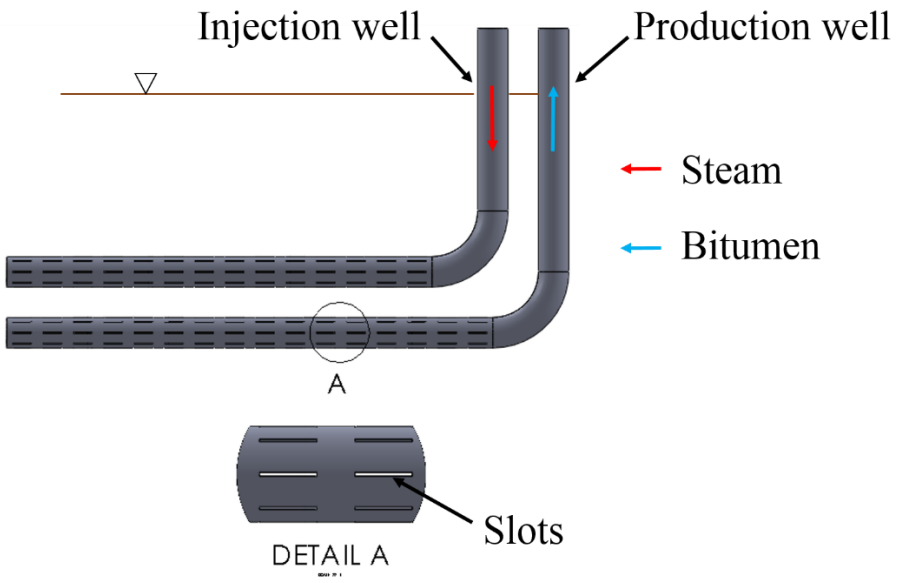

Figure 1-1- Schematic of a typical SAGD process

Non-condensable gases, such as methane, in addition to bitumen (Gunn and Freeston 1991) can potentially exist in some oil reservoirs. Methane is a soluble gas in bitumen. Presuming a specific pressure and temperature of 4 MPa and 80 °C at the production well level in an oil reservoir, methane's solubility is around 5 cm^3/cm^3 (Svrcek and Mehrotra 1982). As bitumen passes through production well slots, pressure drops. There is a potential that methane could come out of the solution and form gas bubbles. In some cases, gas is co-injected with steam in order to reduce bitumen viscosity (Alturki, Gates, and Maini 2010; Nourozieh, Kariznovi, and Abedi

2016). Methane is mostly co-injected with steam, possibly due to low cost of methane among other options (Phenix 2015). The co-injection of methane would promote oil recovery and reduces cSOR (cumulative steam-oil ratio) in comparison to an ES-SAGD (expanding solvent SAGD), in which there is solvent co-injection with steam (Alturki et al. 2010) process when no methane injection is used.

Other fluids, such as gas, condensed water from steam injection, oil etc. might pass through the production well slots along with bitumen. Therefore, the flow of low viscosity bitumen through the production well slots can contain air bubbles, water/oil droplets and sand particles. The typical range of slot width (w) and length (l) are 0.254-6.35 mm and 38.1-76.2 mm respectively (Ansari 2015; Bennion et al. 2009; Kumar, Srivastava, and Kumar 2010). Therefore, the flow of bitumen through the slots is similar to flow through parallel plates. Before entering the slots, the mixture of bitumen and other phases passes through the porous media of the reservoir. The flow of a multiphase fluid through porous media is complex to investigate in details. However, to understand the flow behavior in such a medium, it can be simplified to less complex cases, such as flow of single air bubbles and single oil droplets through a rectangular confining geometry.

1.3 Shape regimes of bubbles and droplets

The parameter involved in determining rising velocity and shape of a rising fluid particle (bubble or droplet) could be summarized as (Grace 1973; Grace, Wairegi, and Nguyen 1976):

$$f(\rho_f, \mu_f, \rho_p, D_e, V_{rel}, \sigma) = 0 \tag{1-1}$$

where ρ_f is fluid medium density, μ_f is fluid medium viscosity, ρ_p is the particle density, V_{rel} represents the terminal velocity relative to surrounding medium and σ represents surface tension.

A particle's shape is not always spherical, hence the equivalent diameter (D_e) is used and defined as the diameter of a sphere with the same volume as that of the fluid particle (Grace 1973) defined by:

$$D_e = \left(\frac{6V}{\pi}\right)^{1/3} \tag{1-2}$$

where V represents the volume of the fluid particle. Graphical correlations of the shape (Clift et al. 1978) of moving bubbles and droplets are based on three dimensionless numbers; Reynolds number (Re), Eötvös number (Eo) and Morton number (Mo) (Grace et al. 1976), defined as:

$$Re = \frac{\rho_f V_{rel} D_e}{\mu_f} \tag{1-3}$$

$$Eo = \frac{g {D_e}^2 (\rho_f - \rho_p)}{\sigma} \tag{1-4}$$

$$Mo = \frac{g {\mu_f}^4}{\rho_f \sigma^3} \tag{1-5}$$

The Eötvös number (Eo) is the ratio of buoyancy forces to surface tension forces (Clift et al. 1978). The viscosity and density ratio between the two phases are also defined as two parameters of κ and δ (Grace 1973):

$$\kappa = \frac{\mu_p}{\mu_f} \tag{1-6}$$

$$\delta = \frac{\rho_p}{\rho_f} \tag{1-7}$$

In small bubbles, all forces acting on bubble approach uniformity (Clift et al. 1978) and the bubble shape becomes spherical (G. Bozzano 2009). In contrast, as the bubble diameter becomes larger, the inertial forces become more dominant than surface tension and/or viscous forces and the shape gradually starts to change. Figure 1-2(a)-(d) shows the four basic types of bubbles and droplets that can be generated according to the flow regime and/or the confining area. Figure 1-2(a) shows a spherical bubble for which the bubble shape is not deformed. If a bubble or droplet becomes elongated with an oval shape interface, they are referred to as "ellipsoidal" particles (Clift et al. 1978), as shown in Figure 1-2(b). "Spherical-cap" particles, as shown in Figure 1-2(c), are bubbles or droplets of large size that start to have a flat shape at the bottom, and hence lose the fore-aft symmetry in their shape (Clift et al. 1978). A large bubble or droplet moving along a confined medium becomes elongated to be able to pass through the bounded space. Figure 1-2(d) indicates a typical example of these long droplets that are referred to "slug" (Clift et al. 1978) and bubbles of this shape are called "Taylor" bubbles.

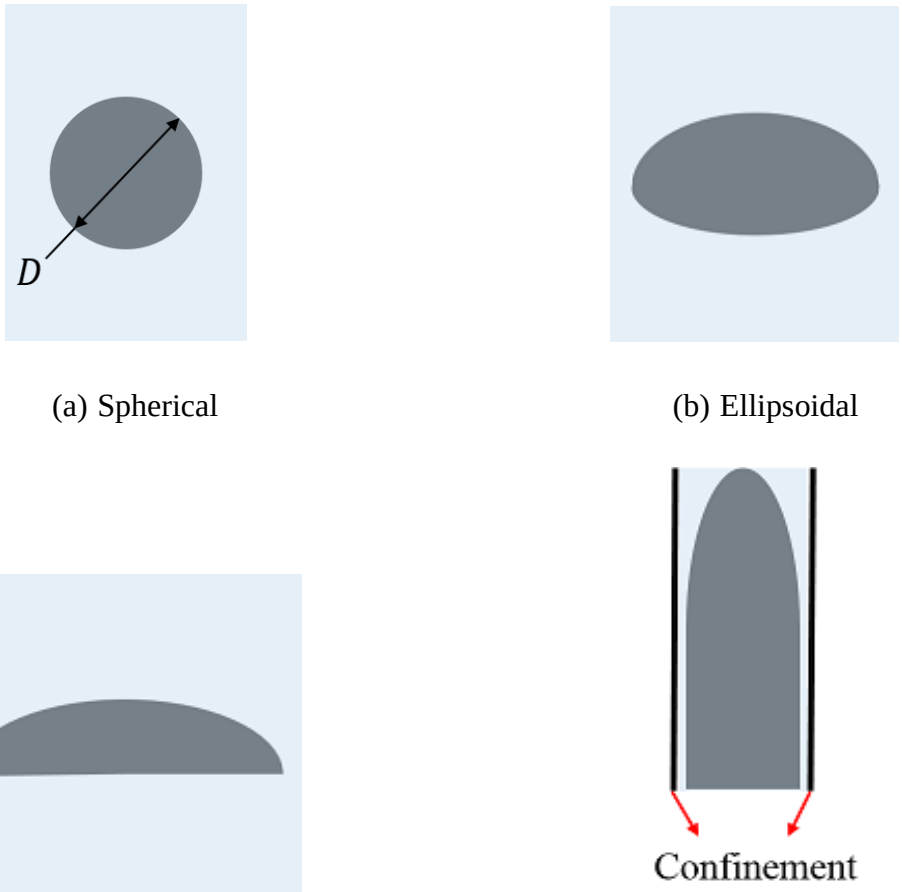

(a) Spherical (b) Ellipsoidal

(c) Spherical-cap (d) Slug flow

Figure 1-2- Different potential shapes of fluid particles (bubbles or droplets) (*after* Clift et al. 1978)

1.3.1 Air bubble shape and rising velocity

The terminal velocity and shape regime of a rising bubble/droplet depend on both phases' properties, such as density, viscosity, surface tension, bulk flow rate, impurity, temperature and the dispersed phase's shape and size (Baz-Rodríguez et al. 2012; Kulkarni and Joshi 2005; Lighthill 1967; Nickens and Yannitell 1987; Okhotskii 2001; Tomiyama et al. 2002). Graphical diagrams of shape regimes of bubbles and droplets have been developed in the literature (Clift et al. 1978; Grace 1973; Grace et al. 1976), based on dimensionless variables defined in Eq. (1-3) to Eq. (1-7). Grace (1973) developed a shape regime graphical correlation for air bubbles rising in a

fluid medium. Since that correlation was developed for air bubbles, the density and viscosity ratios of dispersed and separated phases (γ and κ) were assumed negligible. Experimental data of air bubbles rising in 21 different fluids with Mo number ranging from 3.6×10^{-14} to 1.0×10^{7} and a wide range of Re and Eo numbers were also provided (Grace 1973). Grace (1973) showed that the spherical bubble regime occurs at low Re and Eo, while the ellipsoidal regime lies in relatively high Re and moderate Eo numbers. Bubbles can have ellipsoidal-cap shape when both Re and Eo numbers are high. Since the Re number is defined based on terminal velocity in such systems, the bubble/droplet terminal velocity could also be estimated from Re number from the graphical correlation plot (Clift et al. 1978; Grace 1973; Grace et al. 1976).

Table 1-1 summarizes many investigations in the literature for air bubbles rising through confining geometries, such as circular tubes, parallel plates and rectangular confinements (Böhm et al. 2014; Clift et al. 1978). In Table 1-1, w and t are width and thickness of the rectangular channel respectively, D is the diameter of the circular tube and l is length of the test column. Most of the measurements employed one high speed camera to capture the two-dimensional movement of the bubbles. However, some investigators utilized two cameras (Fujiwara et al. 2004; Sanada, Shirota, and Watanabe 2007; Zaruba et al. 2007) in a shadowgraph configuration to capture 3 dimensional motion of air bubbles.

Table 1-1- Investigations of single air bubble rising in a confined geometry provided in the literature

Author	Measurement setup	Cross sectional area (circ: $D \times l$, rect: $w \times t \times l$)	Bubble diameter	Measured parameters	Remarks
Acharya et al. (1976)	Visual observation/high speed camera	Rectangular: 165 × 165 × 245 mm^3	-	Rising velocity, deformation	Non-Newtonian fluid
Böhm & Kraume (2012)	PIV	Rectangular: 5-7 × 160 × 1500 mm^3	3-9 mm		Velocity field and vorticity
Böhm et al. (2014)	Shadowgraphy	Rectangular: 5-7 × 160 × 1500 mm^3	3-9 mm	Rising trajectory, rising velocity, drag force coefficient	Newtonian and non-Newtonian fluids, co-current flow
Brücker (1999)	PIV	Rectangular: 100 × 100 × 1200 mm^3	4-8 mm	Rising velocity, shape, oscillation frequency, rising trajectory	Counter current flow
Clanet et al. (2004)	Canon camera at 25 Hz	several	Taylor bubbles	Rising velocity	-
Dewsbury et al. (1999) and Hassan et al. (2008)	Shadowgraphy	Rectangular: 300 × 300 × 2400 mm^3	1.5-33 mm	Rising velocity	Non-Newtonian fluid
Drews et al. (2010) and Drews et al. (2008)	Shadowgraphy	Rectangular: 3-11 × 160 × 700 mm^3	3-24 mm	Rising velocity	-
Ellingsen & Risso (2001)	Two high speed video cameras at 1000 Hz	Rectangular: 150 × 150 × 650 mm^3	2.5 mm	Rising trajectory, shape	Re = 800
Figueroa-Espinoza et al. (2008)	Two High speed cameras	Rectangular: 3.6-4.7 × 200 × 400 mm^3	< 1.4 mm	Drag coefficient, rising trajectory	-
Fujiwara et al. (2004) and Fujiwara et al. (2003)	Two CCD cameras for shadowgraph, one for PIV	Rectangular: 50 × 100 × 1000 mm^3	2-6 mm	3D bubble shape	Non-Newtonian fluid
Funfschilling & Li (2001)	PIV	Rectangular: 60 × 60 × 500 mm^3	< 12 mm	Flow around bubbles	Non-Newtonian fluid
Funfschilling & Li (2006)	shadowgraphy	Circular: 300 × 500 mm^2	3-14 mm	Rising velocity	-
Hassan et al. (2001) and Ortiz-Villafuerte et al. (2000)	Shadowgraphy, stereo PIV	Circular: 12.7 × 1300 mm^2	3 mm	Rising velocity and trajectory	-
Kopf-sill and Homsy (1988)	shadowgraphy	Parallel plates, 0.077 cm gap	0.0154 cm	Rising velocity, shape	
Liu et al. (2005)	PIV	Rectangular: 68 × 88 × 450 mm^3	6 mm	Rising trajectory, shape	-
Li et al. (2004)	PIV	Circular: 300 × 1500 mm^2	6.5-7.2 mm	Rising velocity, stress around bubble	Non-Newtonian fluid
Maneri & Zuber (1974)	Video camera	Rectangular: 1.3-9.5 × 63-86 × 914 mm^3	<55 mm	Rising velocity	Inclined channel
Miyahara & Yamanaka (1993)	Video camera	Circular: 10 × 1000 mm^2	2-30 mm	Rising velocity, shape and oscillation	Newtonian and Non-Newtonian fluid

Table 1-1 continued

Author	Measurement setup	Cross sectional area (circ: $D \times l$, rect: $w \times t \times l$)	Bubble diameter	Measured parameters	Remarks
Sanada et al. (2007)	Two high speed cameras	Rectangular: 150 × 150 × 400 mm^3	0.66-.093 mm	Drag coefficient, rising trajectory, shape	-
Sakakibara et al. (2007)	Dual-camera PIV	Rectangular: 150 × 150 × 270/500 mm^3	2.9 mm	Rising trajectory and shape	-
Sathe et al. (2010)	PIV, and Shadowgraph	Rectangular: 200 × 15 × 500 mm^3	0.1-15 mm	shape	-
Sathe et al.(2011)	PIV and shadowgraph	Circular: 150 × 650 mm^2	-	Shape	-
Sathe et al. (2013)	PIV	Rectangular: 200 × 15 × 1000 mm^3	2-35 mm	Bubble diameter	Effect of surfactant
Tokuhiro et al. (1998)	Shadowgraphy and PIV	Rectangular: 100 × 100 × 1000 mm^3	9.12 mm	Rising trajectory, shape	Counter current flow, $1950 \leq Re \leq 2250$
Van Hout et al. (2002)	PIV	Circular: 25 × 4000 mm^2	Taylor bubbles	Velocity profile	-
Wachem & Schouten (2002)	High speed camera at 955 Hz	Rectangular: 15 × 300 × 2000 mm^3	15-80 mm	Rising velocity and shape	Validating CFD model
Zaruba et al. (2007)	PIV, two cameras	Rectangular: 50 × 50 × 1300 mm^3	1-4 mm	Bubble trajectory	-
Zhang et al. (2008)	Shadowgraphy	Rectangular: 210 × 210 × 600 mm^3	2.7-5.2 mm	Rising velocity, drag coefficient	-

Many of the works provided in Table 1-1, investigated the balance of forces for rising air bubbles in a fluid medium (Clift et al. 1978; Figueroa-Espinoza et al. 2008; Haberman and Sayre 1958; Zaruba et al. 2007). There are cases that have experimentally explored the effect of surface forces on bubble flow in circular tubes (Clift et al. 1978; D. Funfschilling and Li 2006; Hassan et al. 2001; Liu et al. 2016) or in parallel plates (Böhm and Kraume 2012). The effect of a co-flow (Böhm et al. 2014) or counter flow (Brücker 1999; Tokuhiro et al. 1998) have also been the studied. However, most of the works seen in the literature are restricted to turbulent flow regimes and simple confining geometries such as parallel plates or circular tubes. Notably, the Reynolds number in these works is defined based on bubble terminal velocity relative to the surrounding fluid, bubble size, and the bulk fluid viscosity and density.

The passage of bubbles in between two parallel plates has drawn special attention from many industrial applications such as filtration processes (Böhm, Brehmer, and Kraume 2016) and microfluidics (Cueto-felgueroso and Juanes 2014; Lee and Baroud 2011; Metz et al. 2010; Selva et al. 2011). In flat sheet membranes, where a number of sheet membranes stack upon each other with a certain spacing, deposition of materials on the surface of the membrane sheets would occur as a result of the filtration process (Böhm et al. 2016). To clean these layers on the membrane sheets, air bubbles are injected with a fluid flow along the surface of the sheets. Since the passage of bubbles increases the shear stress over the surface of the membrane sheets, this process helps to clean the deposited layers (Böhm et al. 2016). The passage of bubbles along with a co-flow over the membrane sheets is an example of a rising bubble through a rectangular channel with high cross-sectional aspect ratio. This is physically similar to the rise of bubbles through a narrow gap between two parallel plates and is often in the creeping flow regime and is termed as Hele-Shaw cell (Kopf-sill and Homsy 1988). Such a system is widely used as an analogy to understand the complex flow behavior in porous media (Homsy 1987) and microfluidics (Cueto-felgueroso and Juanes 2014; Lee and Baroud 2011; Metz et al. 2010; Selva et al. 2011).

The movement of bubbles through a gap in between two parallel plates is a well-examined problem in fluid mechanics using theoretical, numerical and experimental techniques as presented in Table 1-1 (Cueto-felgueroso and Juanes 2014; Drews et al. 2010; Maruvada and Park 1996; Roig, Roudet, and Risso 2012; Taylor and Saffman 1959). Kopf-sill and Homsy (1988) experimentally investigated the rising velocity and shape of bubbles rising through a narrow gap between two horizontal parallel plates of 0.077 cm apart for two different viscous fluid mediums with 115-120 mPa.s and 540-590 mPa.s dynamic viscosities. The ratio of bubble size to plate gap was lower than 0.2 for all bubble sizes and the average co-flow velocity was ranged from $3.3\times10^{-}$

^{3} to 0.7 cm/s. In their experiments, the measured bubble terminal velocity did not match with the theory of Hele-Shaw cell (Taylor and Saffman 1959) for some bubble shapes and this discrepancy was not clearly justified. Maruvada and Park (1996) explained that the mismatching between the theory and the observations of Kopf-sill and Homsy (1988) was due to the presence of surface active contaminants in the fluid. Maruvada and Park (1996) developed an analytical prediction of translational velocity, defined as the velocity due to the displacement of the center of the mass, of elongated bubbles moving in between two vertical parallel plates. The bubble size was larger than the distance between the plates and the fluids were surface active contaminated. However, this prediction was only applicable to high Reynolds number regimes and elongated bubble shapes.

Böhm et al (2014) studied single air bubbles of 3-9 mm diameter rising in water in a co-current flow (0, 10, 12.5, 20, 23.5 cm/s) through rectangular channels of high aspect ratios (5-7 mm × 160 mm × 1500 mm, depth × thickness × height), using high-speed imaging (Table 1-1). The depth of this channel was much smaller than the thickness and hence, the geometry can be considered as two parallel plates with 5-7 mm distance from each other. Thus, the effect of channel thickness on the bubble flow could be ignored. In a range of Re number between 10 – 3000, the rising velocity, rising path and bubble centricity, which is defined as the ratio of minimum-to-maximum diameter of the projected image of the bubble (Böhm et al. 2014), were calculated. A comparison of experimental data of bubble rising velocity in a channel with the theoretical correlation of rising velocity in unbounded mediums showed that the confinement decreases the rising velocity. In addition, comparison of rising velocity of bubbles of the same diameter between the two channel geometries showed that the rising velocity in 5 mm channel depth was lower than the 7 mm case, meaning that a smaller and more compact cross-sectional geometry can decelerate the bubble motion further. At each channel depth (5 mm or 7 mm), air bubbles had relatively

higher rising velocity in higher fluid co-current flows, as expected. For each channel depth, as bubbles enlarge, the rising velocity increased due to the higher buoyancy effect that was dominant comparing the confining wall drag force. Böhm et al. (2014) compared the results of the bubble rising velocity with the theoretical bubble terminal velocity in an unbounded stationary fluid medium. However, they did not include the effect of co-flow to be compared with the experimental results and no correlation was developed/used for rising bubbles in between two parallel plates.

Investigating the single bubbles rising in a rectangular confining geometry, when all of the four confining walls affect bubble motion, is important to understand the complex flow behavior and the effect of confining walls on bubble motion. This investigation can be useful to many industrial applications, such as bubble columns and nuclear and chemical processes (Moujaes and Dougall 1987). There has been many works investigating rising bubbles through rectangular channels experimentally (Ellingsen and Risso 2001; Figueroa-Espinoza et al. 2008; Liu et al. 2005; Sanada et al. 2007; Sathe et al. 2010; Zhang et al. 2008). However, most of these works consider turbulent flow regimes where viscous forces are negligible compared to the inertial forces. Some researchers studied the rising velocity of large air bubbles or Taylor bubbles (Clift et al. 1978) or flow around them as rising through Newtonian fluids in a bounded medium (Bugg and Saad 2002; Clanet et al. 2004; Fabre 2016; Manga and Stone 1995; Polonsky, Shemer, and Barnea 1999).

A more complex case of study can be the flow of single bubble in a rectangular channel in the presence of fluid co-flow/counter co-flow. However, little information is available in the literature on developing an analytical or an empirical predictive model for bubble characteristics in such a complex case. According to Table 1-1, in most of the works, the cross-sectional geometry of the rectangular channel is relatively large compared to the bubble sizes, so the effect of confinement on bubble characteristics is negligible (Ellingsen and Risso 2001; Sanada et al. 2007;

Sathe et al. 2013). In some scenarios, the aspect ratio of the cross-section is relatively high such that the confinement is similar to two parallel plates (Cueto-felgueroso and Juanes 2014; Drews et al. 2010; Maruvada and Park 1996; Roig et al. 2012; Taylor and Saffman 1959).

Table 1-1 also highlights that most of the previous works investigated rising air bubbles in turbulent flow regime and through simple geometries such as circular tubes and parallel plates. However, the effect of complex confining geometries, such as rectangular channels, has not been well examined. Even though some researchers (Böhm et al. 2014) included the effect of fluid co-flow/counter flow in the experiments, the contribution of fluid co-flow/counter flow on the bubble terminal velocity has not been reported clearly.

1.3.2 Measurement approaches for capturing bubble characteristics

As shown in Table 1-1, optical measurement techniques, such as particle image velocimetry (PIV) and particle shadow velocimetry (PSV), have been used to study the velocity field in fluid flows (Raffel et al. 1989). In these imaging techniques, typically, the fluid flow is seeded with tracer particles and a camera captures images of the seeded fluid flow at certain time intervals. Therefore, the displacement of the particles would be determined in between two images (Raffel et al. 1989) and instantaneous velocity is calculated (Raffel et al. 1989) (more details provided in section 3.3). Table 1-1 indicates that the optical measurement setup used by the researchers mainly consisted of a high speed camera and light source to take images of the bubble flow and investigate the bubble motion (shadowgraphy technique, more details are provided in Chapter 3).

Some researchers investigated the velocity field around bubbles rising in circular tubes as the bounding medium (Hassan et al. 2001; Ortiz-Villafuerte et al. 2000). Böhm & Kraume (2012) employed a 2 dimensional PIV system (2D-PIV) to investigate rise of single bubbles through

rectangular channels. The experimental setup was the same as the one used by Böhm et al. (2014). The 2D-PIV system they employed consisted of a Nd:YAG Laser with the double pulse frequency of 15 Hz, and a CCD camera (progressive-scan Imager Pro SX 5M) with 2456×2058 pixel^2 resolution. They have done a general visualization of the rising path and shape of bubbles of different diameters and have also quantified the vorticity behind the bubbles in the Karman vortex sheet region. The same author (Böhm et al. 2016), employed the same experimental setup and same fluid mediums to study the flow structure around rising bubbles. For bubbles of 3 mm to 9 mm diameter, and three co-current average velocities of 0, 10 and 20 cm/s, they quantified the velocity filed around rising bubbles, such that velocity magnitude, vorticity, strain and shear stress were derived from the velocity field. According to the results, by increasing the bubble size and co-current velocity, all of the four measured parameters (velocity magnitude, vorticity etc.) increased. However, the effect of confinement the flow around single bubbles was not quantified in this investigation (Böhm et al. 2016).

Van Hout et al. (2002) determined the velocity field around Taylor bubbles (90 mm in length) rising in still water through a circular tube (4 m long, 25 mm internal diameter) as described in Table 1-1. A PIV measurement system was employed, consisting of a pulsed laser (Nd:YAG Mini Laser III PIV-15) for illumination, and a KODAK ES 1.0 CCD camera with 1008×1018 pixel^2 resolution running at 30 Hz frequency. The velocity profile of the continuous fluid was measured and averaged in the wake region of 100 bubbles, at different distances from the bottom of the bubble. They concluded that the liquid film around the bubbles accelerated up to 1m/s velocity at the bottom of the bubble.

Funfschilling & Li (2001) compared the flow pattern around single bubbles as rising in Newtonian and Non-Newtonian fluids through a vertical square channel ($0.06 \times 0.06 \times 0.5$ m^3,

width × depth × length). As the fluid medium, 3 polyacrylamide solutions of 0.25 %, 0.5 % and 0.75 % concentrations were used as Non-Newtonian solutions, and one glycerol solution was employed as a Newtonian fluid. The flow structure was quantified by mixing fluorescent polymer beads of 75 μm size into the working fluid as tracer particles, and using a PIV measurement setup consisting of a two-pulsed Nd:YAG laser and a camera. This work concluded that for a Newtonian fluid medium (glycerol solution) the fluid flow in the front and behind the rising bubble was in the upward direction (opposite direction of gravity). For the Non-Newtonian fluid mediums, the flow in the front of rising bubble was quite similar to the Newtonian solution; however, in the central area of the bubble wake the flow direction was downward. Two inclined cones of fluid with upward direction surrounded this region of the wake with downward fluid flow.

1.4 Study of rising oil droplets

To observe the fluid motion in a system of rising or falling droplet using optical measurement techniques, such as PIV, the refractive index (*RI*) of the both phases should be matched to avoid light refraction at the droplet interface. Developing quantitative information of a system of rising or falling droplet by carrying out experiment has many difficulties (Ninomiya and Yasuda 2006), such as impurities in the liquid phases and necessity to add surfactants to the fluids, which changes the droplet behavior (Albert et al. 2015).

Many authors performed experimental investigations of rising path, rising velocity, drag coefficient and shape oscillation of oil droplets as moving in an infinite fluid medium (Bäumler et al. 2011; Bertakis et al. 2010; Eiswirth et al. 2011; Thorsen, Stordalen, and Terjesen 1956; Wegener et al. 2007; Wegener, Kraume, and Paschedag 2009). However, experimental investigation of flow inside and around an oil droplet rising in a fluid medium can be challenging

due to the difficulties in running experiments for such a system (Ninomiya and Yasuda 2006). Comparison of the experimental results may not be valid, even for the same system and operating conditions, because the fluids can have different impurities (Wegener et al. 2009). Therefore, mostly numerical approaches have been undertaken to investigate the flow pattern inside and around a rising/falling oil droplets in a fluid medium and the results were validated by empirical correlations and/or collecting experimental data (Bäumler et al. 2011; Bertakis et al. 2010; Eiswirth et al. 2011; Komrakova et al. 2013; Petera and Weatherley 2001).

Albert et al. (2015) developed a 3 dimensional numerical model to investigate the rising path of highly viscous oil droplets (corn oil), ranging from 0.5 mm to 16 mm in size, as rising through stationary water. For all of droplet size cases, the Re number was higher than 1. For relatively smaller droplet sizes of 0.5-2 mm, the numerical model predicted a spherical droplet shape and vertical rising path with no oscillation (Albert et al. 2015). Also, for 0.5-2 mm droplet diameter, the surface tension forces are relatively high due to high curvature of the droplet surface and inertial forces are relatively low because of lower terminal velocity and hence lower inertial forces. Therefore, the droplets of 0.5-2 mm diameter retained the spherical shape as rising in water (Albert et al. 2015).

Komrakova et al. (2013) studied shape deformation and rising velocity of n-butanol droplets of 1-4 mm falling in still water using a numerical simulation. The developed numerical simulation was proved from experiments to be applicable for three shape regimes of spherical, deformed and oscillating droplets, rather than just a limited droplet shape regime.

As a spherical droplet moves in a bounded fluid medium, such as circular tubes, parallel plates and rectangular channels, the confining walls can affect the shape and velocity of the droplet (Clift et al. 1978). As the droplet size increases and the interface becomes closer to the confining

walls, the shape of droplet might be deformed to be able to pass through the confinement, and the droplet velocity might drop because of confining walls drag force (Strom and Kintner 1958).

Even though there has been a number of numerical and experimental investigations of droplets rising or falling in an unbounded fluid medium, study of confined fluid medium systems has not been well examined. For low Re number flow regimes (viscous fluid medium), wall effect on droplets is more pronounced compared to high Re number flows (Clift et al. 1978). Effect of confining walls on the droplets rising velocity in circular tubes have been investigated (Chhabra and Bangun 1997; Clift et al. 1978; Khadamkar, Patwardhan, and Mathpati 2017; Mao, Godfrey, and Slater 1995). In most of the works, the wall effect on the terminal velocity of droplets is addressed by the ratio of droplet diameter to the tube diameter (Clift et al. 1978). Chhabra and Bangun (1997) investigated wall effects on the terminal velocity of falling fluid particles in a stationary fluid medium. They concluded that when $Re << 1$ (viscous fluid medium relative to the fluid droplet), the wall effect on the droplet terminal velocity is only dependent on the droplet to tube diameter ratio (Chhabra and Bangun 1997). Ninomiya and Yasuda (2006) visualized a system of glycerol/water droplet falling into stagnant silicon oil of the same refractive index. They observed two counter rotating vortices inside the droplet and found that as the droplet became smaller, the center of the vortices shifted more to the upstream of the droplet (Ninomiya and Yasuda 2006) (this is in fact one vortex which is imaged on a plane.). A review of the literature shows that little information appears on quantifying flow around and inside oil droplets rising through rectangular confinements with co-current fluid flows.

1.5 Objectives

It can be concluded that in a SAGD process, a mixture of bitumen and other phases can pass through the porous media in the oil reservoir and enter the production well through the slots of the production well. Before entering the production well slots, the flow of bitumen mixture passes through porous media, which can be simplified to the motion of bubbles and oil droplets through a rectangular confinement (Vafai 2005). Flow of a bitumen mixture through the slots, however, is similar to the flow of fluid particles in parallel plates. A review of the literature highlights that the investigation of bubbles rising through confining geometries, such as circular tubes and parallel plates have been carried out widely. However, limited information appears in the literature that quantifies the effect of confining walls and fluid co-flow on the bubble terminal velocity. Limited information appears in the literature regarding the flow around rising bubbles and flow around and inside oil droplets as rising through a rectangular confinement.

A vertical rectangular confining geometry is used as the focus geometry of this investigation on the characteristics of rising bubbles and oil droplets with a net co-flow. The main objectives of this study can be classified as:

- Developing a semi-empirical model to predict the terminal velocity of a single air bubble rising through a rectangular confinement along with a fluid co-flow
- Measurement of tangential velocity at a rising bubble interface and developing a theoretical model to be compared against the experimental data
- Quantifying the fluid flow behavior around and inside an oil droplet rising through a rectangular confinement to investigate the effect of fluid co-flow and bubble size on the flow behavior

Starting with an analytical model for a bubble rising in between two parallel plates in a static flow, an empirical model is developed for predicting the bubble rising velocity and the effect of rectangular geometry and fluid co-flow is included. Using particle shadow velocimetry (PSV) measurements, single bubbles and oil droplets are examined when rising with a co-flow in the opposite direction of gravity. The experiments are undertaken for five different flow rates and for variety of bubble and oil droplet sizes compared to the rectangular confinement.

1.6 Thesis outline

The following is an outline of what will be presented in this thesis.

Chapter 2 describes the theory of rising bubbles through rectangular confinements. A correction factor is developed based on the theory of parallel plates, to predict the bubble terminal velocity through rectangular channels. In addition, the streamlines of the flow surrounding rising bubbles are derived by solving the momentum equation (Navier-Stokes) in spherical coordinates with appropriate boundary conditions.

The experimental setup and PSV, as the optical measurement technique, are described in Chapter 3. The details of the flow loop setup and specifications of components of the experimental setup are presented in this chapter. The image processing approaches undertaken in this study are explained with some examples in details.

In Chapter 4, the bubble characteristics, such as centricity, size and bubble terminal velocity are examined over two main regions of parallel plate region rectangular confinement. The experimental data for bubble terminal velocity through the rectangular confinement region are used to determine the unknown coefficients in the model of bubble terminal velocity trough rectangular channels proposed in Chapter 2.

The fluid flow surrounding bubbles rising through a vertical rectangular confinement in five fluid co-flows are mainly investigated in Chapter 5. A variety of bubble sizes are generated and bubble characteristics, such as size, shape and terminal velocity are investigated. To investigate the flow behavior around bubbles, two image processing approaches of PIV and PTV are employed. The experimental results of fluid tangential velocity at bubble interface from PIV and PTV processing are compared against a developed analytical model for one relatively small bubble size at each co-flow.

Chapter 6 investigates the flow behavior around and inside rising oil droplets through a vertical rectangular confinement in a net co-flow. Two oil droplet sizes are chosen and five net co-flows are provided to flow along with droplets through the rectangular confinement. PIV and PTV image processing approaches are undertaken to process the images and the results of both processing methods are compared in terms of velocity vector resolution.

Chapter 7 summarizes the outcomes and draws conclusions of this research. Ideas and suggestions to improve potential future work on this project are presented according to the concluding remarks.

1.6.1 The Appendix

Extra information on some data measurements and developed image processing/post-processing codes are provided in Appendices. In Appendix A-1., the measurement of KSCN viscosity at different solution concentration is provided. Appendix A-2. contains the information regarding the viscosity and density of Canola oil. Appendix A-3 provides the solid model and drawing for the flow channel used in the present experiments. Appendix A-4 and Appendix A-5. provide the MATLB code for plotting the velocity vector field overlaid on a color map background

in the around bubbles and in the flow around/inside oil droplets from PIV and PTV image processing. Appendix A-5 is the MATLAB manuscript to analyze and plot the results of bubble characteristics, such as centricity, size, terminal velocity and also model modification approach to derive semi-empirical correlations based on the experimental data.

CHAPTER 2. THEORY OF RISING BUBBLES THROUGH RECTANGULAR CHANNELS

2.1 Introduction

In Chapter 1 it was concluded that there is a gap in the literature regarding the investigation of rising bubbles in complex geometries, such as rectangular confinements, where confining walls affect the bubble motion. According to the literature, the effect of fluid co-flow on the bubble terminal velocity has not been investigated in detail, especially within a confining geometry. To understand the effect of rectangular geometry on rising bubbles, the bubble flow through a rectangular confinements should be modeled. In this chapter, the flow of bubbles through a rectangular confinement is modeled in two parts:

1. Developing an analytical model to derive the streamline of the continuous flow in the vicinity of the rising bubbles
2. Predicting the effect of confining walls of rectangular geometry and fluid co-flow on the bubble terminal velocity based on the available theories in the literature

This chapter describes deriving streamlines in the fluid flow surrounding a bubble rising through a rectangular geometry with co-flow, based on Navier-Stokes equations and appropriate boundary conditions. To predict the bubble terminal velocity as rising through such a geometry, a semi-empirical correlation is proposed based on the available theories in the literature and the experimental data, which will be fully examined using experimental data in Chapter 4.

2.1.1 Velocity field around a rising bubble

Typically, for a system of rising bubble, the reference frame can be set at a fixed location (Eulerian frame) to observe the absolute motion of bubble, or on the center of the rising bubble to see the movement of bubble relative to the surrounding fluid (Lagrangian frame). Figure 2-1 shows a single bubble of R radius rising through a rectangular confinement of $w \times t$ (width × thickness) cross sectional geometry. In Figure 2-1(a), the radial distance, r, from bubble center, the polar angle, θ, and azimuthal angle, φ, in the spherical coordinates are also defined. In Figure 2-1(b), the two dimensional bubble flow is observed in the $xy-$ plane assuming that the bubble rises at the center of the rectangular confinement and the effect of channel thickness, t, on the fluid flow behavior being observed in the $xy-$ plane is negligible. In Figure 2-1(b), the reference frame moves along with the bubble center, which means that the surrounding fluid flows over the bubble with $V_y - V_{t-rect}$ velocity, where V_{t-rect} is the bubble terminal velocity and V_y is the velocity profile of bulk fluid in the far field from the bubble is defined as:

$$V_y = V_{f-max}\left(1 - \left(\frac{2x}{w}\right)^2\right) \tag{2-1}$$

where V_{f-max} is the maximum fluid velocity in between the plates and x is the horizontal distance in Cartesian reference frame. Knowing that for the spherical coordinates shown in Figure 2-1(b), $x = -r\sin(\theta)$, Eq. (2-1) can be rewritten:

$$V_y = V_{f-max}\left(1 - \left(\frac{2r\sin(\theta)}{w}\right)^2\right) \tag{2-2}$$

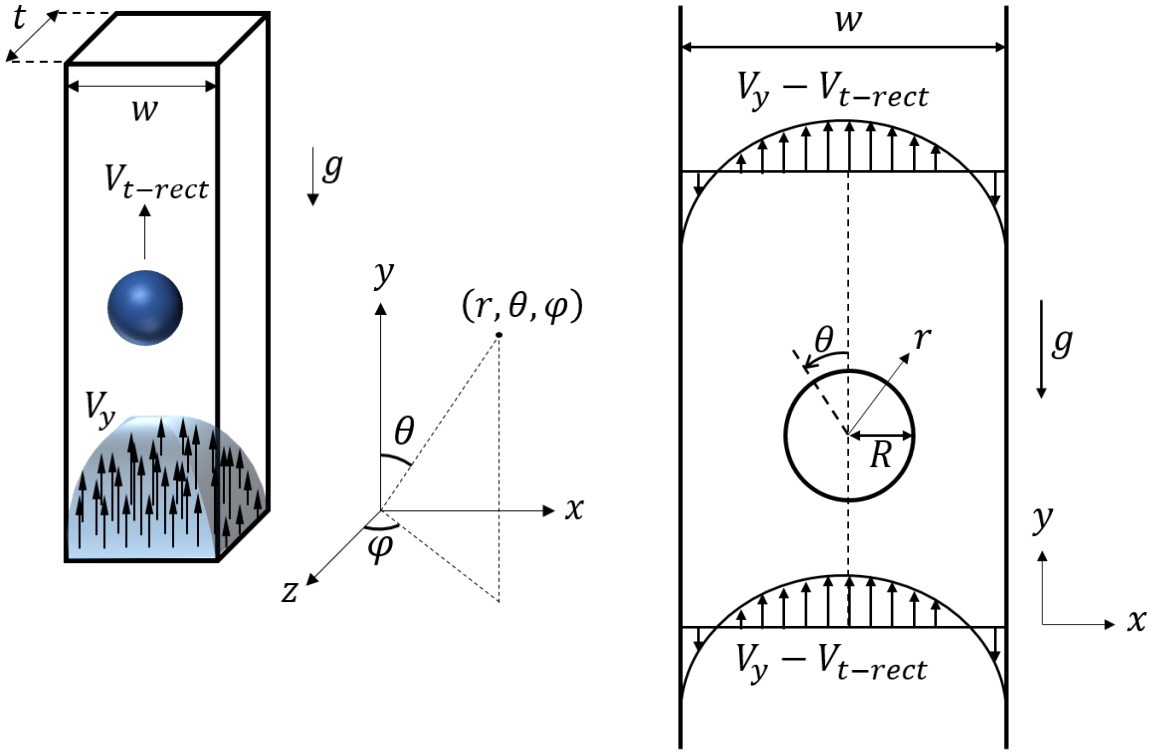

(a) (b)

Figure 2-1- A single air bubble rising through an unbounded fluid medium. the reference frame is fixed at bubble center

For a system of rising bubble with incompressible flow, the continuity equation and general form of Navier-Stokes equation (Clift et al. 1978) can be applied to both fluid medium and sphere as (Clift et al. 1978):

$$\nabla.\vec{V} = 0 \tag{2-3}$$

$$\rho\left(\frac{\partial\vec{V}}{\partial t} + \vec{V}.\left(\nabla\vec{V}\right)\right) = \rho\vec{g} - \nabla p + \mu\nabla^2\vec{V} \tag{2-4}$$

where, ρ is density, $\vec{V}$ is the velocity vector, ∇ is the gradient operator, p is pressure and $\rho\vec{g}$ is the total body forces on the system. An incompressible flow with low Re number (typically $Re << 1$) is called "creeping flow", for which inertia forces become negligible comparing to viscous forces (Clift et al. 1978). When the surface forces, such as surface tension force at the bubble surface and/or viscous forces, are relatively high compared to inertia forces bubbles tend to be spherical (Clift et al. 1978). Therefore, typically in creeping flow regime bubbles are assumed to be spherical if the bubble shape is not affected by confining medium (Clift et al. 1978). Here, using the creeping flow assumption the inertia term, $\rho\left(\frac{\partial\vec{V}}{\partial t}+\vec{V}.\left(\nabla\vec{V}\right)\right)$, in eqn. (2-4) becomes negligible comparing to viscous term, $\mu\nabla^2\,\vec{V}$ (Clift et al. 1978), and the body forces are ignored because of negligible mass of the bubble. Hence, the eqn. (2-4) can be rewritten as (Clift et al. 1978):

$$\nabla p = \mu\nabla^2\,\vec{V} \tag{2-5}$$

and the curl of eqn. (2-5) is:

$$0 = \nabla^2\left(\nabla\times\vec{V}\right) \tag{2-6}$$

The vorticity of flow is defined as (Clift et al. 1978):

$$\omega = \nabla\times\vec{V} \tag{2-7}$$

Inserting eqn. (2-7) into eqn. (2-6) results in:

$$\nabla^2\omega = 0 \tag{2-8}$$

From the creeping flow assumption, the flow around the sphere would be incompressible and axisymmetric, for which the Stokes's stream function, ψ, can be defined. In spherical and

Cartesian coordinates, the velocity components can be defined based on the Stokes's stream function as:

$$V_r = \frac{1}{r^2\, sin(\theta)} \frac{\partial \psi}{\partial \theta} \tag{2-9}$$

$$V_\theta = \frac{-1}{r \sin(\theta)} \frac{\partial \psi}{\partial r} \tag{2-10}$$

$$V_x = \frac{\partial \psi}{\partial y} \tag{2-11}$$

$$V_y = -\frac{\partial \psi}{\partial x} \tag{2-12}$$

where, V_r and V_θ are the radial and tangential velocity components in spherical coordinates respectively. Also, V_x and V_y are the horizontal and vertical components of velocity defined in Cartesian coordinate system. In the spherical coordinates, the three components of vorticity are (Kundu, Cohen, and Dowling 2011):

$$\omega_r = \frac{1}{r\, sin(\theta)} \left(\frac{\partial}{\partial \theta} \left(V_\varphi\, sin(\theta) \right) - \frac{\partial V_\theta}{\partial \varphi} \right) \tag{2-13}$$

$$\omega_\theta = \frac{1}{r} \left(\frac{1}{sin(\theta)} \frac{\partial V_r}{\partial \varphi} - \frac{\partial \left(r V_\varphi \right)}{\partial r} \right) \tag{2-14}$$

$$\omega_\varphi = \frac{1}{r} \left(\frac{\partial}{\partial r} \left(r V_\theta \right) - \frac{\partial V_r}{\partial \theta} \right) \tag{2-15}$$

However, for the two dimensional flow shown in Figure 2-1(b) it can be shown that $\omega_r = \omega_\theta = 0$. Inserting V_r and V_θ (Eq. (2-9) and Eq. (2-10)) into the Eq. (2-15) gives:

$$\omega_{\varphi} = -\frac{1}{r}\left(\frac{1}{sin(\theta)}\frac{\partial^2\psi}{\partial r^2} + \frac{1}{r^2}\frac{\partial}{\partial\theta}\left(\frac{1}{sin(\theta)}\frac{\partial\psi}{\partial\theta}\right)\right) \tag{2-16}$$

and the governing equation is $\nabla^2\omega = 0$. However, because $\omega_r = \omega_\theta = 0$, only $\nabla^2\omega_\varphi = 0$ needs to be solved. Therefore, plugging Using Eq. (2-16) into Eq. (2-8) results in:

$$\left(\frac{\partial^2}{\partial r^2} + \frac{sin(\theta)}{r^2}\frac{\partial}{\partial\theta}\left(\frac{1}{sin(\theta)}\frac{\partial}{\partial\theta}\right)\right)^2 \psi = 0 \tag{2-17}$$

Eq. (2-17) can be applied to the streamlines of the gas inside the bubble (ψ_p), and the surrounding fluid (ψ). To solve Eq. (2-17), relevant boundary conditions need to be applied based on the confinement geometry and the fluid flow conditions.

The two fluid phases are immiscible and the flow does not penetrate at the bubble interface from one phase to the other, meaning that the $V_r(R,\theta) = 0$ (no penetration):

$$\frac{\partial\psi}{\partial\theta}(R,\theta) = 0 \Rightarrow \psi_p(R,\theta) = \psi(R,\theta) = 0 \tag{2-18}$$

At the bubble interface, where both fluid move, the tangential stress should be equalized. Therefore:

$$\frac{\partial}{\partial r}\left(\frac{1}{r^2}\frac{\partial\psi}{\partial r}\right) = \kappa\frac{\partial}{\partial r}\left(\frac{1}{r^2}\frac{\partial\psi_p}{\partial r}\right) \tag{2-19}$$

where, $\kappa = \frac{\mu_g}{\mu_f}$, and μ_g and μ_f are the gas viscosity and viscosity of the fluid medium respectively. For the case of gas bubble, the viscosity ratio, κ, would be almost zero and Eq. (2-19) would be identically zero. This means that the tangential stress at the bubble interface is approximately zero.

Because the bubble is assumed to be stationary and the surrounding fluid is flowing around the bubble, at the rectangular confinement walls, $x = \pm\frac{w}{2}$, the velocity is not zero, but rather the terminal velocity of bubble which has been subtracted from the whole velocity field. Therefore, at the walls:

$$V_\theta = -V_{t-rect}\, sin(\theta)\; at\; x = \pm\frac{w}{2} \tag{2-20}$$

As shown in Figure 2-1(b), and according to Eq. (2-1), at infinity, the velocity profile can be described by:

$$\lim_{r\to\infty} V_\theta = \left(-V_{t-rect} + V_{f-max}\left(1 - \left(\frac{2r\, sin(\theta)}{w}\right)^2\right)\right) sin(\theta) \tag{2-21}$$

Here, by using eqn. (2-9), the stream functions at infinity can be derived to be:

$$\lim_{r\to\infty} \psi = r^2\, sin(\theta)^2 \left(\frac{V_{f-max} - V_{t-rect}}{2} - \frac{V_{f-max} r^2}{w^2} sin(\theta)^2\right) \tag{2-22}$$

Eq. (2-22), which represents the Stokes's stream function at infinity, suggests that the general solution of stream functions for this system (Eq. (2-17)) can be in the form of:

$$\psi = f(r)\, sin(\theta)^2 + g(r)\, sin(\theta)^4 \tag{2-23}$$

where $f(r)$ and $g(r)$ are some functions to be determined. Each part of the stream function in Eq. (2-23), $f(r)\, sin(\theta)^2$ and $g(r)\, sin(\theta)^4$, represent the stream function due to the effect of a constant, and a parabolic velocity profile respectively. The $f(r)\, sin(\theta)^2$and $g(r)\, sin(\theta)^4$ terms in Eq. (2-23) should be solved separately and the boundary conditions introduced in Eqs. (2-18) to

(2-22) (Eqs. (2-21) and (2-22) are the same) should be applied to both. If the separate solution of each term in Eq. (2-23) are named as ψ_1 and ψ_2, the final solution of Eq. (2-17) would be the superposition of each solution:

$$\psi_1 = f(r)\, sin(\theta)^2 \tag{2-24}$$

$$\psi_2 = g(r)\, sin(\theta)^4 \tag{2-25}$$

$$\psi = \psi_1 + \psi_2 \tag{2-26}$$

The general solution of the governing equation, Eq. (2-17), is given as (Haberman and Sayre 1958):

$$\psi(r,\theta) = \sum_{2}^{\infty} C_n^{-\frac{1}{2}}(cos(\theta))(A_n r^n + B_n r^{-n+1} + C_n r^{n+2} + D_n r^{-n+3}) \tag{2-27}$$

where $C_n^{-\frac{1}{2}}(cos\theta)$ is the Gegenbauer polynomial, n is an even number and A_n, B_n, C_n, D_n are constants (Haberman and Sayre 1958). Writing Eq. (2-27) for n = 2 and 4 results in:

$$\begin{aligned}\psi(r,\theta) = sin(\theta)^2 \left(A_2 r^2 + \frac{B_2}{r} + C_2 r^4 + D_2 r\right) \\ + \frac{sin(\theta)^2}{8}\left(4 + 5\, sin(\theta)^2\right)\left(A_4 r^4 + \frac{B_4}{r^3} + C_4 r^6 + \frac{D_4}{r}\right)\end{aligned} \tag{2-28}$$

which after some simplifications can be written in the form of Eq. (2-23) as:

$$\begin{aligned}\psi(r,\theta) &= sin(\theta)^2 \left(A_2 r^2 + \frac{B_2}{r} + C_2 r^4 + D_2 r\right) + sin(\theta)^4 \left(A_4 r^4 + \frac{B_4}{r^3} + C_4 r^6 + \frac{D_4}{r}\right) \\ &= f(r)\, sin(\theta)^2 + g(r)\, sin(\theta)^4\end{aligned} \tag{2-29}$$

By applying the boundary conditions in Eqs. (2-18) to (2-22) to each part of Eq. (2-29), $f(r)\,sin(\theta)^2$ and $g(r)\,sin(\theta)^4$, the stream lines of the flow around a rising bubble can be derived. Using the streamlines in infinity boundary condition, Eq. (2-22), results in:

$$C_2 = 0 \tag{2-30}$$

$$A_2 = \frac{V_{f-max} - V_{t-rect}}{2} \tag{2-31}$$

$$A_4 = -\frac{V_{f-max}}{w^2} \tag{2-32}$$

$$C_4 = 0 \tag{2-33}$$

Using the boundary conditions in Eqs. (2-18) and (2-19) results in two equations with 4 unknowns for ψ_1 and ψ_2. Solving these equations for ψ_1 and ψ_2 gives:

$$B_2 = 0 \tag{2-34}$$

$$D_2 = -\frac{V_{f-max} - V_{t-rect}}{2} R \tag{2-35}$$

$$B_4 = 0 \tag{2-36}$$

$$D_4 = \frac{V_f}{w^2} R^5 \tag{2-37}$$

The final solution stream function can be expressed as:

$$\psi = \frac{V_{f-max} - V_{t-rect}}{2} (r^2 - Rr)\, sin(\theta)^2 - \frac{V_{f-max}}{w^2}\left(r^4 + \frac{R^5}{r}\right) sin(\theta)^4 \tag{2-38}$$

Using Eq. (2-10), the tangential and radial velocity, V_θ and V_r respectively, can be derived as:

$$V_\theta = -\left((V_{f-max} - V_{t-rect})\left(1 - \frac{R}{2r}\right)sin(\theta) - \frac{V_{f-max}}{w^2}\left(4r^2 + \frac{R^5}{r^3}\right)sin(\theta)^3\right) \quad (2\text{-}39)$$

$$V_r = -\left((V_{f-max} - V_{t-rect})\left(1 - \frac{R}{r}\right)\cos(\theta) - \frac{4V_{f-max}}{w^2}\left(r^2 + \frac{R^5}{r^3}\right)sin(\theta)^2\cos(\theta)\right) \quad (2\text{-}40)$$

The derived equations introduced in Eqs. (2-38), (2-39) and (2-40) predict the stream function and tangential velocity in the vicinity of a rising spherical bubble in a rectangular channel. Since the velocity at the walls ($x = \pm\frac{w}{2}$) are not applied to the Eqs. (2-38), (2-39) and (2-40), these equations cannot predict the flow field as bubbles enlarge and approach the size of the confining walls, as the effect of confining walls is not negligible. Eqs. (2-39) and (2-40) were developed for Lagrangian flow field; therefore, the tangential velocity in Eulerian reference frame can be written as:

$$V_\theta = -\left((V_{f-max} - V_{t-rect})\left(1 - \frac{R}{2r}\right)sin(\theta) - \frac{V_{f-max}}{w^2}\left(4r^2 + \frac{R^5}{r^3}\right)sin(\theta)^3 - V_{t-rect}\,sin(\theta)\right) \quad (2\text{-}41)$$

$$V_r = -\left((V_{f-max} - V_{t-rect})\left(1 - \frac{R}{r}\right)\cos(\theta) - \frac{4V_{f-max}}{w^2}\left(r^2 + \frac{R^5}{r^3}\right)sin(\theta)^2\cos(\theta) - V_{t-rect}\cos(\theta)\right) \quad (2\text{-}42)$$

2.2 General forces on a bubble or oil droplet

A system of two phase flow with presence of bubbles has complex dynamics and requires careful attention for being investigated (Kulkarni and Joshi 2005). In such a system, important parameters to be determined are terminal velocity, drag force, shape and size of bubble/droplet.

Assuming there is not heat transfer in the system, Navier-Stokes and continuity equations are the governing equations for such a system. For each phase, these equations need to be solved and proper boundary conditions should be included. Therefore, understanding dominant forces acting on a rising bubble or oil droplet is important to solve the governing equations.

A variety of forces acts on a moving bubble in a fluid medium, which are mainly classified as surface forces and body forces. Surface forces, which only act on the bubble interface, include surface tension forces, viscous forces and surface charge forces (Kulkarni and Joshi 2005). Body forces, which are exerted on the volume of a rising bubble are gravity and drag force (Kulkarni and Joshi 2005). Buoyancy force is derived from the integral of a surface force (pressure) of an object, partially or fully immersed, in a fluid; however, it is neither body force nor surface force. As a bubble starts to be generated within a fluid, the bubble grows until the buoyancy force balances the surface tension, inertia and drag forces exerted on the bubble from the surrounding fluid (Kulkarni and Joshi 2005). Parameters such as gas flow rate, liquid viscosity and nozzle size and configuration can affect the bubble detachment from the nozzle (Kulkarni and Joshi 2005). As the internal diameter of the nozzle increases, the surface tension force on the forming bubble increases and the bubble size becomes larger (Gaddis and Vogelpohl 1986). As a single bubble rises in a fluid, there is an interaction between the dispersed phase surface and the surrounding fluid. Hence, the bubble might become deformed to balance the shear and normal stress on the interface (Clift et al. 1978).

The motion of bubbles in a fluid medium is an example of a flow passing a blunt object(Kulkarni and Joshi 2005). For a rising bubble of any shape, an equivalent diameter, D_e, can be defined as the diameter of a sphere that has the same volume as the bubble. For such systems,

Reynolds number, Re, can be defined based on the bubble equivalent diameter (D_e) and the bubble rising velocity relative to the velocity of the surrounding fluid medium, V_{rel} such that:

$$Re = \frac{\rho_f V_{rel} D_e}{\mu_f} \tag{2-43}$$

where $\rho_f$is the density of the fluid and μ_f is the fluid medium dynamic viscosity. An incompressible flow with $Re << 1$ is considered to be creeping or Stokes flow, for which inertia forces become negligible compared to viscous forces (Clift et al. 1978). Bubbles could be spherical when the surface forces (surface tension at the interface with the fluid) and/or viscous forces are high relative to inertia forces (Clift et al. 1978). As a result, in a creeping flow regime, bubbles are typically assumed to be spherical(Clift et al. 1978). This low Re could be the result of either high viscosity of the fluid medium or low relative velocity between the bubble and the surrounding bulk flow.

Figure 2-2 shows the free body diagram for a spherical bubble in the creeping flow regime and rising in a stagnant fluid medium in equilibrium conditions where the bubble has reached its terminal velocity (Haberman and Sayre 1958). In Figure 2-2, V_{t-inf} is the bubble terminal velocity in an infinite medium, g is gravity, R is the bubble radius and F_B, F_D and F_g are buoyancy force, drag force and gravity force, respectively.

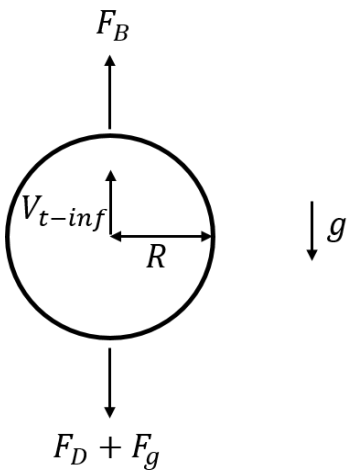

Figure 2-2- Force balance on a single air bubble or oil droplet rising in a fluid medium

The drag force on a sphere in a uniform flow can be derived by integration of normal and tangential forces on the bubble (Clift et al. 1978). This is because a spherical bubble is symmetric; therefore the x-component of the sum of normal and tangential forces are zero. From the drag force, the normal component of the stress can be derived by integration of pressure over the bubble surface. For an air bubble, it can be shown that the shear stress on the bubble surface is almost zero (Clift et al. 1978). Hence, the total drag force consists of all surface forces acting on the bubble including viscous forces and surface tension forces and is expressed as (Clift et al. 1978; Haberman and Sayre 1958):

$$F_D = 2\pi\mu_f V_{t-inf} R \frac{2 + 3\kappa}{1 + \kappa} \tag{2-44}$$

$$\kappa = \frac{\mu_g}{\mu_f} \tag{2-45}$$

where κ is the ratio of the gas viscosity (μ_g) to the viscosity of the fluid medium (μ_f). Considering the parameters shown in Figure 2-2, the buoyant, F_B and gravity forces, F_g can be written as:

$$F_B = \frac{4}{3}\pi R^3 g\rho_f \tag{2-46}$$

$$F_g = \frac{4}{3}\pi R^3 g\rho_g \tag{2-47}$$

where ρ_g is the density of the gas which forms the bubble. Haberman and Sayre (1958) investigated the rising motion of single bubbles in a liquid medium in a creeping flow regime. They derived the drag force on the rising bubble, Eq. (2-44) by summing up the normal and tangential forces acting on the bubble and the liquid interface. By balance of the three forces of drag, Eq. (2-47), buoyancy, Eq. (2-44), and gravity, Eq. (2-45), in equilibrium conditions, the general form of the terminal velocity in an infinite medium is obtained such that:

$$V_{t-inf} = \frac{2gR^2(\rho_f - \rho_g)}{3\mu_f}\frac{(1 + \kappa)}{(2 + 3\kappa)} \tag{2-48}$$

This equation is valid for a spherical bubble rising in a stationary and infinite fluid medium.

A solid particle, liquid droplet or an air bubble can carry electrostatic charges while moving in a liquid medium. These charges on the surface of the moving particle attract any counter ion in the medium. Therefore, a layer of electrostatic charges may be formed on each side of the interface which is called electric double layer (Li 2004). Since the present research aims at a macro-scale flow investigation, the effect of electric double layer on the rising bubble characteristics is neglected.

2.2.1 Wall effect and net co-flow

When a bubble rises in a bounded fluid medium, such as channels of arbitrary cross sections and parallel or non-parallel plates, it interacts with the confining walls. Therefore, the general form of drag force, Eq. (2-44) and terminal velocity, Eq. (2-48) need to be modified for the additional interaction of the rising bubble with the walls. A wall correction factor is typically introduced to modify the drag force and terminal velocity in an infinite medium based on the confining geometry (Clift et al. 1978) such that:

$$F_{D-conf} = k_{conf} F_{D-inf} \tag{2-49}$$

$$V_{t-conf} = \frac{V_{t-inf}}{k_{conf}} \tag{2-50}$$

where k_{conf} is the confining wall factor, and F_{D-conf} and V_{t-conf} are the drag force and terminal velocity, which are corrected based on the confining geometry. Confining walls may increase the velocity gradients in the liquid film between the rising bubble and the bounding walls, which leads to a higher viscous dissipation and hence a higher drag force on the rising bubble (Dabiri and Bhuvankar 2017) as qualitatively shown in Figure 2-3. The presence of a co-flow/counter co-flow of the surrounding fluid can also increase/decrease the bubble rising velocity and needs to be included in the bubble terminal velocity.

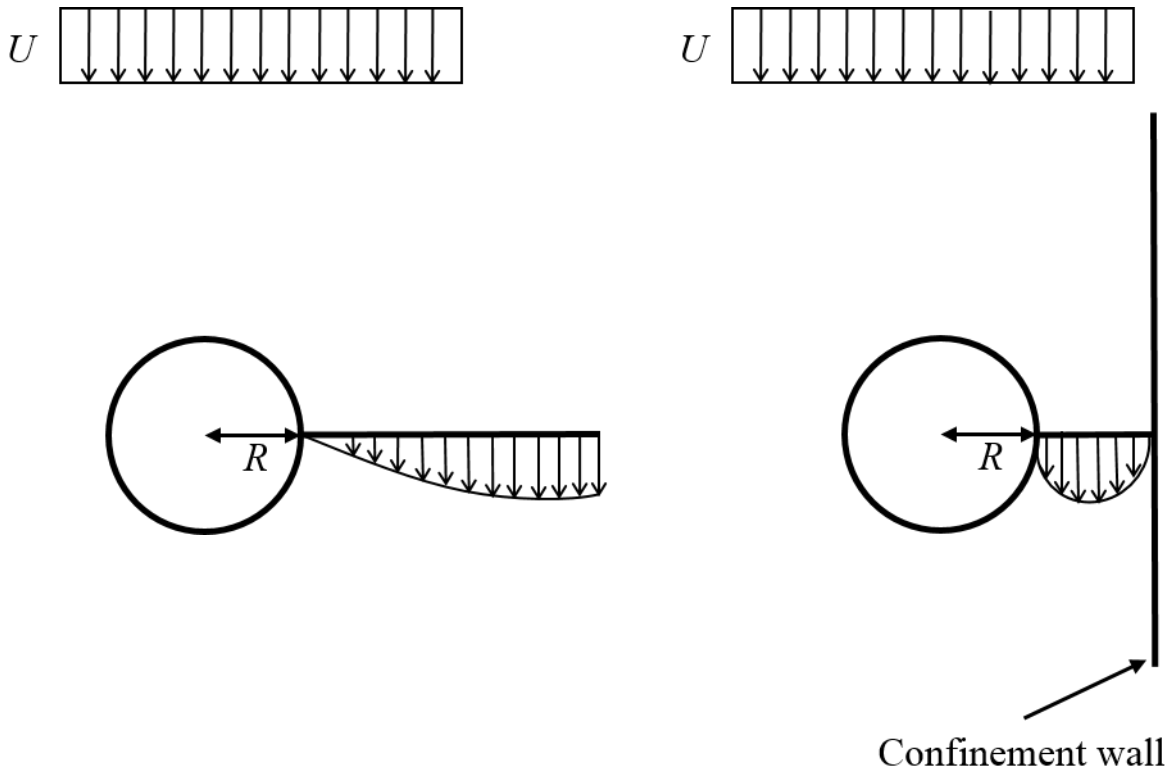

(a) (b)

Figure 2-3- Qualitative velocity at the bubble interface for (a) rising bubble in infinite medium, and (b) rising bubble near a confining wall

2.2.2 Cylindrical geometry

The drag force and the terminal velocity of spheres moving in stationary and moving liquids in circular tubes was obtained by Haberman and Sayre (1958) under the creeping flow regime. Silicone oil and water/glycerol droplets falling in castor oil were investigated experimentally for normalized bubble diameter of $\lambda < 0.8$, where λ is the ratio of the bubble diameter to the diameter of the circular tube Haberman and Sayre (1958). Drag force was obtained theoretically followed by experiments.

Figure 2-4 illustrates a single spherical bubble rising at the centerline of a circular tube with a co-flow. In this figure, D is the tube internal diameter, V_{t-tube} is the bubble terminal velocity in

a circular tube and V_{y-tube} is the fluid parabolic velocity profile in the tube. Haberman and Sayre (1958) obtained a solution for the drag force (F_{D-tube}) and the terminal velocity (V_{t-tube}) of spherical bubbles for the conditions shown in Figure 2-4 . For such a system, Haberman and Sayre (1958) considered the effect of confining walls and net co-flow on the drag force and terminal velocity in a non-dimensional manner using $\lambda = 2R/D_h$ by introducing two correction factors analytically to address the tube wall effect, k_1 and for the effects of fluid co-flow, k_2 described by:

$$k_1 = \frac{1 + 2.2757\lambda^5(\frac{1-\kappa}{2+3\kappa})}{1 - 0.7017\left(\frac{2+3\kappa}{1+\kappa}\right)\lambda + 2.0865\left(\frac{\kappa}{1+\kappa}\right)\lambda^3 + 0.5689\left(\frac{2-3\kappa}{1+\kappa}\right)\lambda^5 - 0.72603\left(\frac{1-\kappa}{1+\kappa}\right)\lambda^6} \quad (2\text{-}51)$$

$$k_2 = \frac{1 - \left(\frac{2\kappa}{2+3\kappa}\right)\lambda^2 + 0.60651(\frac{1-\kappa}{2+3\kappa})\lambda^5}{1 - 0.7017\left(\frac{2+3\kappa}{1+\kappa}\right)\lambda + 2.0865\left(\frac{\kappa}{1+\kappa}\right)\lambda^3 + 0.5689\left(\frac{2-3\kappa}{1+\kappa}\right)\lambda^5 - 0.72603\left(\frac{1-\kappa}{1+\kappa}\right)\lambda^6} \quad (2\text{-}52)$$

Using these factors the corrected drag force and terminal velocity for a rising bubble in a net co-flow and inside a circular tube were obtained as:

$$F_{D-tube} = 2\pi\mu_f R(\frac{2+3\kappa}{1+\kappa})(V_{t-tube}k_1 - V_{f-max}k_2) \quad (2\text{-}53)$$

$$V_{t-tube} = \frac{2gR^2(\rho_f - \rho_p)}{3\mu_f k_1}\frac{(1+\kappa)}{(2+3\kappa)} + \frac{k_2}{k_1}V_{f-max} \quad (2\text{-}54)$$

where V_{f-max} is the bulk flow velocity at the centerline of the circular tube. In Eq. (2-54), $\frac{k_2}{k_1}V_{f-max}$ is the contribution of fluid co-flow on the bubble terminal velocity and $\frac{2gR^2(\rho_f-\rho_p)}{3\mu_f k_1}\frac{(1+\kappa)}{(2+3\kappa)}$ is the corrected bubble terminal velocity in an infinite medium (corrected based

on the circular tube confinement effect). Both Eq. (2-53) and Eq. (2-54) are valid for $R > 0$. If $R = 0$, Eq. (2-54), returns the flow maximum velocity and there is no terminal velocity.

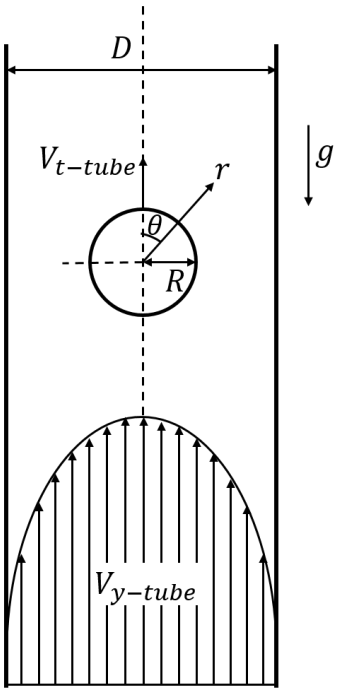

Figure 2-4- Single air bubble rising through a circular tube along with a co-flow of parabolic velocity profile

2.2.3 Rectangular geometry

If the aspect ratio of the rectangular geometry is low enough (relatively close to 1), the bubble motion is affected by all of the four confining walls. In this case, the terminal velocity of a rising bubble through a rectangular confinement might be compared to the terminal velocity of a rising bubble in a circular tube with an equivalent diameter as the hydraulic diameter of the rectangular confinement. However, the flow motion around a bubble in a rectangular confinement is different from the one in a circular tube with the hydraulic diameter of the rectangular cross section. The confining walls and the corners of the rectangular geometry affect the rising bubble in a rectangular

confinement (varying wall distance). Hence, the bulk flow distribution is not uniformly distributed around the bubble. Therefore, the confining wall drag force and bubble terminal velocity are not the same in these two confinement cases.

Shapira and Haber (1988) conducted a theoretical investigation of rising air bubbles in between two parallel plates assuming a creeping flow regime. For a stationary fluid medium and spherical air bubble shapes, the momentum equation was solved and the drag force on the rising bubble was derived such that:

$$F_{D-plates} = 2\pi\mu_f V_{t-plates} R \left(\frac{2+3\kappa}{1+\kappa}\right) k_{w-plates} \tag{2-55}$$

$$k_{w-plates} = \left(1 + \frac{2+3\kappa}{1+\kappa}\frac{2R}{w} C_d\right) \tag{2-56}$$

where $k_{w-plates}$ is the confining wall factor for the effect of parallel plates of w distance from each other, $F_{D-plates}$ is the drag force on the spherical bubble passing through two parallel plates and $V_{t-plates}$ is the terminal velocity of spherical bubble rising in between two parallel plates with a stationary fluid. The C_d parameter in Eq. (2-56) is dependent on the distance from the center of the rising bubble to the nearest plate. For bubbles rising along the centerline of the parallel plates, C_d = 1.338 was obtained by Shapira and Haber (1988). By assessing a balance of forces on the rising bubble, terminal velocity of a spherical bubble moving in the centerline between two parallel plates can be derived as (Shapira and Haber 1988):

$$V_{t-plates} = \frac{2gR^2(\rho_f - \rho_g)}{3\mu_f k_{w-plates}} \frac{(1+\kappa)}{(2+3\kappa)} \tag{2-57}$$

The correlations in Eq. (2-55) to Eq. (2-57) (Shapira and Haber 1988) only assumes spherical bubbles and it cannot be used for elongated bubbles. In addition, this prediction is limited to a stationary fluid and does not consider the effect of co-flow/counter flow of the surrounding fluid medium on the bubble terminal velocity. Even though the wall correction factors introduced in Eq. (2-50) are mostly used in the literature as the wall correction factor for circular bubbles rising through circular tubes, Table 2-1 summarizes the other wall correction factors reported in the literature, for different flow regimes.

Table 2-1- Wall correction factors

Author	Wall correction factor (k_w)	Remarks
Clift, R., Grace, J.R., Weber (1978)	$k_w = \frac{1}{1 - 1.6\lambda^{1.6}}$	$100 \leq Re \leq 10000, \lambda \leq 0.6$
Di Felice (1996)	$k_w = (\frac{1 - \lambda}{1 - 0.33\lambda})^{\alpha}$ $\frac{3.3 - \alpha}{\alpha - 0.85} = 0.1Re$ $\alpha = 2.7$ $\alpha = 0.85$	$Re \leq 200, 0.08 \leq \lambda \leq 0.7$ Viscous flow Turbulent flow
Kehlenbeck & Di Felice (1999)	$\frac{1 - \lambda^p}{1 + (\frac{\lambda}{\lambda_0})^p}$ $\frac{\lambda_0 - 0.283}{1.2 - \lambda_0} = 0.041Re^{0.524}$ $p = 1.44 + 0.5466Re^{0.434}, Re \leq 0.35$ $p = 2.3 + 37.3Re^{-0.8686}, Re \geq 0.35$	$0.2 \leq Re \leq 185, \lambda \leq 0.6$
Achenbach (1973)	$k_w = \frac{1 + 1.45\lambda^{4.5}}{(1 - \lambda^2)^2}$	$Re \leq 105, \lambda \leq 0.92$
Munroe (1889)	$k_w = 1 - \lambda^{1.5}$	$943 \leq Re \leq 11000, 0.11 \leq \lambda \leq 0.83$
Francis (1933)	$k_w = (\frac{1 - \lambda}{1 - 0.475\lambda})^4$	Viscous flow

To predict the effect of rectangular confinement on bubble terminal velocity, the rectangular geometry can be simplified into two cases of parallel plates. A schematic of a bubble rising in a rectangular channel along with a net co-flow is shown in Figure 2-5(a) and Figure 2-5(b). In the figure, V_{t-rect} is the bubble terminal velocity as rising through a rectangular channel, V_y is the parabolic velocity profile of the bulk flow, w is the width of the channel, t is the channel thickness, R is the bubble radius and a_{xy} and a_{yz} are the distances between the center of the bubble to the nearest plate in xy and yz planes, respectively. This simplification, however, does not consider the confining effect from the corners of the rectangular cross-section on the motion of the rising bubble. Thus, the theory of parallel plates needs to be modified to address the complex flow around the bubble in the rectangular geometry (wall effect) and the effect of co-flow/co-current flow.

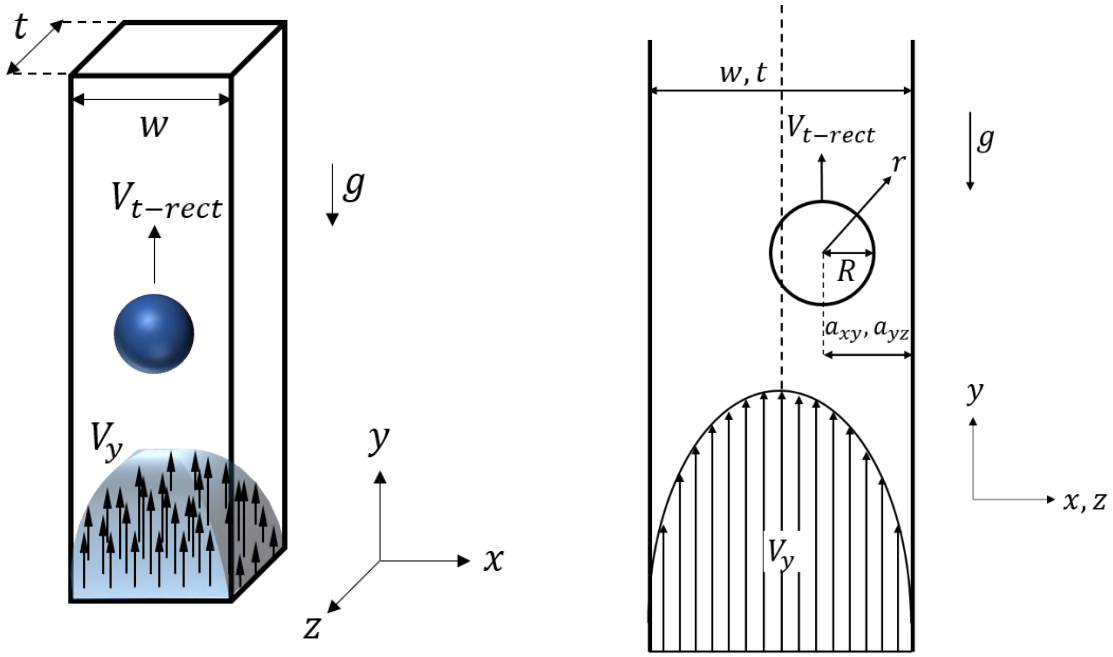

(a) (b)

Figure 2-5- Single air bubble rising in a co-flow through a rectangular channel (a) 3 dimensional view, and (b) 2 dimensional view of xy and yz planes.

Figure 2-5 (a) shows the rise of a single bubble in a rectangular channel that is simplified to two cases of infinite parallel plates (Case A and Case B) and both cases are shown in Figure 2-5 (b). For Case A, the channel is viewed from xy plane where w (width) is the distance between the two plates and Case B is the yz view of the parallel plates with t (thickness) distance between the two plates. For this simplification and neglecting the interaction between the two cases, one wall correction factor can be derived for either of the two cases of parallel plates following Shapira and Haber (1988). Each wall function depends on the bubble size and distance between the two parallel plates. The wall correction factors based on channel thickness and channel width are termed k_t and k_w which can be derived from Eq. (2-56). These wall correction factors are used to obtain a total wall factor that is needed to modify the bubble terminal velocity in an infinite fluid medium for rectangular confining geometry, as shown in Eq. (2-50).

In the present study, the experimental data of bubble terminal velocity in the confined rectangular geometry is used to develop a total wall factor. Using the total wall factor and implementing the flow motion effect, the effect of fluid co-flow on bubble terminal velocity is determined. Having this, the current available model for parallel plates is modified. The model modification is undertaken in two steps; one to consider the effect of the rectangular geometry (confining wall effect), and another step for including the fluid co-flow contribution.

The rising bubble in the rectangular channel has inevitably three dimensional flow effect, because of the asymmetrical flow distribution around the rising bubble. For the model modification based on the rectangular geometry, the total wall correction factor, f, is expressed as a function of the normalized bubble diameter $\lambda = 2R/D_h$, where D_h is the hydraulic diameter of the cross section of the channel, and wall factors k_t and k_w.For a rectangular geometry, the hydraulic diameter is defined as:

$$D_h = \frac{4A}{P} \tag{2-58}$$

where A is the cross-sectional area of the rectangular confinement and P is the perimeter of this cross-section.

The total wall correction factor is used to predict the bubble terminal velocity in the rectangular confining geometry as the first step of the model modification, as shown in Eq. (2-50). Examining several functions that could potentially be chosen for this modification, an exponential function of $\lambda = 2R/D_h$ was chosen to express the total wall correction factor for the rectangular channel. This function, which provided a better trend among the other functions to match the experimental data (data are provided in Chapter 4), is:

$$f = \frac{k_w k_t}{\eta \exp(-(\lambda - \beta)^2)} \tag{2-59}$$

Here, η and β are constants that will be derived by conforming the data from the predicted model to the experimental results.

To include the effect of co-flow on the bubble terminal velocity, the bubble is assumed to rise in a circular tube with a diameter that equals the hydraulic diameter of the rectangular cross section (D_h). Therefore, the terminal velocity of the bubble in a rectangular channel is adjusted by considering the flow velocity as shown in Figure 2-6. Since the fluid flow between the bubble and the confining walls is interacting with the bubble interface, the value of fluid velocity at R (bubble radius) distance from the centerline of a circular tubes of D_h diameter (assuming a parabolic velocity profile) is considered to address the effect of fluid co-flow on the bubble terminal velocity:

$$V_{yR} = (1 - \lambda^2)V_{f-max} \tag{2-60}$$

where V_{f-max} is the maximum fluid velocity at the centerline and V_{yR} is the flow velocity at R distance from the centerline of a tube of D_h diameter. To determine the contribution of V_{yR} on the bubble terminal velocity, a coefficient ζ can be multiplied to the V_{yR}, which needs to be derived based on the experimental data. As a result, the total predicted bubble terminal velocity V_{t-rect} in a rectangular channel can be introduced by considering the effect of rectangular geometry from Eq. (2-59) and fluid co-flow from Eq. (2-60) as:

$$V_{t-rect} = \frac{1}{f} \times \frac{2gR^2(\rho_f - \rho_g)}{3\mu_f} \frac{(1 + \kappa)}{(2 + 3\kappa)} + \zeta(1 - \lambda^2)V_{f-max} \tag{2-61}$$

where the effect of fluid co-flow, $\zeta(1 - \lambda^2)V_{f-max}$, is superposed with the corrected bubble terminal velocity in a rectangular geometry (Haberman and Sayre 1958). To implement this model for V_{t-rect}, experimentaly derived values for f and ζ need to be determined. In chapter 4, the experimental data of bubble terminal velocity through a rectangular confinement are presented, and hence the values of f and ζ will be determined.

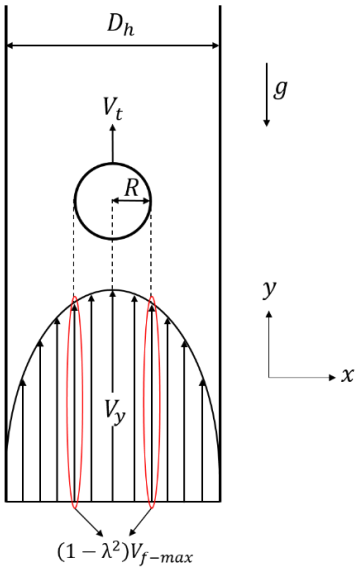

Figure 2-6- Surrounding fluid velocity at the *R* distance from centerline of confining medium

2.3 Conclusion

A theoretical model based on the general solution of flow around a bubble in infinite fluid medium available in the literature, and applying relevant boundary conditions was developed to predict the stream lines around a bubble rising through a rectangular channel. Since the bubbles were assumed to be spherical for solving the Navier-Stokes equations, this prediction does not work for relatively large bubbles, compared to the confining geometry when the bubble flow becomes affected by the confining walls. The theoretical streamlines in the flow around bubbles is used to calculate the tangential velocity at the bubble interface and will be compared against the experimental data in Chapter 5. An empirical model was developed for the terminal velocity of the bubble, which includes the effect of rectangular confining geometry and fluid co-flow. In Chapter 4, the experimental data of bubble terminal velocity are used to determine the unknown coefficients in the predicted model for bubble terminal velocity through rectangular confinements.

CHAPTER 3. EXPERIMENTAL SETUP

Two configurations of experimental setups were developed to investigate the passage of bubbles and oil droplets of different sizes through a vertical rectangular confining geometry. For capturing the bubble acceleration and deceleration on entering and exiting the rectangular confinement, a relatively large field of view (FOV) of 65.87 mm × 84.74 mm was provided in the experimental setup and results are presented in Chapter 4. This allowed a larger range of bubble movement in the flow channel. However, in Chapter 5 and 6, where the flow motion around rising bubbles and flow around and inside rising droplets through a rectangular confinement are investigated, an experimental setup with relatively small FOV of 7.28 mm × 9.11 mm was chosen. This relatively small FOV provided a relatively higher resolution in the images to investigate the details of the fluid flow motion in the continuous phase.

In this chapter, the typical optical measurement techniques are discussed. The flow channel used in the experiments is described in detail along with the geometry of the rectangular confinement. The experimental setup configuration and components are described in the following sections. Image processing approaches and some examples of processing results are provided in this chapter, and uncertainty analysis is discussed in the last section.

3.1 Experimental setup to study rising bubbles and droplets

A PSV, or back-light illumination approach was employed to capture the motion of bubbles rising through the flow cell. Figure 3-1 shows a schematic of a shadowgraph setup for the experiments. The optical setup contained a high speed camera (CMOS SP- 5000M – PMCL, JAI

Inc.) with 2560 pixel × 2048 pixel resolution capable of capturing up to 134 frames-per-second along with a macro lens (Sigma 105 mm f/2.8 EX DG) and an LED (BX0404, Advanced Illumination Inc.) source to provide illumination. The camera was operated with an exposure time of 20 μs to freeze bubble motion and camera frame rate was controlled using a function generator (AFG3021B, Tektronics Inc.). The LED source was aligned on the same optical axis as the camera at the back of flow cell to provide uniform illumination over the region of interest. A field of view (FOV) of 65 mm × 85 mm was captured in the experiments to investigate the bubble acceleration/deceleration as entering and exiting the rectangular confinement. A function generator with square waves, amplitude of 5 Vpp and offset of 2.5 V was used to set the imaging frequency of the camera.

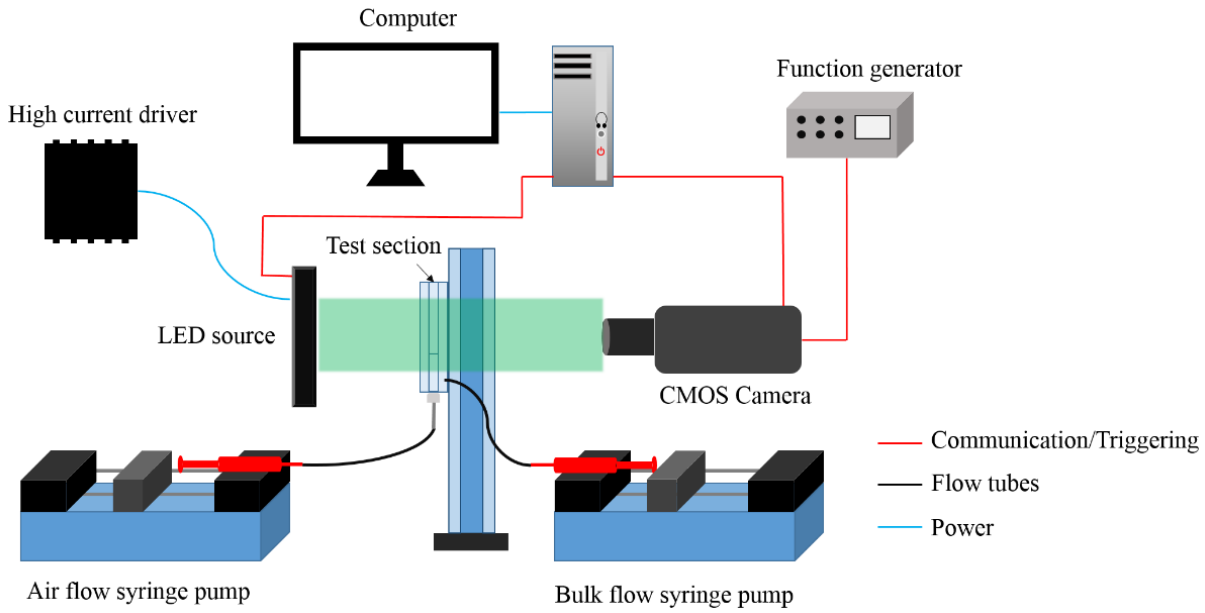

(a)

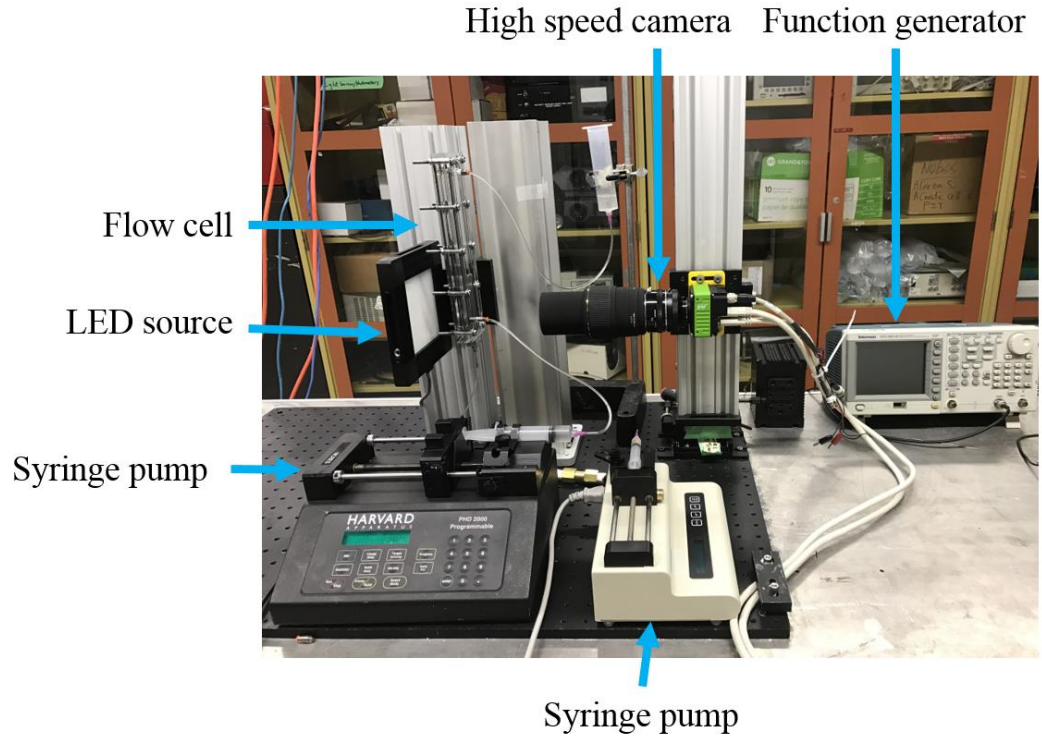

(b)

Figure 3-1- A (a) schematic of the shadowgraph experimental setup (b) image of the actual system in operation

3.1.1 Camera

A high speed camera (CMOS, SP-5000M-PMCL-CX; JAI Inc.) with 2560 × 2048 pixel^2 resolution capable of running up to maximum of 134 frames per second rate was employed. The specifications of the camera are provided in Table 3-1. In the experimental configuration with relatively smaller field of view (7.28 mm × 9.11 mm), an extension tube was added to the macro lens to increase the magnification and hence provide a smaller field of view. The depth of field of the camera for the two experimental configurations with 7.28 mm × 9.11 mm and 84.74 mm × 65.87 mm fields of view was 0.025 mm and 2.192 mm respectively. A summary of exposure time and frame rates used in different experiments is presented in Table 3-2. The frequency of the camera in different experiments was chosen in a way that the maximum displacement of the tracer particles in between sequential images be between 3 to 5 times bigger than the tracer particles diameter.

Table 3-1- The high speed camera specifications

Resolution	2560 × 2048
Pixel size	5 µm
Total pixels	5,242,880
Sensor type	CMOS
Maximum flow rate	134 fps
Shutter speed	10μs to 8 s
Frame rate used in this experiment	90fps
Exposure mode	Timed
Exposure time	20 to 60 µs
Frame start trigger mode	on
Gain	100 units

Table 3-2- Summary of exposure time and imaging frequency used in different experiments

Experiment	Flow rate (ml/hr)	Exposure time (μs)	Imaging frequency (fps)
Rising bubble, FOV of 7.28 mm × 9.11 mm	All	30	60
Rising bubble, FOV of 65.87 mm × 84.74 mm	All	20	8
Rising oil droplet	20	60	30
	40	60	45
	60	60	70
	100	60	90
	150	60	90

3.1.2 LED

In all optical diagnostics setups, a source of illumination, such as a LED or laser, is necessary to freeze the motion of tracer particles in the fluid flow. In this study, a green LED (BX0404, 4" × 4" Side-Fired LED Back Light) source was employed. The LED source was running at continuous mode and at maximum illumination power.

3.1.3 Flow cell design

An experimental setup was developed to investigate the passage of bubbles and oil droplets through a vertical rectangular confining geometry. A variety of bubble sizes were generated to investigate the effect of walls on the rising velocity and shape of bubbles. Figure 3-2(a) shows the 60 mm × 250 mm flow cell design, which consisted of a flow channel sandwiched between two side PMMA windows confining the flow channel and developing the required rectangular shape. The flow channel (5.84 mm depth, Optix acrylic; Plaskolit Inc.) was manufactured using a commercial laser cutter (VersaLaser VLD Version 3.50; Universal Laser Systems) which

provided flexibility in shaping the geometry of the flow channel and hence the experimental design. An inlet orifice of 4 mm diameter were used to inject the working fluid into the flow channel via the rear window relative to the camera view and a similar orifice was used for flow outlet as shown in Figure 3-2(a). An inlet tube was connected to a syringe which was mounted on a syringe pump (‘11’ Plus, Harvard Apparatus Inc.). Air was injected through a nozzle into a fluid medium to create a bubble. To generate bubbles of different sizes, 1/16” gas injection needles with different internal diameters were employed and located in the bottom of the flow channel through the air injection hole as shown in Figure 3-2(a). The solid model of this flow channel with all necessary dimensions are provided in Appendix A-3.

The geometry shown in this figure allows both the parallel plate and rectangular cross-section correlations to be assessed. Figure 3-2(b) shows the different flow regions in the flow cell including a parallel plate region (PPR) (22 mm × 5.84 mm, width × thickness) before and after a rectangular cross sectional region (RCSR) (3 mm × 5.84 mm, width × thickness). The flow cell was mounted vertically in the experimental setup and the bulk flow direction was opposite to the gravity.

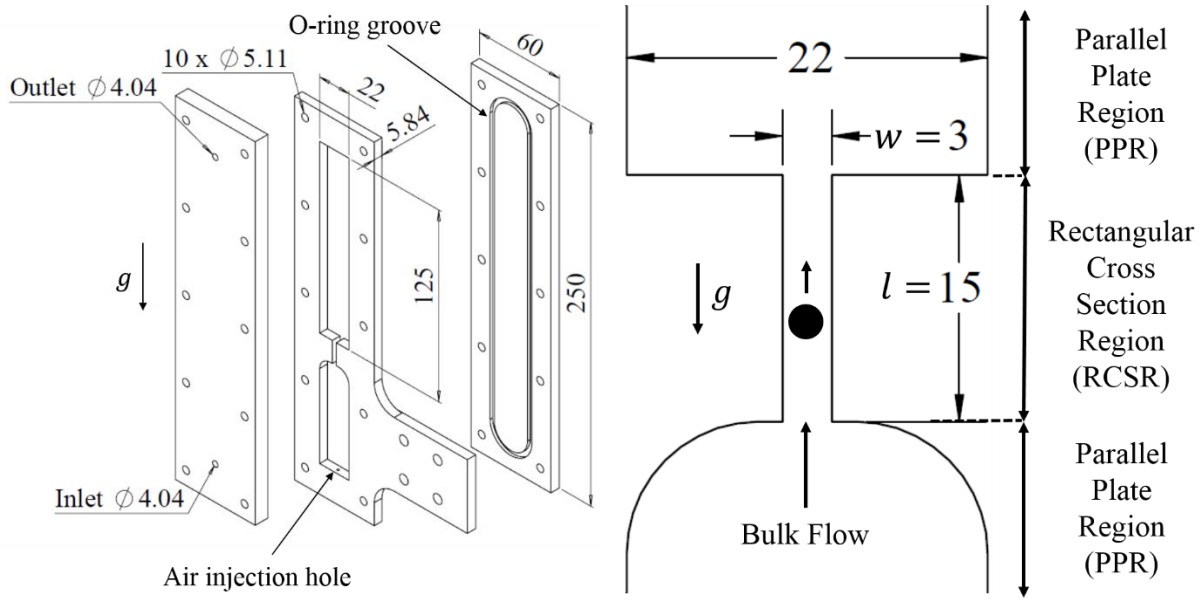

(a) (b)

Figure 3-2- Flow cell design for investigating flow around air bubbles; (a) a disassembled solid model of the flow channel, (b) details of the 2D flow geometry, which has a constant depth of 5.84 mm. All dimensions are in mm

Figure 3-3, which shows an image of the actual constructed flow channel, indicates that the flow channel was mounted vertically in the experimental setup and the flow direction of bulk fluid and fluid particle (bubble and/or oil droplet) is in the opposite direction of gravity. To avoid fluid leakage from the bottom of the flow channel, a needle holder, shown in Figure 3-3, was made via 3-D printer and glued to the flow channel. The injection needles were put into the bottom of the flow channel through the needle holder.

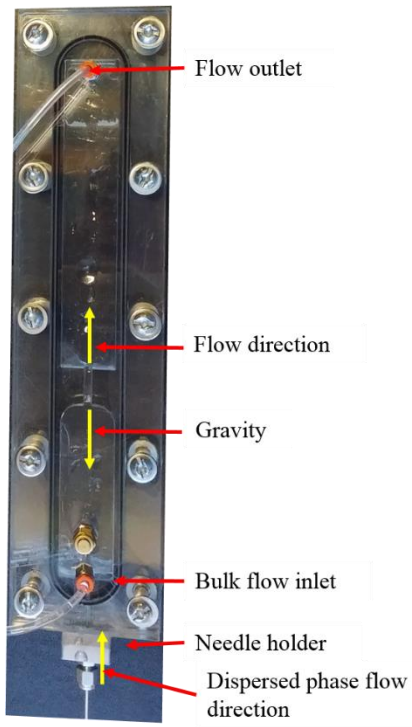

Figure 3-3- Picture of the constructed flow cell

3.1.4 Control fluid and flow rate

Five bulk flow rates of fluid medium were provided to flow along with bubble in the flow cell. To address the average bulk flow rate in different sections of the flow channel, fluid flux q is defined using fluid flow rate Q:

$$q = \frac{Q}{A} \tag{3-1}$$

where, A is the cross-sectional area. The fluid flux q is same as the local average fluid velocity through the rectangular cross-section. A separate experiment was ran for five different inputs to the bulk flow syringe pump and the fluid flux, q, was calculated based on the measured velocity profile. Since the cross-sectional area of the RCSR is smaller than PPR, for a constant fluid flow rate (Q) the fluid flux (q) would be different for the PPR and RCSR, and these are listed in Table

3-3. For a rectangular confining geometry and assuming a parabolic velocity profile for the fluid, the maximum fluid velocity is 1.5 times of the average fluid velocity and the flux q can be rewritten as (White 2011):

$$q = \frac{2}{3} V_{f-max} \tag{3-2}$$

Table 3-3- Fluid fluxes (q) at different regions of the flow channel

	Cross sectional area	
	PPR (22 mm × 5.84 mm)	RCSR (3 mm × 5.84 mm)
q (mm/s)	0.05	0.34
	0.09	0.67
	0.15	1.07
	0.24	1.78
	0.36	2.64

A water/glycerol solution was used as the working fluid for which a relatively high dynamic viscosity of 0.4 Pa.s was chosen to provide a creeping flow regime. Since the viscosity of the fluid is a function of temperature (Segur and Oberstar 1951), the working area temperature was measured in 3 consecutive days (average temperature was 19.8 °C) for calculating the water/glycerol solution viscosity. By interpolation of data acquired from glycerol/water solution viscosity tables (Segur and Oberstar 1951), a Newtonian solution of 93 wt% glycerol/water was selected to have the chosen dynamic viscosity.

In the rising droplet experiment, the refractive index (*RI*) of both fluid phases should have been matched. Hence, two fluids with the same refractive index should have been selected. Even though in the droplet rising experiment the *RI* was the most important factor, the viscosity of the working fluid should still be high enough to slow down the fluid flow and hence the camera can

capture the movement of the tracer particles in between frames. Different available fluids were selected and *RI* of each was measured by a refractometer (Abbe-3L, Bausch and Lomb) and a summary of results is shown in Table 3-4.

Table 3-4- *RI* of different fluids measured by the refractometer

Fluid	*RI*
Soybean oil	1.4740
Canola oil	1.4730
Glycerol	1.4723

RI of a salt solution, such as sodium iodide (NaI), depends on the solution temperature, salt concentration and wavelength (Narrow, Yoda, and Abdel-Khalik 2000). In this experiment, aqueous salt solutions of Potassium thiocyanate (KSCN) were also prepared by mixing different concentrations of KSCN into deionized water (Appendix A-1). Based on the correlation found for RI of KSCN in terms of concentration, a KSCN solution of 62.85 wt % (*RI* = 1.4730) was chosen as the working fluid and glycerol as the oil droplet. However, since the viscosity of KSCN solution was not high enough, leading to relatively high droplet motion, the camera was not able to capture the movement of tracer particles inside the glycerol droplet. Also, the tracer particles did not mix homogenously into the KSCN solution.

For this experiment, glycerol was selected as the working fluid canola oil as the rising oil droplet. The Canola oil viscosity was measured as 0.0738 Pa.s, using Rotational Rheometer (Rheolab QC, Anton Paar GmbH) with double gap measuring cup (DG42, Anton Paar GmbH). (Appendix A-2). The density of Canola oil was also measured as 0.915 kg/m^3 using Force Tensiometer (K100, KRUSS Scientific Instruments, Inc.) with the measuring probe for density

measurements (DE0601, KRUSS Scientific Instruments Inc.) (Appendix A-2). The physical properties of the glycerol used in these experiments are provided in Table 3-5.

Table 3-5- Physical properties of Glycerol

Property	Description
Chemical name	Glycerol
Synonym	Glycerin
Linear formula	$HOCH_2CH(OH)CH_2OH$
Molecular formula	$C_3H_8O_3$
Formula weight	92.09
Physical form	Viscous liquid
Density	1261 kg/m^3
Color	Clear
Dynamic viscosity	1412 kg/(m.s)

3.2 Tracer particles

The principle of PIV and PTV is based on deriving the displacement of tracer particles in a fluid flow in a short time interval (Raffel et al. 1989). Tracer particles should follow the fluid flow, since the velocity vector field of the fluid flow is derived according to the movement of the tracer particles. A criteria describing how well tracer particles follow the fluid flow can be derived based on the Stokes number, Stk, which is defined as (Brennen 2005):

$$Stk = \frac{\tau_p U}{d_p} \tag{3-3}$$

where τ_p is the time response of the particle, d_p is the particle diameter and U is the fluid velocity in the upstream. The time response of the particle is the time needed for the particle at zero velocity to reach 62 % of fluid velocity (Novotny and Manoch 2012):

$$\tau_p = \frac{\rho_p d_p^2}{18\mu_f} \tag{3-4}$$

where $\rho_p$is the fluid density and μ_f is the fluid dynamic viscosity. Combining Eq. (3-3) and Eq. (3-4) the Stokes number could be written as:

$$Stk = \frac{\rho_p d_p U}{18\mu_f} \tag{3-5}$$

As Eq. (3-5) shows, the Stokes number depends on the characteristics of fluid flow (μ_f and U) and particle (ρ_p and d_p); hence, proper tracer particles should be selected so they can follow the fluid flow motion.

The settling velocity of particles in a fluid is (Novotny and Manoch 2012; Raffel et al. 1989):

$$U = \frac{2gR^2(\rho_f - \rho_p)}{3\mu_f} \tag{3-6}$$

which shows that the settling velocity of the tracer particles depend on the density of particles and density and viscosity of the fluid. Therefore, the density of the particles and fluid should be close enough in order that particles suspend in the fluid. As reported in the literature, as long as $St << 1$, the particles follow the fluid flow motion (Novotny and Manoch 2012).

3.2.1 Hollow glass sphere particles of 7 μm size

To investigate the velocity vector field around single air bubbles, hollow glass microsphere particles (110P18, Potters Industries LLC, USA) were used. In the rising bubble experiment with relatively smaller field of view (Chapter 5), only the working fluid was seeded with tracer particles, while for the rising oil droplet (Chapter 6), both of oil droplet and surrounding fluid were seeded with identical tracer particles. Table 3-6 summarizes physical properties of the hollow glass particles used in these experiments. The tracer particles were mixed in the glycerol/water solution before injecting into the flow cell as tracer particles to study the motion of the fluid around the rising bubble. After mixing the tracer particles into the working fluid, the solution was left stationary for 72 hours to separate particles of lighter and heavier weight than the working fluid. Tracer particles and the working fluid at the middle part of solution were selected to be injected into the system. This resulted in tracer particles of 1 to 3 pixels in size in the images captured for the two fields of view investigated in this study. Figure 3-4 shows a sample image of fluid flow seed with hollow glass sphere particles of 7.0 μm mean diameter.

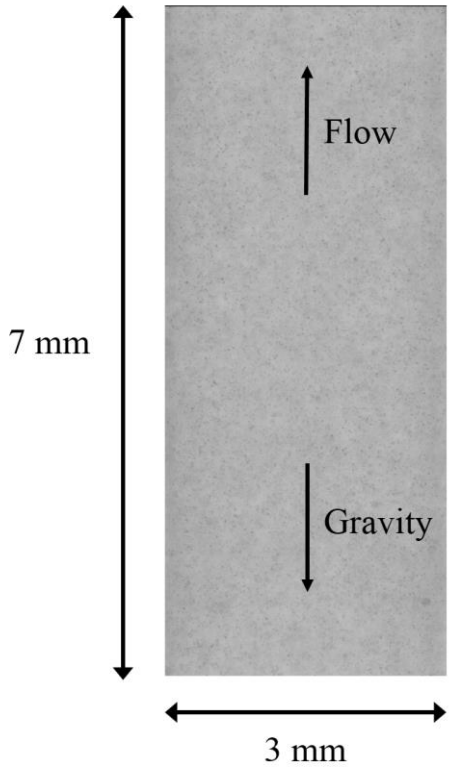

Figure 3-4- Example image of fluid flow seeded with hollow glass sphere particles

For the rising bubble experiment, the Stokes number (Eq. (3-5)) was calculated based on the particle properties presented in Table 3-6, the maximum bulk flow rate (150 ml/hr) and the glycerol/water solution dynamic viscosity of 0.4 kg/(m.s). Since the Stokes number was 4.4×10^{-11} and was much smaller than 1, the tracer particles will follow the expected fluid motion.

Table 3-6- properties of 7 µm particles used in the bubble rising experiment

Property	Description
Mean diameter	7.0 µm
Shape	Hollow non-porous microspheres
Color	White
Composition	Fused Borosilicate Glass (ASTM C169)
Density	1.10 ± 0.05 g/cc
Bulk density	0.49 g/cc
Maximum working pressure	10000 psi

3.2.2 Microbeads particles of 10 µm diameter

For the rising droplet experiment, Microbeads particles (Dynoseeds® TS 10, product of Microbeads ASP. O. Box 265, N-2021 Skedsmokorset, Norway) of 10 µm diameter and 1.05 g/cc density were mixed in the glycerol and canola oil before injecting into the flow cell as tracer particles to study the motion of the fluid. The mixing procedure was the same as for hollow glass sphere particles explained in section 3.2.1. Table 3-7 summarizes the properties of microbeads particles used in this experiment. The Stokes number was calculated based on the microbeads properties in Table 3-7, the maximum bulk flow rate (150 ml/hr), and the viscosity of canola oil (0.0738 kg/(m.s)) and glycerol (1412 kg/(m.s), (Segur and Oberstar 1951)). Therefore, the Stokes number was calculated as 2.345×10^{-10} and 9.83×10^{-15} for canola oil and glycerol respectively.

Table 3-7- Properties of 10mm microbeads tracer particles used in the rising oil experiment

Mean diameter	10.0 µm
Shape	microsphere
Color	White
Composition	Polystyrene
Density	1.05 g/cc

3.3 Optical measurement techniques

For a system of two-phase flow, experimental measurement approaches are employed to carry out detailed measurement of the flow (Crowe et al. 1997). Hence, the dispersed phase properties such as shape, size and rising/falling velocity, and details of the flow behavior in the surrounding fluid can be determined. As shown in Figure 3-5, these measurement techniques are mainly categorized as "sampling methods" and "on-line methods". Sampling methods are applicable in powder technology industries (Crowe et al. 1997). In this method, a couple of samples of the solid particles are collected and analyzed by using a microscope or other mechanical methods. As a result, geometric properties, such as equivalent diameter, surface area, and dimensions of the solid particles (powders) are obtained.

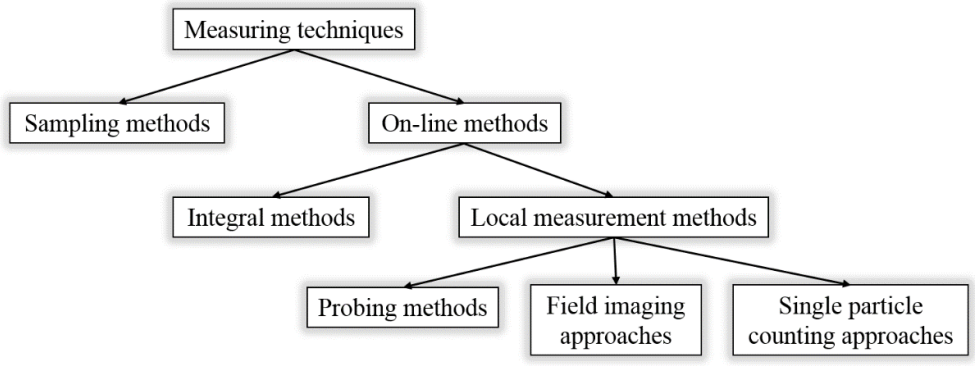

Figure 3-5- Classification of measurement techniques used for a two-phase flow system (Crowe et al. 1997)

Figure 3-5 shows that measurement techniques, typically, are classified into sampling methods and on-line methods (Crowe et al. 1997). In the on-line methods, the properties of both dispersed phase and working fluid can be obtained. Figure 3-5 demonstrates that on-line methods are classified into integral methods and local measurement methods. Integral methods provide averaged properties of a two-phase flow, while local measurement methods determine local properties of the flow with a relatively higher spatial resolution. For on-line methods, optical measurement techniques are mostly used. Probing methods are intrusive in nature meaning they disturb the fluid flow. However, field imaging and single particle counting approaches, such as particle image velocimetry (PIV), particle tracking velocimetry (PTV) and laser Doppler velocimetry (LDV), are nonintrusive optical measurement techniques (Crowe et al. 1997).

3.4 PIV measurement technique

Particle image velocimetry (PIV) is widely used in the experimental investigations of fluid mechanics as a nonintrusive optical measurement technique to study the fluid flows (Keane and Adrian 1990). The PIV method develops quantitative information of the fluid flow by determining the instantaneous flow field velocity (Ristic et al. 2004). As shown in Figure 3-6, a typical PIV setup contains a pulsed laser as the illumination source, and a camera to capture consecutive images of the flow. To study the fluid flow motion, tracer particles should be mixed into the fluid. The pulsed laser sheet illuminates the tracer particles, and the camera captures images of the illuminated tracer particles at certain time intervals (Keane and Adrian 1992). The collected images are analyzed to determine the displacement of the tracer particles in between the frames.

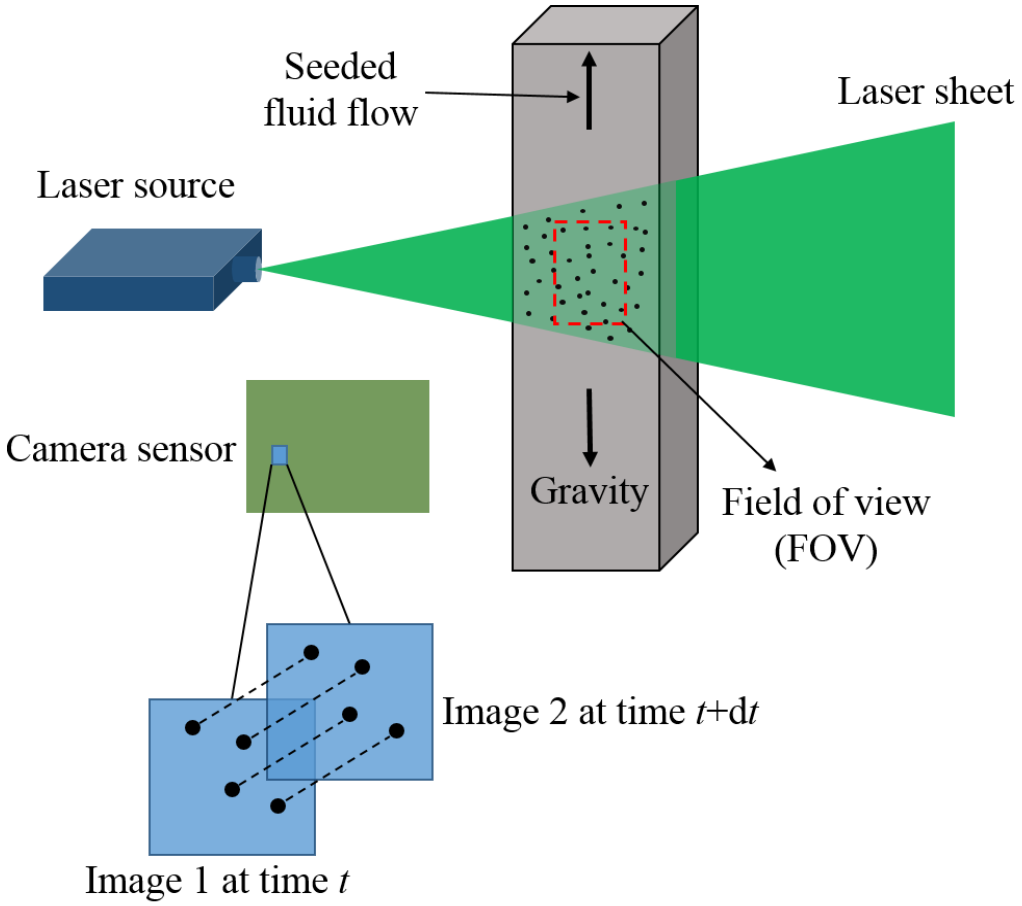

Figure 3-6- Schematic of a particle image velocimetry (PIV) measurement setup

A similar technique to PIV is particle shadow velocimetry (PSV), in which a low power light source, such as light-emitting diode (LED) is used for illumination. As indicated in Figure 3-7, a typical PSV technique is based back-lit illumination approach, meaning that an in-line illumination is provided by the light source onto the camera (Estevadeordal and Goss 2005). Hence, in contrast to PIV measurements, the shadow of particles appear in the PSV images.

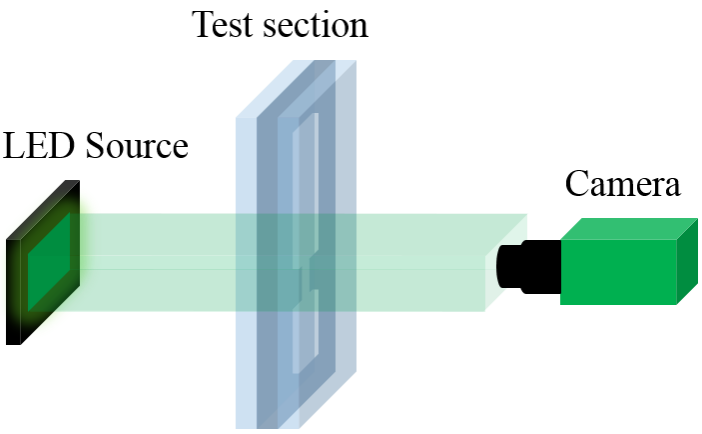

Figure 3-7- Schematic of a particle shadow velocimetry setup

Employing PIV techniques for multiphase flows is limited, since the phase boundaries can potentially restrict the optical illumination to the field of view (Brücker 2000). Figure 3-8 shows a PIV image of flow around an air bubble in still water (Brücker 2000). The light sheet scatters (reflections region in Figure 3-8) as it passes through the bubble and a shadow region appears behind the bubble. Also, a region of ghost particles occur inside the bubble because of the mirroring effect of phase boundary. In these regions of ghost particles, the particles cannot be detected and hence no velocity vector can be derived.

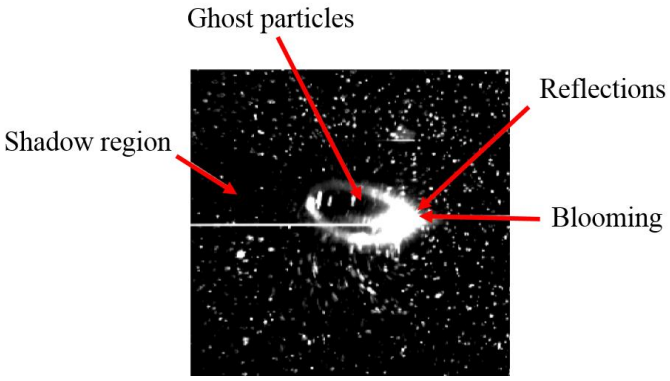

Figure 3-8- An example of PIV image showing light sheet reflection around a bubble (Brücker 2000)

Figure 3-9 indicates two example images of fluid flow with relatively low seeding density, Figure 3-9(a), and relatively high seeding density, Figure 3-9(b). Typically, for a low density image shown in Figure 3-9(a), individual tracer particles can be tracked in the images, which is referred as particle tracking velocimetry (PTV) processing. However, for an image with relatively high seeding density, Figure 3-9(b), images are split into smaller interrogation windows and the group of particles are correlated in each interrogation window, known as PIV processing. Therefore, in PIV image processing, a velocity vector is derived at each interrogation window over the images.

Since in PIV processing the images are scanned with interrogation windows of a particular size, the velocity vectors are given in the form of a regular grid. However, in PTV, one velocity vector is derived for each tracer particle, which results in a sparse data field rather than a regular gird.

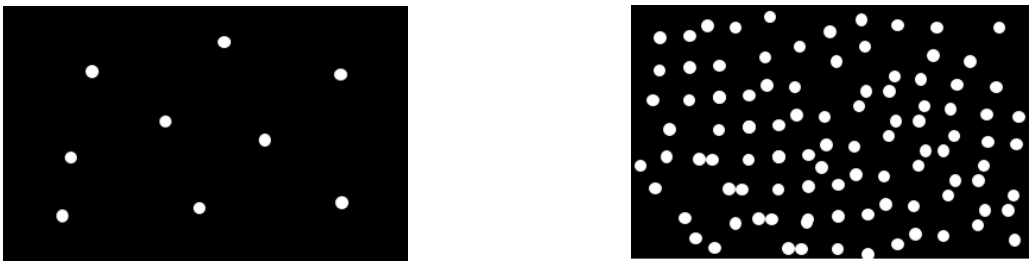

(a) (b)

Figure 3-9- Tracer particle distribution (a) low density (PTV) (b) medium density (PIV)

3.5 Matching refractive index

When optical diagnostic techniques, such as PIV, are employed for investigating a system of two phase flow, light reflections can appear in the images at the interface of the dispersed phase and the surrounding fluid (Budwig 1994). A common method for eliminating this light reflection

is matching the refractive index of the two phases (Budwig 1994). By using the matching *RI* method, light scattering in the images would be minimized and optical access to the measurement region of the fluid will be improved (Hassan and Dominguez-Ontiveros 2008).

3.6 Flow loop setup

The flow loop setup utilized in these experiments consisted of a flow channel, two connection tubes for flow inlet and outlet and two syringe pumps to inject the working fluid and dispersed phase flows. Many potential sources, such as electrical devices running, workers walking around etc., can create vibration to the system, which increases the errors in the results. To minimize the vibrations, the experimental setup was mounted on a steady optical table and the syringe pumps were mounted onto a separate table. The camera and flow cell were also mounted on two optical rails and the rails were secured directly to the optical table.

3.7 Image acquisition and processing

An in-house image acquisition code was developed to collect the images from the camera. Timing between images was set based on the camera frequency to capture images. Commercial software (DaVis 8.4.0, LaVision GmbH 2014) was used to process the collected images that mainly included two steps of image pre-processing and processing. Three processing approaches of PIV, PTV and particle recognition (shadowgraph) were undertaken in the commercial software (DaVis 8.4.0, LaVision GmbH 2014).

3.7.1 Shadowgraph image processing

Shadowgraph (particle recognition) processing (Ghaemi, Rahimi, and Nobes 2008) approach was undertaken to quantify the diameter and rising velocity of the bubbles in different locations of the flow channel. In this step, the bubble area determined based on image intensity difference between the fluid medium and the bubbles. After detecting the bubble area, the number of pixels in the projected bubble image were calculated. This was converted into physical dimensions and an equivalent area diameter (assuming a spherical bubble) was calculated. A minimal filter was used to determine the desired diameter range of bubbles that software should recognize. This eliminates bubbles of smaller sizes and gives information only on bubbles in the desired diameter range. Figure 3-10 an example raw image of a rising bubble through RCSR, Figure 3-10(a), along with the processed image, Figure 3-10(b). In Figure 3-10(b), bubble diameter equivalent diameter and the rising velocity are shown by D_{e-inst} and V_{r-inst} respectively.

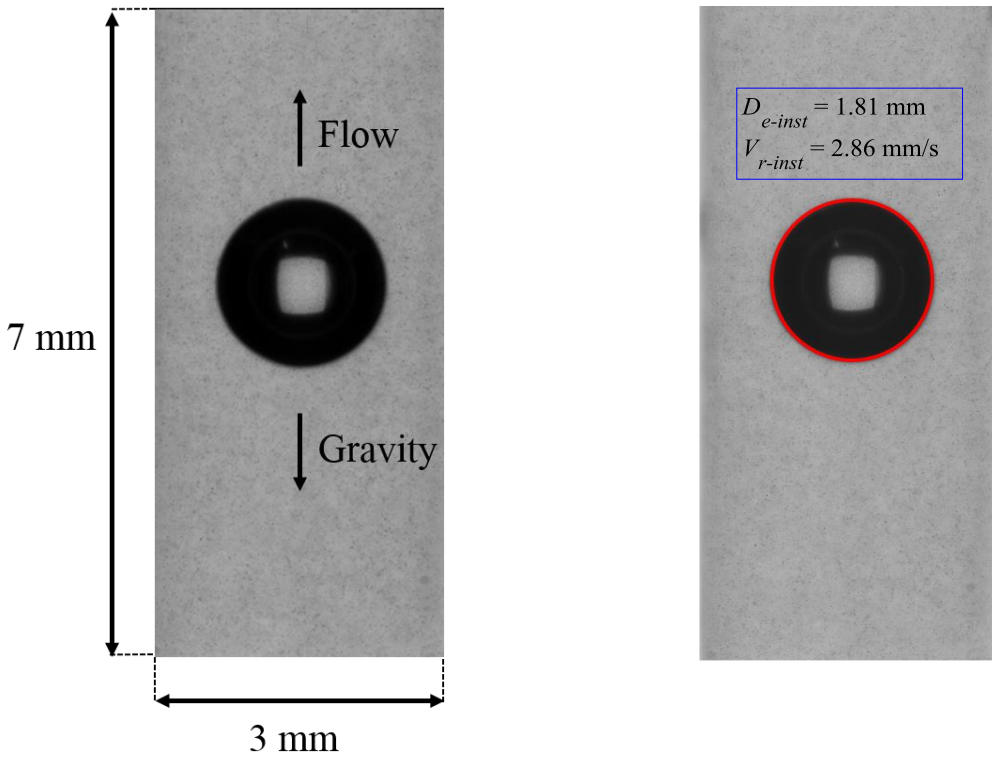

(a) (b)

Figure 3-10- Example of a (a) raw image of a single bubble rising through the RCSR, and (b) processed image with instantaneous bubble equivalent diameter (D_{e-inst}) and rising velocity of bubble (V_{r-inst})

3.7.2 PIV image processing algorithm

Inconsistent light illumination (Deen et al. 2010), background noise, existence of stagnant objects (Deen et al. 2010) and out of plane motion of tracer particles are some examples of problems that can affect image processing results, since the tracer particles in images will not be distinct enough for doing image processing. Image intensity was first inverted so that dark tracers became bright and vice versa, because the raw data was shadowgraph image. A "subtract sliding background" option was used to eliminate non-uniform light intensity. A specific value was subtracted from the intensity of the whole image to make the intensity of most parts of the background closer to zero. Figure 3-11(a) shows a sample image of raw data that was converted

to Figure 3-11(b) after the pre-processing step. Figure 3-11 shows that tracer particles are more distinct after preprocessing a raw data image. Since the intensity of the imaged particles in the fluid region was found to be relatively larger than the bubbles' intensities, a masking algorithm was employed to set intensities of lower than a certain value (around 40) to zero (masking out bubbles). In this way, the software will not process the area covered by bubble where there is no tracer particle.

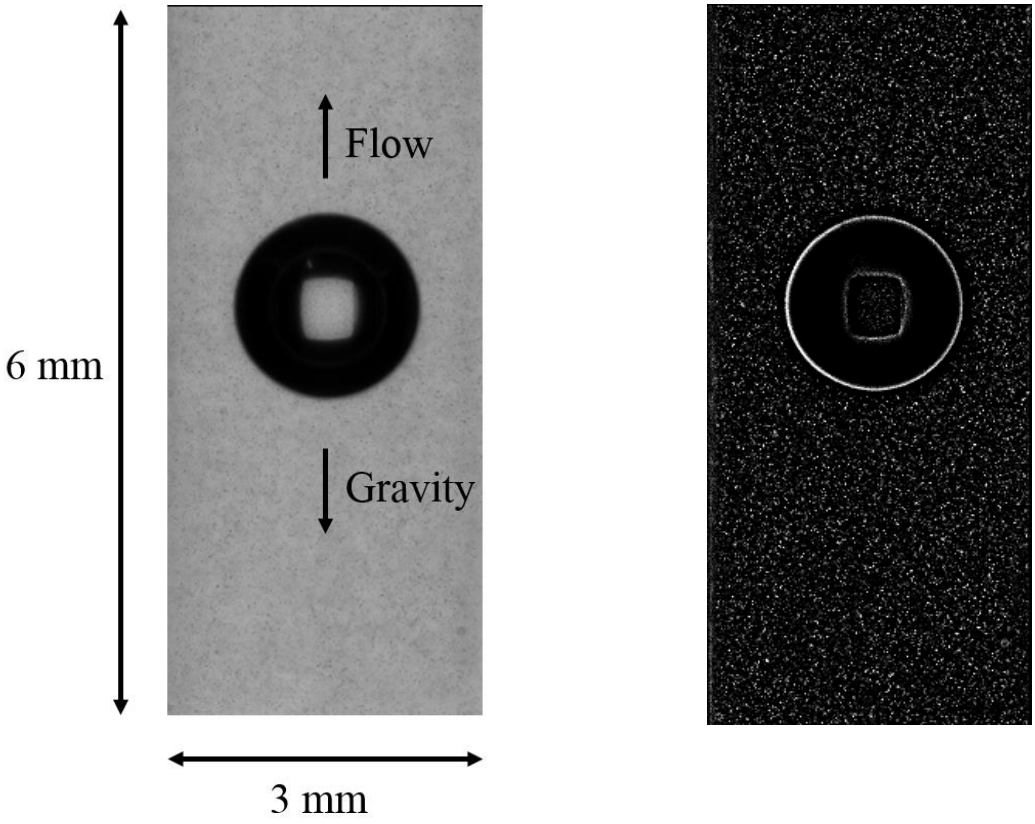

(a) (b)

Figure 3-11- Masking out unnecessary regions and particles recognition by image preprocessing (a) raw image (b) preprocessed image

To determine the relative velocity in the fluid medium, PIV analysis of the seed particles was undertaken. For PIV processing, a multi-pass cross-correlation with decreasing interrogation

window size processing scheme was used to determine the velocity field around single bubbles, and also velocity field inside and around oil droplets. The size of the interrogation windows can affect the results. Smaller interrogation windows can show more detail of the fluid flow motion, because as windows become smaller, the resolution of the derived velocity vectors increases. However, the number of tracer particles will be relatively lower inside the windows as they become smaller. Figure 3-12 compares two sample results of PIV processing with different interrogation window sizes. A 64×64 pixel^2 interrogation window followed by a 32×32 pixel^2 window was tried to process images, as shown in Figure 3-12(a). In the other processing approach shown in Figure 3-12(b), a large interrogating window of 128×128 pixel^2 was first used to capture large changes in the velocity field followed by a 64×64 pixel^2 window. Comparing the results represented in Figure 3-12(a) and Figure 3-12(b), the velocity vectors resulted from using relatively larger interrogation windows (Figure 3-12(b)) are relatively smoother. For each case shown in Figure 3-12(a) and Figure 3-12(b), the number of particles inside the smallest window size were counted as approximately 4 and 10 respectively. Because for the smaller interrogation window case shown in Figure 3-12(b), the number of particles are relatively less sufficient for having reasonable detection probabilities (Keane and Adrian 1992), the 128×128 pixel^2 window size followed by 64×64 pixel^2 window was employed in the PIV processing. Also, first and second interrogating windows were used with three and one passes respectively, and 75% window overlap in between sequential correlations.

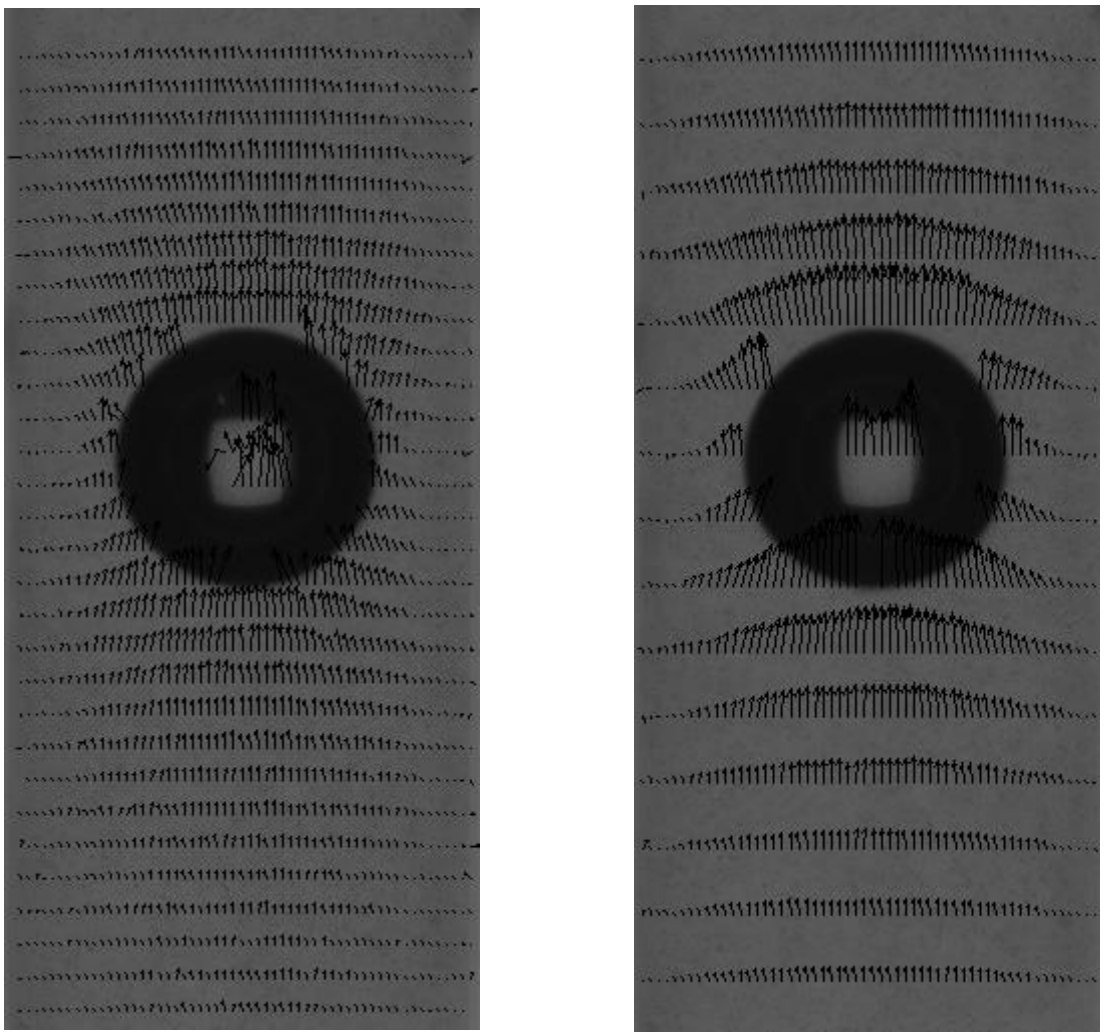

(a) (b)

Figure 3-12- PIV velocity field processing with interrogation windows of (a) 64 × 64 pixel^2 following by 32 × 32 pixel^2, and (b) 128 × 128 pixel^2 following by 64 × 64 pixel^2 size

Vector post-processing is a procedure that identifies and replaces vectors that are unlikely to be valid based on its spatial continuity and correlation strength. Here, a 3 × 3 pixel^2 median filter was used in the commercial software (Davis 8.4.0, LaVision GmbH) to remove outliers and iteratively replace them. Empty spaces were also filled up with velocity vectors by interpolation.

In this way, the velocity vector field was more consistent, allowing better process into instantaneous velocity map.

3.7.3 PTV image processing

PTV image processing, that takes into account the time resolve nature of the data collected, has been conducted in the commercial software (Davis 8.4.0, LaVision GmbH). In this processing, every tracer particle is tracked individually over time. Hence, after detecting each particle and eliminating the background noise, particles can be tracked in between sequential frames and results will be in the form of a sparse field of velocity vectors at the highest possible particle resolution. In PTV pre-processing, images were inverted similar to PIV pre-processing and a "subtract sliding background" and Gaussian smoothing operations were undertaken on the images to minimize noise in the images. For PTV processing, an intensity threshold was set as the particle minimum intensity in the images. A range of velocity for vertical and horizontal components of velocity were allowed based on the approximate particle displacement in between the frames. The tracer particles were tracked over 5 frames and the velocity was calculated.

In PTV processing, typically, tracking particles over more frames gives more confidence in the results. However, by tracking particles over a larger number of frames, some of the particles can disappear and hence the number of tracked particles can decrease (lower velocity vector resolution). In this study, by trial and error, the particles was chosen to be tracked over 5 frames to have a desired velocity vector resolution. Then the spatial coherence of the velocity vectors were checked to the vectors in the neighborhood. There are always gradients in the velocity vector field and the allowable velocity gradient should be checked. In this step, the allowed change in a velocity vector is chosen as a specified velocity gradient times the distance to a velocity vector in the

neighborhood to eliminate invalid vectors in terms of the allowable velocity gradient. For instance, assuming to have 0.1 pixel/pixels allowable velocity gradient, for two velocity vectors of 10 pixels distance, the velocity gradient should be 1 pixel. The sparse vector field can then be mapped onto a regular grid of results for the determination of other parameters.

PTV processing can give a better confidence in terms of validity of the velocity vectors in the results, because the tracer particles can be tracked over more than two frames, in contrast to PIV processing were the particle displacement is analyzed in between two frames.

3.7.3.1 Data post-processing

For further post-processing on the results of each processing approach and plot the results, in-house post-processing codes were developed and employed using commercial software (MATLAB, The Mathworks Inc.).

By employing PIV image processing in the commercial software (Davis 8.4.0, LaVision GmbH) the velocity vector field in the fluid medium was derived and the data were stored as *.VC7 file format. Two post-processing codes were developed to plot the velocity vector map around air bubbles (Appendix A-4), and inside and around rising oil droplets (Appendix A-5). An example of velocity vectors overlaid on a background color map of velocity magnitude is shown in Figure 3-13(a).

PTV processing results in a sparse data field and the background color map cannot be directly generated for velocity field. To derive the color map background of the velocity magnitude, the sparse data field from PTV processing should be converted onto a regular grid. An in-house code was developed to interpolate the sparse PTV data on a grid with 15 pixels resolution (closest distance between the vectors) (Appendix A-4 and Appendix A-5). Figure 3-13(b) indicates one

example of PTV sparse velocity vectors overlaid on the interpolated regular grid as the background color map.

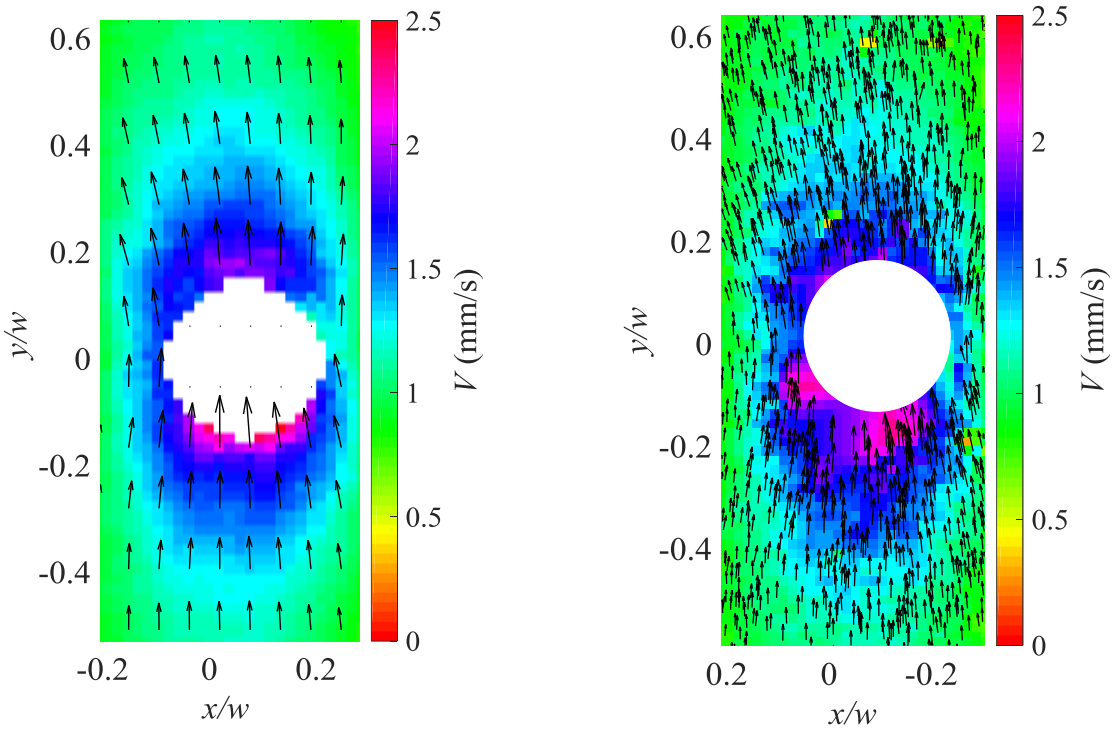

(a) (b)

Figure 3-13- An example of image processing for (a) PIV results with a background color map, and (b) PTV sparse vector field over a regular grid derived by data interpolation

3.8 Uncertainty analysis

In a measurement system, error is defined as the difference between a measured value and the real value (Wheeler and Ganji 2010). In the experiments, since the real value is not known, the error cannot be determined. Uncertainty of measurements is defined as an estimation of the range of error in measuring a quantity (Wheeler and Ganji 2010). In every experiments there are many sources of error, such as imprecision in measurement devices and variation in measured parameters, that may cause uncertainty in the measurement (Wheeler and Ganji 2010).

The uncertainty in experiments can be due to the measurements ("random uncertainty") and imprecision in measurement devices ("bias uncertainty" or "systematic uncertainty") and is usually reported with a confidence level. For instance, a 90 % confidence states that in 90 % of times that uncertainty is derived, the error is within the uncertainty range (Wheeler and Ganji 2010). For a measured parameter Y which is a function of n variables $x_1, x_2, \dots, x_n$, the total uncertainty is defined as (Wheeler and Ganji 2010):

$$u_y = \sqrt{\sum_{i=1}^{n} (\partial x_i \frac{\partial Y}{\partial x_i})^2} \tag{3-7}$$

where, ∂x_i is the uncertainty in variables and $\frac{\partial Y}{\partial x_i}$ is called the sensitivity coefficient of parameter Y respecting to each variable.

For a parameter x that is measured n times in a measurement, the standard deviation of x and standard deviation of mean of x, are respectively defined as:

$$S_x = \sqrt{\sum_{i=1}^{n} \frac{(x_i - \bar{x})^2}{n-1}} \tag{3-8}$$

$$S_{\bar{x}} = \frac{S_x}{\sqrt{n}} \tag{3-9}$$

The contribution of random uncertainty in the total uncertainty (Eq. (3-8)) can be determined as:

$$R_{\bar{x}} = \pm t S_{\bar{x}} \tag{3-10}$$

In Eq. (3-10), $R_{\bar{x}}$ is the random uncertainty and t is a parameter depending on n and can be determined from the literature (Table 6.6 in Wheeler & Ganji 2010). Figure 3-14 shows graph of random uncertainty and bias uncertainty for a parameter, x, that is measured more than once. In Figure 3-14, the Gaussian curve shows the distribution frequency of measurements. The mean value, $\bar{x}$, is different than the population mean and the bias ($B_{\bar{x}}$) and random ($R_{\bar{x}}$) uncertainties are quantitatively shown.

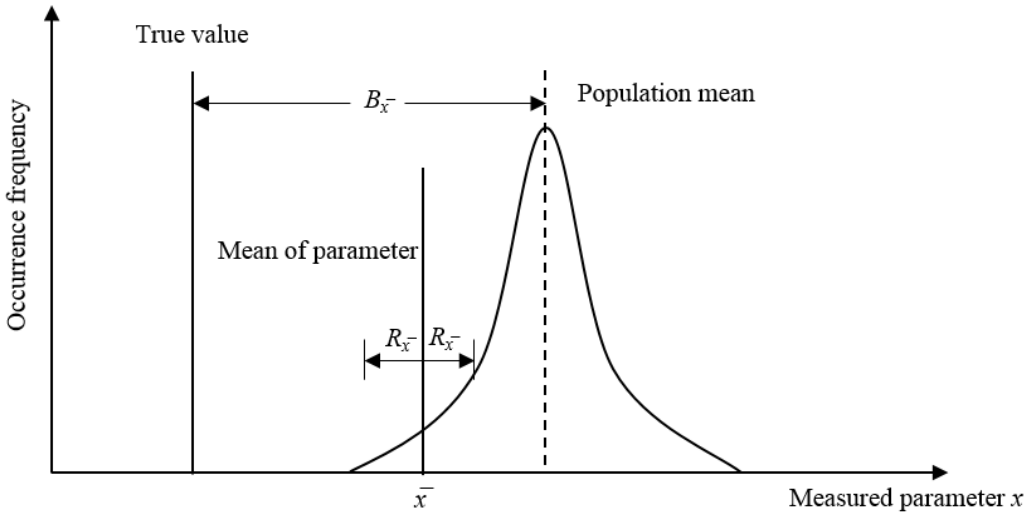

Figure 3-14- Graph of bias and random uncertainties for a measured parameter x

Hence, by deriving the contribution of bias and random uncertainties, the total uncertainty is derived as:

$$u_{\bar{x}} = \sqrt{(R_{\bar{x}}^2 + B_{\bar{x}}^2)} \tag{3-11}$$

3.8.1 Uncertainty in PIV measurements

PIV is a non-invasive optical measurement technique that quantifies the velocity field in a fluid flow (Charonko and Vlachos 2013). In PIV and PSV, the intensity of collected images contain noise, which can be caused by many potential sources, such as inconsistent illumination. In addition, there are other sources of uncertainty, such as image calibration and out-of-plane motion of the tracer particles. This noise can deteriorate the PIV cross correlation and hence increase the total uncertainty in the results (Charonko and Vlachos 2013).

Even though the PIV measurement technique has been gradually improved, the uncertainty of this method has not been widely investigated and quantified in a conclusive framework (Wieneke 2014). All of the components employed in a typical setup, such as camera and illumination, and different algorithms used for image acquisition and processing contain uncertainty. Due to the complexity of calculating the uncertainty of all of the elements, developing a method to quantify uncertainty in PIV is a challenging task.

A "surface uncertainty" method has been developed to quantify the uncertainty in PIV results (Timmins et al. 2012). In this methodology, four elements of velocity gradient (shear), particle size in the images, particle displacement and particle concentration were chosen and measured as the sources of error in a synthetic test case. Each of these four parameters were varied as an input and they were measured for each interrogation window. A PIV algorithm was developed to measure each parameter (particle concentration and etc.) in the synthetic images. By knowing the true value of each parameter, the error was calculated for each velocity vector in an interrogation window. In the "peak-ration" method, a relationship between uncertainty and the ratio of highest to the second highest correlation peak in synthetic data was obtained (Charonko and Vlachos 2013). In the "image matching" method (Sciacchitano, Wieneke, and Scarano 2013), a pair of images from tracer particles in motion are collected. The mean displacement of particles within an interrogation window is then calculated. If the interrogation window in the second image is shifted back onto the first window by the mean displacement, not all of the particles will superimpose. Therefore, some of the tracer particles might disappear in the second image because of out-of-plane motion of tracer particles (Sciacchitano et al. 2013). This residual distance between the particles (matched particle disparity) is the basis of estimating the uncertainty in the velocity vector field (Sciacchitano et al. 2013).

3.9 Conclusion

A description of optical measurement techniques was provided in this chapter. To avoid potential problems, such as light scattering at the bubble/droplet interface because of existence of a laser sheet, a PSV measurement setup was used in the experiments. A flow channel containing a rectangular confinement in the middle was designed to investigate the flow of rising bubbles and oil droplets through the vertical rectangular confinement. The experimental configuration and specifications of the components used in the experimental setup were explained. Three processing approaches of particle recognition, PIV and PTV that are used in the rest of this document were described.

CHAPTER 4. THE PASSAGE OF BUBBLES THROUGH A RECTANGUALR CONFINEMENT[1]

4.1 Introduction

As a single bubble rises through a bounding fluid medium, the cross-sectional geometry of the confinement can affect the shape and terminal velocity of the rising bubbles. In this chapter, the passage of air bubbles with net co-flow through a vertical straight rectangular flow channel is investigated. The flow channel, varying from 22 mm × 5.84 mm to 3 mm × 5.84 mm (width × thickness) was used in the present experimental investigations. This flow channel allows the passage of bubbles from a region through two parallel plates into a confined rectangular channel region. Bubble diameters varied from 0.76 mm to 3.02 mm and their characteristics were captured using particle shadow velocimetry (PSV) technique to provide information on the size and velocity of bubbles. A water/glycerol mixture was used to control the continuous phase viscosity (based on the solution concentration) while providing a net co-flow to the bubble. Results show that in the parallel plate region, the bubbles terminal velocity can be compared against the available theory. In this region, as bubbles become larger in size, their terminal velocity increase due to the relatively higher buoyancy force (comparing to smaller bubble sizes) on the bubbles in the flow and negligible effect of confining geometry on bubble terminal velocity. On entering the rectangular confinement, however, bubbles of relatively large size compared to the rectangular confinement geometry, decelerate to a much lower terminal velocity due to the drag force

[1] Some materials of this chapter are going to be submitted to a journal as: H. Soltani, R. Sabbagh, D. S. Nobes, "The Passage of Bubbles Rising Through a Confining Rectangular Geometry", Physics of Fluids, 2018

expressed by the confining walls. The available theories in the literature cannot predict the confining wall effect on the bubble terminal velocity in the rectangular channel region. Therefore, the semi-empirical model developed in Chapter 2 for determining the bubble terminal velocity in a rectangular geometry is compared to measured motion.

4.2 Bubble shape and size

Figure 4-1 shows examples of a time history image of the passage of one through the flow channel for three general bubble sizes. Shadowgraph processing results of bubble instantaneous equivalent diameter and instantaneous rising velocity are shown as D_{e-inst} and V_{r-inst}, respectively for bubble passing through the RCSR. In this figure, each image in Figure 4-1(a)-(c) is a composite image of several image sets of bubbles at different spatial locations. These locations are separated by 10 frames resulting in a time between each spatial location of 1.125 seconds. In Figure 4-1since the timing between the spatial location of bubbles is constant for all images, the distance between bubbles at different time steps changes according to the bubble rising velocity at each time step. Figure 4-1(a) indicates that through the RCSR, the spatial location of bubbles become farther from each other compared to PPR, indicating that the bubble is accelerated on passing through RCSR. However, in Figure 4-1(b) and Figure 4-1(c) the instantaneous location of bubble through RCSR becomes closer to each other due to lower rising velocity of bubble compared to its velocity in the PPR.

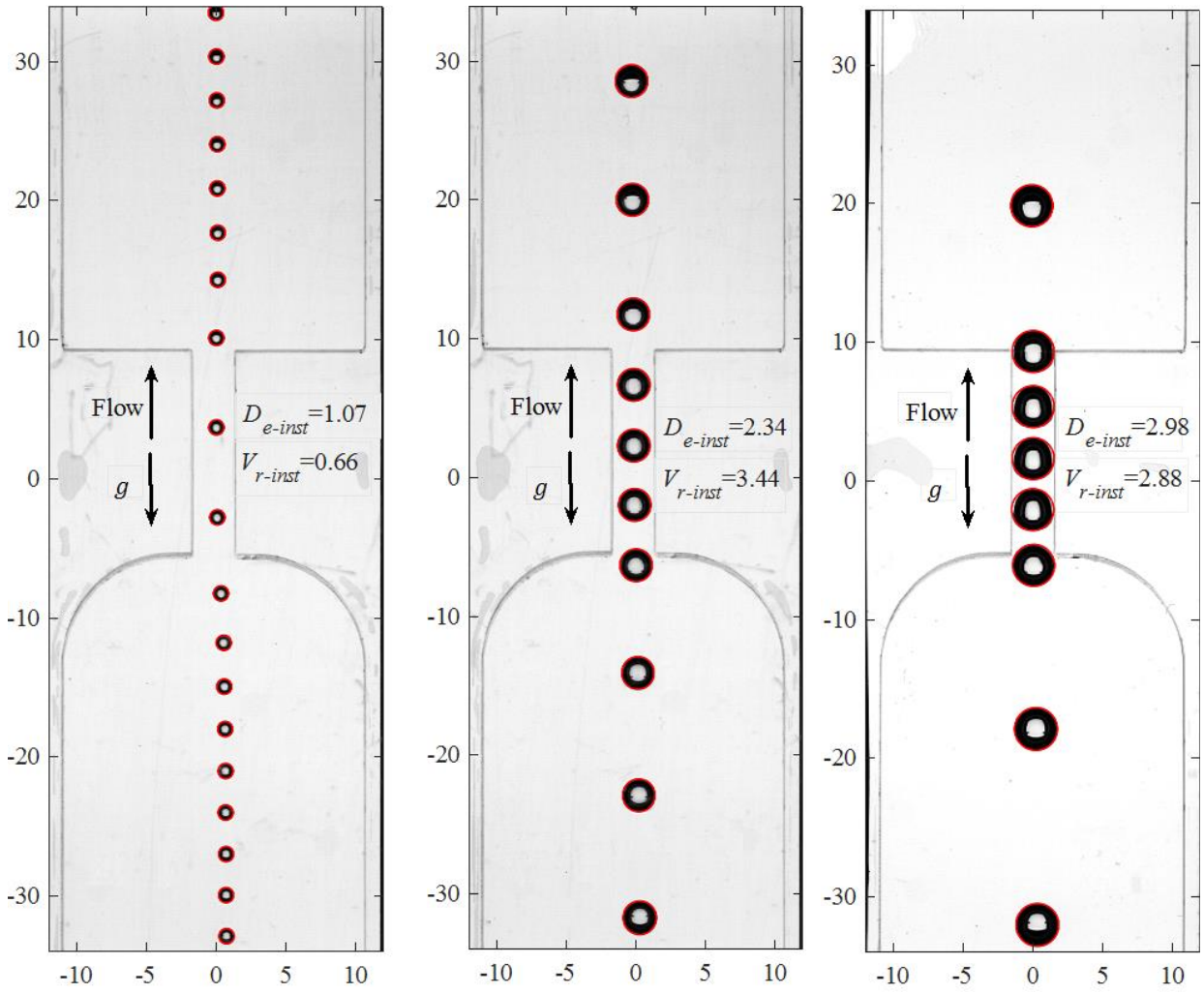

(a) (b) (c)

Figure 4-1- Example composite images of processed bubble characteristics for three different bubble sizes: (a) bubble size is smaller than then channel width, *w*, (b) bubble size is approximately close to *w* (c) bubble is elongated because the diameter is close to *w*. In each image, the spatial location of a single bubble is shown at different times with the time between each images of 1.125 seconds

4.2.1 Evolution of bubble diameter

Bubble equivalent diameter was quantified over the full range of the flow channel. Figure 4-2 shows a plot of the instantaneous bubble equivalent diameter (D_{e-inst}) rising through the flow channel for all of the fluid fluxes, q. In the figure, the y-axis is the instantaneous bubble equivalent diameter normalized by the rectangular channel width (w). This normalization is to observe how bubble sizes vary relative to the confining geometry. In this figure, the x-axis indicates the lengthwise vertical position in the flow cell (y) normalized by the length, l of the confining rectangular region, RCSR. On the abscissa, y/l from -0.5 mm to 0.5 mm is the RCSR where the origin (y/l = 0) is the center of the RCSR. The PPR is associated with y/l of -2 mm to -0.5 mm and 0.5 mm to 2 mm.

As it can be seen from Figure 4-2(a)-(e), bubble size is nearly constant along the flow cell for all cases. However, a sudden change in bubble diameter is typically observed for the largest bubble sizes at the entrance (y/l = -0.5) and exit of the confining region (y/l = 0.5). As relatively larger bubbles (D_{e-inst} > 0.8) enter the confinement, they stretch into an oval shape due to the effect of the change in geometry, which changes the number of pixels in the bubble projected image. Because the thickness of the RCSR, t = 5.84 mm, is larger than the RCSR width, w = 3 mm, as bubble diameter becomes closer to the RCSR width, w, bubbles might decompress along the width and elongate along the thickness of the RCSR. Thus, the number of pixels observed in the projected image inside the bubble becomes smaller which results in a smaller bubble area and hence a smaller bubble diameter. Likewise, when large bubbles exit the confinement, they experience a three-dimensional change in the shape at the sudden expansion in the width of the confinement which leads to a higher number of pixels inside the bubble area detected during the image processing which gives a larger bubble diameter.

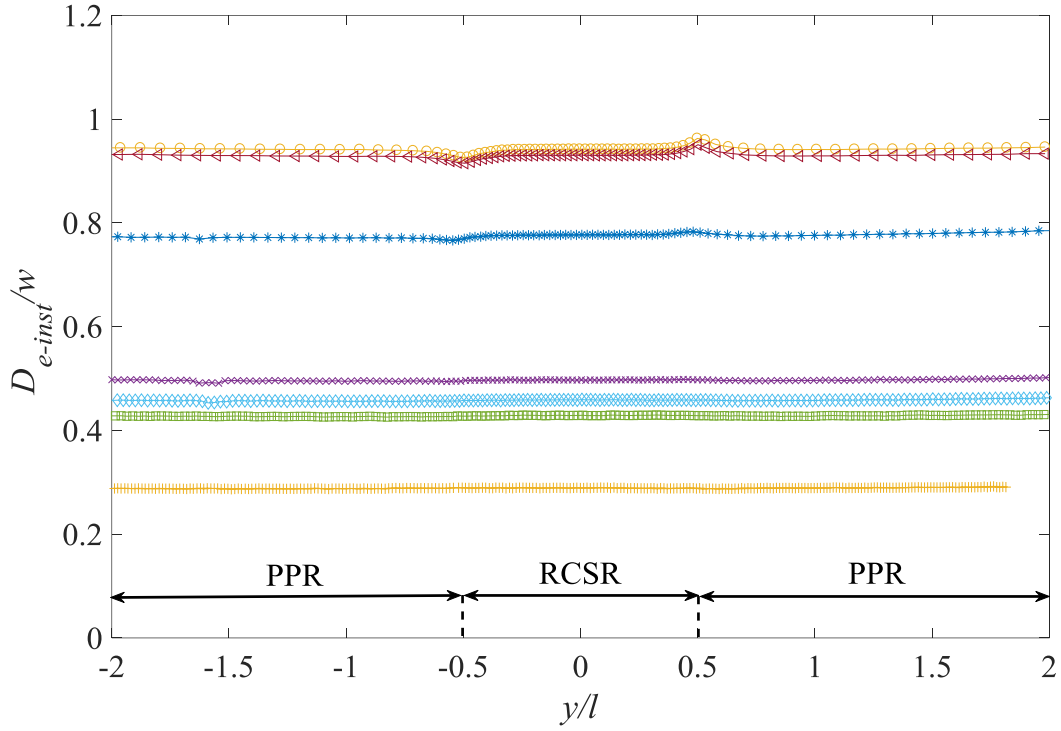
1.2
1
0.8
0.6
0.4
0.2
0
$D_{e\text{-}inst}/w$
PPR
RCSR
PPR
-2
-1.5
-1
-0.5
0
0.5
1
1.5
2
y/l

(a) $q = 0.34$

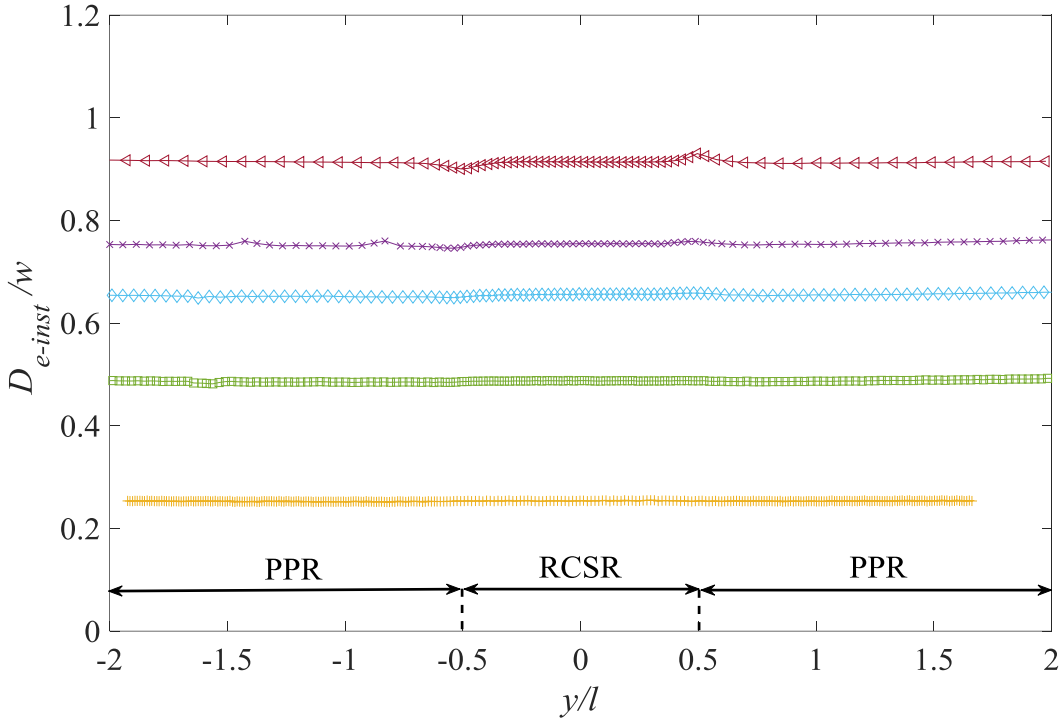
1.2
1
0.8
0.6
0.4
0.2
0
$D_{e\text{-}inst}/w$
PPR
RCSR
PPR
-2
-1.5
-1
-0.5
0
0.5
1
1.5
2
y/l

(b) $q = 0.67$

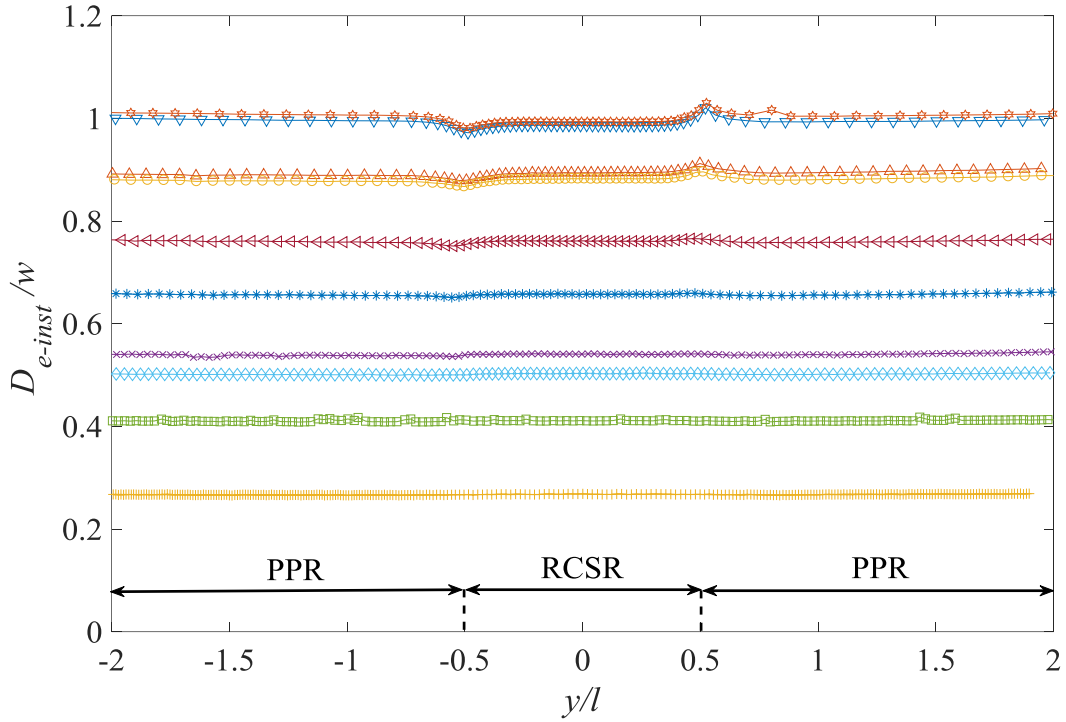
1.2
1
0.8
0.6
0.4
0.2
0
$D_{e\text{-}inst}/w$
PPR
RCSR
PPR
-2
-1.5
-1
-0.5
0
0.5
1
1.5
2
y/l

(c) q = 1.07

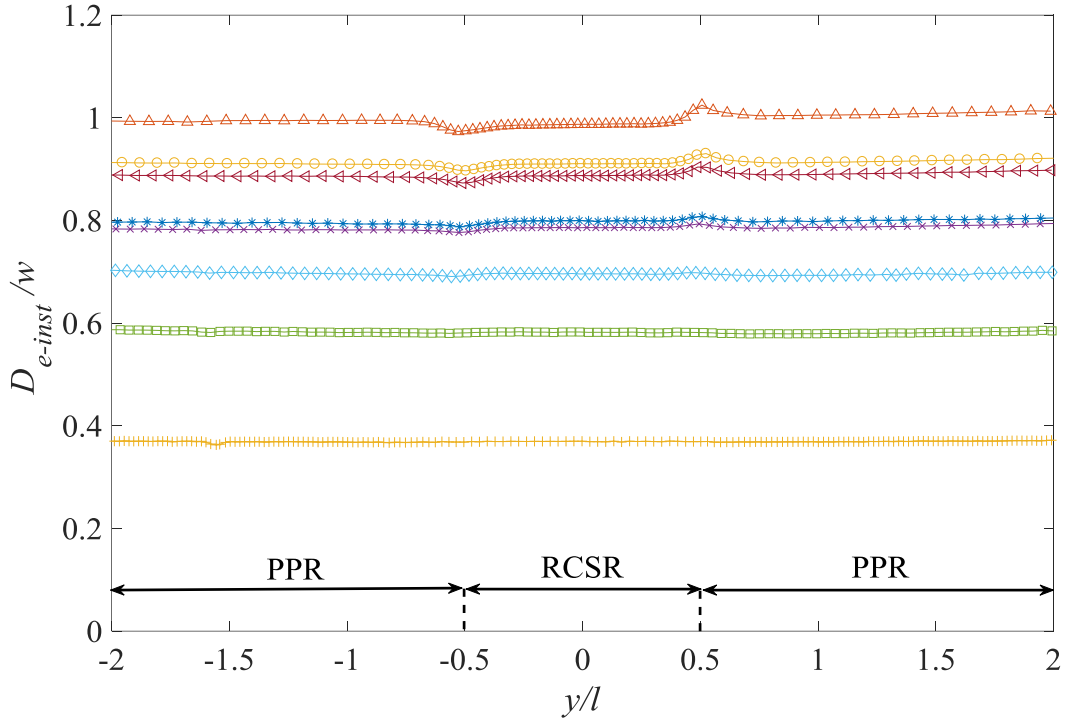
1.2
1
0.8
0.6
0.4
0.2
0
$D_{e\text{-}inst}/w$
PPR
RCSR
PPR
-2
-1.5
-1
-0.5
0
0.5
1
1.5
2
y/l

(d) q = 1.78

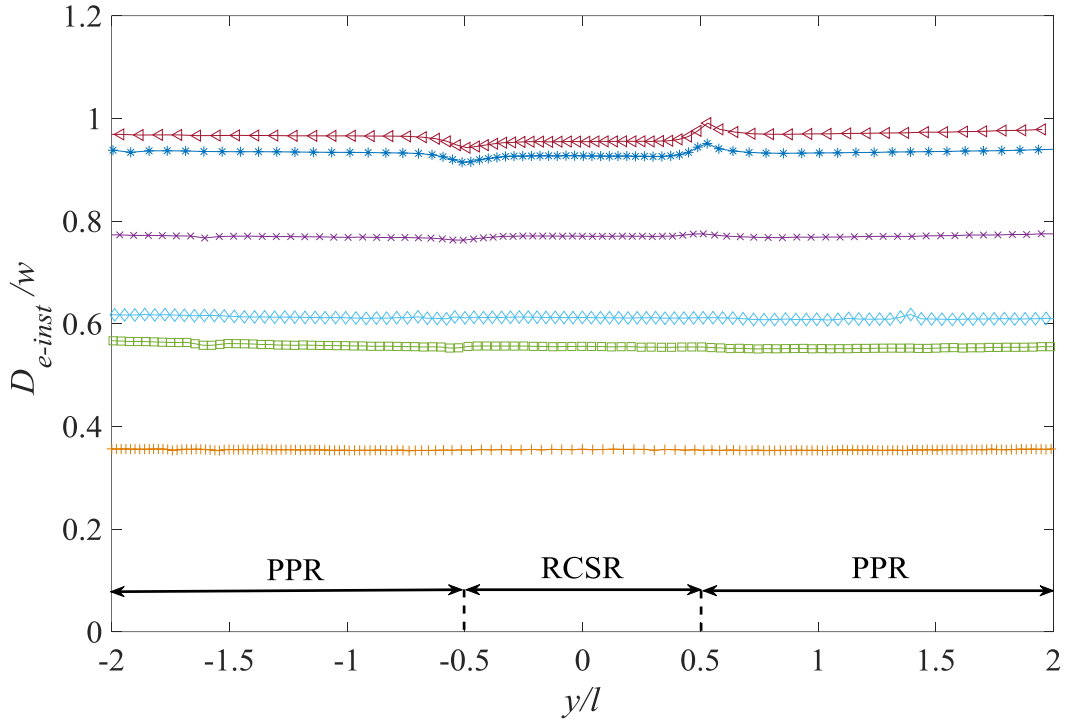

(e) q = 2.64

Figure 4-2- Air bubble diameter as rising through the flow cell

4.2.2 Evolution of bubble shape (centricity)

For a bubble or object of an arbitrary geometry, centricity, C, is defined as the ratio of minimum diameter to maximum diameter (Ghaemi, Rahimi, and Nobes 2010). The instantaneous centricity of the detected bubbles was calculated based on the minimum and maximum diameter collected in each frame. Figure 4-3 shows a detected air bubble for which the minimum and maximum diameter, D_{min} and D_{max} respectively, are derived by commercial software (DaVis 8.4.0, LaVision GmbH 2014). For this example the centricity would be equal to $\frac{D_{min}}{D_{max}}$ which is approximately 0.88.

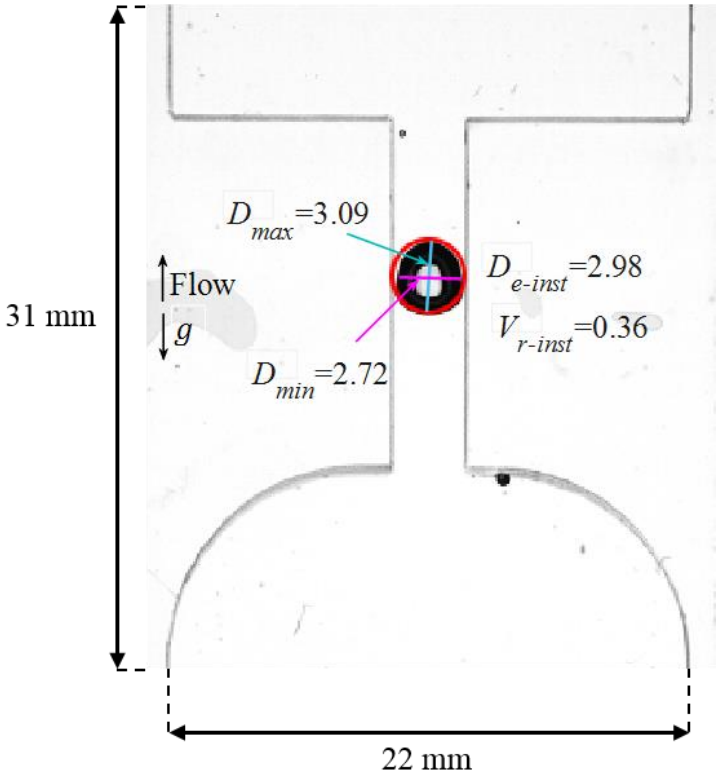

Figure 4-3- Instantaneous rising velocity of the largest and smallest bubble sizes of each bulk flow rate. The diameters are in mm and the V_{r-inst} is in pixels/frame

The bubble instantaneous centricity (C_{inst}) is plotted at lengthwise location of the flow channel for q = 2.64 mm/s in Figure 4-4. As a bubble size becomes smaller, the number of pixels in the bubble projected image decreases. Therefore, the minimum and maximum measured diameter, D_{min} and D_{max} of the bubble become lower (becoming closer to 1 pixel), which leads to an increase in the measurement error of centricity (Ghaemi et al. 2010). As shown in Figure 4-4, the centricity trends for detected bubble sizes in the images are fluctuating due to the measurement error and for relatively smaller bubble sizes, the fluctuations become more pronounced. For all bubble sizes, the centricity remains almost the same in the PPR, which means that bubble shape is not affected by flow cell thickness t = 5.84 mm in those regions. However, for relatively large

bubbles as a single bubble approach the rectangular confinement, the centricity decreases because bubble is elongated to pass through the confinement i.e. C_{inst} decreases.

In Figure 4-4(a)-(e), there is a sudden change in the C_{inst}, at y/l = -1.5. This is because around this location, there was a scratch on the window; therefore, it can affect the measurements on the bubbles that are detected around this location (y/l = -1.5). Also, because some of the bubbles do not rise at the centerline of the flow channel, they might hit the corner of the entrance of the RCSR before entering it. Therefore, the bubble shape can change at the entrance of the RCSR, which appears as a sudden change in some of the C_{inst} trends plotted in Figure 4-4(a)-(e) around y/l = -0.5.

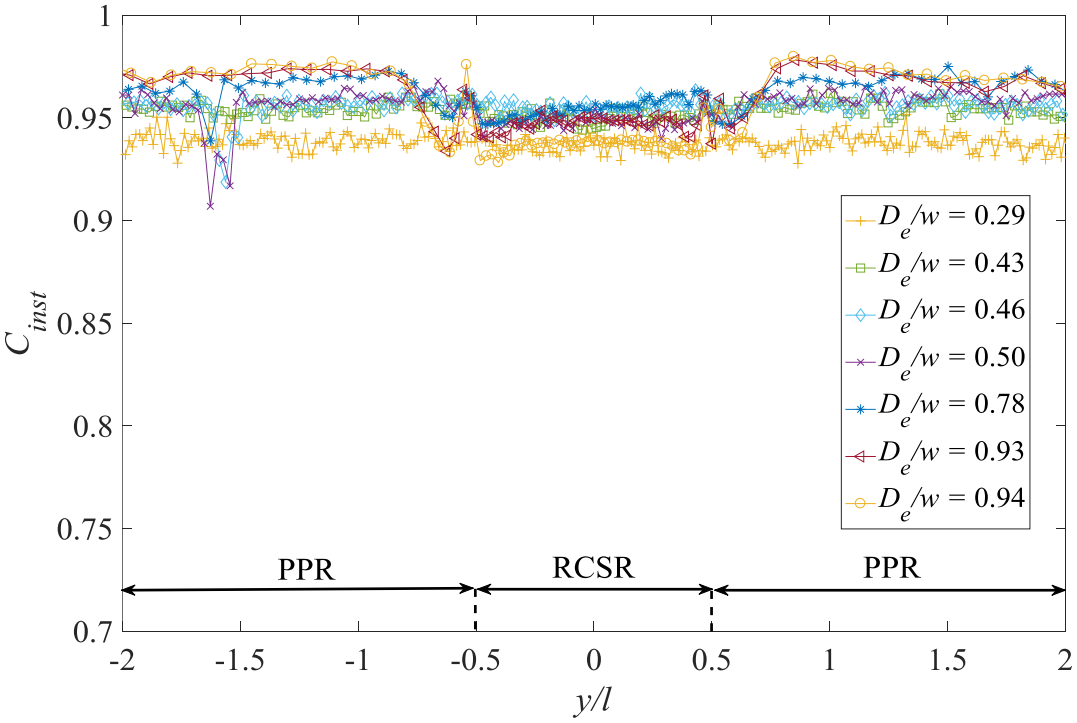

(a) q = 0.34 mm/s

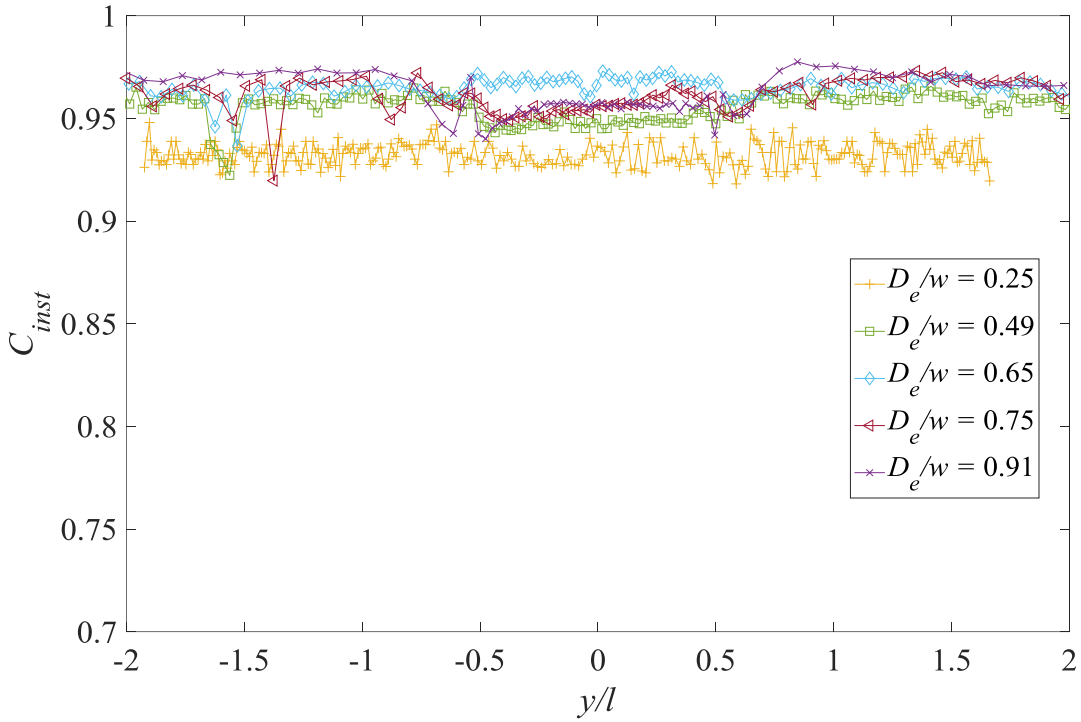

(b) q = 0.67 mm/s

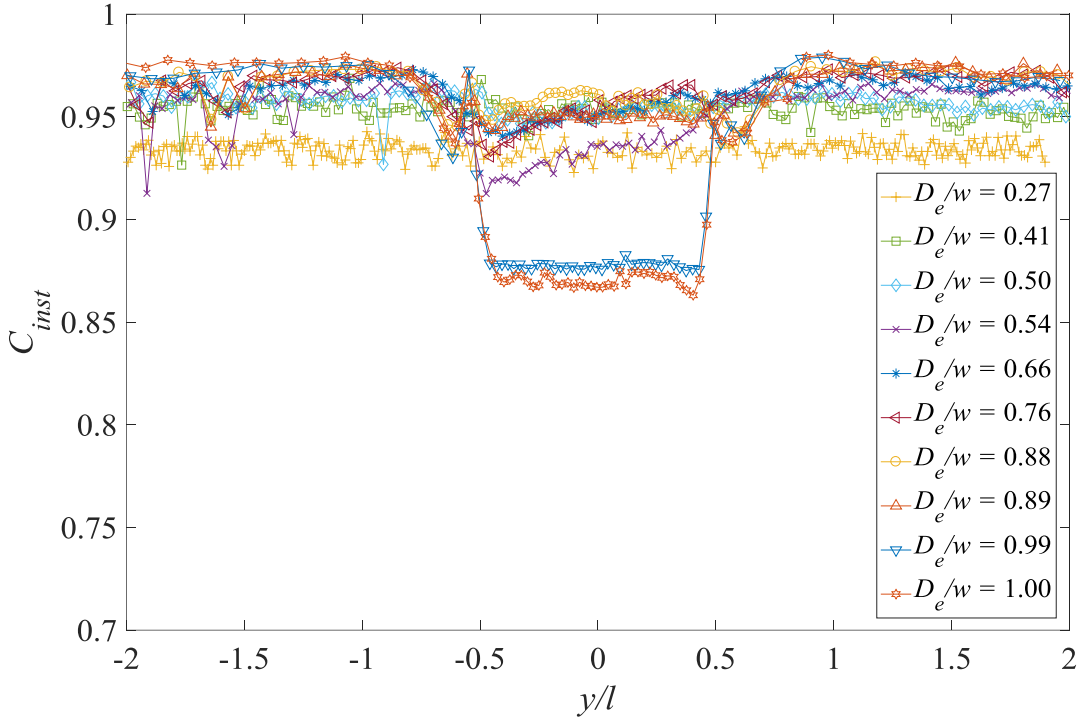

(c) q = 1.07 mm/s

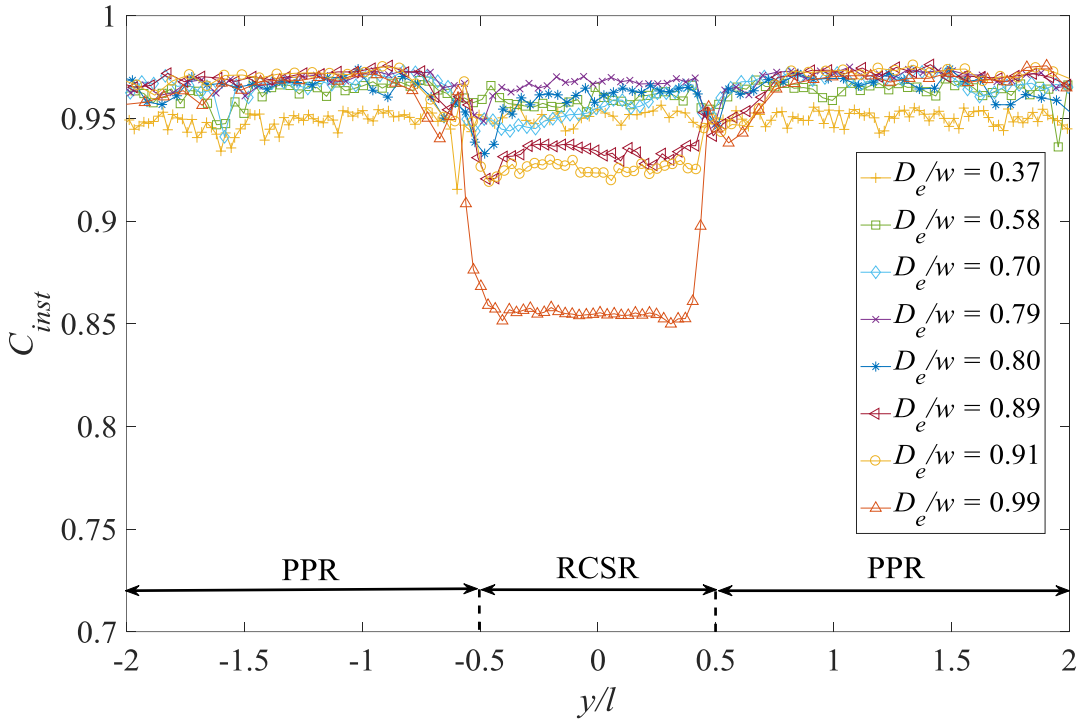

(d) q = 1.78 mm/s

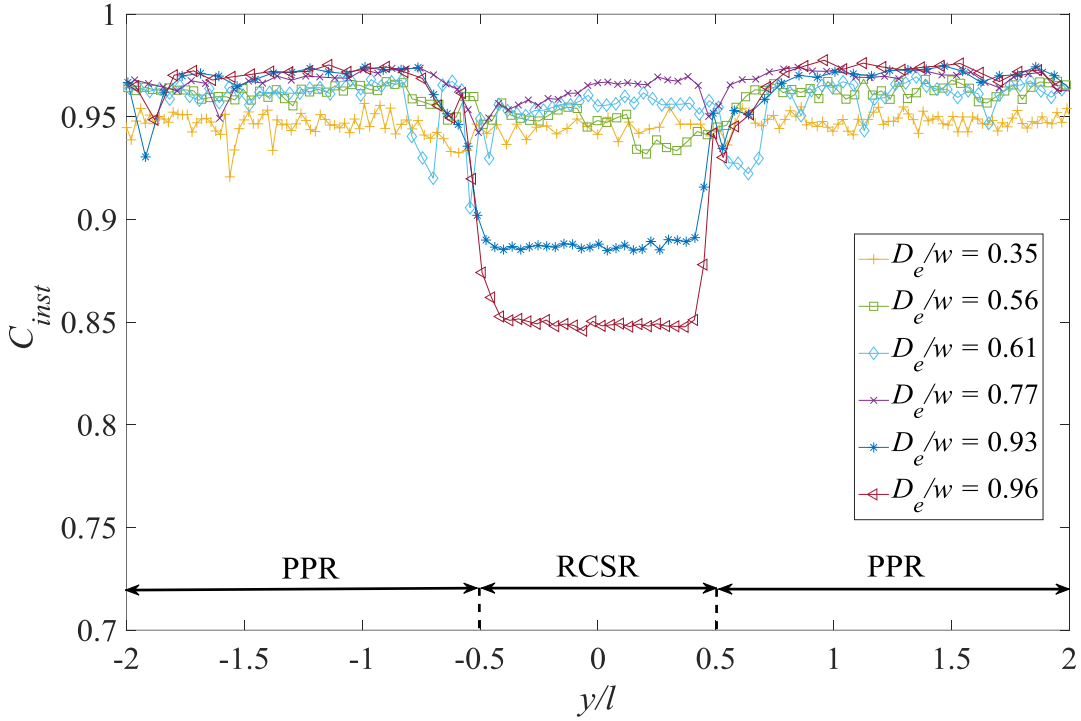

(e) q = 2.64 mm/s

Figure 4-4- Instantaneous centricity (C_{inst}) of bubbles along the flow channel

The instantaneous centricities plotted in Figure 4-4 are averaged over the two regions of PPR and RCSR. The results are plotted in Figure 4-5(a) and Figure 4-5(b) against non-dimensional bubble diameter. In this figure, q_{1-RCSR} to q_{5-RCSR} and q_{1-PPR} to q_{5-PPR} show the fluid flux through RCSR and PPR regions. In the PPR, the thickness (t = 5.842 mm) is smaller than the width of these regions (22 mm) and has more effect on the bubble characteristics. Therefore, for the average centricity of bubbles through the RCSR, C_{b-RCSR}, the flow channel thickness, t, is used to normalize the bubble size, as shown in Figure 4-5(a). For the RCSR, however, the width (w =3 mm) is smaller than the thickness (t = 5.84 mm) and for the average centricity of bubbles over RCSR, C_{b-RCSR}, the bubble size is normalized with the rectangular confinement width, w, as shown in Figure 4-5 (b). In Figure 4-5, a second x-axis is added to the top of the plot which shows the bubble equivalent diameter (D_e) in pixels in the images.

Air bubbles can have different behaviors in different sections of the flow channel due to the changes in the confinement cross sectional geometry. A relatively large bubble moving along a confined medium is typically elongated to be able to pass through the bounded space, while bubbles of smaller sizes (relative to the cross-sectional geometry) may not see a considerable change as rising through the bounded medium. Figure 4-5(a) shows that in the PPR, the bubbles centricities slightly increases as bubbles enlarge from the smallest measured bubble size up to the largest diameter. Relatively smaller bubbles tend to be more spherical due to higher surface forces relative to viscous forces (Clift et al. 1978); hence, the centricity is expected to be close to 1 for relatively smaller bubbles (Ghaemi et al. 2008). As bubbles enlarge, the centricity should remain the same unless the confinement affects the bubble shape. As a result, the increasing trend of centricity shown in Figure 4-5(a) is not expected to happen.

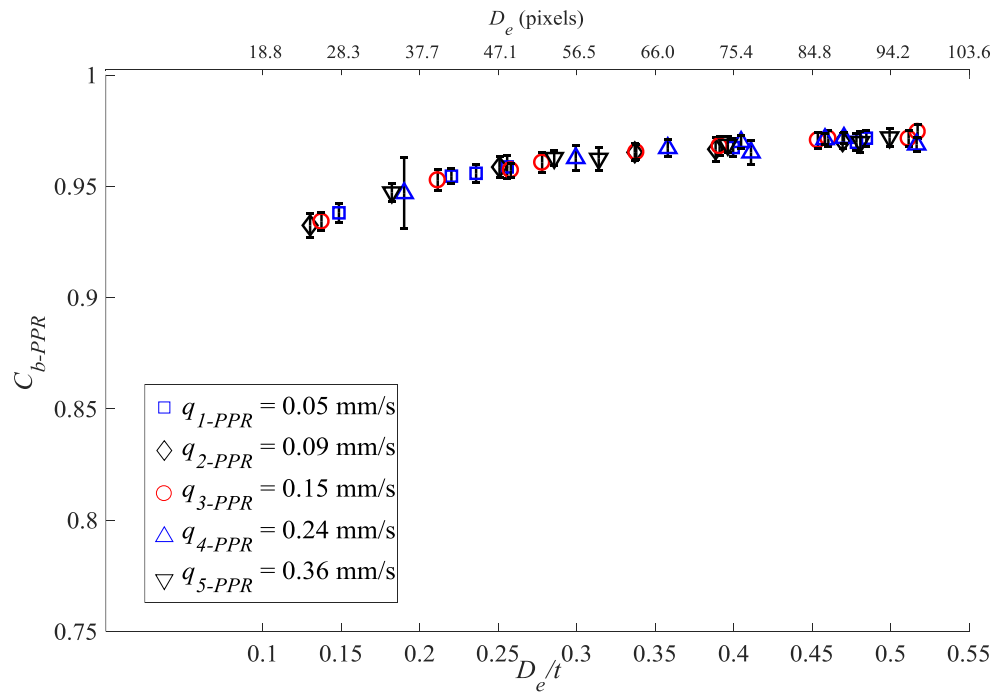

(a)

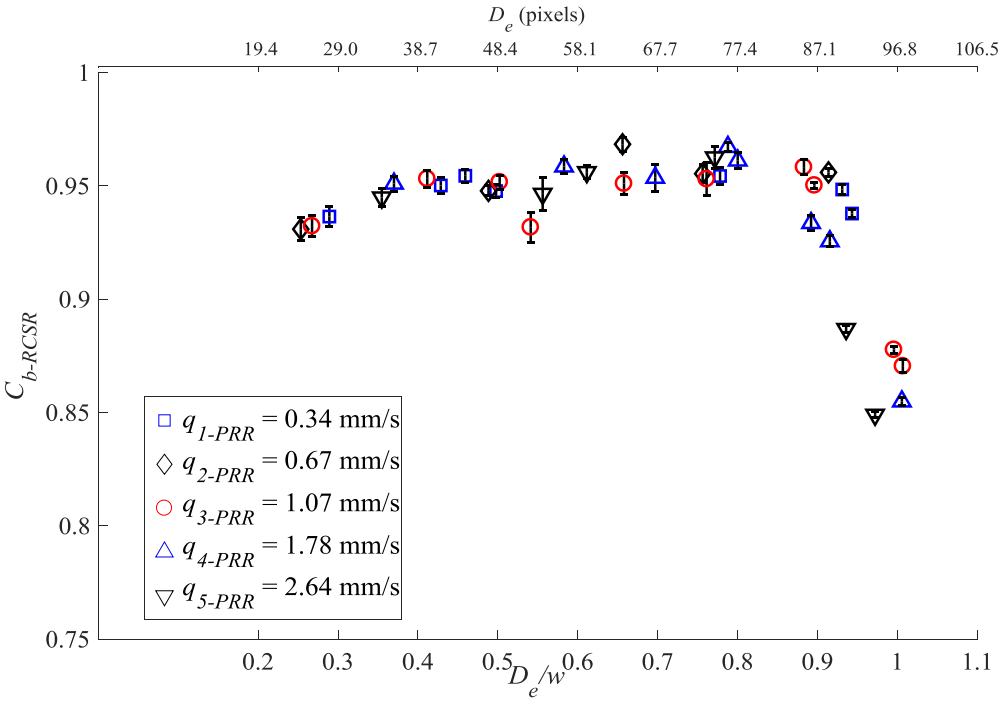

(b)

Figure 4-5- Air bubble average centricity over (a) PPR, and (b) RCSR

The reason for this increasing trend of centricity shown in Figure 4-5(a) is explained in the literature (Ghaemi et al. 2008). Figure 4-6(a) and 4-6(b) indicate a relatively small and large bubble discretized in a camera sensor and each grid is 1 pixel × 1 pixel. In the figure, the shaded grids are assumed to be the area that is detected as the projected areas of the bubble. Figure 4-6(a) shows that the number of pixels inside the relatively small bubble is lower than the larger bubble (Figure 4-6(b)) and the D_{min} and D_{max} will not be the same; therefore, the centricity is lower than 1 (Ghaemi et al. 2008). As indicated in Figure 4-6(b), as bubbles enlarge the number of pixels inside the bubble increase and the discretized image of the bubble becomes smoother (Ghaemi et al. 2008). Hence, the D_{min} and D_{max} become about the same value and centricity increases toward 1. Figure 4-5(b) indicates that centricity increases through the RCSR up to D_e/w of 0.8 due to the increase of bubble image resolution (larger number of pixels in the bubble projected area). However, after this size, centricity drops. This decrease in the bubble centricity is not due to image discretization error, but it is because as bubbles enlarge and the diameter becomes closer to the RCSR width (w, 3 mm), the bubbles shapes deform and become elongated and as a results centricity decreases. The error bars in Figure 4-5 are derived based on averaging the collected data, and they do not include the uncertainty due to the number of pixels across the bubbles.

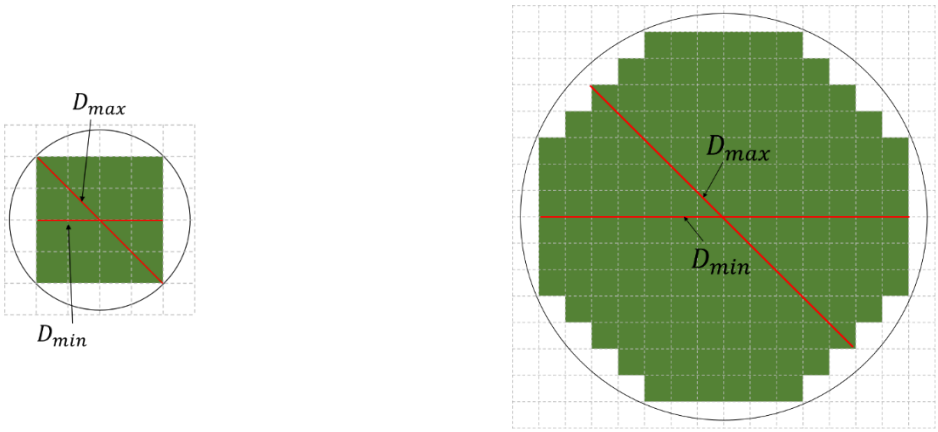

(a) (b)

Figure 4-6- Discretized image of a relatively (a) small, and (b) bubble in a camera sensor

Ghaemi, Rahimi, and Nobes (2008) investigated the centricity for different diameters of a droplet. They concluded that the diameter of a spherical particle (bubble, droplet etc.) should be at least 150 pixels in order to have centricity of close to 1 from the measurements. According to the bubble equivalent diameters (D_e) in pixels on the second x-axis in Figure 4-5(a) and Figure 4-5(b), the measured bubble equivalent diameters (D_e) are below 150 pixels for all of the measured bubble sizes.

The error in measuring the centricity for relatively small bubble sizes can affect many parameters associated with the bubble shape (Ghaemi et al. 2008). As an example, Figure 4-5(b) shows that bubble centricity in RCSR, C_{b-RCSR}, for D_e/w of 0.25 and 0.9 is approximately 0.93. However, for D_e/w = 0.25 the C_{b-RCSR} is lower than 1 due to the measurement error explained in the previous paragraph, and for D_e/w = 0.9 the C_{b-RCSR} is lower than 1 because the confinement elongated the bubble.

4.3 Bubble rising velocity

The characteristics of terminal velocity of rising bubbles for all fluid fluxes, q, are plotted in Figure 4-7. In this figure, V_{r-inst} is the instantaneous rising velocity (not the terminal velocity) of the bubbles, y is the lengthwise location and l is the RCSR length. The figure shows the results for different bubble sizes based on the average equivalent area diameter, D_e, normalized by the RCSR width, w. Here, to exclude the effect of inlet and outlet of RCSR, D_e is the averaged D_{e-inst} in the range $-2 < \frac{y}{l} < -1$ and $1 < \frac{y}{l} < 2$.

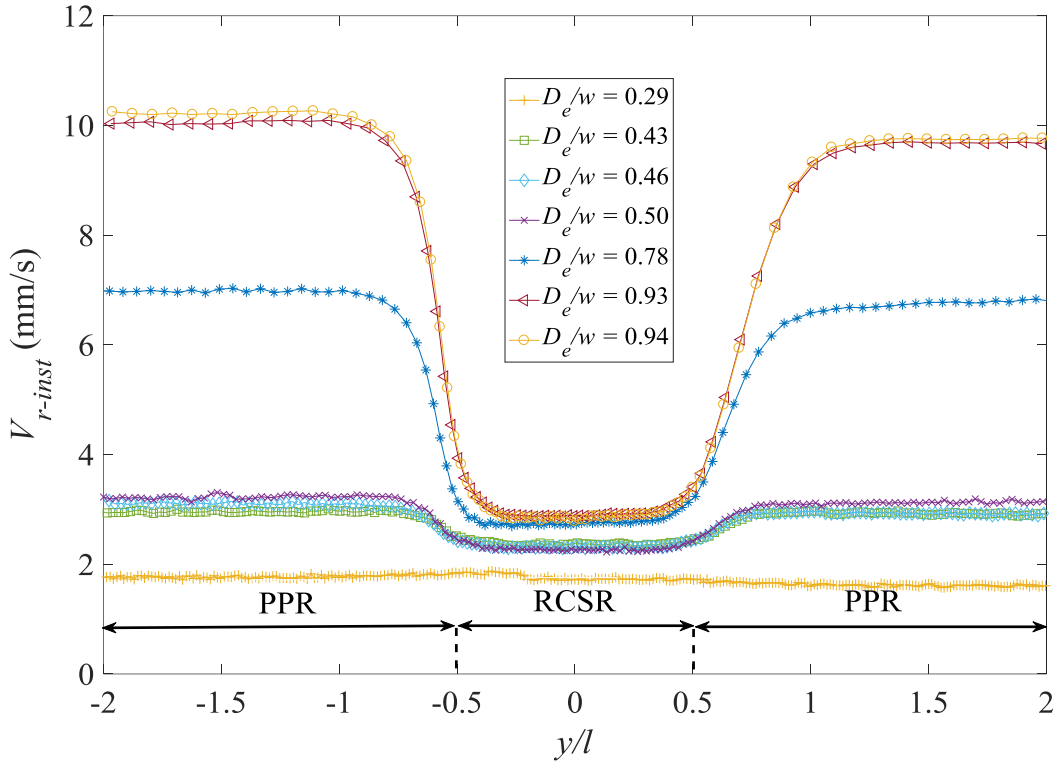

(a) q = 0.34 mm/s

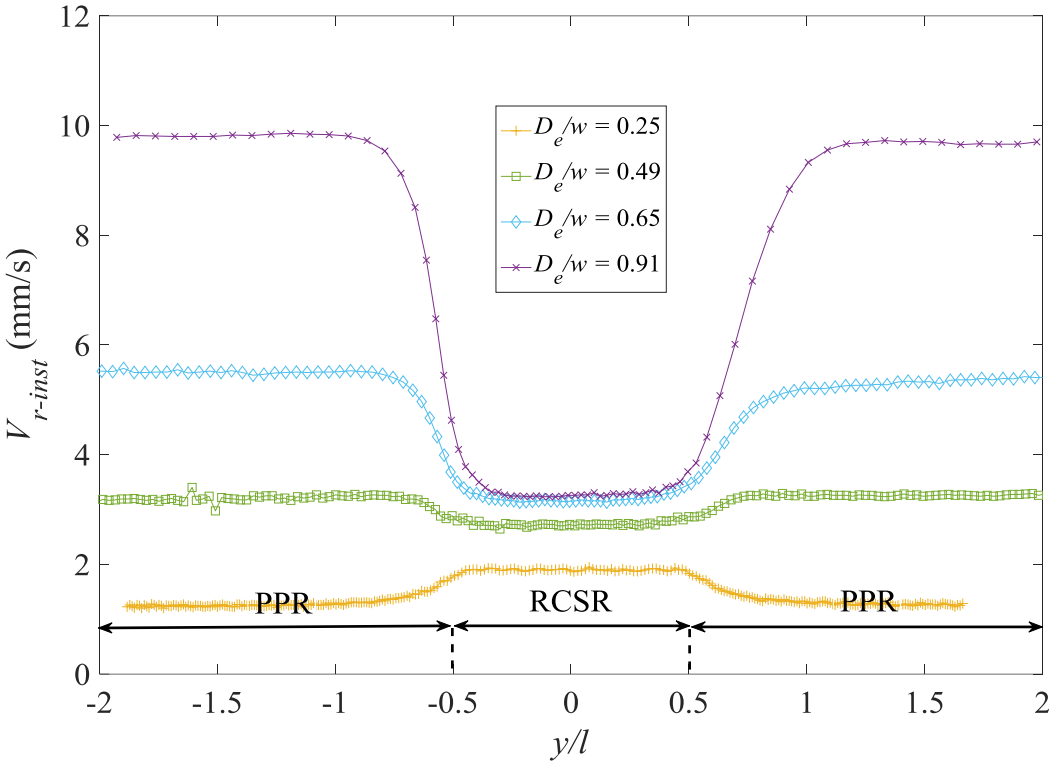

(b) q = 0.67 mm/s

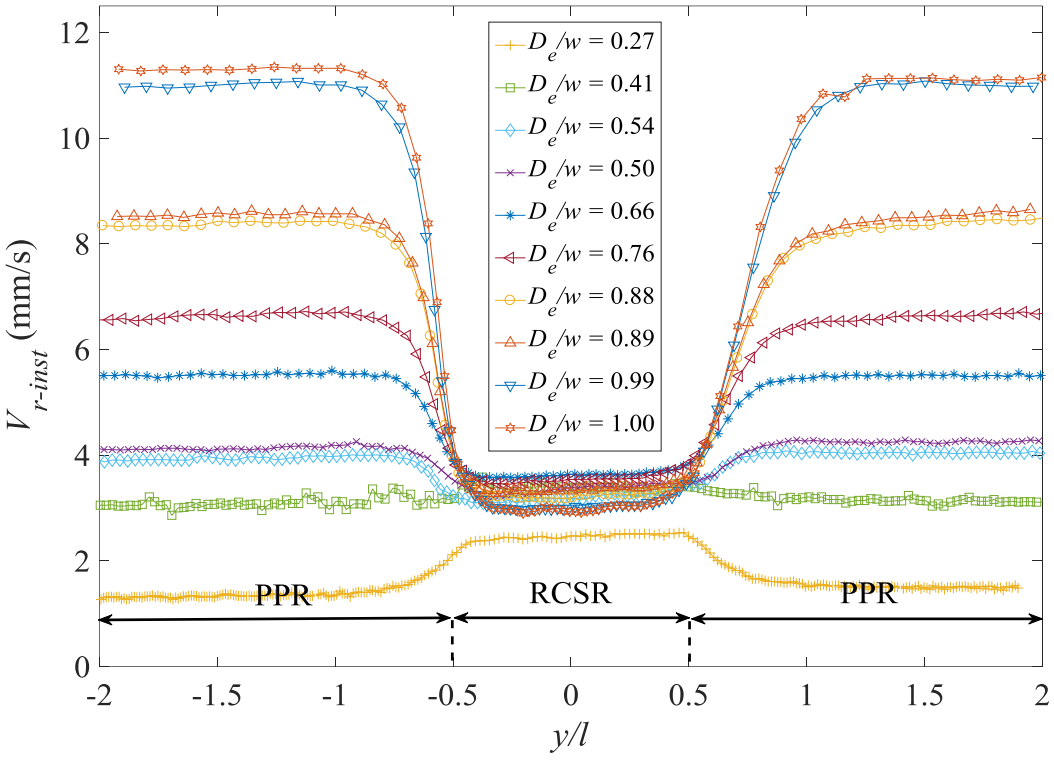

(c) q = 1.07 mm/s

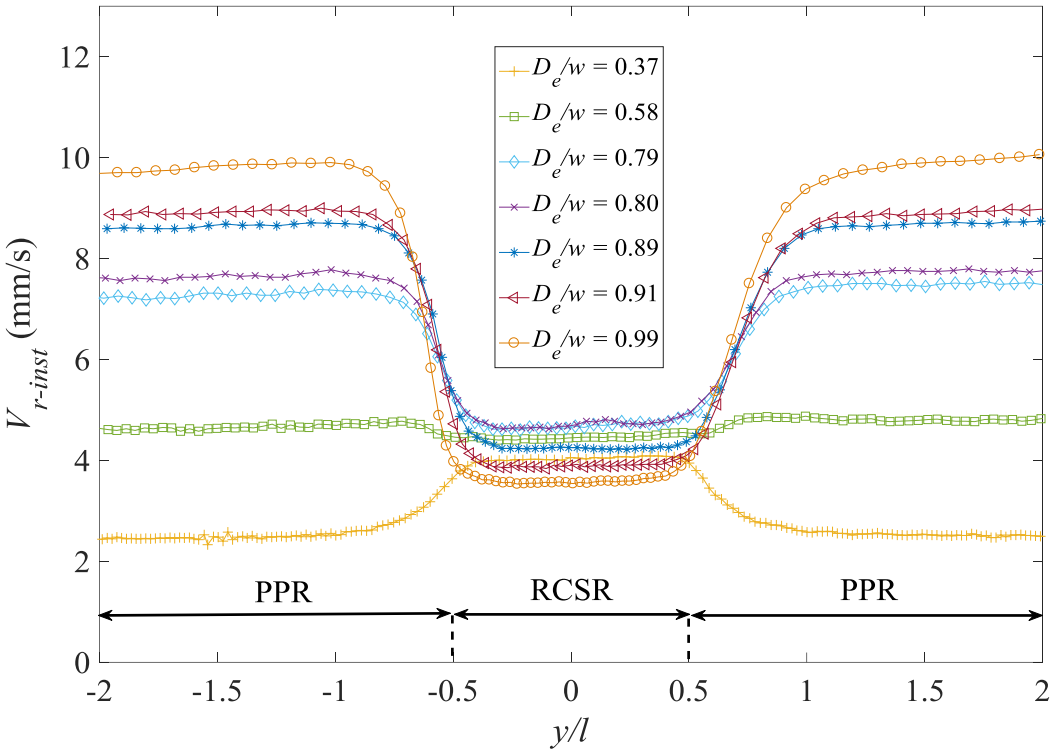

(d) q = 1.78 mm/s

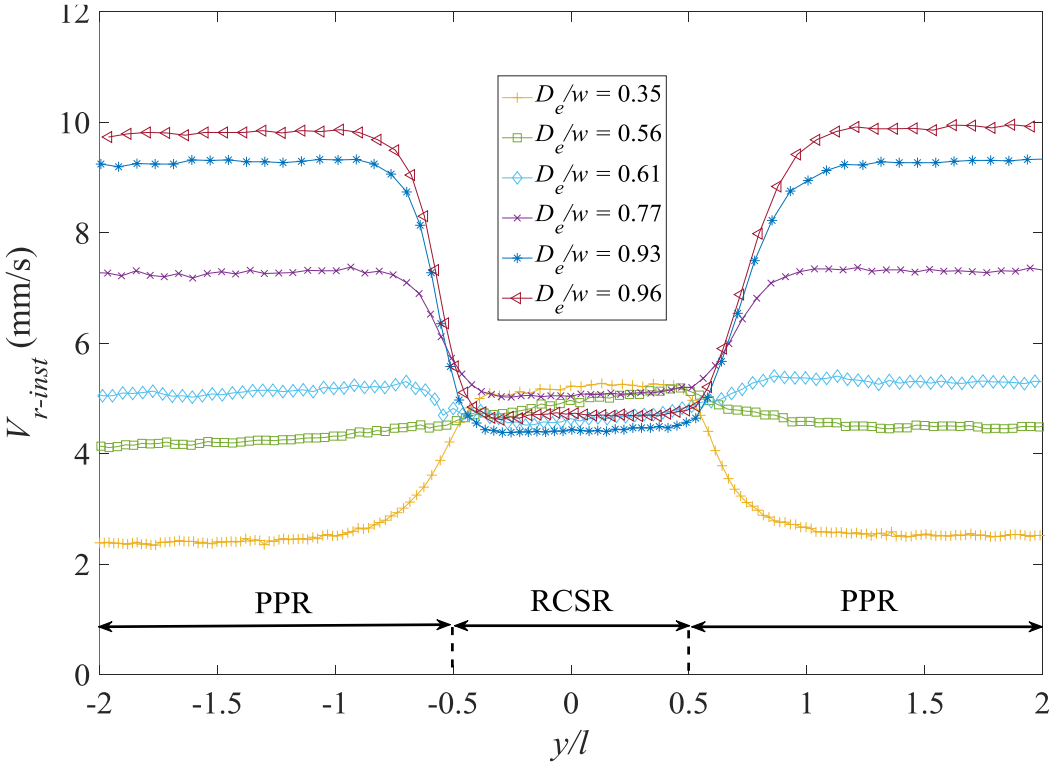

(e) q = 2.64 mm/s

Figure 4-7- Bubble rising velocity in the flow channel

The bubble instantaneous velocity plot in Figure 4-7 shows that all bubble sizes move with a constant rising velocity in the PPR, far from the RCSR. This indicates that they have reached their terminal velocity before entering the confinement region. As bubbles approach the rectangular confinement, RCSR, there is a region that affects bubble velocity. Bubbles with $D_e/w \geq 0.6$ decelerate to a certain velocity just before the entrance of the RCSR. The decelerating trend that occurs as the bubbles moves toward the confining region is due to the change of the flow cell geometry as approaching the RCSR and then entering the RCSR that increases the drag force on single bubbles. As bubbles exit the RCSR, all bubbles with $D_e/w \geq 0.6$ appear to accelerate back to their previous terminal velocity, where the larger bubbles have a higher terminal velocity.

Due to the smaller cross sectional area, the fluid flow velocity is higher in the confinement region in Figure 4-7, relative to the other regions in the flow channel. While, through the RCSR, the cross sectional area is smaller, the wall drag force is higher inside the confinement relative to the PPR. Therefore, although the bubble rising velocity tends to increase due to a higher fluid velocity (higher kinetic energy), it is hindered due to a high resistance from wall friction force. This wall friction influence is expected to be less dominant for small bubbles passing through RCSR. As an example, Figure 4-7(e) shows that an air bubble with $D_e/w = 0.35$ size, which approximately has the same velocity as the average velocity of the bulk flow ($q = 2.64$), accelerates on entering the RCSR and decelerates when it exits. This acceleration occurs because the effect of confining drag force from the RCSR walls is negligible comparing to the effect of increase in bulk flow local velocity. The balance between the forces due to kinetic energy and the wall friction effect in the RCSR determines the flow velocity in the confinement region.

For a slightly larger bubbles (for instance, $D_e/w \approx 0.29$ in Figure 4-7(a), $D_e/w \approx 0.41$ in Figure 4-7(c), $D_e/w \approx 0.58$ in Figure 4-7(d) and $D_e/w \approx 0.56$ in Figure 4-7(e)), it can be seen

from Figure 4-7(a)-(e) that it tends to retain its rising velocity as it enters and exits the confinement region. This can be interpreted as the extra confining drag force is canceled by the effect of increase in fluid local velocity through the confinement. The threshold for this phenomenon is where the confining effect and the kinetic energy effect balance each other and depends on fluid properties, geometry of the rectangular channel and the bubble size.

To compare the effect of fluid flow on the bubble rising velocity, the instantaneous rising velocity through the flow channel for the smallest and the largest bubble size observed at each bulk flow rate is plotted in Figure 4-8 for all five fluid flow rates. In this figure, the fluid flux through the RCSR, q_{RCSR}, is shown to address the five different bulk flow rates. Figure 4-8(a) plots the instantaneous bubble rising velocity, V_{r-inst}, and Figure 4-8(b) presents the instantaneous bubble rising velocity normalized by the fluid flux, V_{r-inst}/q. As it can be seen from Figure 4-8(a) andFigure 4-8(b), the rising velocity is always lower in the PPR for smaller bubbles than the larger bubbles observed at different flow rates. In the RCSR, for q = 0.34 mm/s and D_e/w = 0.29, the rising velocity nearly leveled off, which indicates that the terminal velocity of this bubble size is not affected by the change in the fluid flux, nor by the confining wall drag force through the confinement region. However, as the fluid flux increases, bubbles with relatively small sizes (D_e/w < 0.4) accelerate on passing through the confinement region. Figure 4-8(a) shows that for q equals 0.34, 0.67 and 1.07 mm/s, the rising velocity of relatively smaller bubble sizes (D_e/w < 0.4) is always lower than the larger bubble sizes (D_e/w > 0.9) rising velocity through the RCSR. For q = 1.78 mm/s and 2.64 mm/s, however, the rising velocity of smaller bubble size becomes approximately the same as the rising velocity trend of larger bubble diameter inside the RCSR. This implies that as air bubbles become smaller relative to the confining geometry, the effect of co-flow may become more dominant than confining wall drag effect. As shown in Figure

4-8(a) andFigure 4-8(b), the largest bubble sizes at each fluid flux (q) decelerate as approaching the RCSR, due to the higher wall drag force exerted from the confining walls. These large bubble sizes have an approximately constant velocity as traveling through RCSR (similar to smallest bubble sizes) and they accelerate again as exiting this confining region (RCSR).

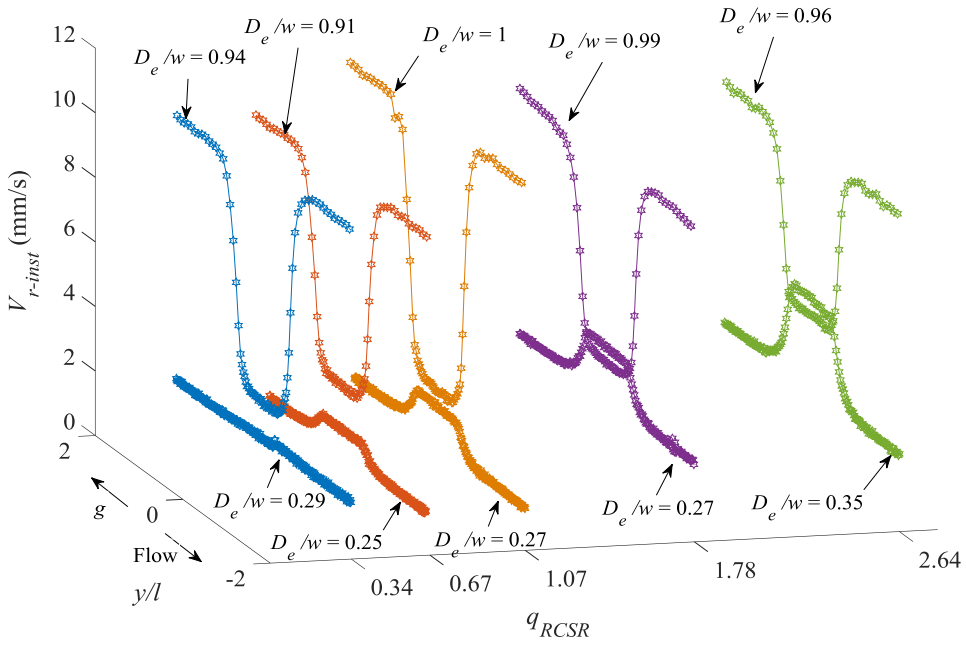

(a)

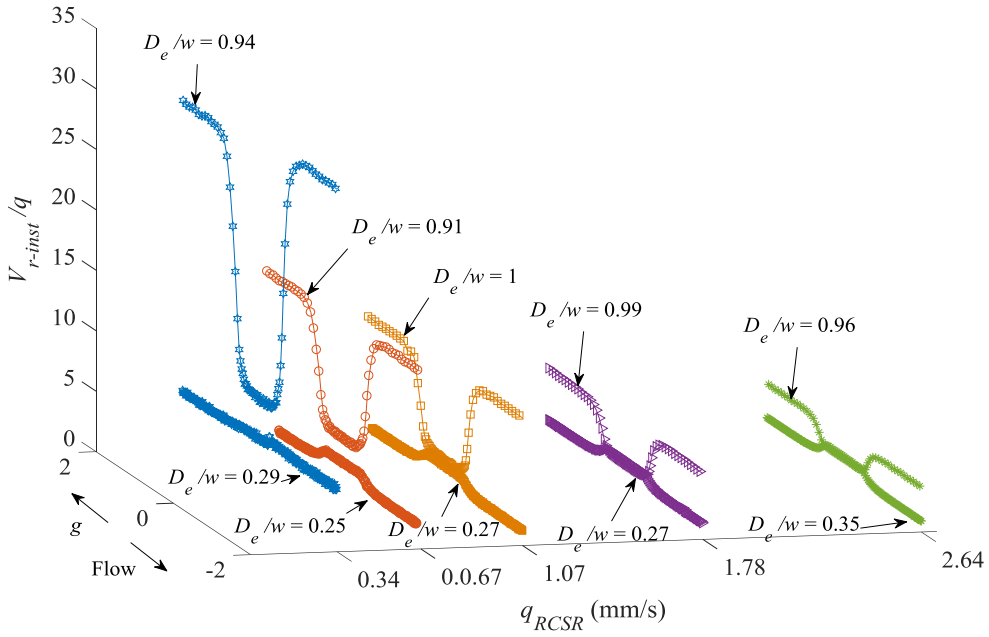

(b)

Figure 4-8- The with (a) non-normalized, and (b) normalized instantaneous rising velocity of the largest and smallest bubble sizes

4.4 Relative rising velocity in the PPR

The plotted data in Figure 4-7 and Figure 4-8 highlight that the bubble rising velocity can change on entering and exiting the rectangular confinement in the flow channel. Similar to bubble diameter, this instantaneous rising velocity was averaged in the range, $-2 < \frac{y}{l} < -1$ and $1 < \frac{y}{l} < 2$ for each bubble size and for all fluid fluxes to define an average terminal velocity, V_{t-PPR}. for a particular flux.

Since the bubbles mostly move at the flow channel centerline, the local fluid flow velocity in the centerline, V_{f-PPR}, can be subtracted from V_{t-PPR} to give a relative bubble velocity of $V_{t-PPR} - V_{f-PPR}$. This subtraction removes the effect of fluid motion and allows comparing the results with the available correlation for bubble motion in a stationary fluid. Figure 4-9 plots the relative terminal velocity through PPR, $V_{t-PPR} - V_{f-PPR}$, against the bubble diameter normalized by flow channel thickness, D_e/t. Since in PPR, the flow channel thickness (t, 5.84 mm) is smaller than the flow channel width (22 mm), the thickness is used to normalized the bubble equivalent diameter on x-axis. In Figure 4-9, the standard deviation (STD) of each data point was calculated when averaging the data, and the results are shown as error bars for each data point in this figure. In this region, flow channel width (22 mm) is much larger than the thickness (t, 5.84 mm). Therefore, the motion of bubbles through the PPR is similar to the motion of bubbles between two parallel plates. As a result, the parallel plate theory can be applied and the correlation represented in Eq. (2-55) is compared to the experimental results. In Eq. (2-55) the thickness of the channel (t, 5.84 mm) is used as the distance between two parallel plates to derive the confining wall factor, k_t, based on channel thickness. This is plotted in Figure 4-9 and indicates that as the bubble diameter increases, the relative rising velocity increases. This is due to the fact that in the bubble

size measured, buoyancy is dominant comparing to the drag force in the PPR. RMS error is an indication of the difference between the experimental data points and the predicted model, and R-squared (goodness of the fit) is a parameter showing how close the actual data points are to the model (Soong 2004). Typically, R-squared of 1 shows that the data points completely follow the prediction model. For the plotted data in Figure 4-9, the RMS error and R-squared between the experimental data and the prediction from Eq. (2-55) were calculated as 0.55 and 0.97. This confirms that rise of bubbles in PPR (22 mm × 5.84 mm) is similar to the case of rising bubbles in between two infinite parallel plates. In Figure 4-9, some of the experimental data of $D_e/w \approx 0.5$ is further form the theory, Eq. (2-55), relative to the smaller bubble sizes. This disagreement is because as bubbles enlarge and approach the channel size, they start to deform, becoming non-spherical, which is in contrast to the spherical bubble assumption in the theory Eq. (2-55).

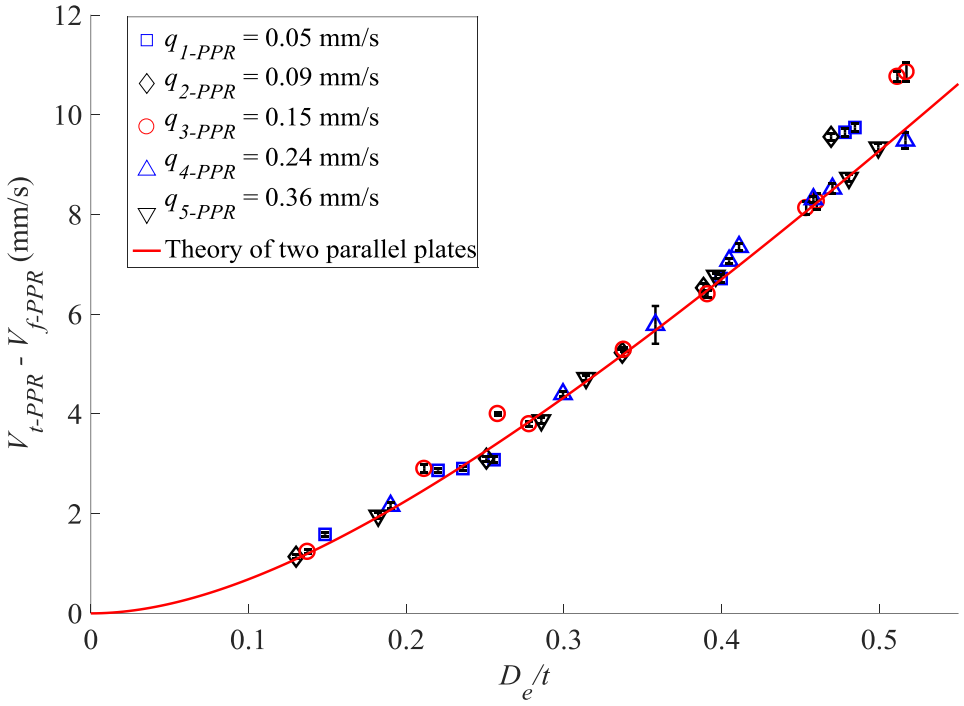

Figure 4-9- Average bubble rising velocity over PPR

4.5 Relative rising velocity in the RCSR

The bubble terminal velocity in a rectangular confinement can be compared to the bubble terminal velocity rising through a circular tube with a hydraulic diameter of the rectangular cross section when the aspect ratio of the rectangular cross section is not high. Figure 4-10 shows the averaged terminal velocity through the RCSR region versus the bubble diameter normalized by RCSR width, w for different bulk flow rates. As the figure shows, there is no agreement between the experimental data and the theory, Eq. (2-54). This is especially noticeable for D_e/w in the range of 0.4 to 0.8. For the experimental data of V_{t-RCSR} and the Haberman and Sayre (1958)'s correlation, Eq. (2-54), plotted in Figure 4-10, the RMS error and R-squared are calculated as

0.87 mm/s and 0.08 respectively, which means that the model, Eq. (2-54), does not well predict the experimental data. In Eq. (2-54), as bubble diameter goes to zero, bubble velocity tends to the maximum flow velocity, V_{f-max}, shown by red stars in Figure 4-10.

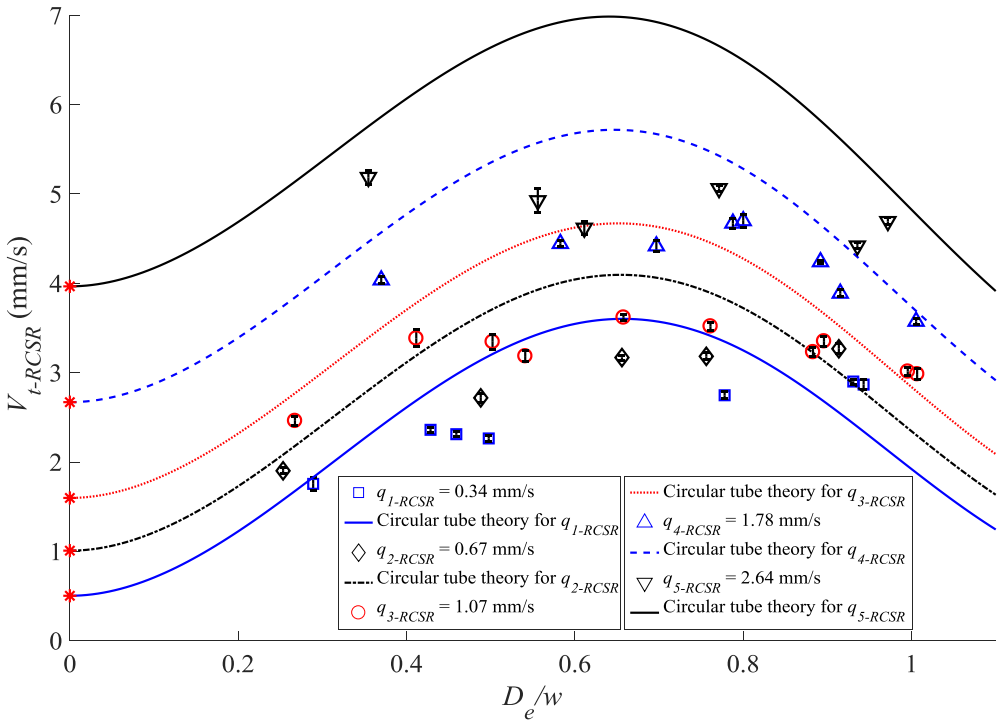

Figure 4-10- Average bubble rising velocity over RCSR and comparing with circular tube theory, Eq. (2 54). The red stars show the bubble terminal velocity when the bubble size is zero

Figure 4-11 illustrates the average rising velocity of bubbles through the RCSR (V_{t-RCSR}) relative to the maximum fluid velocity in this region (V_{f-RCSR}) for five fluid co-flows. In the figure, the x-axis represents the average equivalent diameter of bubbles normalized with the RCSR width (w = 3 mm). For comparison, the theoretical rising velocity in between two parallel plates for both t and w distances with associated $k_t$and k_w wall factors is plotted using solid and dashed lines. It can be concluded from Figure 4-11 that the theoretical trends based on parallel plate theory do not

match with the experimental data. Therefore, the theory of parallel plates should be modified for the rectangular channel geometry. In addition, because the bubble terminal velocity relative to the fluid velocity, $V_{t-RCSR} - V_{f-RCSR}$, is plotted in Figure 4-11, it is expected that the experimental data collapse on each other for the same bubble diameters. However, as it is observed in Figure 4-11, the bubbles of the same diameter have different relative (to the surrounding fluid) terminal velocity. This occurs because the contribution of fluid co-flow on bubble terminal velocity is not necessarily as much as the fluid maximum velocity through the RCSR. Therefore, the effect of co-flow on bubble terminal velocity is determined based on the experimental results and for all of the co-flows to develop a modified bubble rising velocity for rectangular channel geometries.

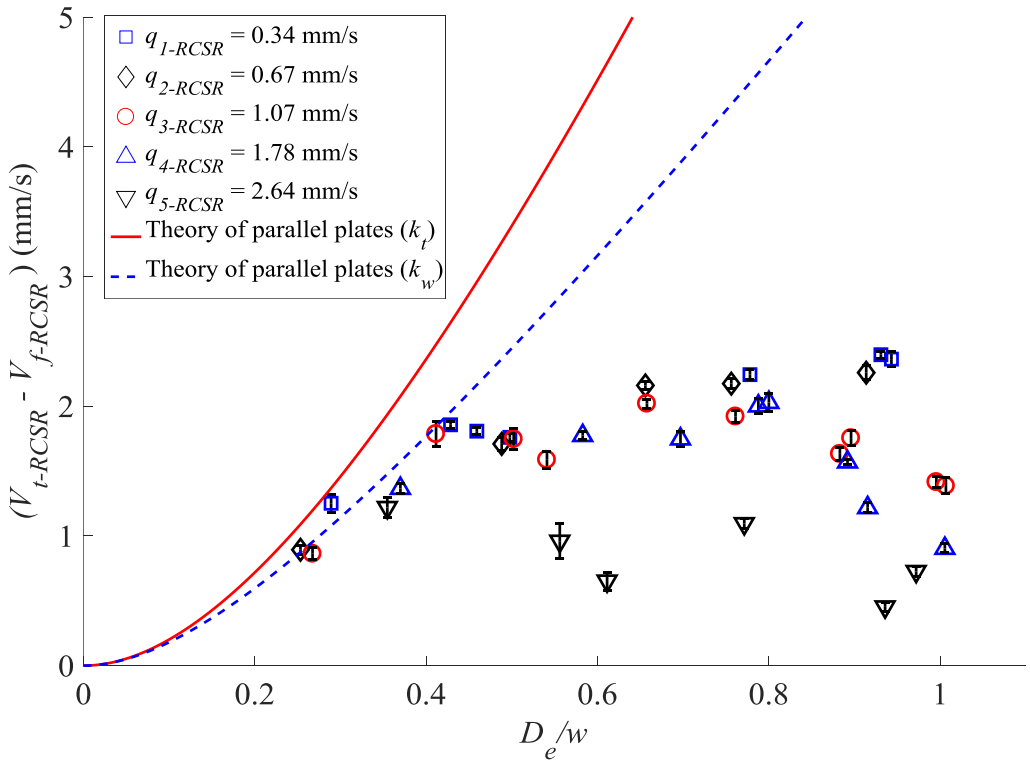

Figure 4-11- Relative bubble rising velocity in the RCSR. None of theories based on parallel plate wall factors (k_w and k_t) can well predict the relative velocity.

To modify the bubbles rising through the RCSR for the rectangular geometry and the co-flows, the correlation for rectangular channels developed as Eq. (2-61) is used. Rewriting Eq. (2-61) based on the bubble equivalent diameter (D_e) and maximum velocity of the fluid at the centerline of the RCSR (V_{f-RCSR}) gives:

$$V_{t-RCSR} = \frac{1}{f} \times \frac{g D_e^2 (\rho_f - \rho_g)}{6\mu_f} \frac{(1 + \kappa)}{(2 + 3\kappa)} + \zeta(1 - \lambda^2) V_{f-RCSR} \tag{4-1}$$

Nonlinear regression was employed to find the unknown parameters of Eq. (4-1) to predict the experimental data of bubble rising velocity through the RCSR. The regression results give the values for parameters of total wall factor (η, β) and the net co-flow correction function (ζ) appeared in Eq. (4-1). The regression parameters are derived for terminal velocity of single air bubbles rising through the rectangular confinement with 3 mm × 5.842 mm cross section for five different co-flows including 36 data points. The resulted values are shown in Table 4-1. The p-value parameter in Table 4-1 shows the significance of the estimated correlation for the regression analysis(Soong 2004). A high R-squared of 0.94 and a low p-value in the table show a good match between the regression and the experiment data with significant values for the model parameters.

Table 4-1- Non-linear regression parameters value for rising bubble through the RCSR

η	β	ζ	p-value	R-squared	RMS error
1.52	0.096	0.95	6.09E-40	0.94	0.23

Using the values from Table 4-1, the total bubble terminal velocity for a rectangular geometry is obtained as:

$$V_{t-RCSR} = \frac{1.52\exp(-(\lambda - 0.096)^2)}{k_w k_t} \times \frac{gD_e^2(\rho_f - \rho_g)}{6\mu_f} \frac{(1+\kappa)}{(2+3\kappa)} + 0.95(1-\lambda^2)V_{f-RCSR} \quad (4\text{-}2)$$

As represented in Table 4-1, the predicted value of ζ is 0.95 (close to 1), which means that almost 95 % of the fluid flow velocity at R distance from centerline of the medium contributes on the rising velocity of a bubble with R radius. A relatively low RMS error of 0.23 mm/s for this predicted model, Eq. (4-2), comparing to the high RMS error of 0.87 mm/s for the circular tube model, Eq. (2-54), implies that the predicted model, Eq. (4-2), has a better agreement with the experimental data.

The experimental data of bubble rising velocity through the RCSR (V_{t-RCSR}) is plotted versus normalized bubble diameter (to RCSR width, w) in Figure 4-12 and compared with the modified model in Eq. (4-2). Since the developed correlation in Eq. (4-2) includes the effect of fluid flow on bubble terminal velocity, the local fluid velocity is not subtracted from bubble rising velocity in Figure 4-12. As it is observed from Figure 4-12, the experimental data is in good agreement with the predicated model, relative to Shapira and Haber (1988)'s correlation plotted in Figure 4-11. It is seen from Figure 4-12 that trends of the rising velocity plots for different fluid flow rates become closer to each other as bubble diameters increase. This is due to the shape of the bubbles and as the bubbles enlarge the value of λ becomes larger in Eq. (4-2). Therefore, the contribution of fluid flow velocity on bubble terminal velocity i.e. $0.95(1-\lambda^2)V_{f-RCSR}$, decreases and the total wall friction becomes a dominant factor influencing the bubbles motion.

Eq. (4-2) is physically held for $\lambda \neq 0$, i.e. $D_e \neq 0$ to be a meaningful expression for bubble terminal velocity. If the diameter of bubble approaches zero (λ = 0), Eq. (4-2) returns $0.95V_{f-RCSR}$.

In Figure 4-12, the value of velocity, V_{t-RCSR}, for each fluid flux correlation at $D_e/w = 0$ is $0.95V_{f-RCSR}$, which according to Eq. (2-2) is $1.425q$ (shown by red star in Figure 4-12). Due to the relatively higher buoyancy force, bubble terminal velocity increases as D_e/w increases to 0.8, through the RCSR. However, for D_e/w of larger than 0.8, bubbles interface become closer to the RCSR walls and as bubbles enlarge, the rising velocity drops due to higher confining drag force. It should be noted that the modified correlation in Eq. (4-2) has been developed for the experimental conditions of the present research and may deviate for other applications.

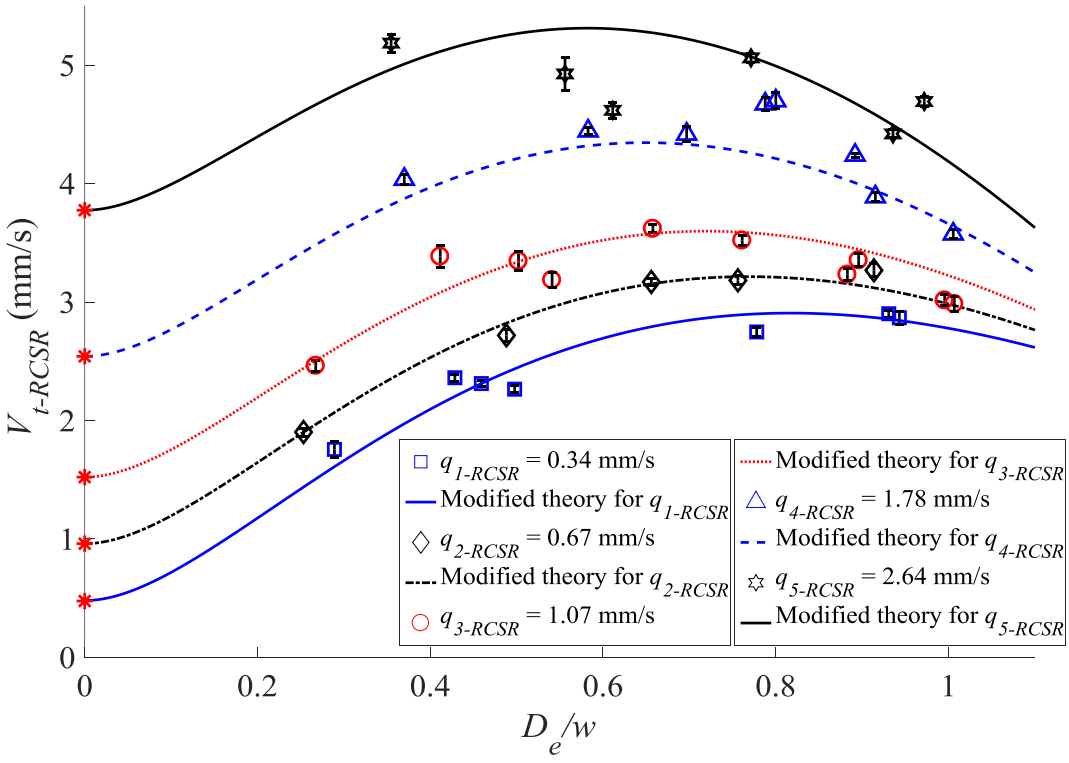

Figure 4-12- Average bubble rising velocity in the RCSR validated with the modified model

In the predicted model, Eq. (4-2), the contribution of fluid co-flow on bubble terminal velocity is introduced as $0.95(1 - \lambda^2)V_{f-RCSR}$. Therefore, in this model, Eq. (4-2), if the co-flow

contribution be zero (stationary fluid medium), the model predicts the bubble terminal velocity in a rectangular confinement with no co-flow. Figure 4-13 plots the experimental data of bubble terminal velocity through RCSR, V_{t-RCSR}, where the co-flow contribution $(0.95(1 - \lambda^2)V_{f-RCSR})$ is subtracted from the experimental data. In this figure, the experimental data are compared against the predicted model, Eq. (4-2), when there is no co-flow in the system, where the experimental data and the semi-empirical model, Eq. (4-2), are normalized to the bubble rising velocity in infinite medium, V_{t-inf}. Figure 4-13 shows that the experimental data collapse on each other as the effect of co-flow is subtracted from data and match with the predicted model, Eq. (4-2).

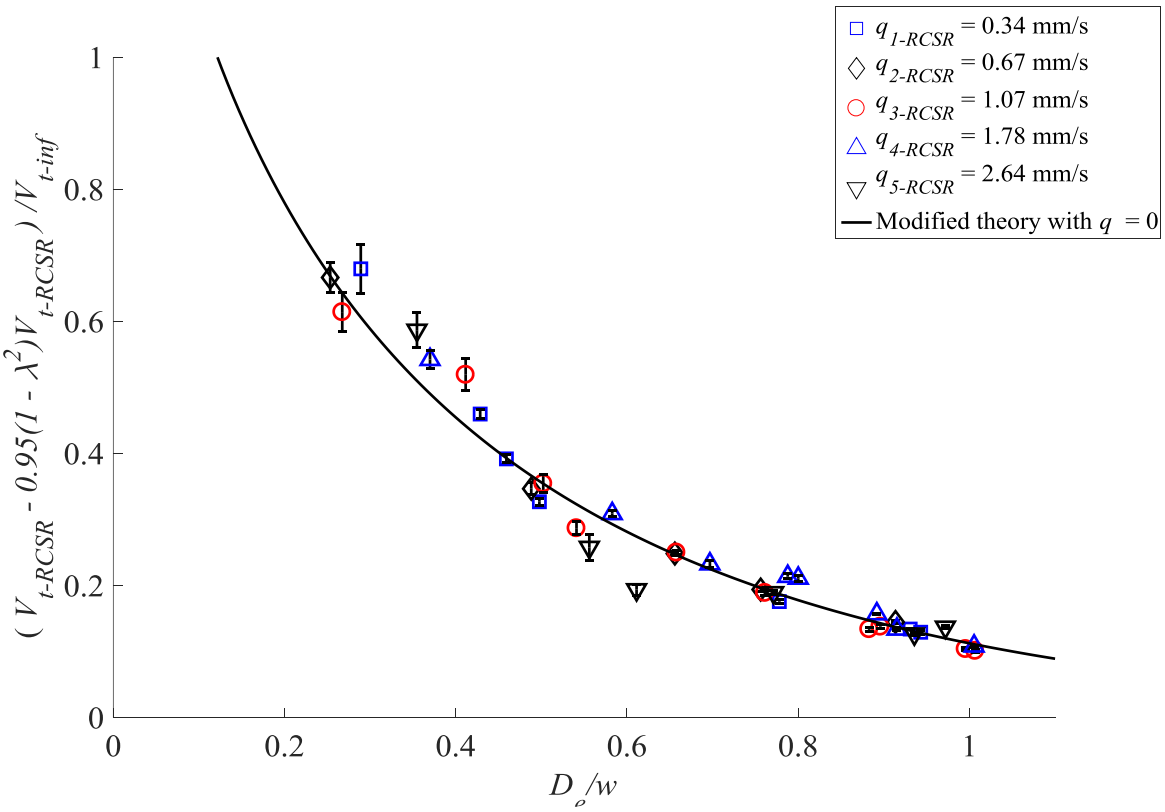

Figure 4-13- Average bubble rising velocity in the RCSR compared against the predicted model, Eq. (4-2), when the fluid medium is stationary.

4.6 Conclusion

Single air bubble rising through a rectangular confining geometry (3 mm × 5.842 mm cross section) inside a rectangular flow channel (22 mm × 5.842 mm cross section) along with five net co-flow were investigated in this chapter. Bubble sizes ranged from 0.76 mm to 3.02 mm and water/glycerol solution of 93 wt% concentration was chosen as the fluid medium to flow with bubbles. Air bubble characteristics were calculated and compared in two main regions of parallel plates region (PPR) and rectangular cross section region (RCSR). Because in the regions with 22 mm × 5.84 mm cross section (PPR), the width (22 mm) is relatively large, theoretical correlation of rise of bubbles in between two parallel plates (Shapira and Haber 1988) was used to validate the measured rising velocity in these regions. However, this theory cannot be used for rectangular geometry because the rise of bubbles through a rectangular geometry is different and more complex, comparing to two parallel plates. The bubble terminal velocity through RCSR was compared with theoretical terminal velocity through a circular tube of hydraulic diameter of the RCSR (Haberman and Sayre 1958). This theory showed a poor agreement with the experimental data as fluid flux increased and the standard deviation (STD) was calculated as 0.87 mm/s. The rise of bubbles through the RCSR was treated as two simpler cases of parallel plates, and the derived wall correction factor for each case (k_w and k_t) were combined together to develop a the total wall correction factor for the rectangular RCSR. A model modification approach based on the experimental results of rising velocity through the RCSR was undertaken to predict the bubble rising velocity in a rectangular confining geometry. Quantitatively, it was shown that the modified correlation that includes the effect of co-flow and rectangular geometry, well predicts the experimental data for bubble terminal velocity in a rectangular geometry, based on the analysis of p-value, R-squared and RMS error.

CHAPTER 5. FLOW AROUND BUBBLES RISING THROUGH A RECANGULAR CONFINEMENT[2]

5.1 Introduction

As a single bubble rises through a confinement, such as rectangular confinement, the flow motion in the surrounding fluid can change according to the bubble terminal velocity, bulk flow flux and size of the bubble. In this chapter, the flow behavior in the flow surrounding air bubbles rising through the vertical RCSR region with 3 mm × 5.84 mm (width × thickness) cross section in co-flows is measured. A much smaller FOV of 7.28 mm × 9.11 mm, compared to the FOV provided in Chapter 4 to allow for the resolution needed to perform PIV and PTV. For each co-flow, only one bubble size was chosen to quantify the velocity vector map of fluid around the bubble using particle shadow velocimetry (PSV) technique. A glycerol/water mixture was used as the working fluid to flow along with single air bubbles through the rectangular confinement. On the collected images of the bubble flow, two image processing approaches of PIV and PTV were undertaken to investigate the tangential velocity at the bubble interface, and compare the spatial resolution of the velocity vectors in the images for both processing approaches.

[2] Some parts of this chapter will be submitted to a publication journal as: H. Soltani, R. Sabbagh, D. S. Nobes, "Theoretical and Experimental Investigation of Fluid Flow around Single Bubbles as Flowing in a Rectangular Confinement", Physics of Fluids, 2018

5.2 Bubble shape and size

Particle recognition processing, outlined in Chapter 3, was performed to quantify the size (diameter) and rising velocity of the bubbles at different locations of RCSR. The bubble equivalent diameter was measured for all bubble sizes and in five different fluid flow fluxes, q. Figure 5-1 plots the instantaneous bubble equivalent diameter normalized by the RCSR width (w, 3 mm) over the rectangular confinement length for all bubble sizes and all fluid fluxes (q). In this figure, the y-axis is the averaged bubble equivalent diameter, D_{e-inst}, normalized by RCSR width, w, and the x-axis represents is the lengthwise location of RCSR which is also normalized by the RCSR width, w. Figure 5-1 shows that bubble sizes remain approximately constant when passing through the confinement region, as expected. It can be seen in Figure 5-1 that for the largest bubble sizes at each fluid flux, q, the minimum and maximum y/w on each trend line (the first and last locations that bubble center is detected in the images) occurs at a relatively farther location from the bottom and top of the images (y/w = -1 and y/w = 1 respectively). This is because in the bubble recognition processing step, the bubbles can be recognized when the whole bubble interface appears in the image. Therefore, as bubbles enlarge, the bubble center (y/w), in the first and last detected images of bubble shift farther from y/w of -0.8 and 0.8 respectively.

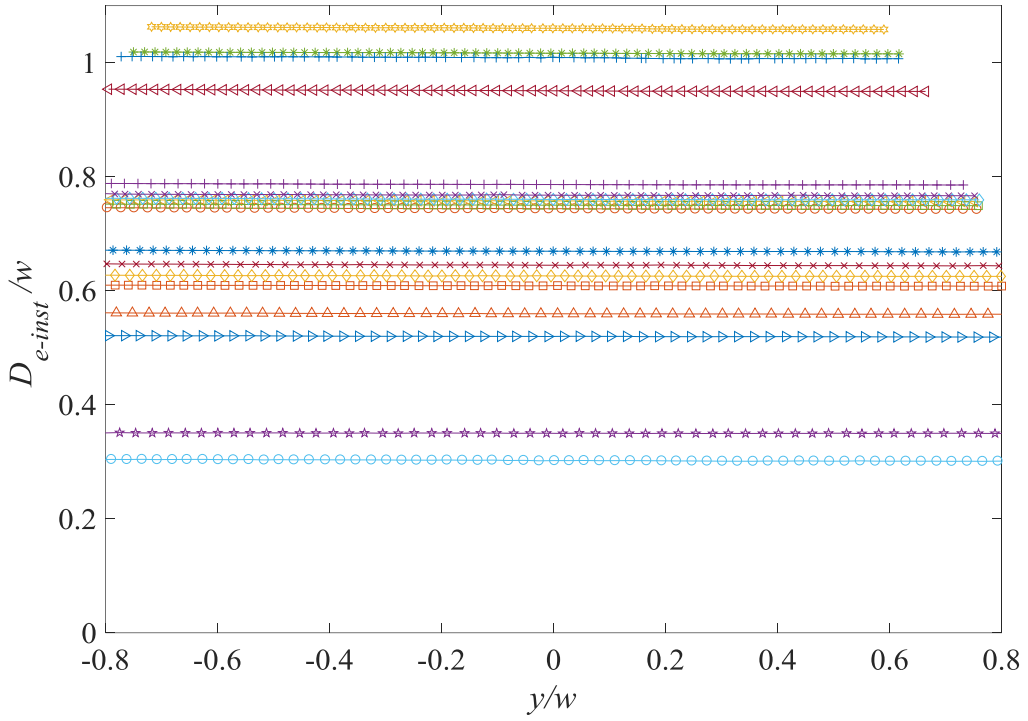

(a) q = 0.34 mm/s

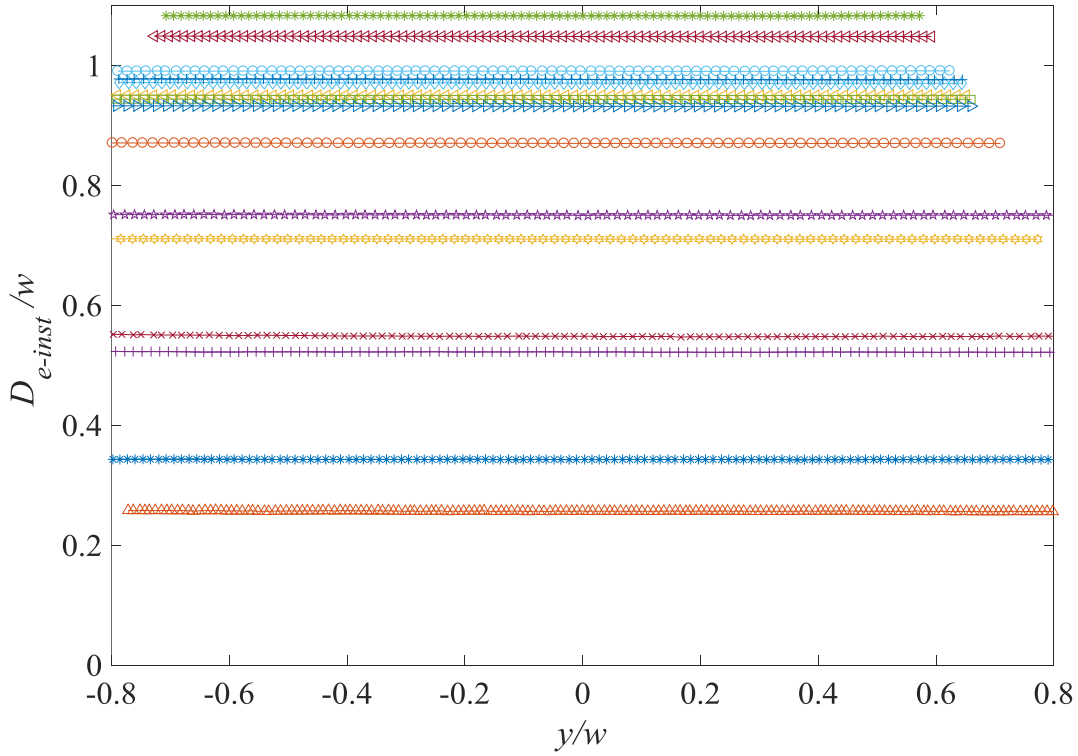

(b) q = 0.67 mm/s

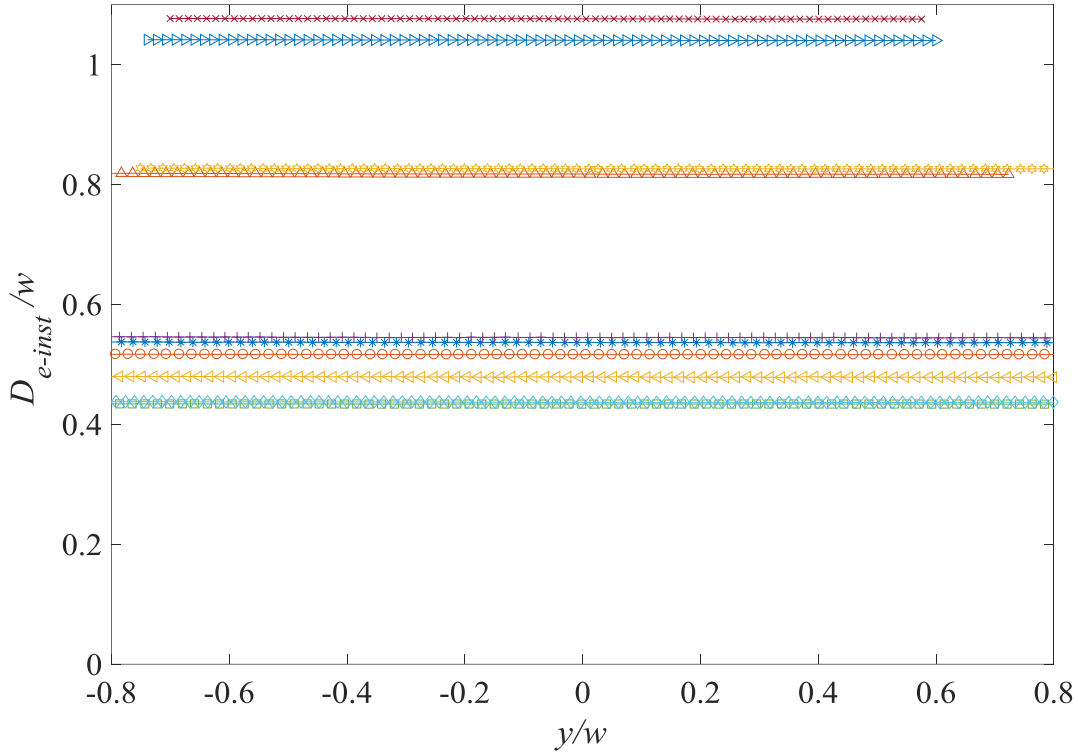

(c) q = 1.07 mm/s

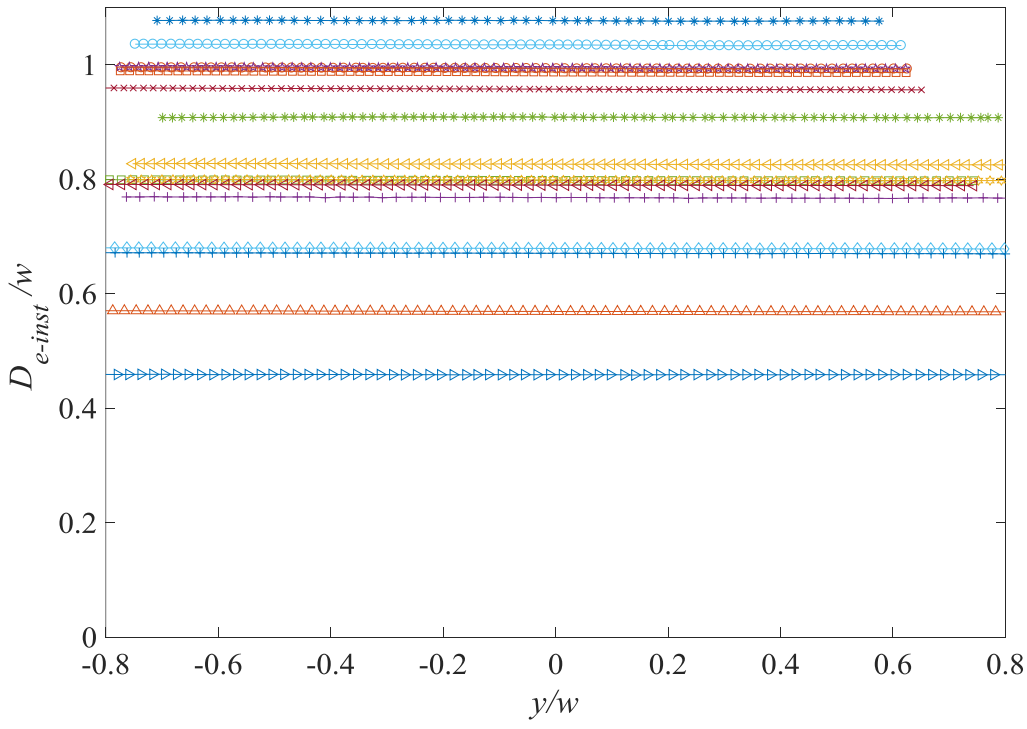

(d) q = 1.78 mm/s

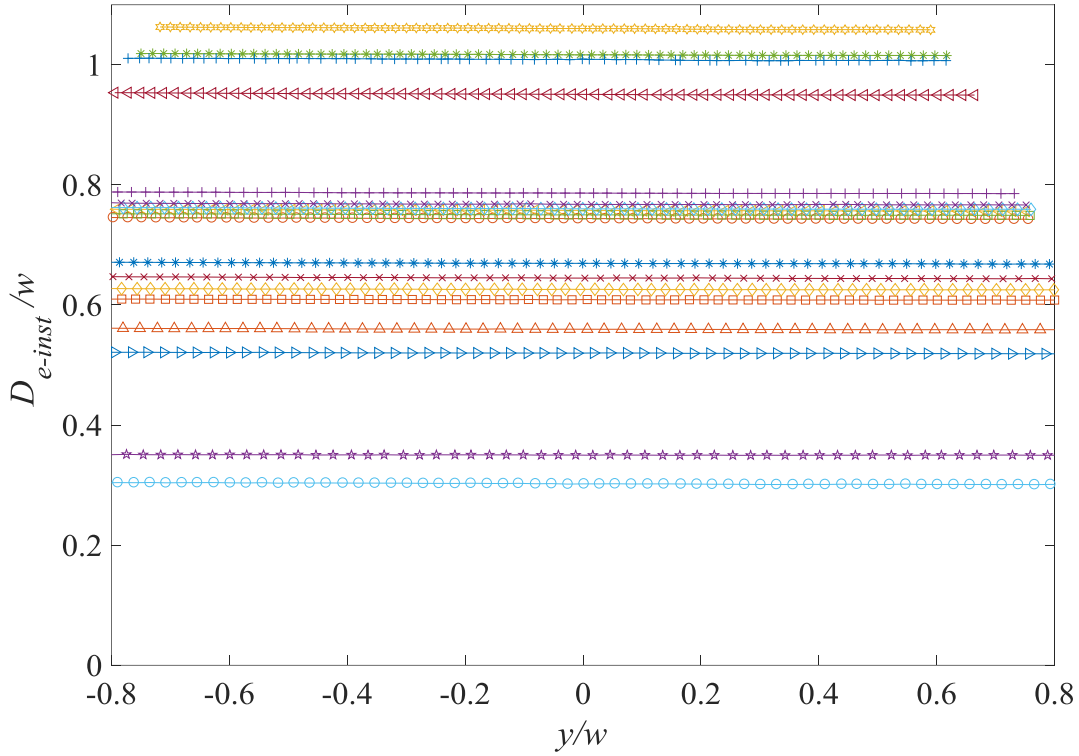

(e) q = 2.64 mm/s

Figure 5-1- Air bubble diameter as rising through the flow cell

As discussed in Chapter 3 and Chapter 4, the minimum and maximum bubble diameter can be calculated from the particle recognition processing. Therefore, the bubble centricity can be derived for each bubble size as rising through the RCSR. Figure 5-2 plots the bubble instantaneous centricity (C_{inst}) (Ghaemi et al. 2010) against the lengthwise location of the RCSR for all of the fluid fluxes (q) and bubble sizes. As shown in Figure 5-2, the centricity trends for relatively smaller bubble sizes are scattered, due to lower number of pixels inside a relatively small bubble (more explanation provided in Chapter 4). This figure shows that for all bubble sizes, the centricity remains almost the same for all bubble sizes and all fluid fluxes (q), This means that in this region of the RCSR, the bubble shape has been stabilized and there is negligible change in the bubble shape.

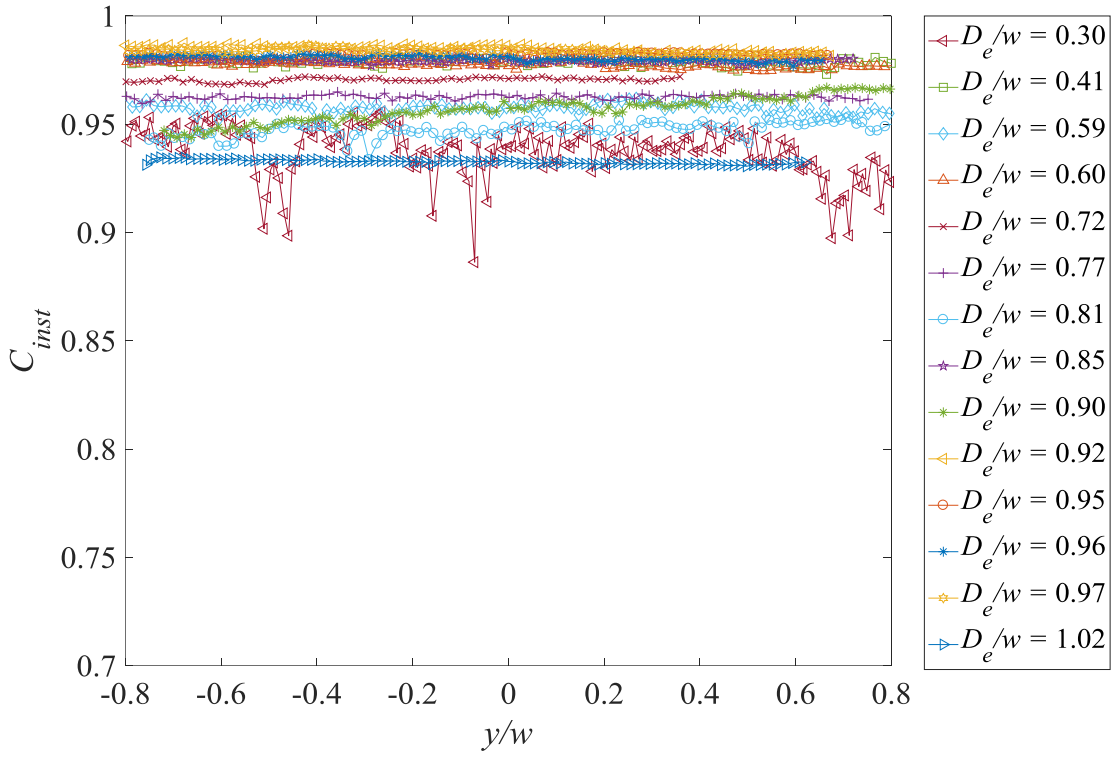

(a) q = 0.34 mm/s

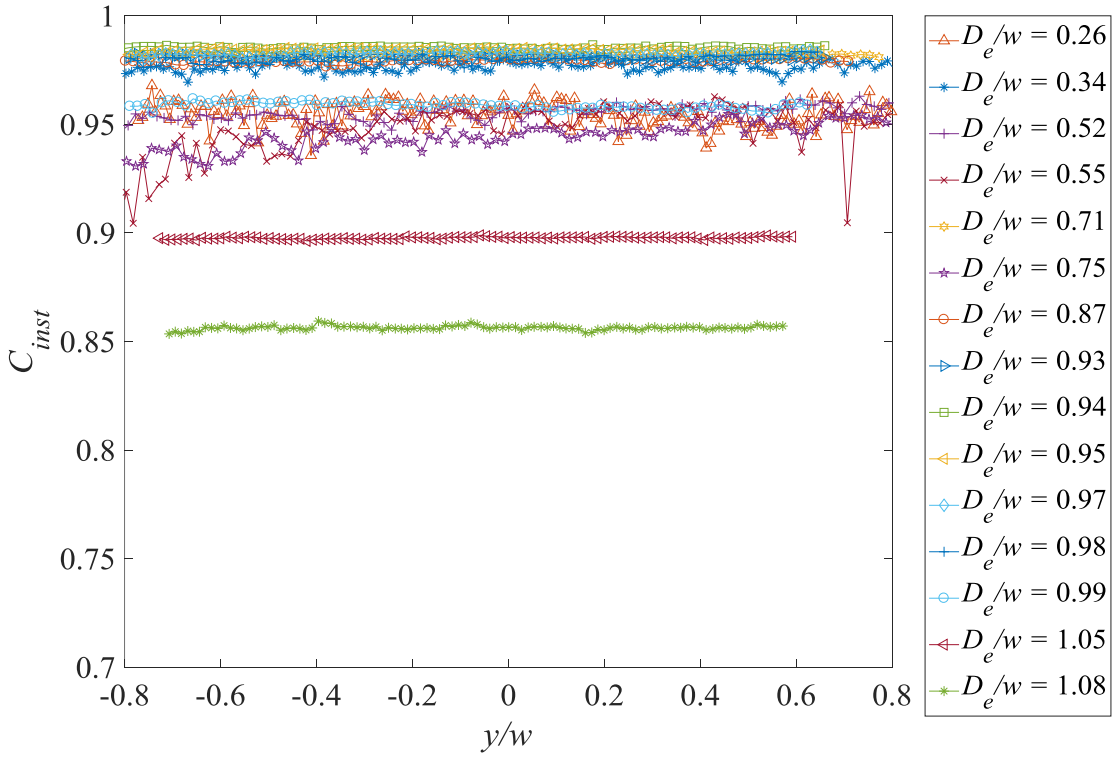

(b) q = 0.67 mm/s

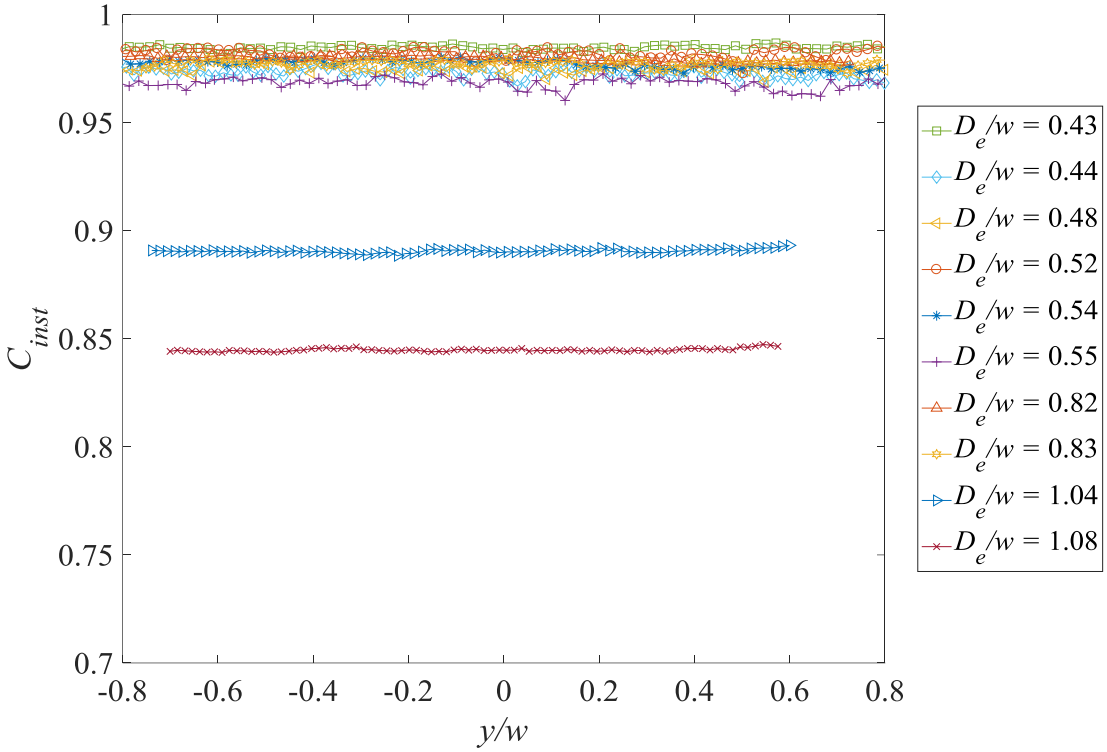

(c) q = 1.07 mm/s

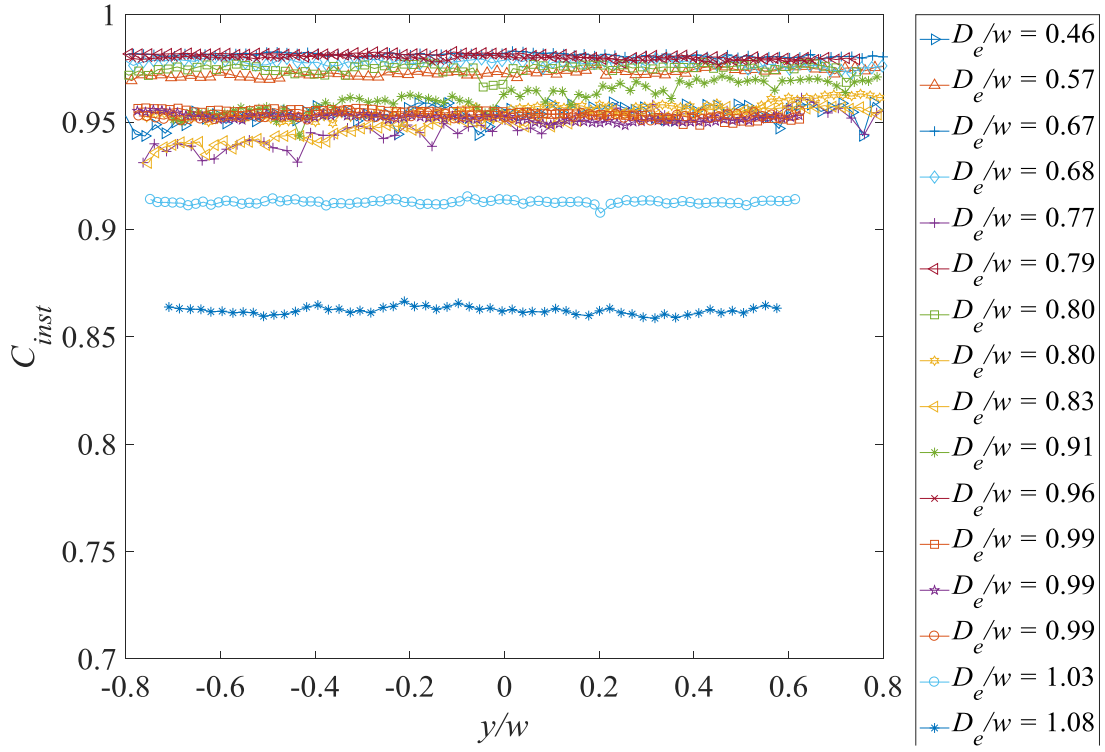

(d) q = 1.78 mm/s

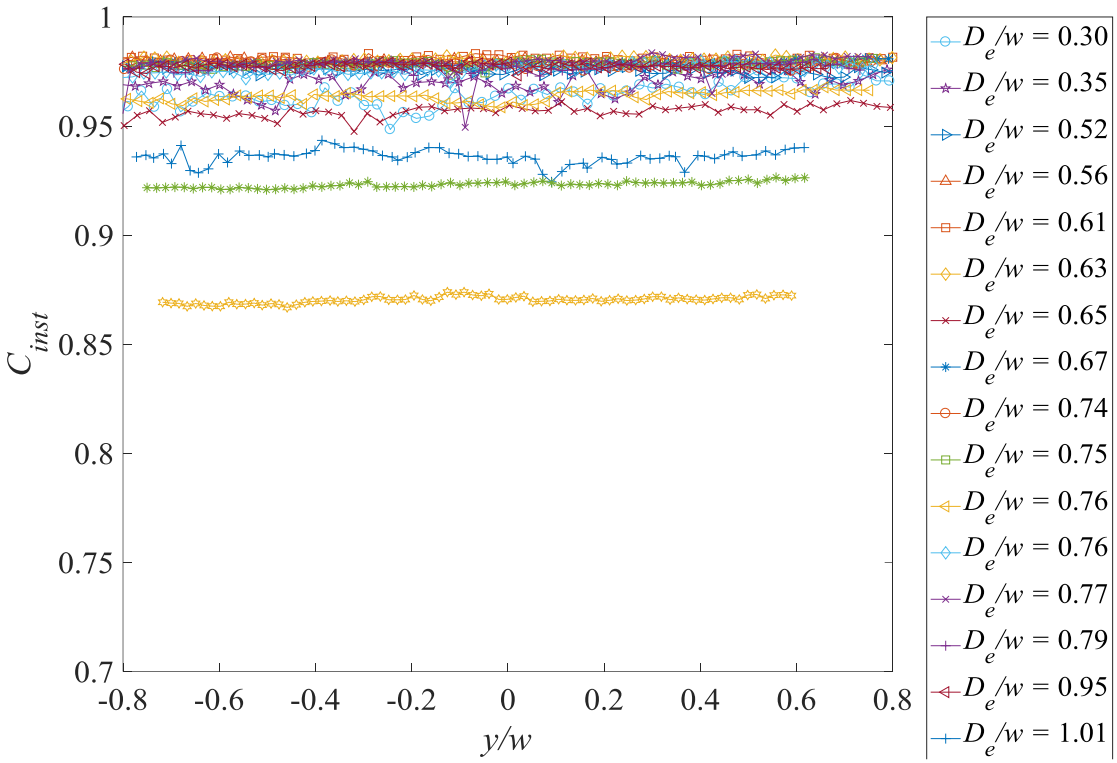

(e) q = 2.64 mm/s

Figure 5-2- Instantaneous centricity (C_{inst}) of bubbles along the flow channel

To understand the effect of bubble size on centricity in more details, the instantaneous centricities plotted in Figure 5-2, are averaged over the lengthwise location of the RCSR from y/w = -0.7 to 0.7. The results are plotted in Figure 5-3 against non-dimensional bubble diameter to RCSR width, w. In this figure, q_{1-RCSR} to q_{5-RCSR} show the fluid flux through RCSR and a second x-axis is added to the top of the figure representing the bubble equivalent diameter (D_e) in pixels. This figure shows that all bubble sizes are larger than 160 pixels, which is the threshold of bubble diameter to have reasonable measurement of centricity (Ghaemi et al. 2008). Figure 5-3 shows that the centricity trend is approximately levelled off as bubble sizes increase up to D_e/w = 0.8, due to having enough resolution in the measurements. As indicated in Figure 5-3, for

air bubbles with $D_e/w > 0.8$, the centricity through RCSR, C_{b-RCSR}, decreases, because the bubbles are deformed after this size due to the effect of confining walls.

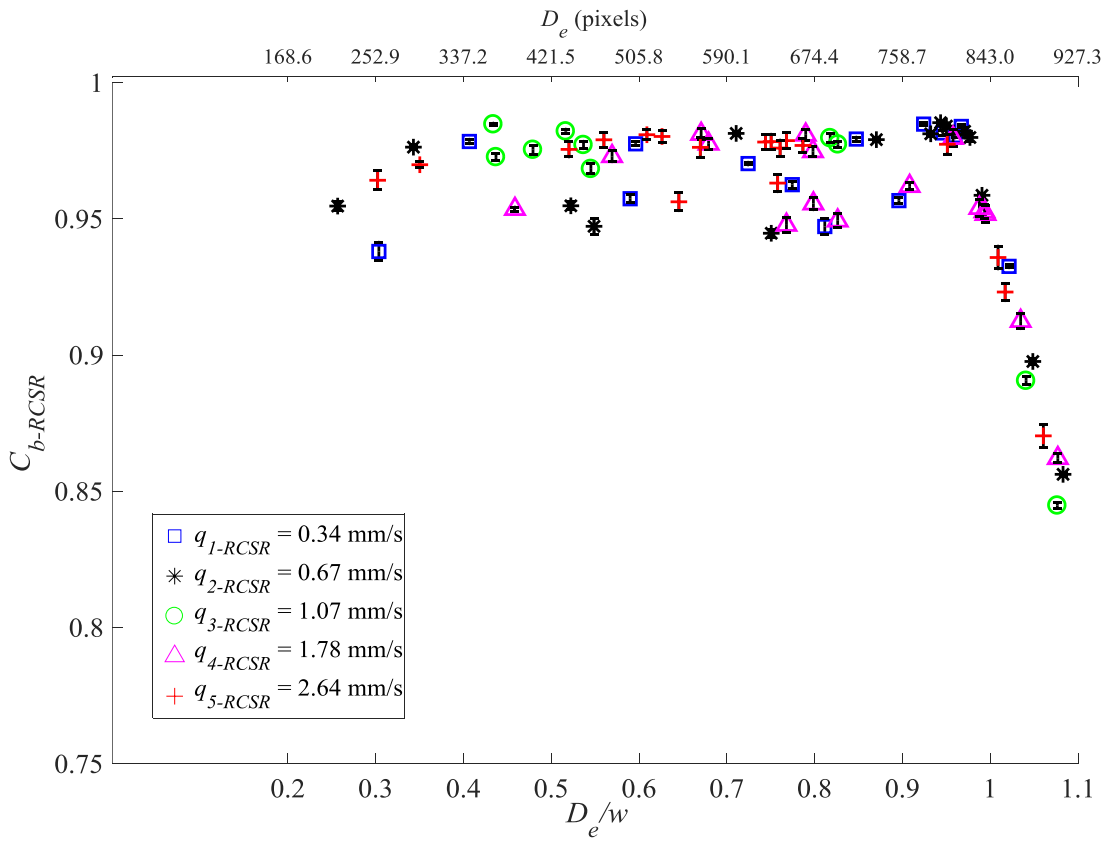

Figure 5-3- Air bubble average centricity over RCSR

5.3 Bubble rising velocity

As described in the Chapter 2, the rising velocity of the bubbles were determined based on the displacement of bubble center. As a bubble is generated in a fluid medium, the rising velocity gradually increases until it becomes almost constant and reaches the terminal velocity. As it was shown in Chapter 3, the bubble rising velocity might change as it enters the RCSR from the parallel plate region (PPR) due to the change in the confining geometry. Therefore, just after entering the

RCSR, the bubbles may need to travel a certain distance until they reach a steady terminal velocity. Figure 5-4 plots the bubble rising velocity, V_{r-inst}, for all bubble sizes and fluid fluxes, q, along the lengthwise location of the flow channel normalized by the RCSR width (y/w). In this figure, the ordinate is the instantaneous rising velocity, V_{r-inst}, and abscissa is the lengthwise location along the RCSR, normalized by RCSR width, w. For the rising velocity trends for each bubble size, a linear regression was fitted and the slope of this regression is reported as m in the legend in Figure 5-4. As shown in the figure legend, m varies from 0.00 to 0.3, which means that the rising velocity has upward trend as bubbles rise through RCSR. However, compared to the rising velocity of bubbles, the slope of this trend is low. Therefore, because there is negligible change in the bubble rising velocity trend, it can be concluded that bubbles have reached the terminal velocity as rising through the RCSR. The slight increase in bubble rising velocity can be because of the effect of approaching the exit of RCSR, y/w = 1, which makes the bubble accelerate as rising along this region of the flow channel.

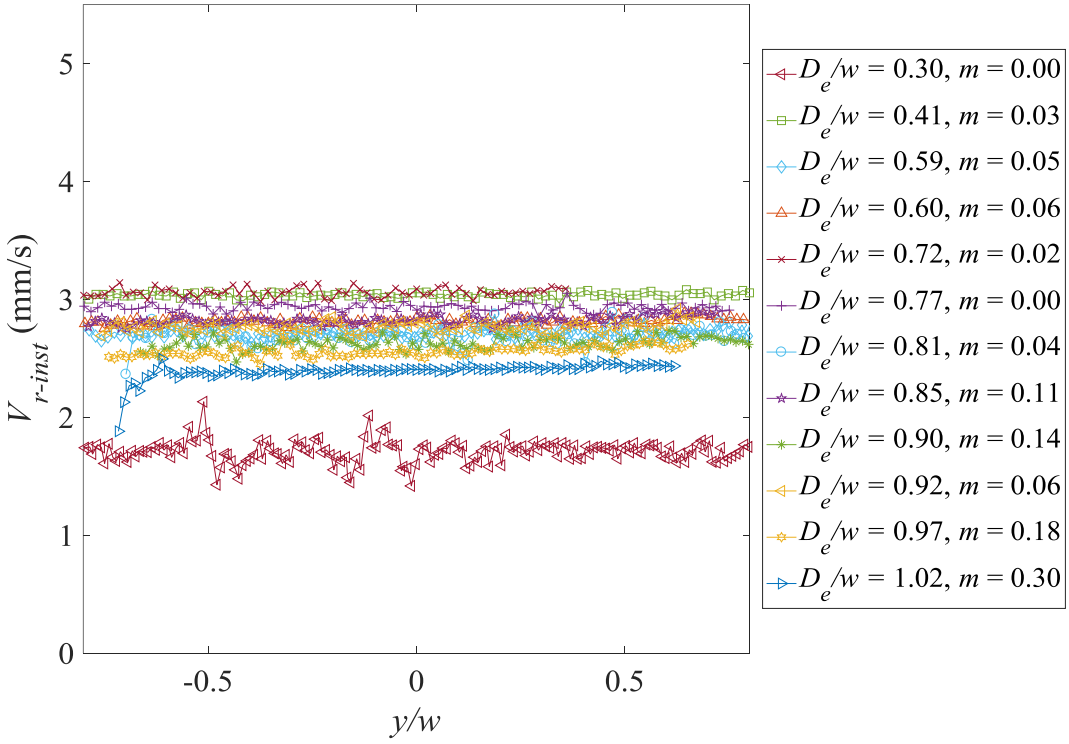

(a) q = 0.34 mm/s

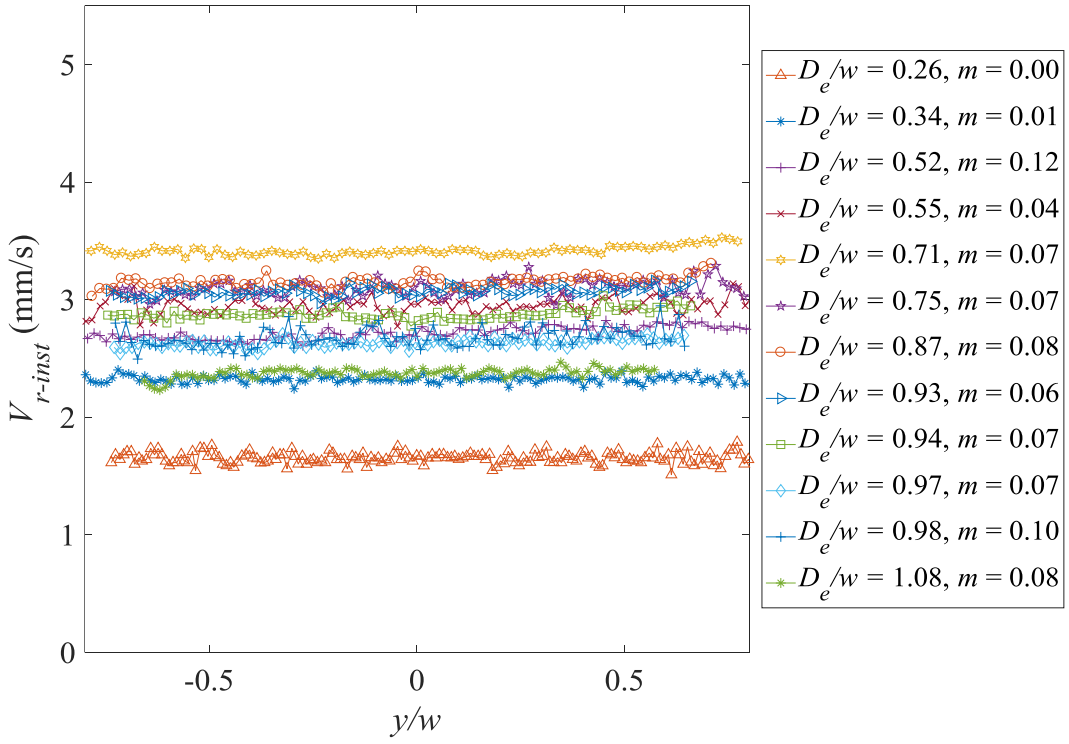

(b) q = 0.67 mm/s

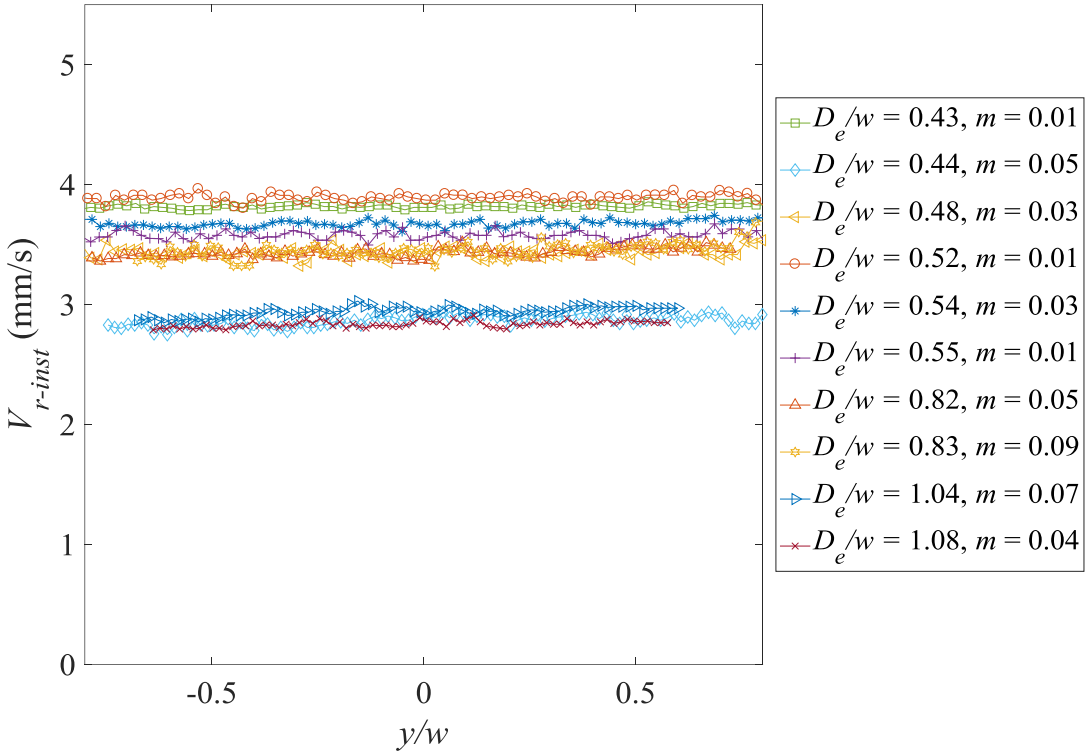

(c) q = 1.07 mm/s

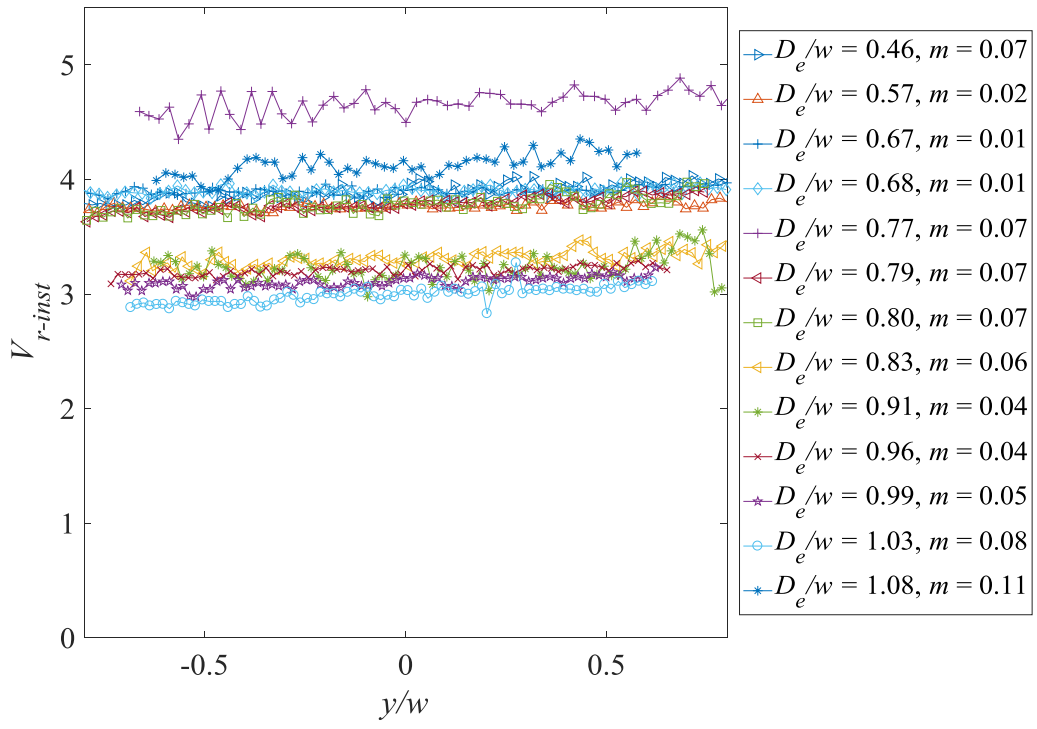

(d) q = 1.78 mm/s

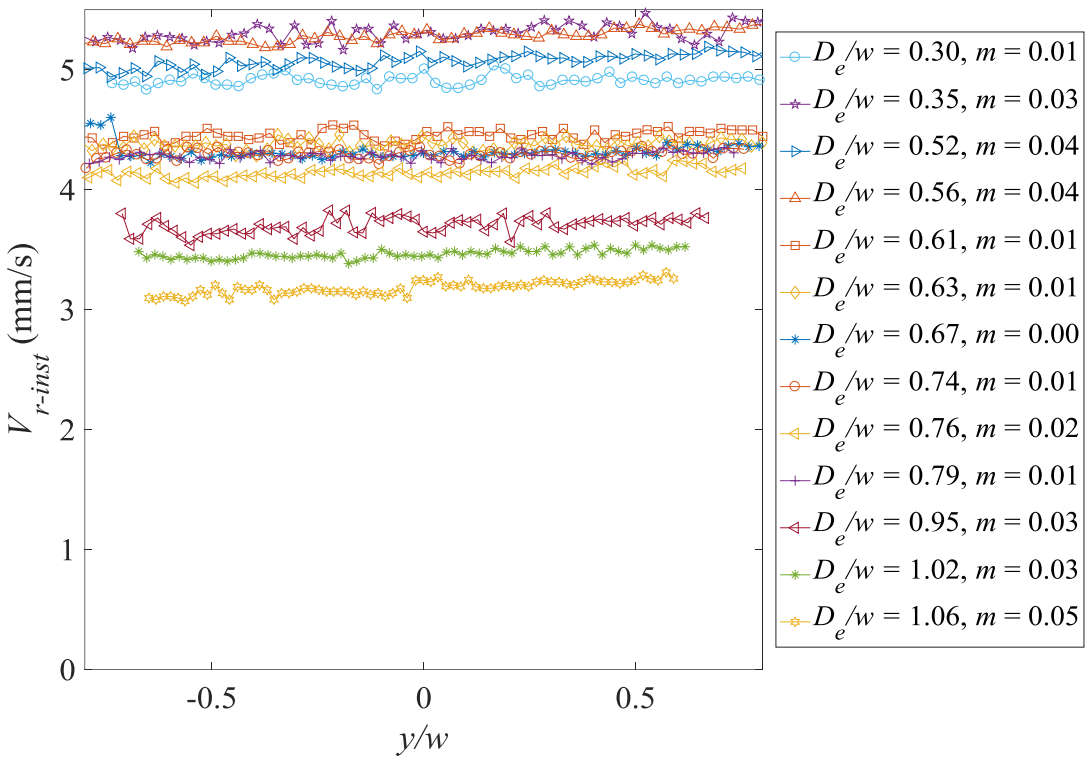

(e) q = 2.64 mm/s

Figure 5-4- Bubble rising velocity in the flow channel

5.4 Average rising velocity in the RCSR

The bubble terminal velocity through the RCSR, can be compared to the developed semi-empirical model for bubble terminal velocity through rectangular channels, Eq. (2-61). Using the approach developed in Chapter 4, the unknown parameters in Eq. (2-61) are determined using non-linear regression and results are presented in Table 5-1.

Table 5-1- Non-linear regression parameters value for rising bubble through the RCSR

η	β	ζ	p-value	R-squared	RMSE
1.73	-0.11	0.95	1.36E-68	0.84	0.31

Therefore, the bubble terminal velocity through a rectangular confining geometry is derived as:

$$V_{t-RCSR} = \frac{1.73\exp(-(\lambda+0.11)^2)}{k_w k_t} \times \frac{g D_e^2(\rho_f - \rho_g)}{6\mu_f} \frac{(1+\kappa)}{(2+3\kappa)} + 0.95(1-\lambda^2)V_{f-RCSR} \quad (5\text{-}1)$$

As indicated in Table 5-1, the values derived for η and β are close to the ones obtained in Chapter 4. In addition, having a p-value close to zero (1.36×10^{-68}), R-squared close to 1 (0.84), and a relatively low RMS error (0.31) show that the derived correlation in Eq. (5-1) is a reasonable prediction of the bubble terminal velocity through a rectangular confinement.

The instantaneous bubble terminal velocity presented in Figure 5-4 were averaged from y/w = -0.7 to 0.7, and the results are plotted in Figure 5-5 and compared against the predicted model in Eq. (5-1). In this figure, y-axis is the bubble average velocity through RCSR, and x-axis represents the bubble equivalent diameter, D_e, normalized by the RCSR width, w.

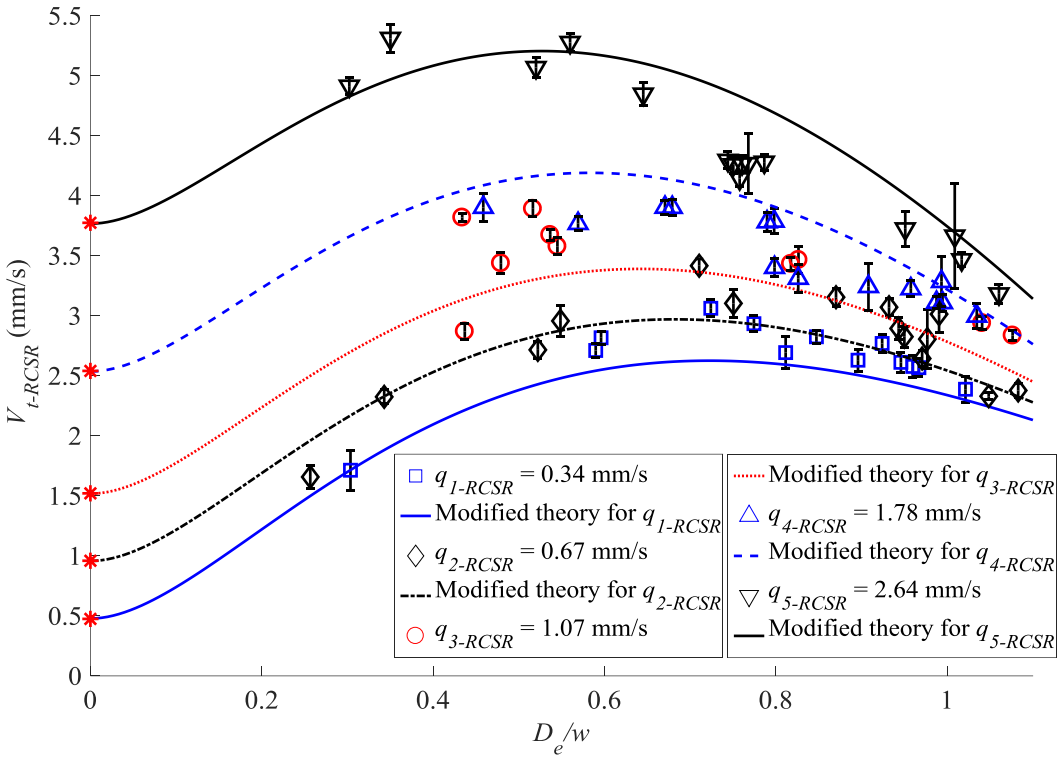

Figure 5-5- Average bubble rising velocity in the RCSR validated with the modified model

Similar to Figure 4-13 in Chapter 4, Figure 5-6 plots the experimental data of bubble terminal velocity through RCSR, V_{t-RCSR}, where the co-flow contribution $(0.95(1-\lambda^2)V_{f-RCSR})$ is subtracted from the experimental data. In this figure, the experimental data is compared against the predicted model, Eq. (5-1), when there is no co-flow in the system. Both experimental data and the prediction model, Eq. (5-1), are normalized with the bubble terminal velocity in infinite medium, V_{t-inf}.

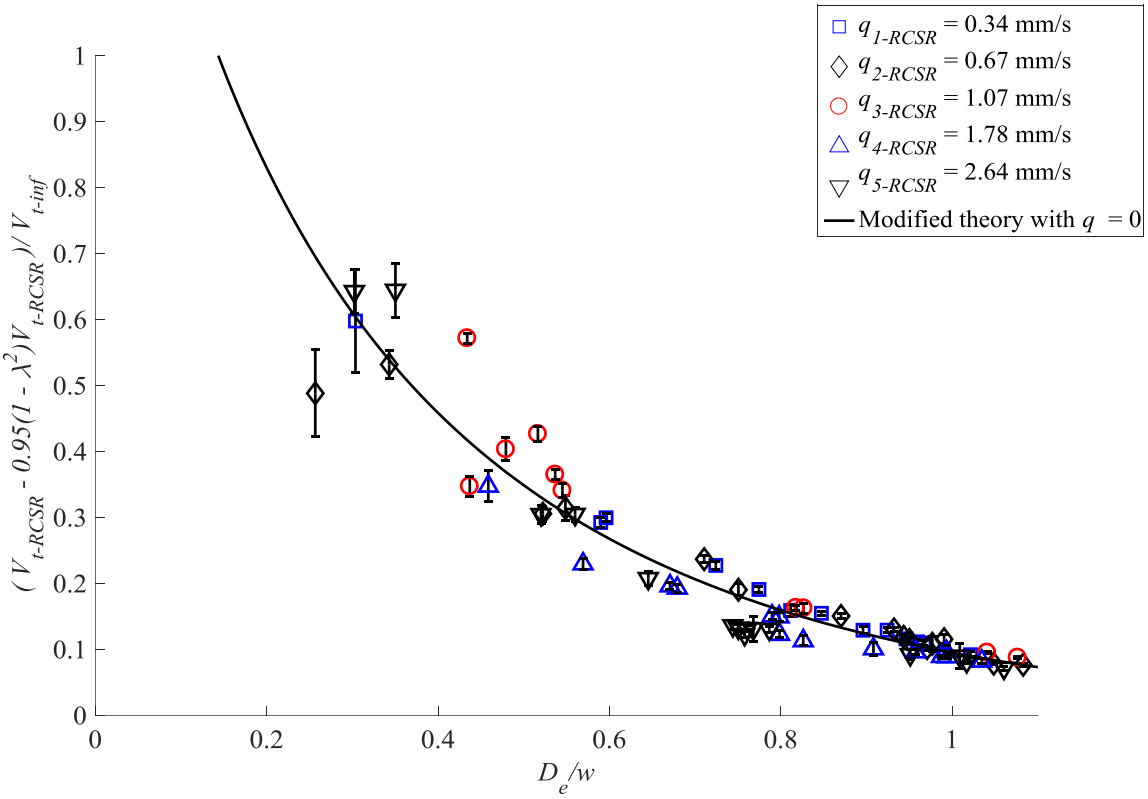

Figure 5-6- Average bubble rising velocity in the RCSR validated with the modified model

5.5 Flow around rising bubbles (PIV and PTV processing)

In this study, for each of the five fluid fluxes, q, provided in Table 3-3, one bubble size is chosen to be investigated. For the collected images, two processing approaches of PIV and PTV were undertaken to analyze the displacement of the tracer particles and hence derive the velocity field. As discussed in the Chapter 3, in PTV image processing, tracer particles can be tracked for more than 2 frames, comparing to PIV. For PTV processing in this chapter, the tracer particles were tracked over 5 frames which results in 4 velocity vectors for each tracked particle. Therefore, for the tracer particles that disappear or cannot be tracked for 4 frames no velocity vector would

be derived. As discussed in Chapter 4, the PTV processing results in a sparse vector field; therefore, the velocity vectors cannot be mapped onto a color map background.

Figure 5-7(a) shows an example of a raw image of a single bubble rising in a net co-flow. The PIV processing result on this raw image is shown in Figure 5-7(b), where the black vectors represent the velocity vectors overlaid on a color map background. Figure 5-7(c) shows the PTV image processing results on the raw image shown in Figure 5-7(a). It can be seen from Figure 5-7(c) that the velocity vectors are sparse and as highlighted in the previous paragraph, they cannot be mapped on a color map background. In addition, Figure 5-7(c) indicates that the sparse velocity vectors appear cluttered and it is hard to see the velocity profile in the image Therefore, the PTV data are interpolated onto a regular grid of 15 pixels resolution in order to overlay the PTV results onto a color map background and compare them to PIV processing results. Figure 5-7(d) plots the interpolated PTV velocity vectors, which are overlaid on a color map background. Comparison of Figure 5-7(c) and Figure 5-7(d) highlights that the interpolated PTV vectors overlaid on a color map background show the velocity profile in the flow field much clearer than the sparse data field.

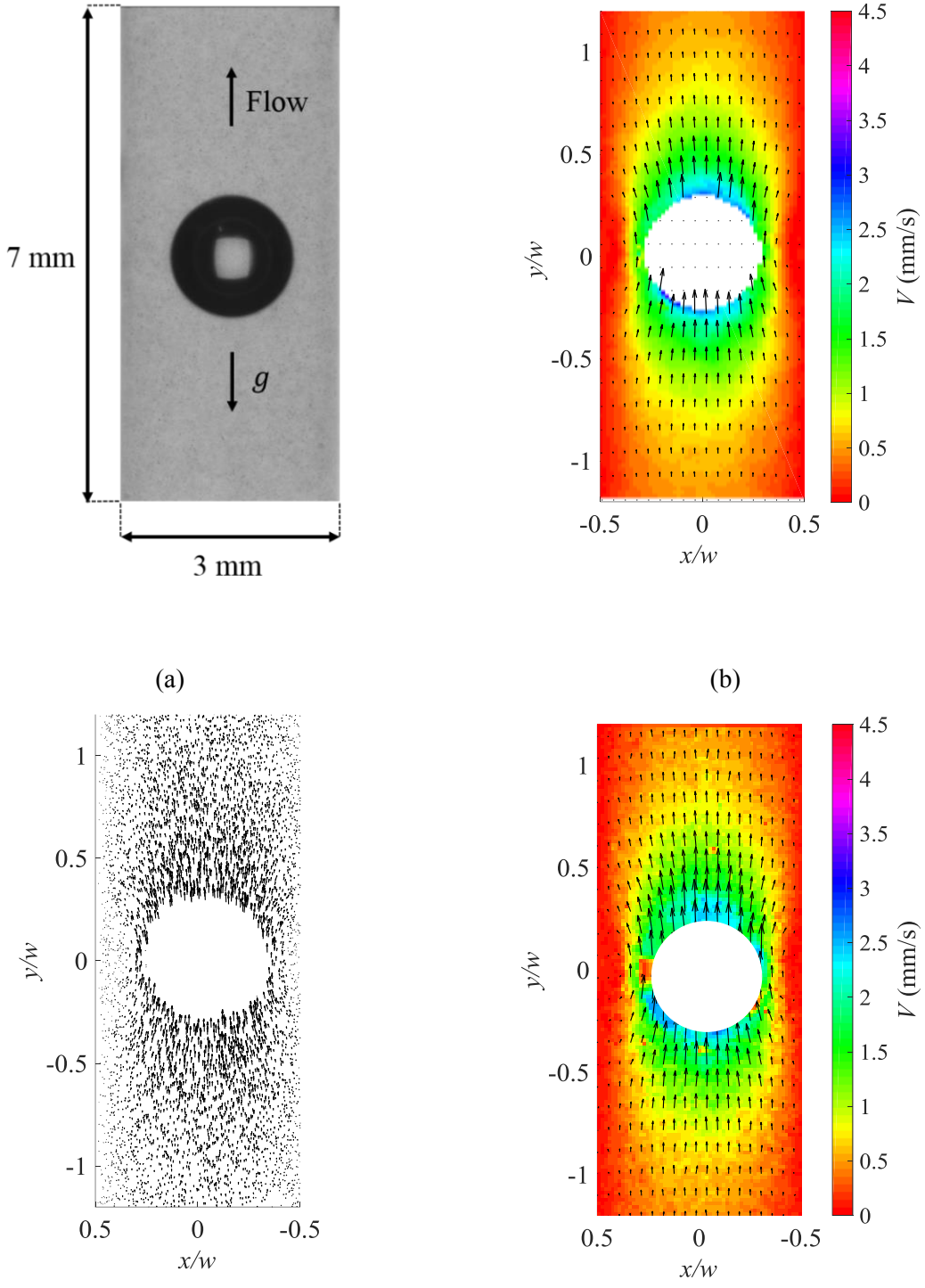

Figure 5-7- An example of (a) image of the raw data, with (b) PIV, (c) sparse PTV, and (d) interpolated PTV processing results

5.5.1 A comparison of the flow fields with PIV and PTV processing

Figure 5-8 shows a background color map of the velocity field overlaid with a velocity vector map for one bubble size at each bulk flow flux, q. The bubble sizes are chosen to be approximately the same and small relative to the RCSR width, w, to minimize the wall effect on the fluid flow surrounding the bubble. Figure 5-8(a),Figure 5-8(c), Figure 5-8(e), Figure 5-8(g) and Figure 5-8(i) show the PIV image processing results, and Figure 5-8(b), Figure 5-8(d), Figure 5-8(f), Figure 5-8(h) and Figure 5-8(j) indicate the PTV data, where the interpolated velocity vectors are overlaid on a color map background. Bubbles and working fluid flow direction is upward in the images and gravity points downward. In Figure 5-8, x-axis and y-axis are the RCSR widthwise and lengthwise directions respectively and are normalized by the RCSR width, w. The points -0.5 and 0.5 on y-axis represent the left and right sides of the RCSR walls. The y/w = 1.2 line is just before the top of RCSR.

In Figure 5-8(a)-(j), the instantaneous bubble equivalent diameter, D_{e-inst}, and instantaneous rising velocity, V_{r-inst}, calculated in bubble recognition processing, were averaged for all of the image frames and are reported as D_e/w and V_{t-rect} in Table 5-2. Figure 5-8(a)-(j) demonstrate the velocity field right at the front and rear of the bubble interface has almost the same value as the bubble terminal velocity, V_{t-rect}. In addition, as fluid flux, q, increases, the velocity field increases at the bubble surroundings, due to the higher bubble terminal velocity (the velocity magnitude does not significantly change close to the RCSR walls because of no-slip boundary condition).

Table 5-2- The bubble characteristics at each fluid flux, q

Fluid flux, q	D_e/w	Terminal velocity, V_{t-rect}
0.34 mm/s	0.6	2.82 mm/s
0.67 mm/s	0.34	2.32 mm/s
1.07 mm/s	0.38	3.82 mm/s
1.78 mm/s	0.57	3.77 mm/s
2.64 mm/s	0.52	5.07 mm/s

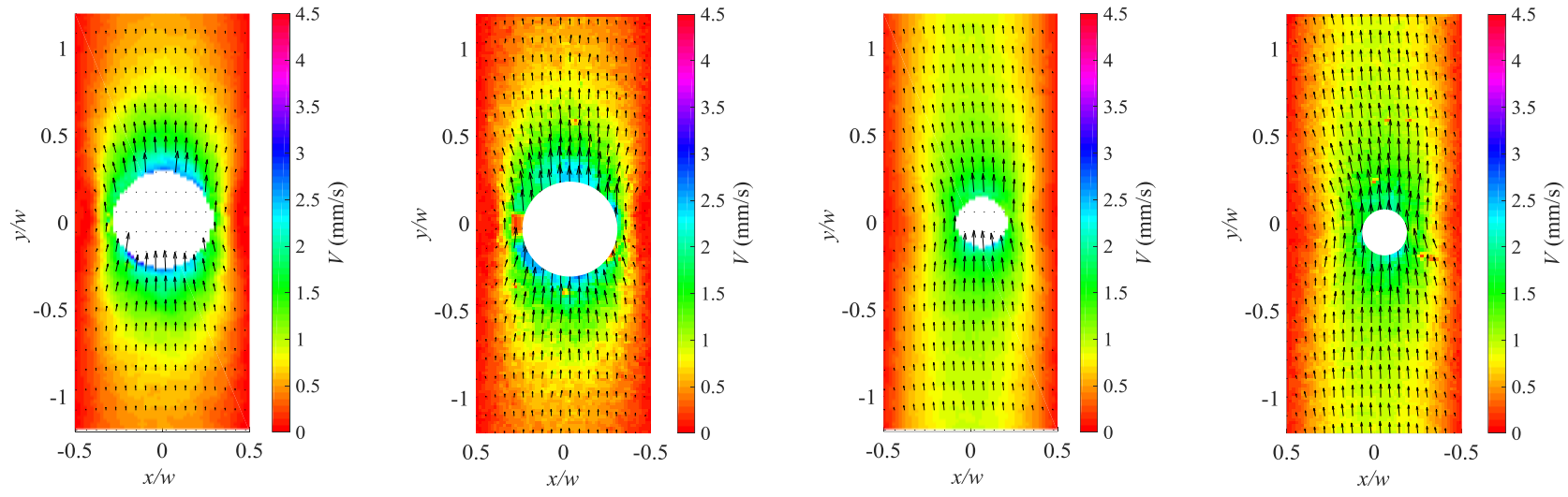

(a) q = 0.34 mm/s, PIV (b) q = 0.34 mm/s, PTV (c) q = 0.67 mm/s, PIV (d) q=0.67 mm/s, PTV

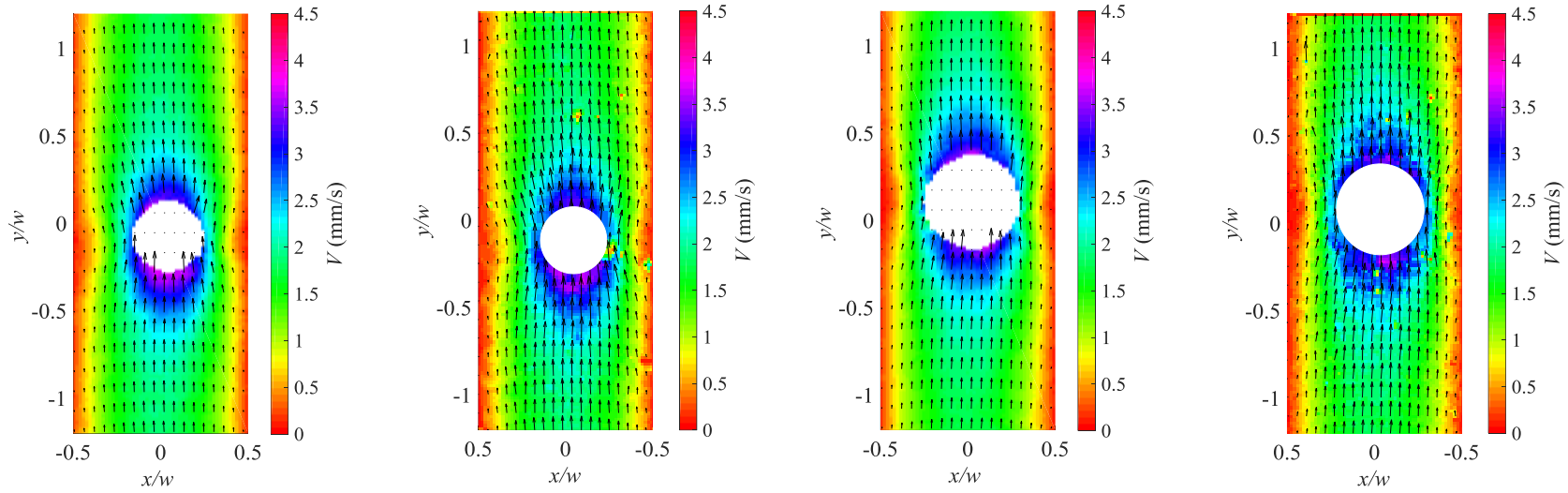

(e) q=1.07 mm/s, PIV (f) q=1.07 mm/s, PTV (g) q=1.78 mm/s, PIV (h) q=1.78 mm/s, PTV

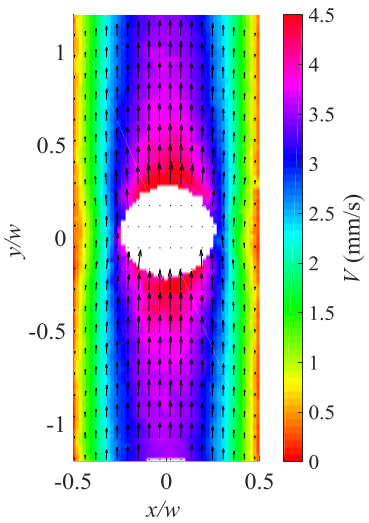

(i) q = 2.64 mm/s, PIV

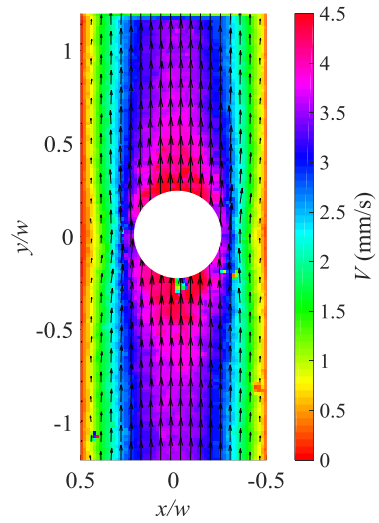

(j) q = 2.64 mm/s, PTV

Figure 5-8- Velocity vector map around single rising bubbles with a background color map for velocity

5.5.2 Comparison of the centerline velocity for PIV and PTV processing

The fluid flux, q, was measured in a separate experiment, where the single phase flux (q) was prescribed according to the syringe pump input settings and the measured velocity profile in the flow. Since in the single phase flow experiment there was no bubble in the system, the fluid flux, q, might be different for the same syringe pump input settings when bubbles flow through the flow channel as well. It was noticed that the fluid flux stabilizes after a certain amount of time, and this space of time becomes relatively longer for higher fluid fluxes, q. Therefore, for the same syringe pump input, the fluid flux, q, when bubbles flow through the channel along with the bulk fluid can be different than the measured value in the single phase flow experiment.

As shown in Figure 5-8, the velocity magnitude varies at different spatial location in the surrounding fluid. To further investigate the effect of fluid flux, q, on the velocity field at different distances from the bubble center, one image in which the bubble is approximately at the center of the image (y/w = 0) is chosen. The velocity magnitude along a vertical line passing from the center of the bubble is derived from PIV and PTV processing and results are plotted in Figure 5-9(a)-(j). The experimental data in Figure 5-9 show that for all fluid fluxes, q, the velocity magnitude is maximum at the front and rear of the bubble, as expected. Farther from the front and rear of the bubble, the velocity magnitude decreases, as expected from Figure 5-8.

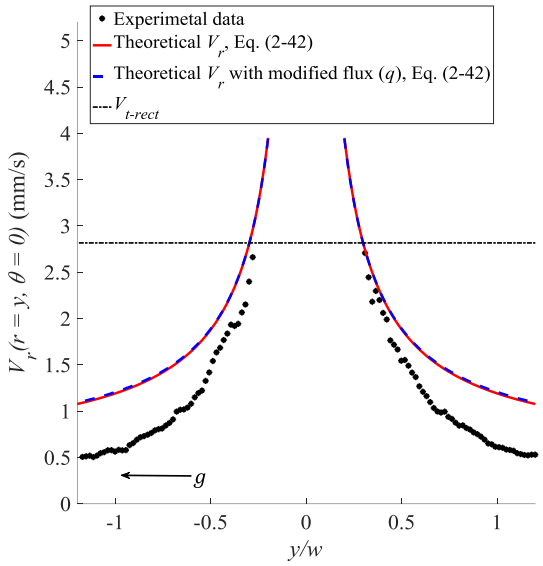

(a) q = 0.34 mm/s, D_e = 1.79 mm, V_{t-rect} =2.82 mm/s, PIV

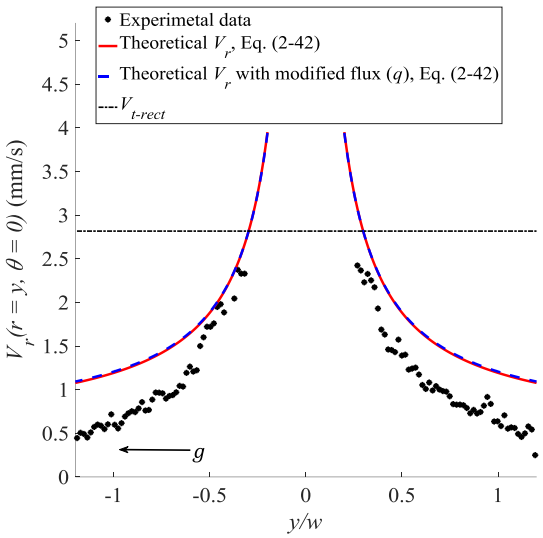

(b) q = 0.34 mm/s, D_e = 1.79 mm, V_{t-rect} =2.82 mm/s, PTV

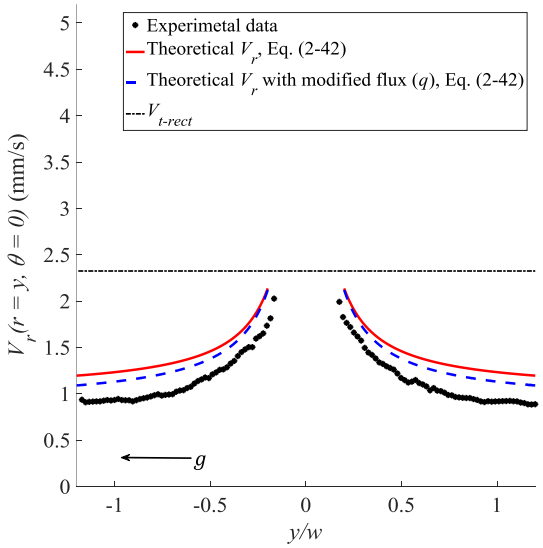

(c) q = 0.67 mm/s, D_e = 1.03 mm, V_{t-rect} =2.32 mm/s, PIV

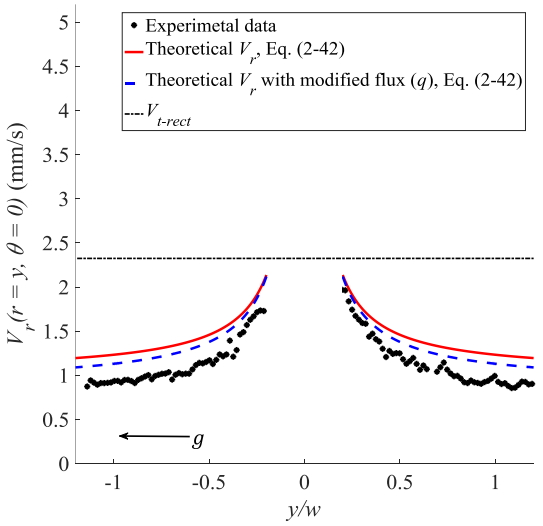

(d) q = 0.67 mm/s, D_e = 1.03 mm, V_{t-rect} =2.32 mm/s, PTV

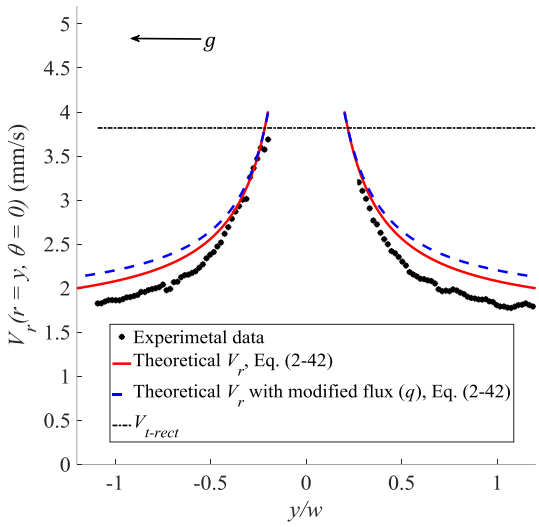

(e) q = 1.07 mm/s, D_e = 1.13 mm, V_{t-rect} =3.82 mm/s, PIV

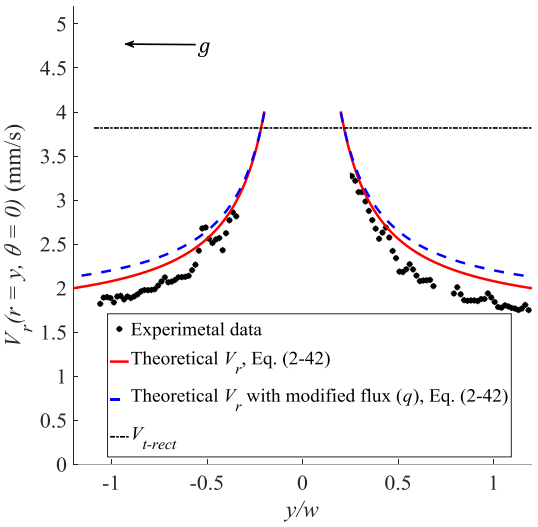

(f) q = 1.07 mm/s, D_e = 1.13 mm, V_{t-rect} =3.82 mm/s, PTV

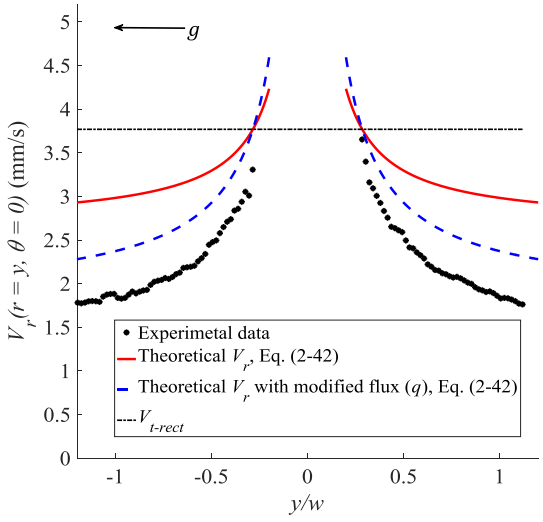

(g) q = 1.78 mm/s, D_e = 1.71 mm, V_{t-rect} =3.77 mm/s, PIV

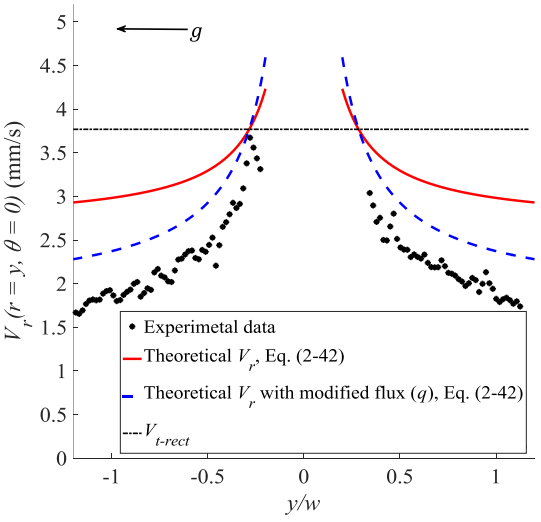

(h) q = 1.78 mm/s, D_e = 1.71 mm, V_{t-rect} =3.77 mm/s, PTV

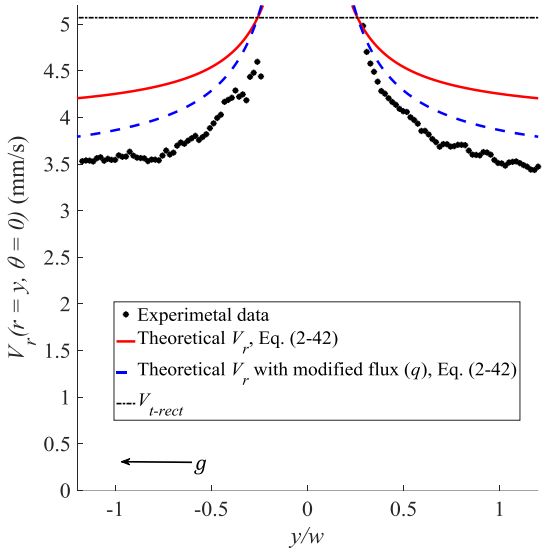

(i) q = 2.64 mm/s, D_e = 1.56 mm, V_{t-rect} =5.07 mm/s, PIV

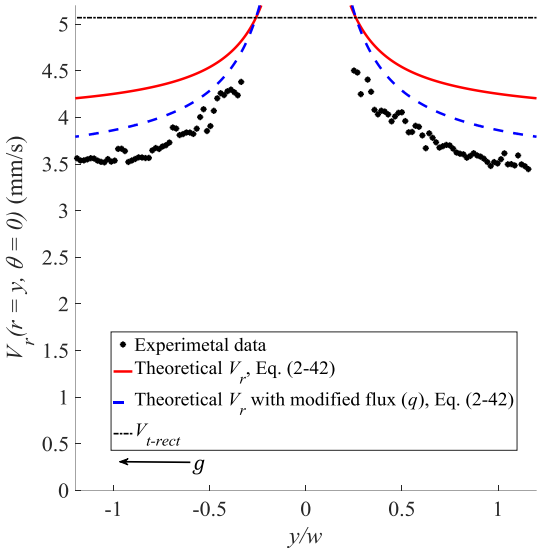

(j) q = 2.64 mm/s, D_e = 1.56 mm, V_{t-rect} =5.07 mm/s, PTV

Figure 5-9- Velocity magnitude along a vertical line passing through the center of the bubble

The bulk fluid velocity at the RCSR centerline is equal to radial velocity, V_r, at $\theta = 0$. Therefore, in Figure 5-9, the theoretical radial velocity at θ = 0, Eq. (2-42), is plotted as the red solid line to be compared against the experimental data, where the fluid flux measured in the single phase flow experiment is used as the V_{f-max}. In Figure 5-9, comparison of the theoretical radial velocity (V_r) plotted as the red solid line, Eq. (2-42), to the experimental data highlights that except for the lowest fluid flux, q = 0.34 mm/s, the theoretical V_r, Eq. (2-42), with V_{f-max} derived from the single phase flow experiment does not well predict the velocity at the RCSR centerline. As highlighted earlier in this section, the fluid flux, q, might be different than the measured value in the single phase flow experiment. Therefore, the fluid velocity at the centerline of RCSR, in the far field from rising bubbles, is taken from the experimental data shown in Figure 5-9 (velocity

around y = -1.1 and y = 1.1). This velocity from the experimental data is then used in the theoretical model, Eq. (2-42) as the V_{f-max} and results are plotted as the blue dashed line in Figure 5-9. Figure 5-9 indicates that the theoretical V_r,, Eq. (2-42), with modified flux, q, has a better agreement to the experimental data and it well predicts the centerline velocity in the near field and far field from the rising bubbles.

In Figure 5-9, the horizontal dashed line plots the bubble terminal velocity, V_{t-rect} calculated in the shadowgraph processing step. Comparison of the experimental data, the theoretical radial velocity, V_r, (Eq. (2-42)) and the theoretical radial velocity with modified fluid flux, (Eq. (2-42)) shows that in the flow field near the bubble, the fluid velocity at the RCSR centerline is close to the bubble terminal velocity, V_{t-rect}. This means that the flow field in the front and rear of the rising bubble is highly affected by the bubble terminal velocity.

In Figure 5-9, comparison of the experimental data for PIV and PTV processing shows that both processing approaches have approximately the same results. From Figure 5-9, it can be observed that the PTV data are more scattered, relative to PIV. This is because in PIV, the particles are tracked over interrogation windows and the data can be smoothed through these windows. In PTV processing, however, the particles are tracked individually (no interrogation window) and relatively less filtering is employed as tracking the individual particles compared to PIV processing approach.

5.5.3 The tangential fluid velocity around bubbles

The date processing used gives the velocity field in the fluid flow surrounding bubble in Cartesian coordinates. As a single bubble rises in a fluid medium with seeding particles, the particles at bubble interface might disappear in between the sequential images, because the flow

around bubble is more complex than a 2-D flow. As outline in the discussion of theory in Chapter 1, the flow around a bubble can be similar to flow around a blunt object. To investigate the velocity components at bubble interface, velocity field derived from PIV and PTV processing steps should be mapped onto spherical coordinates by using this transformation:

$$V_r = V_y \cos(\theta) - V_x \sin(\theta) \tag{5-2}$$

$$V_\theta = -V_x \cos(\theta) - V_y \sin(\theta) \tag{5-3}$$

The transformations in Eq. (5-2) and Eq. (5-3) were used to map the velocity fields, derived from PIV processing, from Cartesian to spherical coordinates. Figure 5-10 indicates the angle, θ, around a single air bubble, where the positive direction of θ is counter-clockwise and the zero value of angle assigns to the front of the rising bubble.

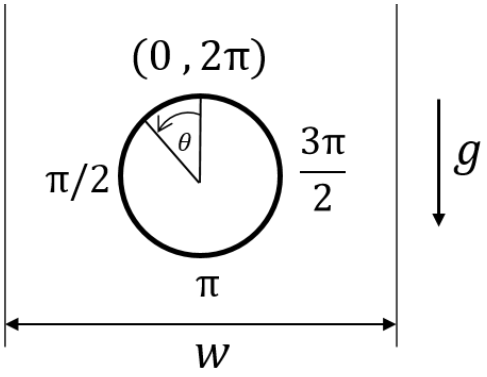

Figure 5-10- Annotation of the positive angle direction around a rising bubble

The tangential velocity, V_θ, for $r/R = 1$ to $r/R = 1 + 0.1/R$ radial distance from the center of the bubble for the same bubble sizes and fluxes introduced in Figure 5-8 and Figure 5-9, is calculated and the results are plotted for all of the 5 images concurrently in Figure 5-11(a)-(j). In

Figure 5-11, the theoretical tangential velocity, V_θ, at for $r = R$ (bubble interface) introduced in Eq. (1-47) is plotted as the solid line. As shown in Figure 5-11, the experimental data matched with the developed analytical model, Eq. (2-41).

As indicated in Figure 5-11, the maximum tangential velocity magnitude occurs at $\theta = \frac{\pi}{2}, \frac{3\pi}{2}$ and zero tangential velocity occurs at $\theta = 0,\ \pi$ (refer to Figure 5-10), as expected. Figure 5-11 indicates that both PIV and PTV data are scattered at $\theta = \frac{\pi}{2}, \frac{3\pi}{2}$ where the bubble has the closest distance to the confining wall. However the PTV data appears to be relatively more scattered, comparing to PIV processing results (for instance, at $\theta = \frac{3\pi}{2}$). This can be explained as the bubble size increases and becomes closer to the confining walls, the fluid flow behavior in the regions between the bubble and the confining walls become more complex than a two-dimensional flow. Because in PIV processing, the data are averaged over interrogation windows, the complex fluid flow behavior at $\theta = \frac{\pi}{2}, \frac{3\pi}{2}$ may be filtered over the interrogation windows. In PTV processing, however, less filtering is employed on the data and the particles are tracked individually. For instance, comparing the tangential velocity, V_θ, in Figure 5-11(a) and Figure 5-11(b) at $\theta = \frac{3\pi}{2}$, shows that the PIV data are relatively smoothed, while the PTV data show a functional relationship around $\theta = \frac{3\pi}{2}$ region. This means that the scattered data observed at $\theta = \frac{\pi}{2}, \frac{3\pi}{2}$ in Figure 5-11 are due to the complex fluid flow behavior and PTV processing can capture this flow motion in more details, comparing to PIV.

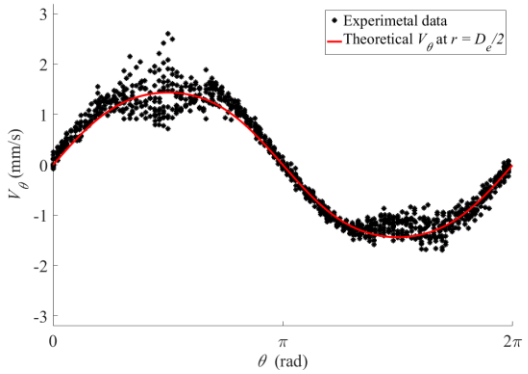

(a) q = 0.34 mm/s, D_e/w = 0.6, V_{t-rect} =2.82 mm/s, PIV

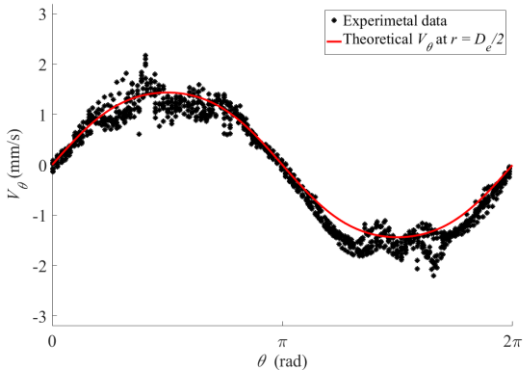

(b) q = 0.34 mm/s, D_e/w = 0.6, V_{t-rect} =2.82 mm/s, PTV

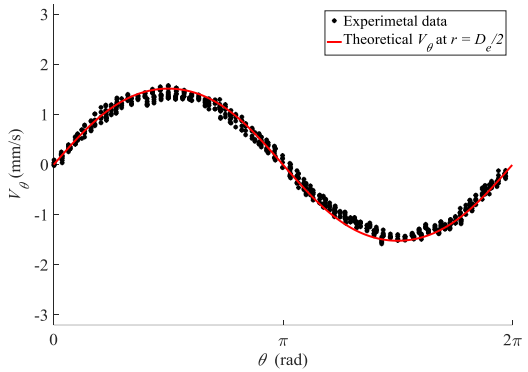

(c) q = 0.67 mm/s, D_e/w = 0.34, V_{t-rect} =2.32 mm/s, PIV

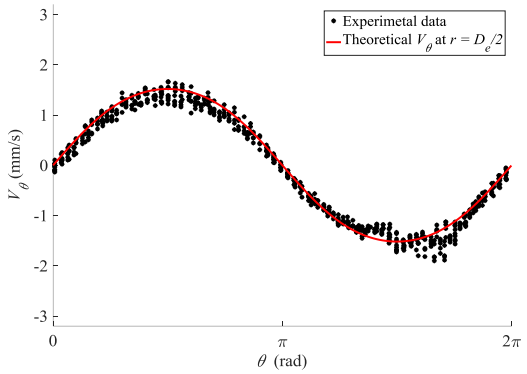

(d) q = 0.67 mm/s, D_e/w = 0.34, V_{t-rect} =2.32 mm/s, PTV

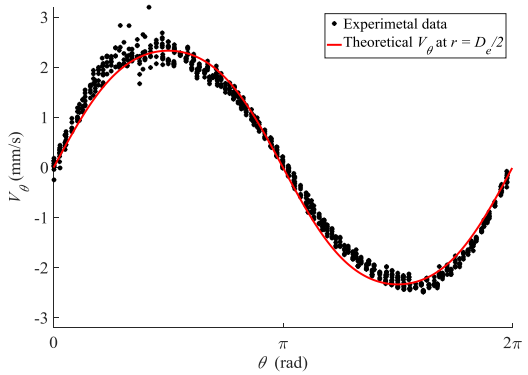

(e) q = 1.07 mm/s, D_e/w = 0.38, V_{t-rect} =3.82 mm/s, PIV

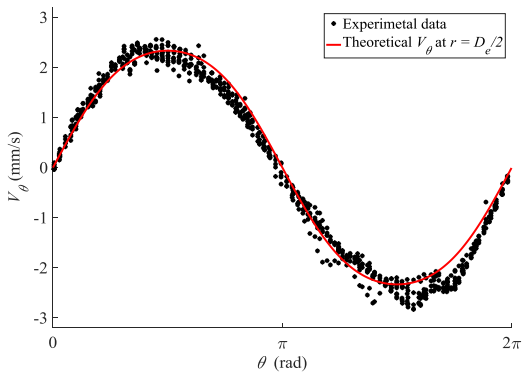

(f) q = 1.07 mm/s, D_e/w = 0.38, V_{t-rect} =3.82 mm/s, PTV

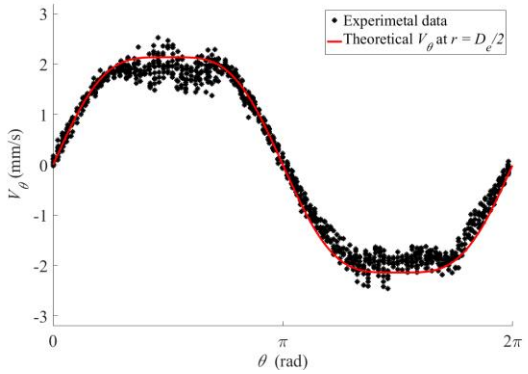

(g) q = 1.78 mm/s, D_e/w = 0.57, V_{t-rect} =3.77 mm/s, PIV

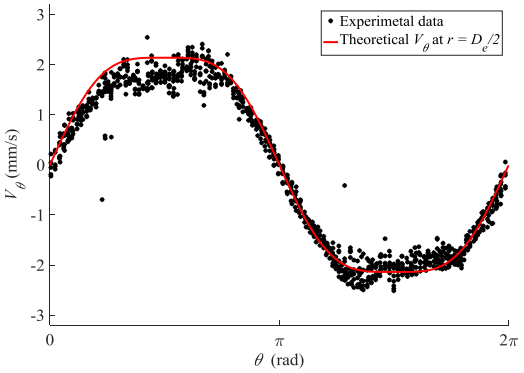

(h) q = 1.78 mm/s, D_e/w = 0.57, V_{t-rect} =3.77 mm/s, PTV

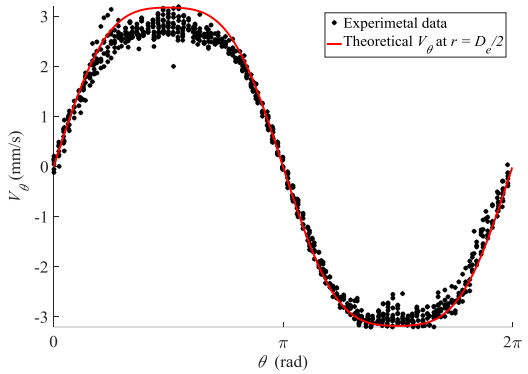

(i) q = 2.64 mm/s, D_e/w = 0.52, V_{t-rect} =5.07 mm/s, PIV

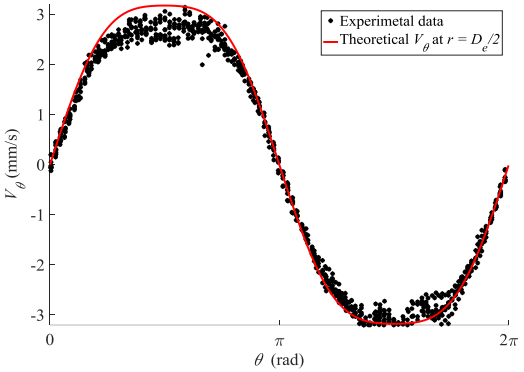

(j) q = 2.64 mm/s, D_e/w = 0.52, V_{t-rect} =5.07 mm/s, PTV

Figure 5-11- Tangential velocity, V_θ at bubble interface for five fluid fluxes (q) and one bubble size at each flux from PIV ((a), (c), (e), (g), (i)) and PTV ((b), (d), (f), (h), (j)) image processing results

5.6 Conclusion

The flow of single bubbles as rising through the rectangular confinement region, RCSR, has been measured. Bubbles with D_e/w = 0.26 to 1.08, were generated and five fluid fluxes, q, were provided to flow with the bubbles through the rectangular confinement region (RCSR). The bubble characteristics, such as diameter, centricity and terminal velocity were quantified through the RCSR. At each fluid flux, one bubble size of approximately the same diameter, was chosen to investigate the fluid flow motion around them. Two image processing approaches of PIV and PTV were undertaken to analyze the displacement of tracer particles in the flow surrounding the rising bubbles. For the PTV sparse data field, an interpolation was performed over a regular grid of 15 pixels spatial resolution in order to underlay the PTV velocity vectors on a color map velocity background and compare the results with PIV. The tangential velocity at the bubble interface was measured from PIV and PTV processing and they well matched with the analytical model developed in Chapter 2. The experimental data and the analytical model of tangential velocity at bubble interface showed that the maximum tangential velocity occurs in the bubble vicinity close to confining walls, as expected.

The fluid flow velocity at the RCSR centerline versus lengthwise location of the channel was investigated when bubbles were approximately at the center of the image. The theoretical radial velocity when $\theta = 0$, developed in Chapter 2, was used to be compared against the experimental data. The fluid flux measured in the single phase flow experiment, with no flow of bubbles, was used in the analytical model of radial velocity and it was compared with the experimental data. However, the analytical model did not well predict the experimental data in the far field.

Since the fluid fluxes were measured in a single phase bulk flow separately, the fluid flux when bubbles also flow through the channel, may not be the same as the values measured in the

single phase flow experiment for the identical syringe pump input. Therefore, it was concluded that the mismatch between the experimental data of fluid velocity at the centerline with the analytical model, is perhaps because the fluid flux, q, in the rising bubble experiment is not the same as the one measured in the single phase flow experiment. The centerline fluid velocity in the far field from the bubbles was taken from the experimental data as the fluid maximum velocity. This far field velocity from the experimental data was used to address the fluid flux in the theoretical model, reported as the modified analytical model . It was shown that this modified analytical model showed a more reasonable agreement with the experimental data of fluid velocity at the flow channel centerline.

CHAPTER 6. INVESTIGATION OF OIL DROPLETS FLOWING THROUGH A RECTANGULAR CONFINEMENT

6.1 Introduction

Flow of an oil droplet rising in a net fluid co-flow through a vertical rectangular confinement is investigated in this chapter. Transparent canola oil was used as the oil droplet and glycerol was chosen to be the working fluid as it allowed the refractive index (*RI*) of both phases be matched. Since the refractive index (*RI*) of the droplet and surrounding fluid is matched, the flow motion inside the droplet and at the droplet interface can also be observed. The passage of an oil droplet through a 3 mm×5.84 mm (width × thickness) rectangular confinement, where five fluid co-flows and two droplet sizes are chosen, is monitored. To quantify the velocity vector field, PIV and PTV processing approaches were undertaken on the collected images and results were compared to understand the differences between these two image processing approaches. Analysis of vorticity map is undertake to monitor the fluid flow motion inside and around the oil droplet and results are compared for different fluid co-flows and droplet sizes. In addition, special cases, such as passage of two oil droplets from the confinement and an oil droplet rising near to one of the confining walls, are investigated quantitatively in detail.

6.2 Velocity field inside and around rising oil droplets

The flow field was quantified inside and around two droplet sizes of relatively larger and smaller than the RCSR width, w, at each fluid flux, q. Each droplet size is chosen in a way to be

approximately the same size for all of the fluid fluxes, q. In PTV processing, the particles are tracked over 5 frames which gives 4 velocity vectors for each tracer particle, similar to the rising bubble experiment in Chapter 5.

6.2.1 Comparing the flow field with PIV and PTV processing: droplet approximately larger than the RCSR width

To capture the flow motion inside the oil droplet and in the surrounding fluid, PIV and PTV image processing are undertaken to analyze the displacement of tracer particles in the fluid flow. Figure 6-1(a) shows a typical raw image of a relatively large droplet passing through RCSR. This example highlights the seeding of both the droplet and surrounding fluid, which are both flowing in the opposite direction of gravity through the RCSR. Since the *RI* of the oil droplet (Canola oil) and surrounding fluid (glycerol) is matched, the droplet is not visible in the raw images. However, the rear of rising droplets can be recognized due to the accumulation of relatively heavier tracer particles in these regions. Figure 6-1(b) indicates the PIV processing result on the raw image shown in Figure 6-1(a), with velocity vectors shown as black vectors overlaid on a color map background. As explained in Chapter 3 and Chapter 5, the PTV image processing results in a sparse velocity vector field and hence it cannot be overlaid on a color map background. Figure 6-1(c) shows the sparse velocity vectors (black arrows) from PTV processing on the raw image shown in Figure 6-1(a). In addition, Figure 6-1(c) indicates that the sparse velocity vectors appear cluttered and it is hard to see the velocity profile in the image. Hence, likewise Chapter 5, the PTV sparse data are interpolated onto a regular grid of 15 pixels resolution in order to derive the color map background and be able to compare the PTV results to PIV. Figure 6-1(d) plots the interpolated PTV velocity vectors from PTV processing, which are overlaid on a color map background. Comparison of

Figure 6-1(c) and Figure 6-1(d) show that the interpolated PTV vectors overlaid on a color map background show the velocity profile in the flow field much clearer than the sparse data field.

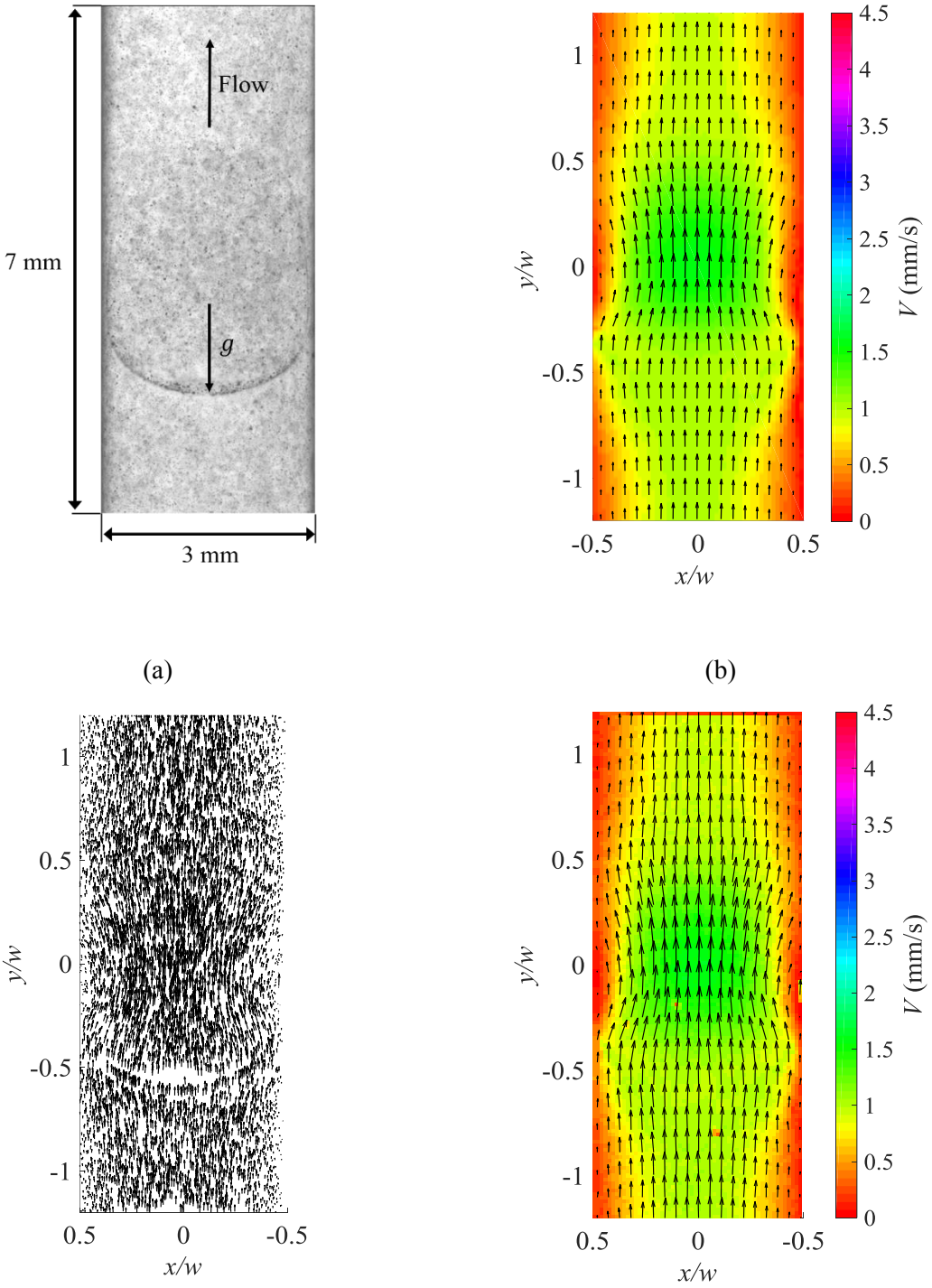

Figure 6-1- An example of (a) image of the raw data, with (b) PIV, (c) sparse PTV, and (d) interpolated PTV processing results

The velocity field derived from PIV and PTV processing for the relatively larger droplet size are shown for some example images in Figure 6-2. In this figure, the black arrows represent the velocity vectors derived from either processing approaches, V is the velocity magnitude and x and y are respectively the horizontal and vertical locations normalized by the confinement width, w. The points -0.5 and 0.5 on the x-axis represent the left and right sides of RCSR and oil droplet and working fluid flow directions are in the opposite direction of gravity. Figure 6-2(a), Figure 6-2(c),Figure 6-2(e), Figure 6-2(g) and Figure 6-2(i) plot the PIV velocity vectors on a color map background (DaVis 8.4.0, LaVision GmbH 2014). For the PTV data, the sparse velocity vectors are interpolated, and hence mapped onto a regular grid. In Figure 6-2(b), Figure 6-2(d), Figure 6-2(f), Figure 6-2(h) and Figure 6-2(j) the PTV velocity vectors are plotted on the velocity colored background, both derived from interpolated velocity field (DaVis 8.4.0, LaVision GmbH 2014).

As shown in Figure 6-2, for PTV data there are some spots with no velocity vector, because no tracer particle is detected in those regions. From PIV and PTV processed images in Figure 6-2, the velocity profile inside the oil droplet is parabolic in the same direction of the droplet flow (Ma et al. 2014), and the maximum velocity magnitude inside the rising oil droplet increases with increasing flux, q.

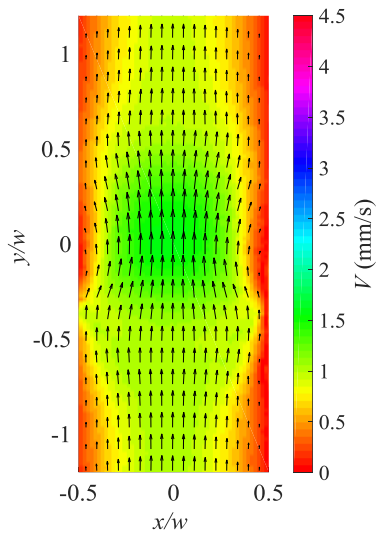

(a) PIV, q = 0.34 mm/s

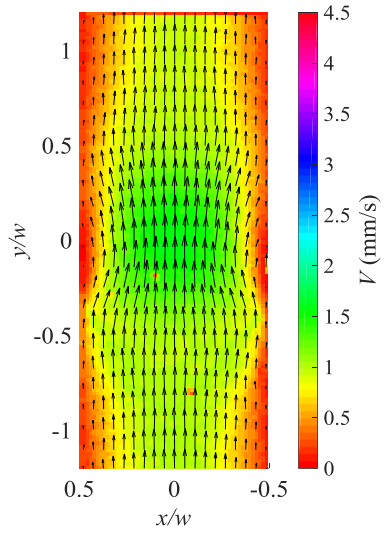

(b) PTV, q = 0.34 mm/s

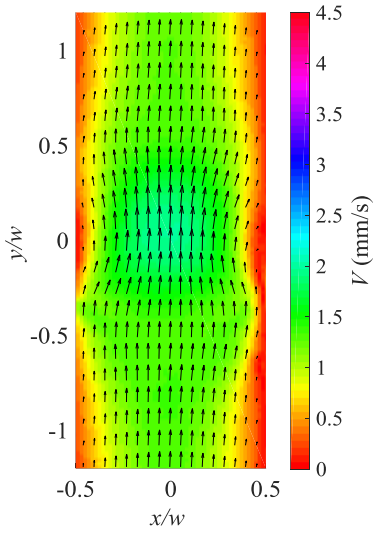

(c) PIV, q = 0.67 mm/s

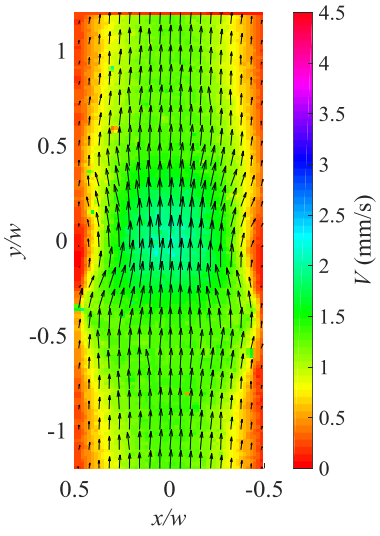

(d) PTV, q = 0.67 mm/s

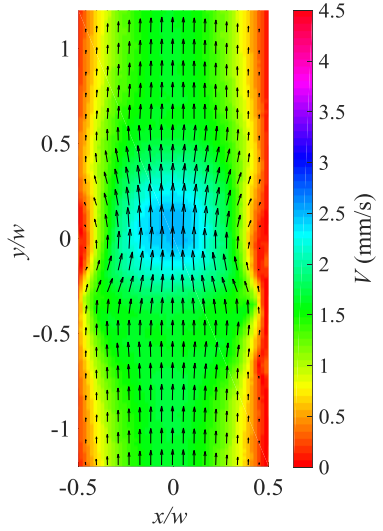

(e) PIV, q = 1.07 mm/s

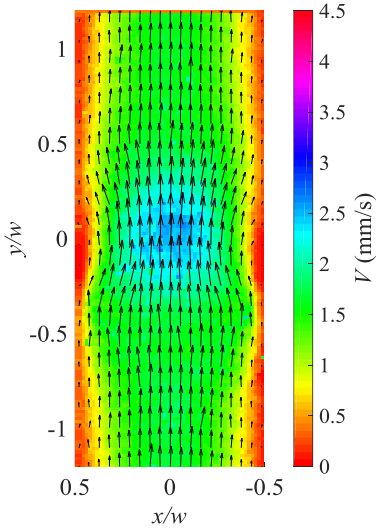

(f) PTV, q = 1.07 mm/s

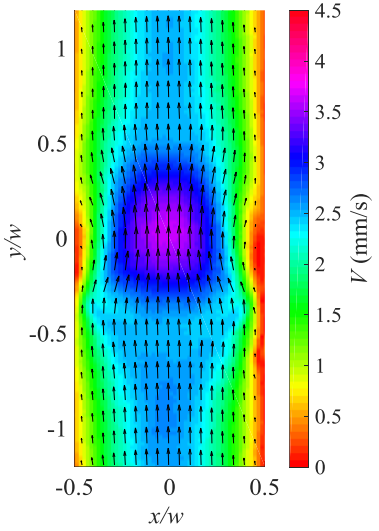

(g) PIV, q = 1.78 mm/s

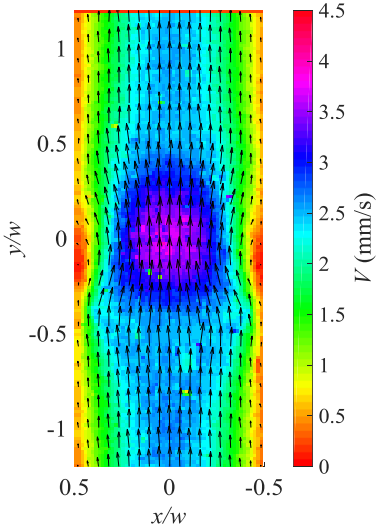

(h) PTV, q = 1.78 mm/s

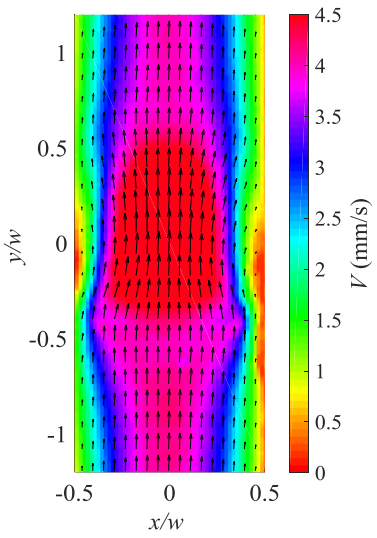

(i) PIV, q = 2.64 mm/s

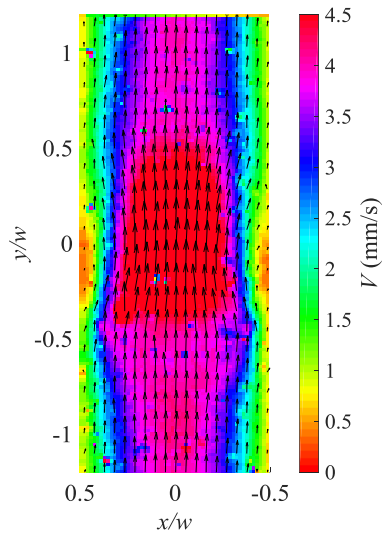

(j) PTV, q = 2.64 mm/s

Figure 6-2- Examples of velocity field from PIV and PTV processing approaches for relatively large oil droplet size at 5 fluxes, q

6.2.2 Comparing the flow field with PIV and PTV processing: droplet smaller than the RCSR width

An oil droplet of smaller diameter than the RCSR width, w, has been investigated as rising through the confinement. Figure 6-3 indicates the velocity field around a droplet of smaller diameter than the RCSR width, w. In this figure, PTV results are mapped onto an interpolated velocity background in the same way as processing droplets of relatively larger diameter. Figure 6-3 shows that as the fluid flux, q, increases, the velocity magnitude inside the droplet becomes higher, because the droplet terminal velocity increases. As shown in the q = 1.78 mm/s data (Figure 6-3(e) and Figure 6-3(f)), for $-1.2 \leq y \leq -1$ there is a region of relatively high velocity magnitude. This is because in this region, there is another oil droplet and therefore the velocity magnitude at this location ($-1.2 \leq y \leq -1$) is higher.

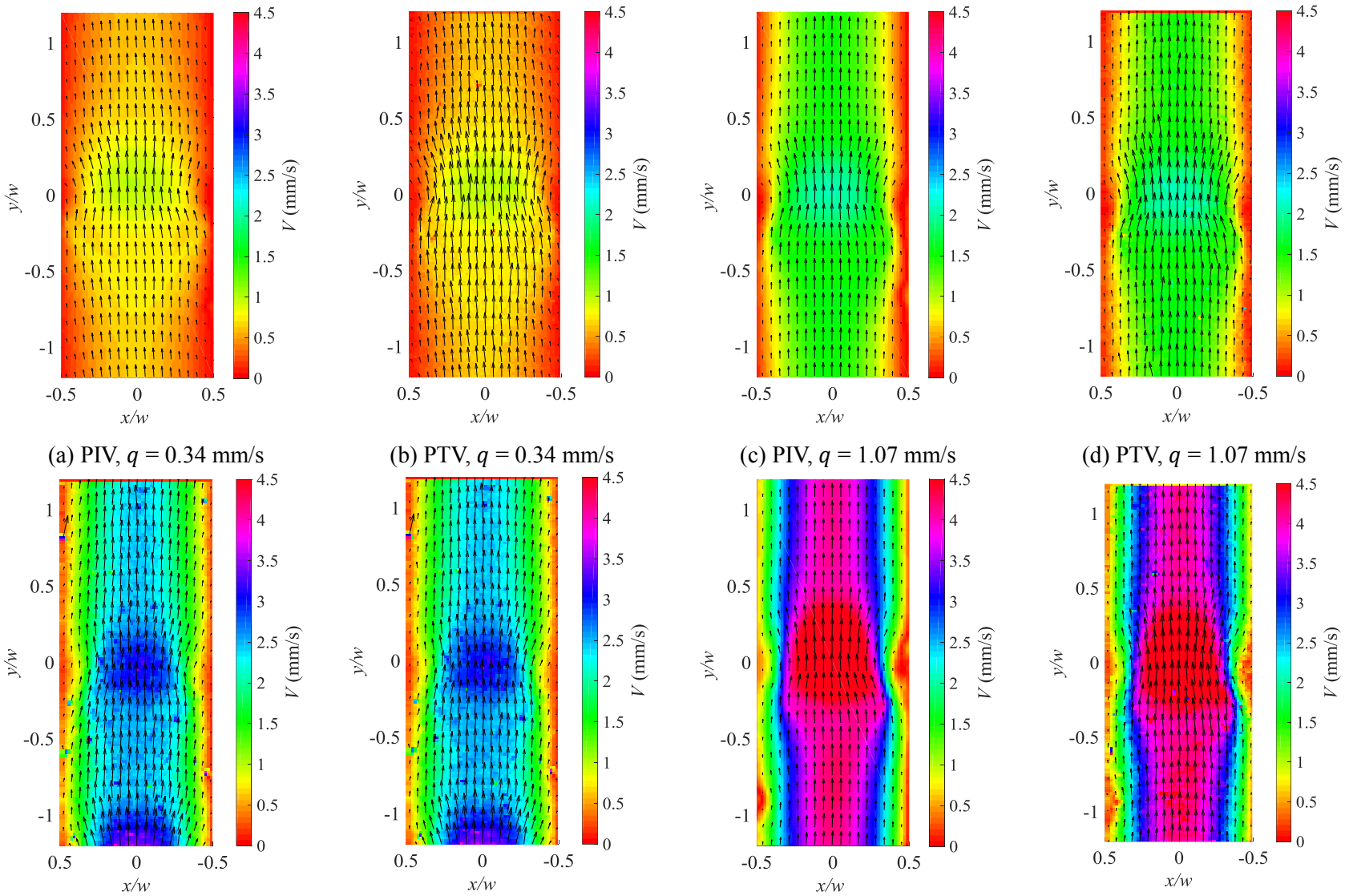

(a) PIV, q = 0.34 mm/s (b) PTV, q = 0.34 mm/s (c) PIV, q = 1.07 mm/s (d) PTV, q = 1.07 mm/s

(e) PIV, q = 1.78 mm/s (f) PTV, q = 1.78 mm/s (g) PIV, q = 2.64 mm/s (h) PTV, q = 2.64 mm/s

Figure 6-3- Examples of velocity field from PIV and PTV processing for relatively small oil droplet at 5 fluid fluxes, q

6.2.3 Droplet motion in a Lagrangian reference frame: droplet approximately larger than the RCSR width

To observe the fluid motion inside the droplet relative to the surrounding fluid, the reference frame is perhaps best fixed on the center of the rising droplet, moving the velocity field into a Lagrangian reference frame. Here, to have the results in Lagrangian frame, a value close to the droplet terminal velocity is subtracted from the y-component of velocity vectors. Due to the matched *RI* of the fluids, the droplet cannot be recognized and hence, the droplet movement in between the frames cannot be tracked to calculated the terminal velocity. Because the rear of the droplets are relatively more distinct due to accumulation of heavy tracer particles (refer to Figure 6-1(a)), the displacement of the rear of the droplets is calculated manually to derive the approximate droplet terminal velocity. By subtracting this approximate terminal velocity from the whole velocity field, the velocity vectors in Lagrangian reference frame were derived for the same conditions introduced in Figure 6-3. In addition, the vorticity map was calculated based on the velocity field data for PIV and interpolated PTV processing results.

Figure 6-4 plots the velocity vectors in Lagrangian reference frame, over a vorticity color map background for relatively large oil droplets from PIV and interpolated PTV results. An interesting observation in this figure is existence of two counter-rotating vortices on either sides of the oil droplet, according to the velocity vectors and the vorticity color map. This flow motion occurs inside the droplet because of the mechanical force exerted on the droplet from the surrounding fluid and the confining walls. Figure 6-4 indicates that the counter-rotating vortices become stronger as the fluid flux, q, increases, which means that as the fluid flux and droplet terminal velocity increase, the momentum on the droplet increases as well (Khadamkar et al. 2017).

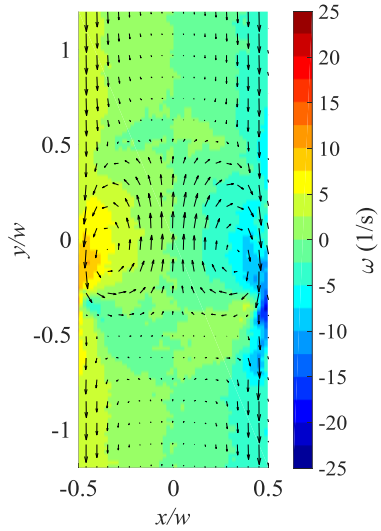

(a) PIV, q = 0.34 mm/s

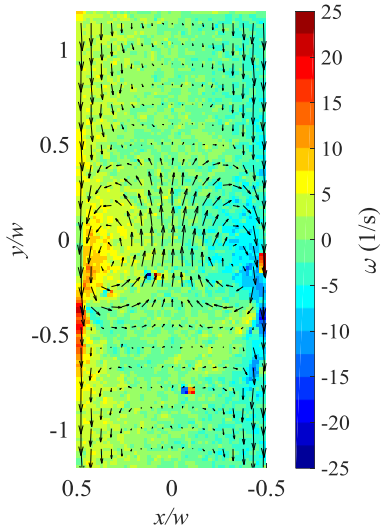

(b) PTV, q = 0.34 mm/s

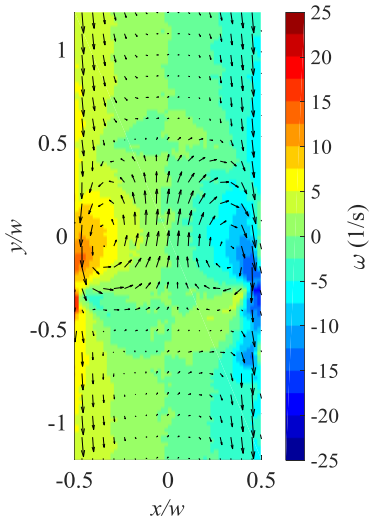

(c) PIV, q = 0.67 mm/s

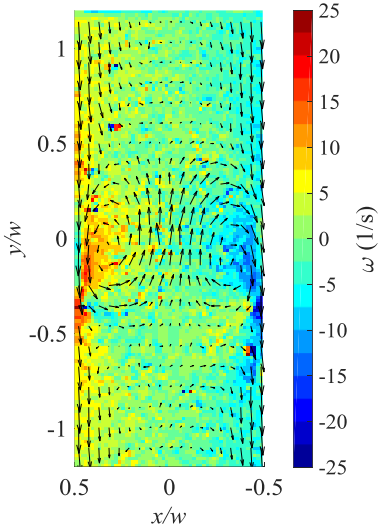

(d) PTV, q = 0.67 mm/s

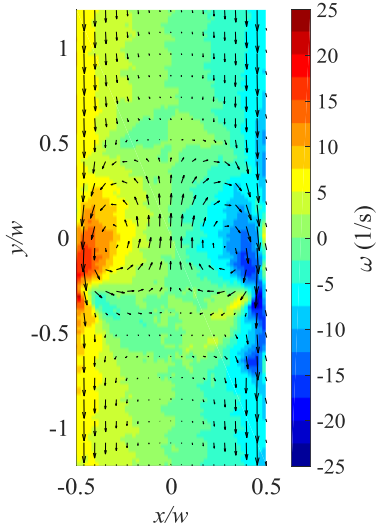

(e) PIV, q = 1.07 mm/s

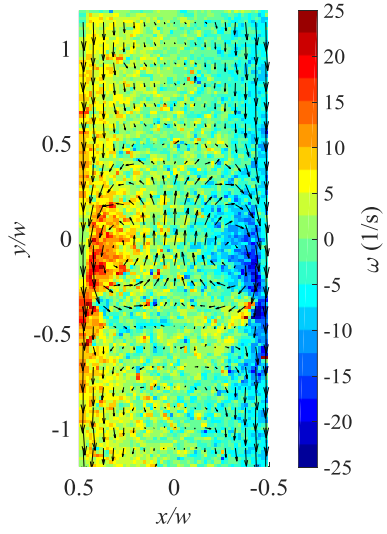

(f) PTV, q = 1.07 mm/s

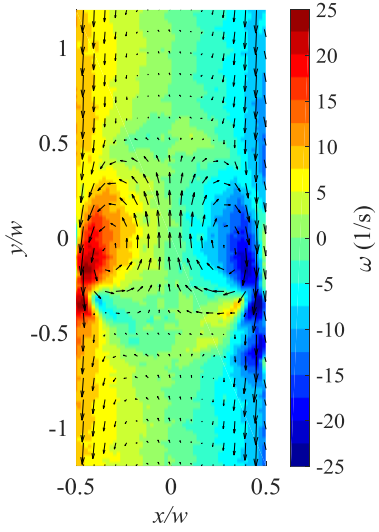

(g) PIV, q = 1.78 mm/s

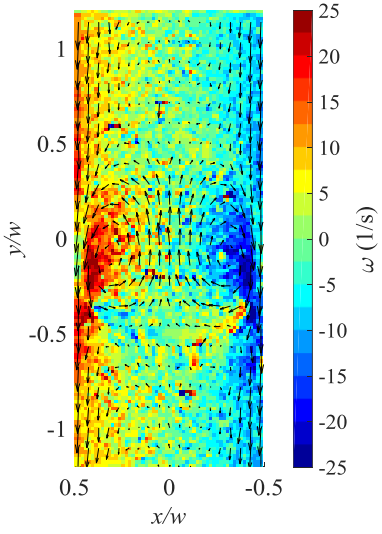

(h) PTV, q = 1.78 mm/s

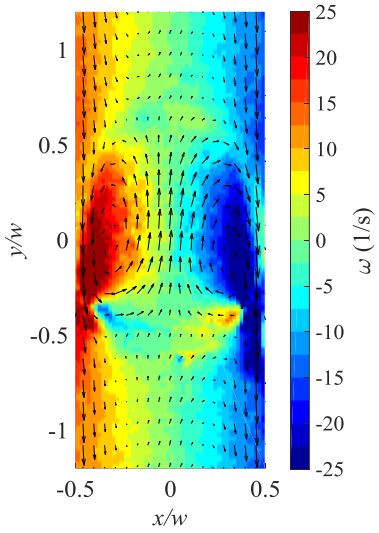

(i) PIV, q = 2.64 mm/s

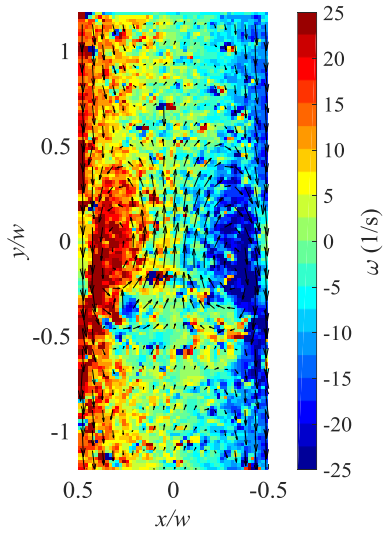

(j) PTV, q = 2.64 mm/s

Figure 6-4- Examples of velocity field from PIV and PTV processing for relatively small oil droplet at 5 fluid fluxes, q

6.2.4 Droplet motion in a Lagrangian reference frame: droplet smaller than the RCSR width

The same approach used in section 6.2.3 is followed to derive the velocity vectors in Lagrangian frame overlaid onto the vorticity map, for relatively small oil droplets from PIV and interpolated PTV results. Figure 6-5 plots the velocity vectors in Lagrangian reference frame with the vorticity as the color map background. This figure shows that the counter-rotating vortices exist inside the relatively small droplets exist, similar to the large droplets investigated in section 6.2.3. A comparison of the vorticity map for different fluid fluxes, q, indicates that as fluid flux increases, the vorticity magnitude at the vortices regions becomes higher. This means that as fluid flux, q, increases, the counter-rotating vortices become stronger because the droplet has a higher terminal velocity and hence momentum force on the rising droplets increases.

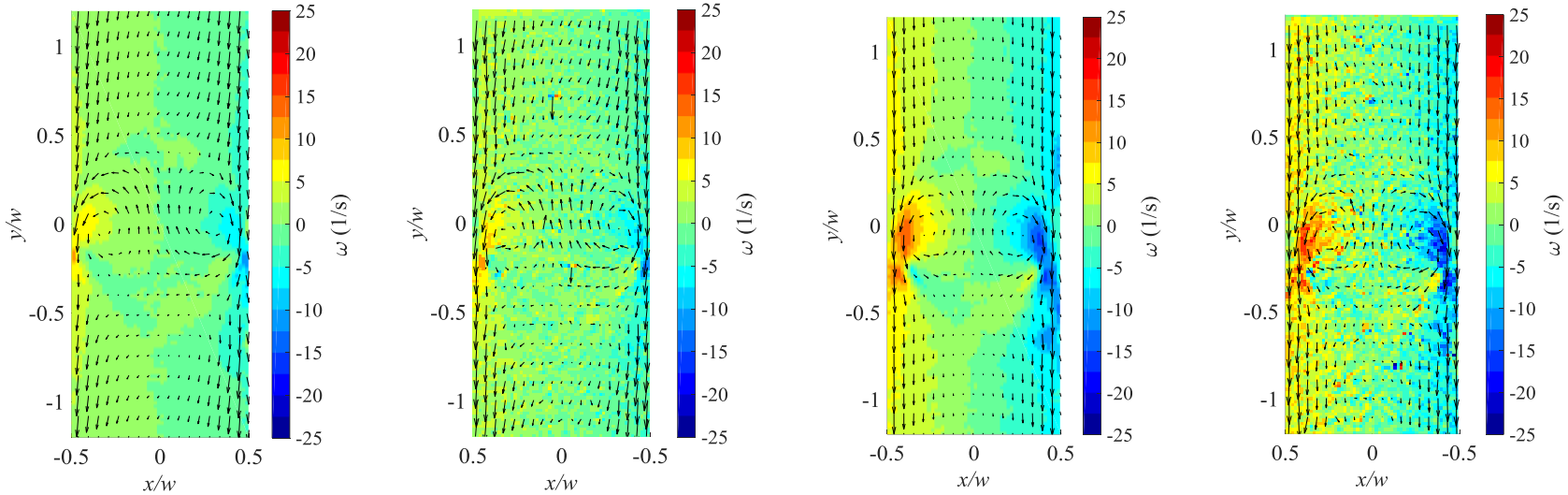

(a) PIV, q = 0.34 mm/s (b) PTV, q = 0.34 mm/s (c) PIV, q = 1.07 mm/s (d) PTV, q = 1.07 mm/s

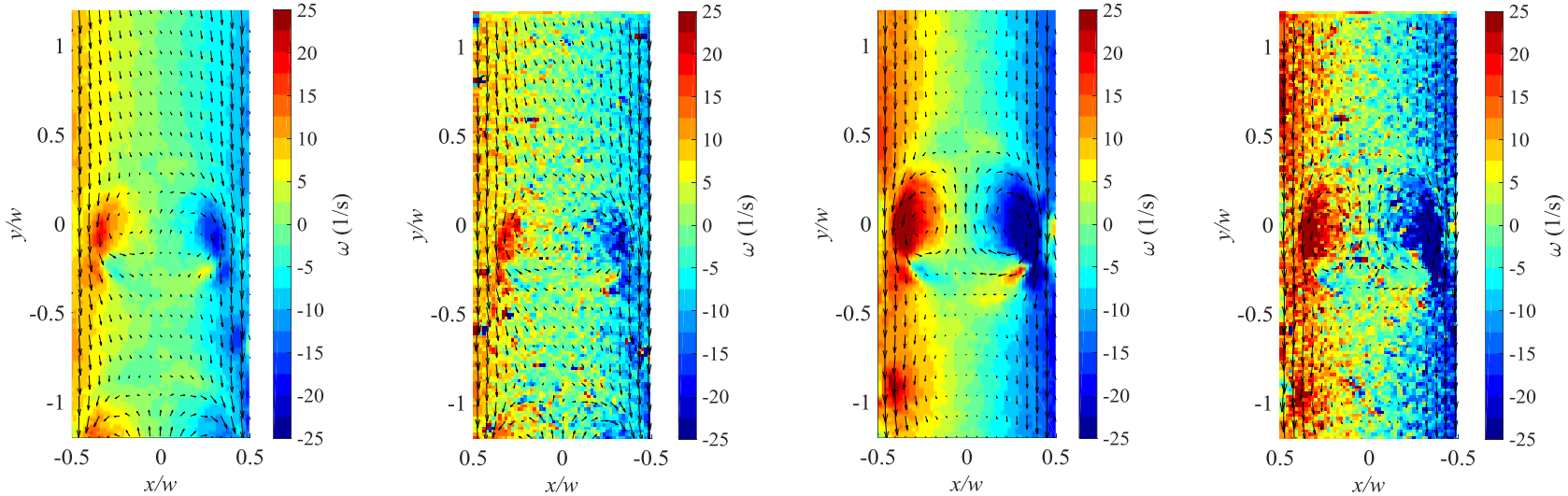

(e) PIV, q = 1.78 mm/s (f) PTV, q = 1.78 mm/s (g) PIV, q = 2.64 mm/s (h) PTV, q = 2.64 mm/s

Figure 6-5- Examples of vorticity field from PIV and PTV processing for relatively small droplets at 5 fluid fluxes, q (Lagrangian frame)

6.3 Passage of two relatively small oil droplets through the RCSR

Figure 6-6(a) and Figure 6-6(b) show a different case where two droplets are rising at a close distance to each other through the RCSR, each of which highlighted by a region of relatively higher velocity magnitude. The smaller droplet is closer to the confining walls on the right side, while the left side of this droplet is farther from the left RCSR wall. To understand the flow behavior in the in this case, the velocity field should be further investigated in detail using vorticity map analysis.

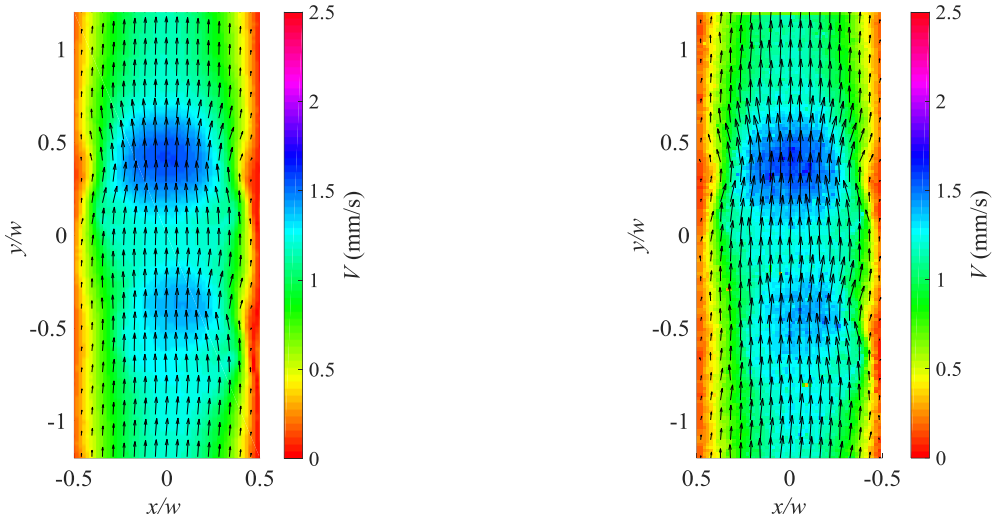

(a) PIV (b) PTV

Figure 6-6- Example of velocity field from PIV and PTV processing for two rising oil droplets at q = 0.67 mm/s

For the case of two droplets rising through the RCSR, shown in Figure 6-6(a) and Figure 6-6(b), the velocity vectors in Lagrangian reference frame are plotted with the vorticity map background in Figure 6-7(a) and Figure 6-7(b). As shown in Figure 6-7(a) and Figure 6-7(b), the vortex on the right side of this relatively smaller droplet is stronger relative to the left side. It can be concluded that the vortices are highly affected by the confining walls and as the droplet becomes

closer to the confinement walls, the vortices become stronger. Figure 6-7 shows that the vorticity map around the two vortices is about the same for the relatively larger droplet, because the droplet has approximately the same distance from the two confining walls.

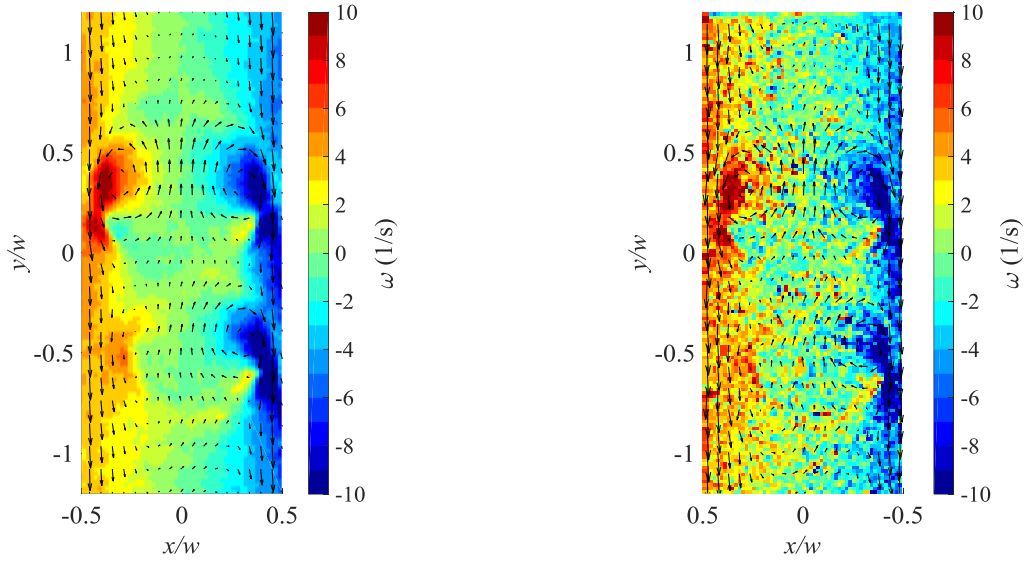

(a) PIV (b) PTV

Figure 6-7- Example of vorticity field from PIV and PTV processing for two rising oil droplets at q = 0.67 mm/s (Lagrangian reference frame)

6.4 Fluid velocity at the RSCR centerline: droplet approximately larger than the RCSR width

The velocity at the centerline of confining channel can be derived from PIV and PTV processing results, for all the droplet sizes and conditions introduced previously in this chapter. Figure 6-8 plots the fluid velocity at the channel centerline, which is equal to radial velocity at $\theta = 0$, $V_r(r = y, \theta = 0)$, versus the lengthwise location of the rectangular channel normalized by the RCSR width, y/w. Comparison of Figure 6-8(a) and Figure 6-8(b) shows that the PIV and PTV processing give approximately the same results; however, the PTV data are relatively more

sparse. This is because in PIV processing, the images are processed over relatively large interrogation windows, while in PTV smaller windows are chosen to pre-process the images and filter the noise. Therefore, the noise in PTV processed images would be relatively more than PIV processed data. As shown in Figure 6-8(a) and Figure 6-8(b), the local velocity of the fluid is relatively higher inside the droplet comparing to the other regions, as expected. In addition, the maximum velocity (the velocity around the droplet center) increases as the fluid flux, q, increases. It is expected that as becoming farther away from the droplet, the local velocity at the centerline of the channel becomes approximately close to the maximum velocity of the fluid flow, $3q/2$. Figure 6-8 highlights that the centerline velocity, $V_r(r = y, \theta = 0)$, approximately merges to the maximum velocity of the fluid flux, $3q/2$, except for q = 0.34 mm/s condition. In the experiments, it was noticed that the rising droplet for this fluid flux (q = 0.34 mm/s) was followed in a certain distance by another large droplet. This following oil droplet can highly affect the velocity field, due to having relatively higher velocity than the fluid flux, and hence the terminal velocity of the droplet shown in Figure 6-8 for q = 0.34 mm/s. As a result, the local fluid velocity at the centerline, $V_r(r = y, \theta = 0)$, does not merge to the maximum fluid velocity, $3q/2$ for the rising droplet at q = 0.34 mm/s.

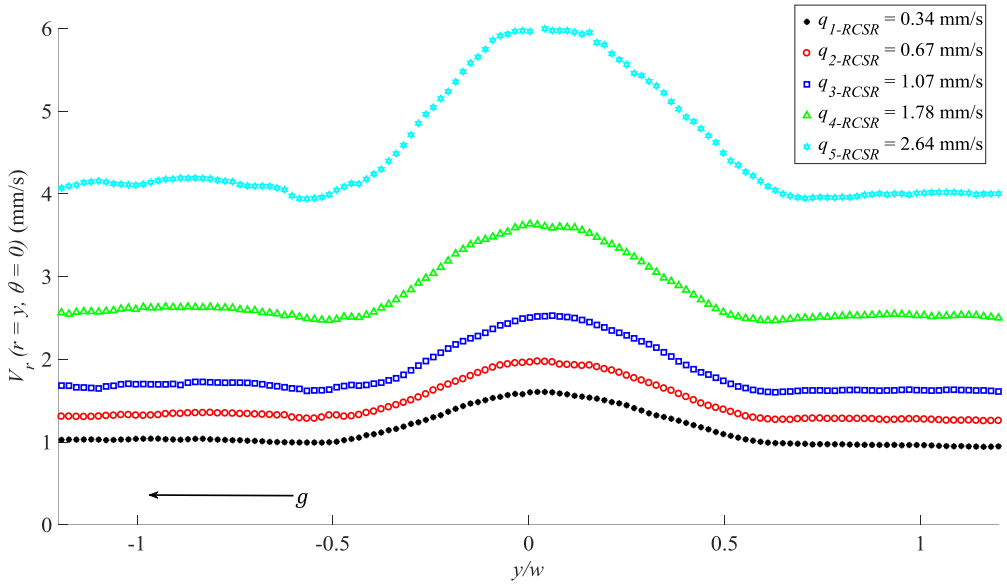

(a)

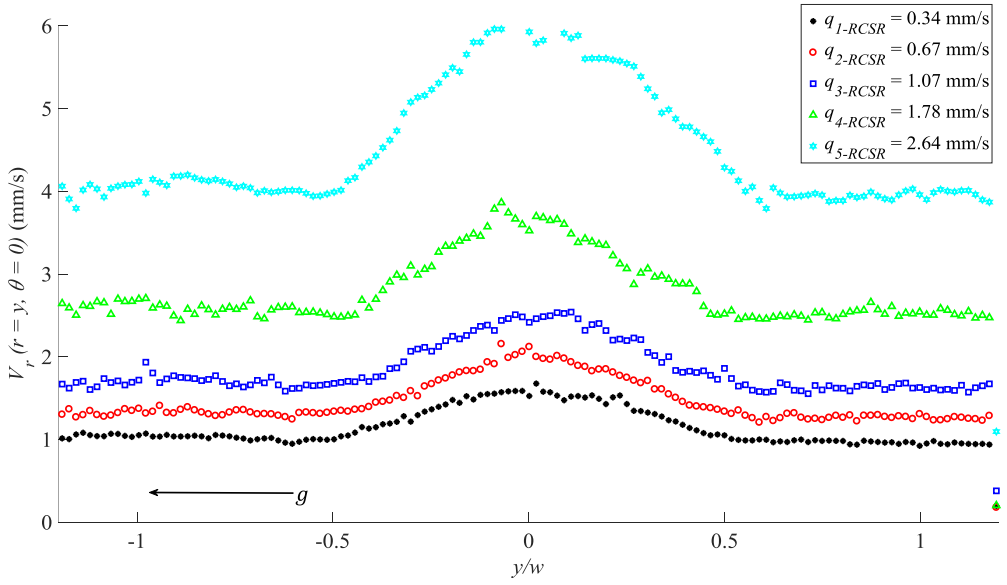

(b)

Figure 6-8- The local velocity alonf the centerline of the RCSR from (a) PIV, and (PTV) for the relatively large oil droplets

6.5 Fluid velocity at the RSCR centerline: droplet approximately smaller than the RCSR width

The local fluid velocity at the droplet centerline, $V_r(r = y, \theta = 0)$, is plotted against the vertical location of the channel normalized by the RCSR width, y/w in Figure 6-9(a) and Figure 6-9(b). Similar to the large droplets, $V_r(r = y, \theta = 0)$ increases inside the oil droplet due to the higher velocity in this region. Figure 6-9 highlights that as becoming farther from the droplet, the local fluid velocity at the channel centerline, $V_r(r = y, \theta = 0)$, approaches to the maximum velocity of the bulk fluid when there is not droplet, as expected. Figure 6-9(e) and Figure 6-9(f) indicate that for the q = 1.78 mm/s data, the local fluid velocity, V_{y-max}, for $-1.2 < \frac{y}{w} < -1$, has a relatively higher value than the fluid centerline velocity, because a second droplet exists at this location.

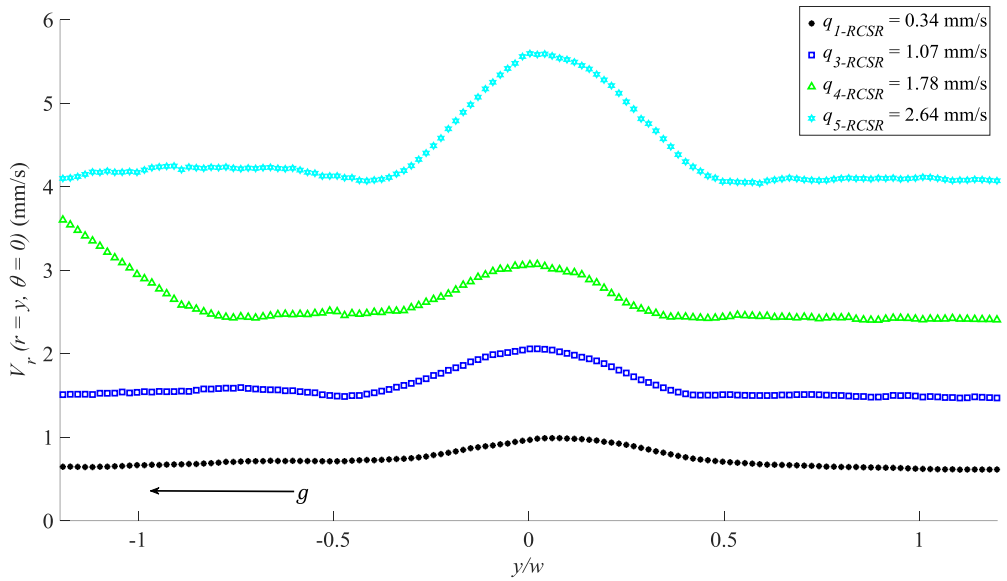

(a)

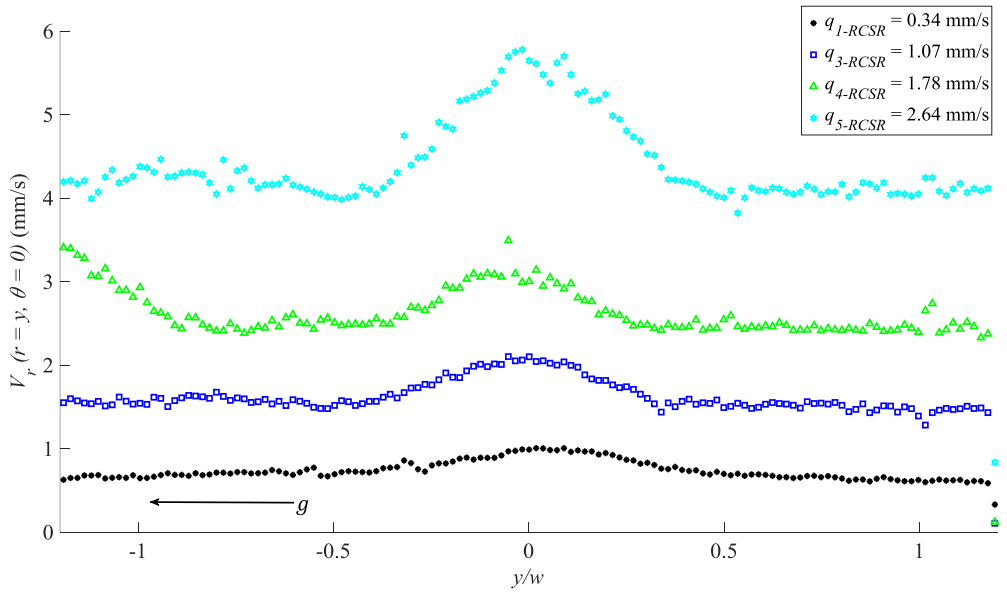

(b)

Figure 6-9- The local velocity alonf the centerline of the RCSR from (a) PIV, and (PTV) for the relatively small oil droplets

6.6 Fluid velocity at the RSCR centerline: two small droplets rising trough RCSR

The fluid velocity at the centerline is derived for the case of two rising oil droplets introduced in Figure 6-6 and Figure 6-7, and results are plotted in Figure 6-10(a) and Figure 6-10(b) for PIV and PTV data. This figure shows that there are two relatively high velocities in the velocity trend, each of which representing the two droplets. As explained in the previous sections, because of having two oil droplets, rising in a close distance from each other, through the confinement, the fluid velocity at the centerline does not approach the maximum bulk flow velocity, $2q/3$, in the far field from the droplet.

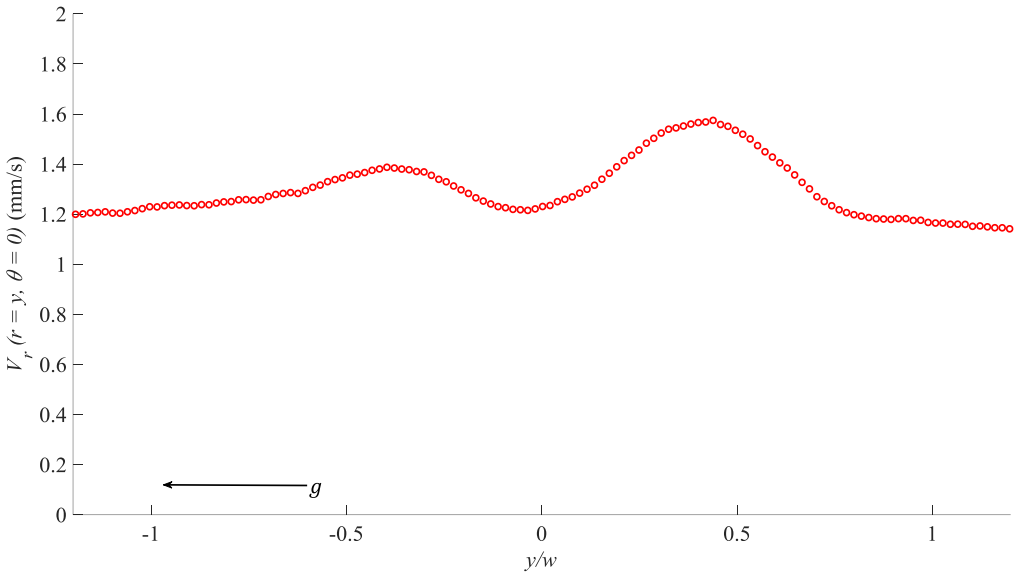

(a)

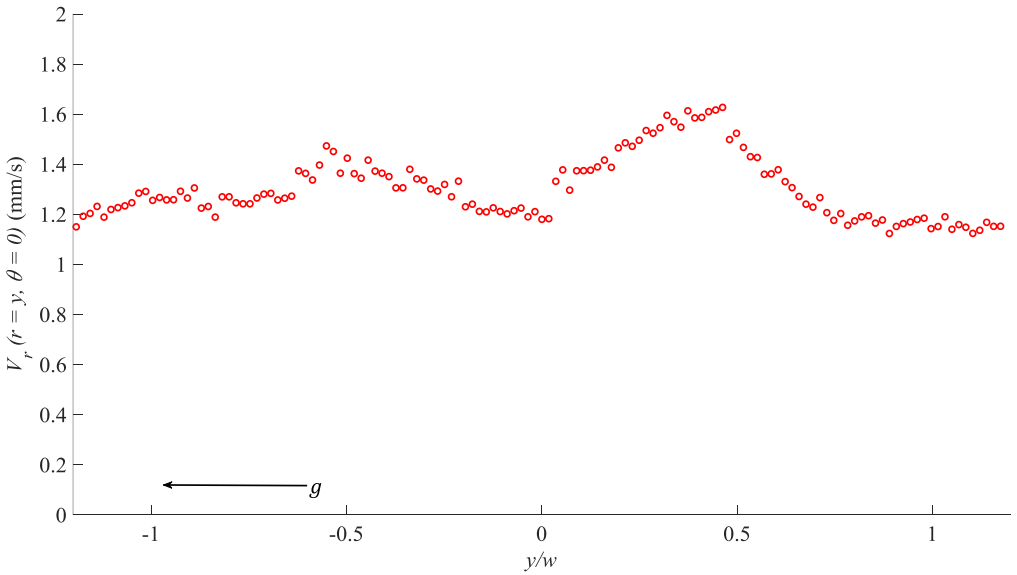

(b)

Figure 6-10- The local velocity along the centerline of the RCSR from PIV and PTV processing for two rising oil droplets at q = 0.67 mm/s (Lagrangian reference frame)

6.7 Conclusion

In this chapter, two droplet sizes of relatively smaller size than the RSCR width, w, and relatively larger size were chosen to be investigated. Transparent Canola was used as the oil droplet fluid and glycerol was chosen as the bulk fluid which has the same *RI* with Canola. 5 fluid fluxes, q, were chosen to flow along with the oil droplets through the rectangular confinement. The two image processing techniques of PIV and PTV were employed to analyze the displacement of tracer particles in the flow around and inside the rising oil droplets. It was shown qualitatively that the PIV and PTV processing approaches give the same result; however, the PTV results were relatively more scattered due to containing relatively more noises in the images comparing to PIV.

It was shown that as the fluid flux increases, the velocity magnitude in the velocity field increases as well, because of higher terminal velocity of the droplet and higher bulk flow flux. To investigate the flow motion inside the droplets in more details, the terminal velocity of oil droplets were subtracted from the whole velocity field (Lagrangian reference frame). Therefore, the flow motion in the surrounding fluid was observed relative to the rising droplet. Results showed that there are two counter-rotating vortices on either sides of the rising oil droplet, and the vortices become stronger as the fluid flux increases because of relatively higher momentum force on the droplet in a higher fluid flux. An interesting case of an oil droplet rising near one of the confining walls was separately investigated, which highlighted that the confining walls can increase the counter-rotating vortex inside the droplet, due to the extra force on the droplet from the confining walls.

Investigation of two oil droplets rising through the RCSR showed the flow field can be highly affected by having two droplets traveling close to each other through the confinement. Results

showed that rise of two close droplets through the confinement can highly increase the velocity in the bulk flow near the rising droplets region.

CHAPTER 7. CONCLUSION

Investigation of air bubbles and oil droplets rising through a rectangular channel has been studied. Five fluid co-flows were chosen to flow with air bubbles and oil droplets through the flow channel. The flow channel, varying from 22 mm × 5.84 mm to 3 mm × 5.84 mm (width × thickness) was used in the present experimental investigations. This varying geometry allowed the passage of bubbles from a two parallel plates region to a rectangular confining geometry. This study can be classified into two main investigations of: 1) rising oil droplets, and 2) rising bubbles. For the rising bubble experiments, bubble sizes of approximately 0.75 mm to 3.2 mm were generated to quantify the bubble characteristics, such as size, centricity and terminal velocity and water/glycerol solution of 93 wt% concentration was chosen as the fluid medium to flow with bubbles. For the rising oil droplets, however, two droplet sizes of relatively smaller than the confinement width, w, and relatively larger size were investigated. To match the *RI* of both fluid phases, glycerol was used as the working fluid and transparent Canola oil was used as the droplet.

7.1 Rising bubbles through a rectangular confinement

A review of the literature showed that few works have been undertaken investigating the motion of rising bubble through a rectangular confinement where the confinement geometry affects the rise of bubbles. Therefore, in this study a variety of bubble sizes relative to the rectangular confinement width were investigated as passing through this confinement along with 5 fluid co-flows. Air bubble characteristics, such as rising velocity, centricity and bubble size, were

calculated and compared in two main regions of parallel plates region (PPR) and rectangular cross section region (RCSR). Since in the parallel plates region, the width (w, 22 mm) is relatively larger than the thickness (t, 5.84 mm), theoretical correlation of rise of bubbles in between two parallel plates (Shapira and Haber 1988) was used to validate the experimental data of bubble terminal velocity in parallel plates regions. However, this theory cannot be used for rectangular geometry, because the flow of bubbles through a rectangular geometry is relatively more complex, comparing to two parallel plates. To model the bubble terminal velocity through RCSR, this flow was treated as two simpler cases of parallel plates, and the wall correction factor for each case were combined together to represent the total wall correction factor for the rectangular RCSR. A model modification approach based on the experimental data and available theory of parallel plates was undertaken to predict the bubble rising velocity in a rectangular confining geometry. This semi-empirical model includes the effect of rectangular confining geometry and fluid co-flow, and it well predicts the bubble terminal velocity in a rectangular geometry.

The flow around rising bubbles was investigated quantitatively for one bubble size at each fluid flux. PIV and PTV image processing were undertaken to analyze the displacement of tracer particles in the flow around the rising bubbles. Because in PTV processing, tracer particles are tracked individually, the data field would be sparse. Quantitatively, it was highlighted that PTV processed images appeared to be cluttered and the fluid velocity profile was hard to be seen. Hence, the PTV sparse data was interpolated and mapped onto a regular grid of 15 pixels spatial resolution. In this way, the interpolated PTV data showed relatively clearer fluid velocity profile, and therefore it was relatively easier to compare them with PIV processed data. Results showed that the PTV and PIV results of velocity field in the flow surrounding bubbles were approximately similar, which gives more confidence in the results. An analytical model developed in Chapter 2

for the streamlines, and hence the velocity components, in the flow surrounding rising bubbles was used to be compared against the experimental data from PIV and PTV processing. It was shown that this analytical model well predicts the tangential velocity at the bubble interface as compared to the experimental data. The experimental data and the analytical model of tangential velocity at bubble interface showed that the maximum tangential velocity occurs in the bubble vicinity close to confining walls, as expected. In addition, the fluid flow velocity at the RCSR centerline versus lengthwise location was examined. Quantitatively, the experimental data showed that the centerline velocity was relatively close to the bubble terminal velocity in the region near the front and rear of the bubble. This means that in the front and rear of the bubble, the flow field highly depends on the bubble terminal velocity. As becoming farther from the bubble, however, the centerline velocity decreased. It was shown that in the near field to the bubble, the theoretical radial velocity matched with the experimental data. However, the theoretical radial velocity did not well predict the centerline velocity in the far field for some of the provided fluid fluxes. This mismatch was because in the analytical model, the fluid flux measured in a separate experiment, where the bulk fluid flowed through the flow channel with no bubble, was used. However, for the same syringe pump input, the fluid flux might be different for a single phase flow, and when there is flow of bubble through the flow channel.

7.2 Rising oil droplet experiment

The same approach of PIV and PTV image processing were undertaken to investigate the flow around and inside the rising oil droplets. Results showed that there are two counter-rotating vortices on either sides of the rising oil droplet according to the velocity field from PIV and PTV processed data. An interesting case of rise of two droplets through the slot, where one of the

droplets was relatively closer to one of the confining walls was investigated. It was shown that for this case, the counter-rotating vortex appeared on the droplet side that was relatively closer to one of the confining walls. This means that the confining walls can highly affect the fluid flow behavior inside the rising oil droplet. For each droplet size, the fluid velocity at the RCSR centerline was plotted against the lengthwise location of the RCSR. It was shown that the centerline velocity has the maximum value at the center of the droplet and it drops as becoming farther from the droplet center, as expected.

7.3 Future work

Further investigations on the current experimental and theoretical study can be performed as:

- Developing a theoretical model for bubble terminal velocity in rectangular channels in fluid co-flows, instead of proposing a semi-empirical correlation from the experimental data.
- Investigation of two bubbles rising in a relatively close distance through a rectangular confinement along with co-flows. This work can explore the terminal velocity of a bubble that flows in a wake of another rising bubble.
- Investigation of rising bubbles through a pore, which is similar to flow of a single bubble through porous media. The effect of varying geometry of the pore on the bubble shape and terminal velocity can be quantified for different bubble sizes and fluid fluxes.
- Developing a facility that is able to generate oil droplets of a wider size range. In this study, using injection nozzles of different internal diameters did not lead to

providing a wide range of droplet sizes and only two droplet diameters were investigated at each fluid flux.

- Detecting a rising oil droplet when the *RI* is matched with the surrounding fluid. Because the fluid streamlines at the droplet interface should be close to zero, the droplet interface might be detected based on the streamlines derived from the experimental data. This allows calculating the droplet terminal velocity and diameter, and being able to use the theoretical model of tangential and radial velocity developed in Chapter 2 to be compared against the experimental data.
- Investigation of droplet rising velocity as flowing from the parallel plate region (PPR) to the RCSR. This can be done by dying the oil droplet and hence being able to detect that in a relatively large field of view (FOV).
- Rising droplets through a pore can be modeled analytically. The change of the droplet rising velocity and shape might be different from a case of rising bubble of the same size through a pore, because of different interfacial tensions. The change of the counter-rotating vortices inside the droplet as passing through a pore can be investigated in detail.

References

Acharya, A., R. A. Mashelkar, and J. Ulbrecht. 1976. “Mechanics Deformation of Bubble Motion in Non-Newtonian Media.” *Chemical Engineering Science* 32(8):863–72.

Achenbach, Elmar. 1973. “The Effects of Surface Roughness and Tunnel Blockage on the F L O W Past Spheres.” *Journal of Fluid Mechanics* 65:113–25.

Albert, C., J. Kromer, A. M. Robertson, and D. Bothe. 2015. “Dynamic Behaviour of Buoyant High Viscosity Droplets Rising in a Quiescent Liquid.” *Journal of Fluid Mechanics* 778:485–533.

Alturki, A. A., I. D. Gates, and B. B. Maini. 2010. “Co-Injection of Noncondensable Gas Improves ES-SAGD Performance in Shallow Oil Sands Reservoirs With a Small Top Water Zone.” Pp. 1–17 in *Society of Petroleum Engineers*.

Ansari, Shadi. 2015. “Newtonian and Non-Newtonian Flows through Mini-Channels and Micro-Scale Orifices for SAGD Applications.” University of Alberta.

Bäumler, K., M. Wegener, A. R. Paschedag, and E. Bänsch. 2011. “Drop Rise Velocities and Fluid Dynamic Behavior in Standard Test Systems for Liquid/liquid Extraction-Experimental and Numerical Investigations.” *Chemical Engineering Science* 66(3):426–39.

Baz-Rodríguez, S., A. Aguilar-Corona, and A. Soria. 2012. “Rising Velocity for Single Bubbles in Pure Liquids.” *Revista Mexicana de Ingeniería Química* 11(2):269–78.

Bennion, D. B., S. Gupta, S. Gittins, and D. Hollies. 2009. “Protocols for Slotted Liner Design for Optimum SAGD Operation.” *Journal of Canadian Petroleum Technology* 48(11):21–26.

Bertakis, Evangelos et al. 2010. “Validated Simulation of Droplet Sedimentation with Finite-Element and Level-Set Methods.” *Chemical Engineering Science* 65(6):2037–51.

Böhm, Lutz, Manuel Brehmer, and Matthias Kraume. 2016. “Comparison of the Single Bubble Ascent in a Newtonian and a Non-Newtonian Liquid : A Phenomenological PIV Study.” *Chemie Ingenieur Technik* (1):93–106.

Böhm, Lutz and Matthias Kraume. 2012. “Investigation of Single Bubbles Rising in Narrow Rectangular Channels with Particle Image Velocimetry.” Pp. 9–12 in *16th Int Symp on Applications of Laser Techniques to Fluid Mechanics Lisbon, Portugal*.

Böhm, Lutz, Tokihiro Kurita, Katsuki Kimura, and Matthias Kraume. 2014. “Rising Behaviour of Single Bubbles in Narrow Rectangular Channels in Newtonian and Non-Newtonian Liquids.” *International Journal of Multiphase Flow* 65:11–23.

Breitz, Nigel D. 1989. “Ambient and Transient Bubble Spectral Densities in Quiescent Seas and Under Spilling Breakers.” *Journal of Geophysical Research* 94(C9):751–59.

Brennen, Christopher. 2005. *Fundamentals of Multiphase Flows*. Cambridge University Press.

Brücker, Christoph. 1999. “Structure and Dynamics of the Wake of Bubbles and Its Relevance for Bubble Interaction.” *Physics of Fluids* 11(7):1781–96.

Brücker, Christoph. 2000. “PIV in Two-Phase Flows.” Pp. 1–28 in *Lecture Series 2000-01 “Particle Image Velocimetry and associated techniques.”*

Budwig, R. 1994. “Refractive Index Matching Methods for Liquid Flow Investigations.” *Experiments in Fluids* 17(5):350–55.

Bugg, J. D. and G. A. Saad. 2002. “The Velocity Field around a Taylor Bubble Rising in a Stagnant Viscous Fluid: Numerical and Experimental Results.” *International Journal of Multiphase Flow* 28(5):791–803.

Charonko, John J. and Pavlos P. Vlachos. 2013. “Estimation of Uncertainty Bounds for Individual Particle Image Velocimetry Measurements from Cross-Correlation Peak Ratio.” *Measurement Science and Technology* 24(6):65301.

Chhabra, R. P. and J. Bangun. 1997. “Wall Effects on the Terminal Velocity of Spherical Particles in Newtonian and Non-Newtonian Fluids.” *Canadian Journal of Chemical Engineering* 75(5):817–22.

Clanet, Christophe, Pierre Heraud, and Geoffrey Searby. 2004. “On the Motion of Bubbles in Vertical Tubes of Arbitrary Cross-Sections: Some Complements to the Dumitrescu–Taylor Problem.” *Journal of Fluid Mechanics* 519:359–76.

Clift, Roland, John. R. Grace, and M. E. Weber. 1978. *Bubbles, Drops and Particles*. New York; London: Academic Press.

Crowe, Clayton T. .., John D. .. Schwarzkopf, Martin Sommerfeld, and Yutaka Tsuji. 1997. *Multiphase Flows with Droplets and Particles*. 2nd ed. CRC Press.

Cueto-felgueroso, Luis and Ruben Juanes. 2014. “A Phase-Field Model of Two-Phase Hele-Shaw Flow.” *Journal of Fluid Mechanics* 758:522–52.

Dabiri, Sadegh and Pramod Bhuvankar. 2017. “Scaling Law for Bubbles Rising near Vertical Walls.” *Physics of Fluids* 28(6):62101.

Deen, Niels G. et al. 2010. “On Image Pre-Processing for PIV of Single-and Two-Phase Flows over Reflecting Objects.” *Experiments in Fluids* 49(2):525–30.

Dewsbury, K., D. Karamanev, and A. Margaritis. 1999. “Hydrodynamic Characteristics of Free Rise of Light Solid Particles and Gas Bubbles in Non-Newtonian Liquids.” *Chemical Engineering Science* 54(21).

Drews, Anja, Helmut Prieske, and Heinz Brauer. 2008. “Optimierung Der Blasen- Und Zirkulationsströmung in Membranbelebungsreaktoren.” *Chemie Ingenieur Technik* 80(12):1795–1801.

Drews, Anja, Helmut Prieske, Eva-lena Meyer, Gerrit Senger, and Matthias Kraume. 2010. “Advantageous and Detrimental Effects of Air Sparging in Membrane Filtration : Bubble Movement , Exerted Shear and Particle Classification.” *Desalination* 250(3):1083–86.

Eiswirth, R. T., H. J. Bart, T. Atmakidis, and E. Y. Kenig. 2011. “Experimental and Numerical Investigation of a Free Rising Droplet.” *Chemical Engineering and Processing: Process Intensification* 50(7):718–27.

Ellingsen, Kjetil and Frederic Risso. 2001. “On the Rise of an Ellipsoidal Bubble in Water: Oscillatory Paths and Liquid-Induced Velocity.” *Journal of Fluid Mechanics* 440:235–68.

Estevadeordal, Jordi and Larry Goss. 2005. “PIV with LED: Particle Shadow Velocimetry (PSV).” Pp. 1–10 in *43rd AIAA Aerospace Sciences Meeting and Exhibit*.

Fabre, Jean. 2016. “A Long Bubble Rising in Still Liquid in a Vertical Channel : A Plane Inviscid Solution.” *Journal of Fluid Mechanics* 797:1–10.

Di Felice, R. 1996. “A Relationship for the Wall Effect on the Settling Velocity of a Sphere at Any Flow Regime.” *International Journal of Multiphase Flow* 22(3):527–33.

Figueroa-Espinoza, B., R. Zenit, and D. Legendre. 2008. “The Effect of Confinement on the Motion of a Single Clean Bubble.” *Journal of Fluid Mechanics* 616:419–43.

Francis, Alfred W. 1933. “Wall Effect in Falling Ball Method for Viscosity.” *Journal of Applied Physics* 4(11).

Fujiwara, A., Y. Danmoto, K. Hishida, and M. Maeda. 2004. “Bubble Deformation and Flow Structure Measured by Double Shadow Images and PIV / LIF.” *Experiments in Fluids* 36:157–65.

Fujiwara, Akiko, Yuki Danmoto, and Koichi Hishida. 2003. “Bubble Deformation and Surrounding Flow Structure Measured by PIV/LIF and Shadow Image Technique.” Pp. 4–5 in *Hawaii, USA, July 6–11, 2003 Proceedings of ASME FEDSM’03 4th ASME_JSME Joint Fluids Engineering Conference Honolulu, Hawaii, USA, July 6-10, 2003*.

Funfschilling, D. and H. Z. Li. 2006. “Effects of the Injection Period on the Rise Velocity and Shape of a Bubble in a Non-Newtonian Fluid.” *Chemical Engineering Research and Design* 84(A 10):875–83.

Funfschilling, D. and H. Z. Li. 2006. “Effects of the Injection Period on the Rise Velocity and Shape of Bubbles in a Non-Newtonian Fluid.” *Chemical Engineering Research and Design* 84(A10).

Funfschilling, Denis and Huai Z. Li. 2001. “Flow of Non-Newtonian Fluids around Bubbles : PIV

Measurements and Birefringence Visualisation." 56(3):1137–41.

G. Bozzano, M.Dente. 2009. "Single Bubble and Drop Modeling." P. vol. 9 in *AIDIC Conference Series*.

Gaddis, E. S. and A. Vogelpohl. 1986. "Bubble Formation in Quiescent Liquids under Constant Flow Conditions." *Chemical Engineering Science* 41(1):97–105.

Ghaemi, Sina, Payam Rahimi, and David S. Nobes. 2008. "Measurement of Droplet Centricity and Velocity in the Spray Field of an Effervescent Atomizer." Pp. 7–10 in *14th Int Symposium on Applications of Laser Techniques to Fluid Mechanics*.

Ghaemi, Sina, Payam Rahimi, and David S. Nobes. 2010. "Evaluation of Digital Image Discretization Error in Droplet Shape Measurement Using Simulation." *Particle & Particle Systems Characterization* 26(2009):243–55.

Grace, J. R. 1973. "Shapes and Velocities of Bubbles Rising in Infinite Liquids." *Transactions of the Institution of Chemical Engineers* 51:116–20.

Grace, J. R., T. Wairegi, and T. H. Nguyen. 1976. "Shapes and Velocities of Single Drops and Bubbles Moving Freely through Immiscible Liquids." *Transactions of the Institution of Chemical Engineers* 54:167–73.

Gunn, Calum and Derek Freeston. 1991. "An Integrated Steady-State Simulation and Analysis Package." Pp. 161–66 in *13th New Zealand Geothermal Workshop*.

Haberman, W. L. and R. M. Sayre. 1958. "Motion of Rigid and Fluid Spheres in Stationary and Moving Liquids inside Cylindrical Tubes." *David Taylor Model Basin Report, Washington*

D. C., U. S. Navy Deptartment.

Hassan, N. M. S., M. M. K. Khan, and M. G. Rasul. 2007. "Bubble Rise Velocity and Drag Co-Efficient at High Reynolds Number in Power-Law Fluids." Pp. 123–28 in *5th IASME / WSEAS International Conference on Fluid Mechanics and Aerodynamics, Athens, Greece*.

Hassan, N. M. S., M. M. K. Khan, M. G. Rasul, and D. W. Rackemann. 2008. "An Experimental Investigation of Bubble Rise Characteristics in a Crystal Suspended Non – Newtonian Fluid." in *The XVth International Congress on Rheology: The Society of Rheology 80th Annual Meeting, Monterey, California.*

Hassan, Yassin A. and E. E. Dominguez-Ontiveros. 2008. "Flow Visualization in a Pebble Bed Reactor Experiment Using PIV and Refractive Index Matching Techniques." *Nuclear Engineering and Design* 238(11):3080–85.

Hassan, Yassin A., Javier Ortiz-villafuerte, and William D. Schmidl. 2001. "Three-Dimensional Measurements of Single Bubble Dynamics in a Small Diameter Pipe Using Stereoscopic Particle Image Velocimetry." *International Journal of Multiphase Flow* 27:817–42.

Homsy, G. M. 1987. "Viscous Fingering in Porous Media." *Annual Review of Fluid Mechanics* 19:271–311.

Van Hout, R., A. Gulitski, D. Barnea, and L. Shemer. 2002. "Experimental Investigation of the Velocity Field Induced by a Taylor Bubble Rising in Stagnant Water." *International Journal of Multiphase Flow* 28(4):579–96.

Kanwisher, John. 1963. "On the Exchange of Gases between the Atmosphere and the Sea." *Deep-*

Sea Research 10(1373):195–207.

Keane, Richard D. and Ronald J. Adrian. 1990. “Optimization of Particle Image Velocimeters. Part I : Double Pulsed Systems.” *Measurement science and technology* 1(11):1202–15.

Keane, Richard D. and Ronald J. Adrian. 1992. “Theory of Cross-Correlation Analysis of PIV Images.” *Applied Scientific Research* 49(3):191–215.

Kehlenbeck, Ralf and R. Di Felice. 1999. “Empirical Relationships for the Terminal Settling Velocity of Spheres in Cylindrical Columns.” *Chemical Engineering Technology* 21:303–8.

Khadamkar, Hrushikesh P., Ashwin W. Patwardhan, and Channamallikarjun S. Mathpati. 2017. “Computational Fluid Dynamics Simulations of Single Drops in Confined Geometries.” *Industrial & Engineering Chemistry Research* 56(29):8311–29.

Komrakova, A. E., D. Eskin, and J. J. Derksen. 2013. “Lattice Boltzmann Simulations of a Single N-Butanol Drop Rising in Water.” *Physics of Fluids* 25(4):42102.

Kopf-sill, Anne R. and G. M. Homsy. 1988. “Bubble Motion in a Hele – Shaw Cell.” *Physics of Fluids* 31(1):18–26.

Kulkarni, Amol a and Jyeshtharaj B. Joshi. 2005. “Bubble Formation and Bubble Rise Velocity in Gas - Liquid Systems : A Review.” *Industrial & Engineering Chemistry Research* 44:5873–5931.

Kumar, Avinav, Anil Srivastava, and Ravi Kumar. 2010. “Design Optimization of Slotted Liner Completions in Horizontal Wells of Mumbai High Field.” *Proceedings of SPE Asia Pacific Oil and Gas Conference and Exhibition*.

Kundu, Pijush, Ira M. Cohen, and David R. Dowling. 2011. *Fluid Mechanics*. 5th ed. Academic Press.

Lee, Sungyon and Charles N. Baroud. 2011. "Trapping Microfluidic Drops in Wells of Surface Energy." *Physical Review Letters* 107(12):1–4.

de Leeuw, Gerrit et al. 2014. *Ocean-Atmosphere Interactions of Particles*. edited by P. S. Liss and M. T. Johnson. Berlin, Heidelberg: Springer Berlin Heidelberg.

Li, Dongqing. 2004. *Electrokinetics in Microfluidics*. Toronto, Ontario, Canada: Academic Press.

Li, Huai Z., X. Frank, D. Funfschilling, and P. Diard. 2004. "Bubbles ' Rising Dynamics in Polymeric Solutions." *Physics Letters A* 325:43–50.

Lighthill, James M. 1967. "Waves in Fluids." *Communications on Pure and Applied Mathematics* 20(2):267–93.

Liu, Liu, Hongjie Yan, Guojian Zhao, and Jiacai Zhuang. 2016. "Experimental Studies on the Terminal Velocity of Air Bubbles in Water and Glycerol Aqueous Solution." *Experimental Thermal and Fluid Science* 78:254–65.

Liu, Zhengliang, Ying Zheng, Lufei Jia, and Qikai Zhang. 2005. "Study of Bubble Induced Flow Structure Using PIV." *Chemical Engineering Science* 60:3537–52.

Ma, Shaohua, Joseph M. Sherwood, Wilhelm T. S. Huck, and Stavroula Balabani. 2014. "On the Flow Topology inside Droplets Moving in Rectangular Microchannels." *Lab Chip* 14(18):3611–20. Retrieved (http://xlink.rsc.org/?DOI=C4LC00671B).

Maneri, C. C. and N. Zuber. 1974. "An Experimental Study of Plane Bubbles." *International*

Journal of Multiphase Flow 1(5):623–45.

Manga, Michael and H. A. Stone. 1995. "Low Reynolds Number Motion of Bubbles , Drops and Rigid Spheres through Fluid-Fluid Interfaces." *Journal of Fluid Mechanics* 287:279–98.

Mao, Z.-Q, J. C. Godfrey, and M. J. Slater. 1995. "Single Liquid Drop Velocities and Breakage Mechanism in Sections of Structured Packings." *Chemical Engineering & Technology* 18(1):33–40.

Maruvada, S. R. K. and C. Park. 1996. "Retarded Motion of Bubbles in Hele – Shaw Cells Retarded Motion of Bubbles in Hele – Shaw Cells." *Physics of Fluids* 8(12):3229–33.

Metz, Tobias, Nils Paust, Roland Zengerle, and Peter Koltay. 2010. "Capillary Driven Movement of Gas Bubbles in Tapered Structures." *Microfluid Nanofluid* 9:341–55.

Miyahara, Toshiro and Shuichi Yamanaka. 1993. "Mechanics of Motion and Deformation of a Single Bubble Rising Through Quiescent Highly Viscous Newtonian and Non-Newtonian Media." *Journal of Chemical Engineering Japan* 26(3).

Moujaes, S. and R. S. Dougall. 1987. "Experimental Investigation of Cocurrent Two-Phase Flow in a Vertical Rectangular Channel." *The Canadian Journal of Chemical Engineering* 65(5):705–15.

Munroe, Henry Smith. 1889. *The English versus Continental System of Jigging—is Close Sizing Advantageous?* New York City: Transactions of teh American Institude of Mining Engineers.

Narrow, T. L., M. Yoda, and S. I. Abdel-Khalik. 2000. "A Simple Model for the Refractive Index of Sodium Iodide Aqueous Solutions." *Experiments in Fluids* 28(3):282–83.

Nickens, H. V. and D. W. Yannitell. 1987. “The Effects of Surface Tension and Viscosity on the Rise Velocity of a Large Gas Bubble in a Closed, Vertical Liquid-Filled Tube.” *International Journal of Multiphase Flow* 13(1):57–69.

Ninomiya, N. and K. Yasuda. 2006. “Visualization and Piv Measurement of the Flow around and inside of a Falling Droplet.” *Journal of Visualization* 9(3):257–64.

Nourozieh, H., M. Kariznovi, and J. Abedi. 2016. “Measurement and Modeling of Solubility and Saturated-Liquid Density and Viscosity for Methane/athabasca-Bitumen Mixtures.” *SPE Journal* 21(1).

Novotny, Jan and Lukas Manoch. 2012. “The Criterion of Choosing the Proper Seeding Particles.” *Engineering Mechanics* (201):945–54.

Okada, Kenji, Yasuharu Akagi, Masahiko Kogure, and Naoya Yoshioka. 1990. “Effect on Surface Charges of Bubbles and Fine Particles on Air Flotation Process.” *The Canadian Journal of Chemical Engineering* 68(3):393–99.

Okhotskii, V. B. 2001. “Rise of Single Bubbles in a Confined Medium.” *Theoretical Foundations of Chemical Engineering* 35(5):510–12.

Ortiz-Villafuerte, J., W. D. Schmidl, and Y. A. Hassan. 2000. “Three-Dimensional Ptv Study of the Surrounding Flow and Wake of a Bubble Rising in a Stagnant Liquid.” *Experiments in Fluids* 29(1):202–10.

Petera, J. and L. R. Weatherley. 2001. “Modelling of Mass Transfer from Falling Droplets.” *Chemical Engineering Science* 56(16):4929–47.

Phenix, Trevor. 2015. “Gas Co-Injection.” *Journal of the Canadian Heavy Oil Association* 16–21.

Polonsky, S., L. Shemer, and D. Barnea. 1999. “The Relation between the Taylor Bubble Motion and the Velocity Field ahead of It.” *International Journal of Multiphase Flow* 25(6–7):957–75.

Raffel, M., C. Willert, S. Wereley, and J. Kompenhans. 1989. *Particle Image Velocimetry*.

Ristic, Slavica, Jovan Isakovic, Biljana Ilic, and Goran Ocokoljic. 2004. “Review of Methods for Flow Velocity Measurement in Wind Tunnels.” *Scientific- Technical Review* (3):60–71.

Roig, Véronique, Matthieu Roudet, and Frédéric Risso. 2012. “Dynamics of a High-Reynolds-Number Bubble Rising within a Thin Gap.” *Journal of Fluid Mechanics* 707:444–66.

Sakakibara, K., M. Yamada, Y. Miyamoto, and T. Saito. 2007. “Measurement of the Surrounding Liquid Motion of a Single Rising Bubble Using a Dual-Camera PIV System.” *Flow Measurement and Instrumentaiton* 18:211–15.

Sanada, Toshiyuki, Minori Shirota, and Masao Watanabe. 2007. “Bubble Wake Visualization by Using Photochromic Dye.” *Chemical Engineering Science* 62(24):7264–73.

Sathe, Mayur J. et al. 2011. “Investigation of Flow Structures and Transport Phenomena in Bubble Columns Using Particle Image Velocimetry and Miniature Pressure Sensors.” *Chemical Engineering Science* 66(14):3087–3107.

Sathe, Mayur J., Iqbal H. Thaker, Tyson E. Strand, and Jyeshtharaj B. Joshi. 2010. “Advanced PIV / LIF and Shadowgraphy System to Visualize Flow Structure in Two-Phase Bubbly Flows.” *Chemical Engineering Science* 65(8):2431–42.

Sathe, Mayur, Jyeshtharaj Joshi, and Geoffrey Evans. 2013. “Characterization of Turbulence in Rectangular Bubble Column.” *Chemical Engineering Science* 100:52–68.

Sciacchitano, Andrea, Bernhard Wieneke, and Fulvio Scarano. 2013. “PIV Uncertainty Quantification by Image.” *Measurement Science and Technology* 24.

Segur, J. B. and Helen E. Oberstar. 1951. “Viscosity of Glycerol and Its Aqueous Solutions.” *Industrial & Engineering Chemistry* 43(9):2117–20.

Selva, Bertrand et al. 2011. “Temperature-Induced Migration of a Bubble in a Soft Microcavity Temperature-Induced Migration of a Bubble in a Soft Microcavity.” *Physics of Fluids* 23(5):52002.

Shapira, M. and S. Haber. 1988. “Low Reynolds Number Motion of a Droplet Between Two Parallel Plates.” *International Journal of Multiphase Flow* 14(4):483–506.

Soong, T. T. 2004. *Fundamentals of Probability and Statistics for Engineers*. John Wiley & Sons.

Strom, J. R. and R. C. Kintner. 1958. “Wall Effect for the Fall of Single Drops.” *AIChE Journal* 4(2):153–56.

Svrcek, William Y. and Anil K. Mehrotra. 1982. “Gas Solubility, Viscosity and Density Measurements for Athabasca Bitumen.” *Journal of Canadian Petroleum Technology* 21(4):31–38.

Taylor, Sir Geoffrey and P. G. Saffman. 1959. “A Note on the Motion of Bubbles in a Hele-Shaw Cell and Porous Medium.” *The Quarterly Journal of Mechanics and Applied Mathematics* 12(3):265–79.

Thorsen, G., R. M. Stordalen, and S. G. Terjesen. 1956. “On the Terminal Velocity of Circulating and Oscillating Liquid Drops.” *Chemical Engineering Science* 2(4):444–47.

Timmins, Benjamin H., Brandon W. Wilson, Barton L. Smith, and Pavlos P. Vlachos. 2012. “A Method for Automatic Estimation of Instantaneous Local Uncertainty in Particle Image Velocimetry Measurements.” *Experiments in Fluids* 53(4):1133–47.

Tokuhiro, A., M. Maekawa, K. Iizuka, K. Hishida, and M. Maeda. 1998. “Turbulent Flow Past a Bubble and an Ellipsoid Using Shadow-Image and PIV Techniques.” *International Journal of Multiphase Flow* 24(8):1383–1406.

Tomiyama, A., G. P. Celata, S. Hosokawa, and S. Yoshida. 2002. “Terminal Velocity of Single Bubbles in Surface Tension Force Dominant Regime.” *International Journal of Multiphase Flow* 28(9):1497–1519.

Vafai, Kambiz, ed. 2005. *Handbook of Porous Media*. 2nd ed. Taylor & Francis Group.

Wachem, B. G. M. Van and J. C. Schouten. 2002. “Experimental Validation of 3-D Lagrangian VOF Model : Bubble Shape and Rise Velocity.” *AIChE Journal* 48(12).

Wegener, M., J. Grünig, J. Stüber, A. R. Paschedag, and M. Kraume. 2007. “Transient Rise Velocity and Mass Transfer of a Single Drop with Interfacial Instabilities - Experimental Investigations.” *Chemical Engineering Science* 62(11):2967–78.

Wegener, Mirco, Matthias Kraume, and Anja R. Paschedag. 2009. “Droplet Microfluidics on a Planar Surface.” *Fluid Mechanics and Transport Phenomena* 56(1):2–10.

Wheeler, Anthony J. and Ahmad R. Ganji. 2010. *Introduction to Engineering Experimentation*.

3rd ed. San Francisco, California: Pearson Education.

White, Frank M. 2011. *Fluid Mechanics*. 7th ed. McGraw Hill.

Wieneke, Bernhard. 2014. “Generic a-Posteriori Uncertainty Quantification for PIV Vector Fields by Correlation Statistics.” Pp. 1–9 in *17th International Symposium on Applications of Laster Techniques to Fluid Mechanics*.

Woolf, David K. and S. A. Thorpe. 1991. “Bubbles and the Air-Sea Exchange of Gases in near-Saturation Conditions.” *Journal of Marine Research* 435–66.

Al Yousef, Zuhair, Hussain AlDaif, and Mohammed Al Otaibi. 2014. “An Overview of Steam Injection Projects in Fractured Carbonate Reservoirs in the Middle East.” *Journal of Petroleum Science Research* 3(3):101–10.

Zaruba, Alexander, Dirk Lucas, Horst-michael Prasser, and Thomas Höhne. 2007. “Bubble-Wall Interactions in a Vertical Gas – Liquid Flow: Bouncing , Sliding and Bubble Deformations.” *Chemical Engineering Science* 62:1591–1605.

Zhang, Li, Chao Yang, and Zai-sha Mao. 2008. “Unsteady Motion of a Single Bubble in Highly Viscous Liquid and Empirical Correlation of Drag Coefficient.” *Chemical Engineering Science* 63:2099–2106.

Appendix

A-1. Measurement of KSCN refractive index (*RI*) at 20 C

The KSCN/water solutions were made at different concentrations and the *RI* was measured using the refractometer (Abbe-3L, Bausch and Lomb) at 20°C temperature. The results are plotted in Figure A- 1. A correlation was fitted to the experimental data as:

$$RI_{KSCN} = 0.1713c^2 + 0.0645c + 1.3641 \quad \text{(A-1)}$$

Where RI_{KSCN} is the refractive index of KSCN and c represents the solution concentration.

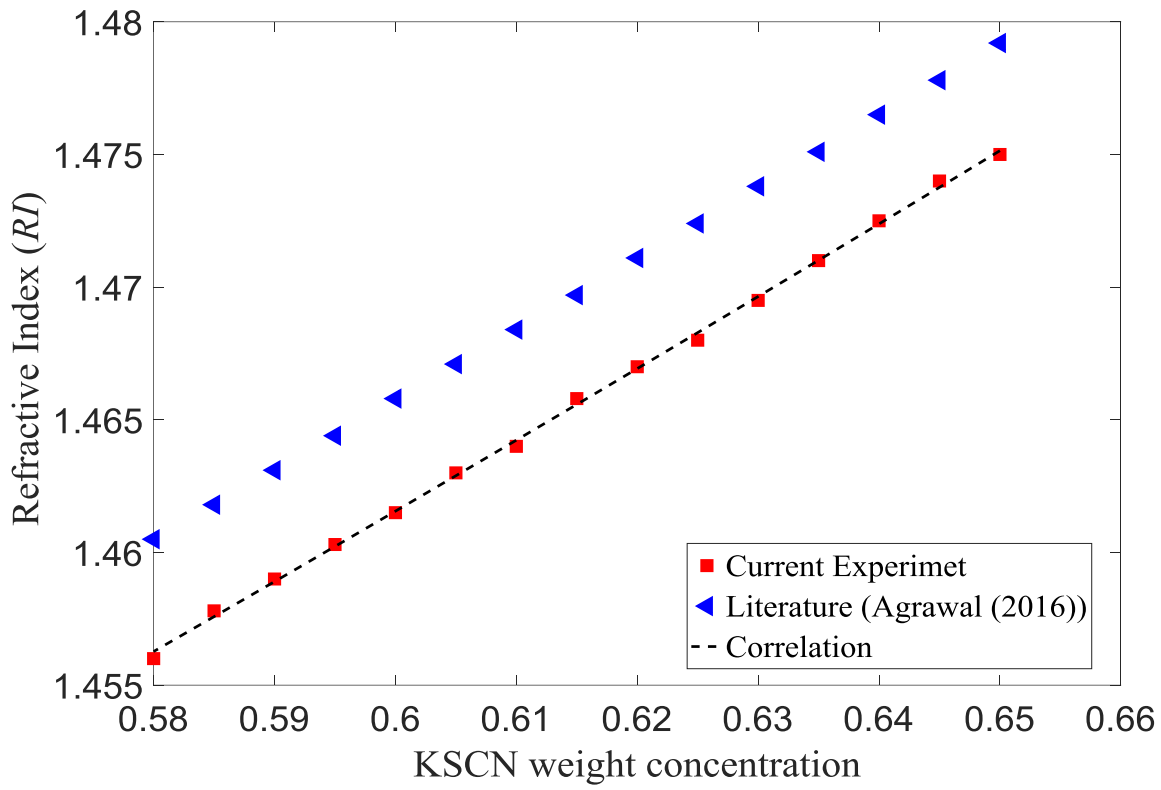

Figure A- 1- KSCN RI at different solution concentrations

A-2. Canola oil properties

The properties of Canola oil were measured experimentally. The Canola oil density was measured using Force Tensiometer (K100, KRUSS Scientific Instruments, Inc.) with the measuring probe for density measurements (DE0601, KRUSS Scientific Instruments Inc.), and the results are plotted in Figure A- 2(a). By averaging the results, the density of Canola oil was measured as 0.915 kg/m^3. Figure A- 2(b) plots the viscosity of Canola oil versus time, which was measured using Rotational Rheometer (Rheolab QC, Anton Paar GmbH) with double gap measuring cup (DG42, Anton Paar GmbH). As shown in Figure A- 2(b), there is an increasing trend for viscosity at the beginning of the measurements; however, after approximately 3 seconds, the viscosity trend becomes roughly levelled off. The viscosity data plotted in Figure A- 2(b) was averaged from t =10 s to t = 20 s, calculated as 0.0738 Pa.s.

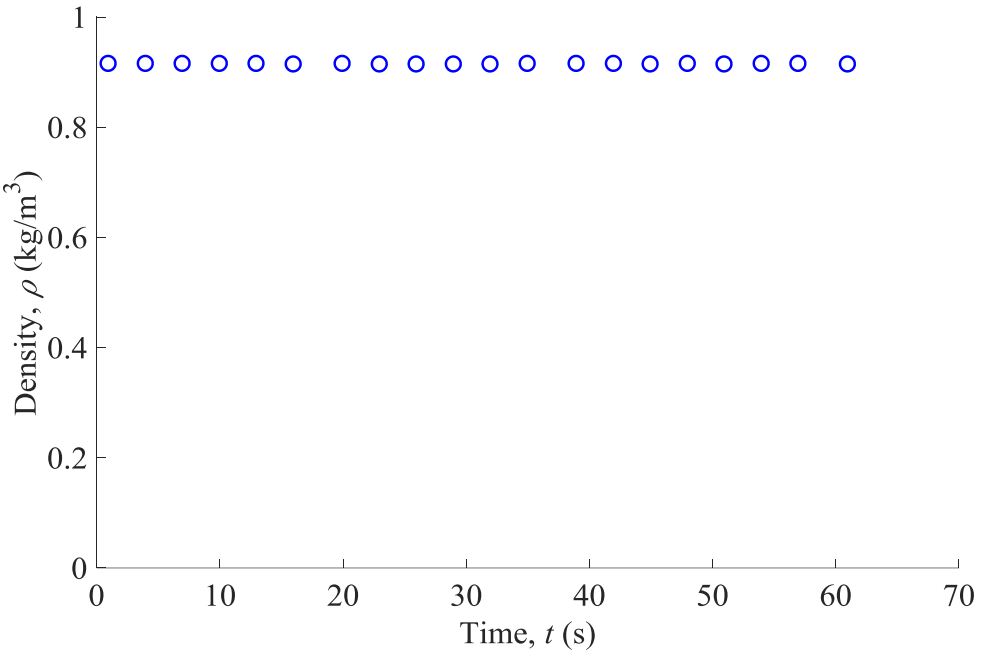

(a)

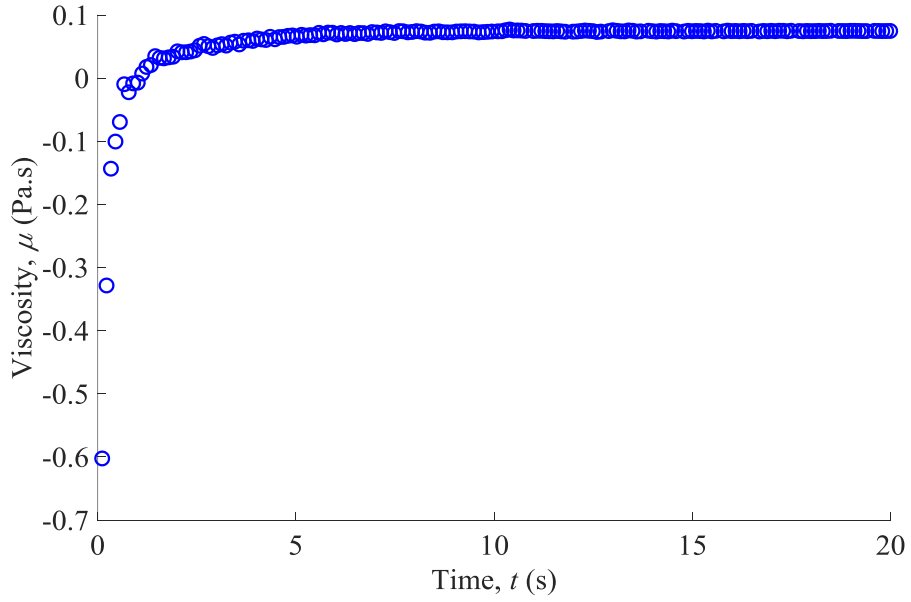

(b)

Figure A- 2- Measurement of Canola oil (a) density, and (b) viscosity versus time

A-3.Solid model of the flow channel

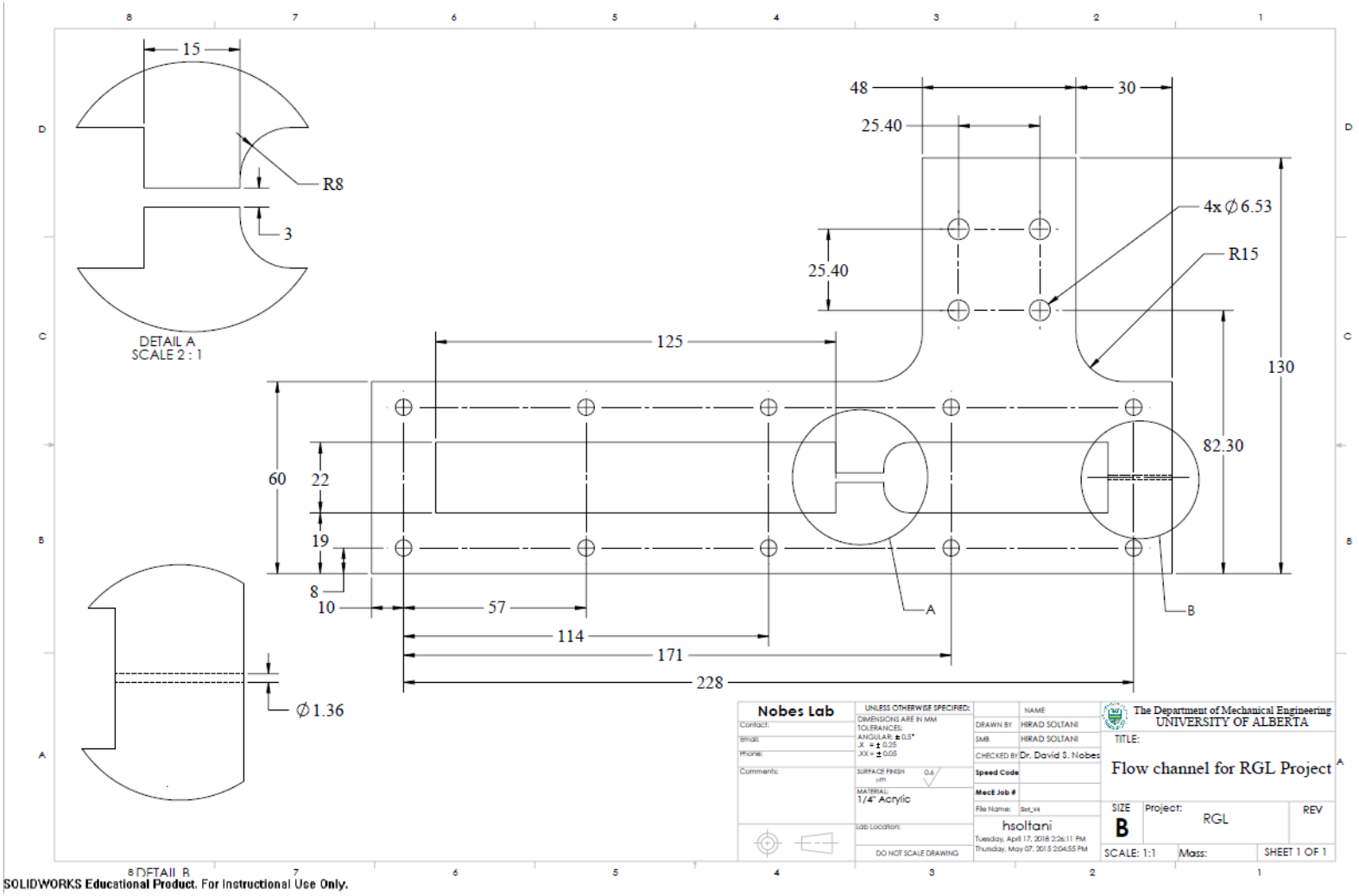

A-4.Post-processing code to plot the velocity field around bubbles (PIV and PTV)

```
%%%%%%%%%%%%%%%%%%%%%%%%%%%%%%%%%%%%%%%%%%%%%%%%%%%%%%%%%%%%%%%%%%%%%%%%%%%%
% This code has been developed to derive velocity vector and vorticity map
% around air bubbles rising through the rectangular confinement

% time_stamp should be defined first for velocity measurement.
% August, 2016
% hsoltani@ualberta.ca
%%%%%%%%%%%%%%%%%%%%%%%%%%%%%%%%%%%%%%%%%%%%%%%%%%%%%%%%%%%%%%%%%%%%%%%%%%%%
%clearing all variables
clear all;
%closing all figures
close all;
%clearing the command area
clc;
warning('off')
```

Set default fonts

```
set(0, 'DefaultAxesFontName', 'Times New Roman');
set(0, 'DefaultUIControlFontName', 'Times New Roman');
set(0, 'defaultUitableFontName', 'Times New Roman');
set(0, 'defaultTextFontName', 'Times New Roman');
set(0, 'defaultUipanelFontName', 'Times New Roman');
font_size = 26;
line_width_size=2;
marker_size = 7;
Viscosity = 0.4; % Glycerol/water solution viscosity
% Parameters for slot geometry
w = 3; % Slot/Flow cell width, mm
A = 5.842 * w;   % mm2
Dh = 4*5.842*w/(2*(w + 5.842));% , [mm]
% ************************************************************************

% Set Parameters
Ox = 2.2; % offset for x-axis
Oy = -3;  % offset for y-axis
w = 3; % Slot/Flow cell width, mm
A = 5.842 * w;   % mm2

% Camera frequency
f = 60;
```

```
Q = [20 40 60 100 150];

% Maximum velocity through the mini-slot (in [mm/s])
V_max20_Slot = 0.503;
V_max40_Slot = 1.008;
V_max60_Slot = 1.598;
V_max100_Slot = 2.67;
V_max150_Slot = 3.966;
```

Reading the shadowgraph processing data to find the centre of the bubble

Pop up window to select the name of data file

```
        prompt = {'Enter the data name:'};
name = inputdlg(prompt);
% [fname, pname] = uigetfile('*.csv');
% [fname, pname] = uigetfile('*.csv');
if name{1}(1:2) == '20'
    fullFileName = ['X:\01_Current_Students\HIRAD SOLTANI\Publicaitons_HS\Journal Papers\Paper
2\MATLAB & Figures\CSV Files_Nov 3(93.38%)\Q20\ParticleList' name{1} '.csv'];
    V_f = V_max20_Slot;
elseif name{1}(1:2) == '40'
    fullFileName = ['X:\01_Current_Students\HIRAD SOLTANI\Publicaitons_HS\Journal Papers\Paper
2\MATLAB & Figures\CSV Files_Nov 3(93.38%)\Q40\ParticleList' name{1} '.csv'];
    V_f = V_max40_Slot;
elseif name{1}(1:2) == '60'
    fullFileName = ['X:\01_Current_Students\HIRAD SOLTANI\Publicaitons_HS\Journal Papers\Paper
2\MATLAB & Figures\CSV Files_Nov 3(93.38%)\Q60\ParticleList' name{1} '.csv'];
    V_f = V_max60_Slot;
elseif name{1}(1:2) == '10'
    fullFileName = ['X:\01_Current_Students\HIRAD SOLTANI\Publicaitons_HS\Journal Papers\Paper
2\MATLAB & Figures\CSV Files_Nov 3(93.38%)\Q100\ParticleList' name{1} '.csv'];
    V_f = V_max100_Slot;
elseif name{1}(1:2) == '15'
    fullFileName = ['X:\01_Current_Students\HIRAD SOLTANI\Publicaitons_HS\Journal Papers\Paper
2\MATLAB & Figures\CSV Files_Nov 3(93.38%)\Q150\ParticleList' name{1} '.csv'];
    V_f = V_max150_Slot;
end
%fprintf(1, 'Now reading %s\n', fullFileName);
fileID = fopen(fullFileName);
%   date_time = textscan(fileID,'Date %s Time %s','HeaderLines',1);
%   column_headers = textscan(fileID,'%s',41,'delimiter', '\t');
column_headers  = regexp(fgetl(fileID ),';','split');

counter =1;
while (~feof(fileID))
```

```
    [data,position] = textscan(fileID,'%s',10,'delimiter', ';');
    real_data{counter,:} = data;
    counter = counter + 1;
end
counter = counter - 2;
fclose(fileID);
for row_number = 1 : counter
    subcounter = 1;
    temp = real_data{row_number,1}{1,1};
    for column_number = 1 : 10
        %             if  (~isnan(temp(column_number)))
        data(row_number,subcounter) = temp(column_number);
        final_data_cell{row_number+1,subcounter} = temp(column_number);

        subcounter = subcounter + 1;
        %             end
    end
end
final_data_cell = cellfun( @(x) str2double(strrep(x, ',', '.')), final_data_cell,
'uniformoutput', false);

data = cell2mat(final_data_cell);
final_data_cell(1,:) = column_headers;

[r,c] = size(data);

% Multiplying camera frequency to vy and vz of bubbles to obtain the
% rising velocity in mm/s
data (4:r,7)= f.*(data (4:r,1)-data (2:r-2,1))/2;
data (4:r,8)= f.*(data (4:r,2)-data (2:r-2,2))/2;
data (4:r,9)= sqrt(data (4:r,7).^2 + data (4:r,8).^2);

Bubble_Rising_Velocity = nanmean(data(2:end,9));
AverageDiameter = nanmean(data(2:end,4));

% Centre of the bubble
y1 = min(data(:,2));
```

Plotting the results of PIV processing

Loading velocity vector field for all images containing the bubble

```
       path = ['D:\MyProjects\RGL_BubbleRise_November 3\' name{1} '\TR_PIV_MP(1x64x64_75%ov)\'];
% Img1: The first image that we want to read.
% ImgNum: The first image in which the bubble is recognized
% FVV and Img2: The image that is used to plot the instantaneous velocity vector
% and vorticity maps in Figure(3)
% FVVV: The images we want to read to plot the velocity profile in the
% liquid film between the bubble and the walls
```

```
num = str2num(name{1});
if num == 205
    FV = 'B[32:37].vc7';
    ImgNum = 24;
    Img1 = 32;
    Img2 = 82;
    FVV = 'B00082.vc7';
    FVVV = 'B[32:92].vc7';
elseif num == 2013
    FV = 'B[47:52].vc7';
    ImgNum = 34;
    Img1 = 47;
    Img2 = 81;
    FVV = 'B00081.vc7';
    FVVV = 'B[45:105].vc7';
elseif num == 2016
    FV = 'B[60:65].vc7';
    ImgNum = 53;
    Img1 = 60;
    Img2 = 111;
    FVV = 'B00111.vc7';
    FVVV = 'B[60:120].vc7';
    elseif num == 2019
    FV = 'B[130:135].vc7';
    ImgNum = 124;
    Img1 = 130;
    Img2 = 174;
    FVV = 'B00174.vc7';
    FVVV = 'B[130:190].vc7';
elseif num == 4010
    FV = 'B[45:50].vc7';
    ImgNum = 6;
    Img1 = 45;
    Img2 = 85;
    FVV = 'B00085.vc7';
    FVVV = 'B[35:95].vc7';
elseif num == 403
    FV = 'B[20:25].vc7';
    ImgNum = 1;
    Img1 = 20;
    Img2 = 50;
    FVV = 'B00050.vc7';
    FVVV = 'B[20:80].vc7';
elseif num == 607
    FV = 'B[90:95].vc7';
    ImgNum = 64;
    Img1 = 90;
    Img2 = 111;
    FVV = 'B00111.vc7';
    FVVV = 'B[90:150].vc7';
elseif num == 6018
    FV = 'B[74:79].vc7';
    ImgNum = 39;
```

```
    Img1 = 74;
    Img2 = 81;
    FVV = 'B00081.vc7';
    FVVV = 'B[69:129].vc7';
elseif num == 1007
    FV = 'B[35:40].vc7';
    ImgNum = 13;
    Img1 = 35;
    Img2 = 60;
    FVV = 'B00060.vc7';
    FVVV = 'B[30:90].vc7';
elseif num == 1004
    FV = 'B[42:47].vc7';
    ImgNum = 22;
    Img1 = 42;
    Img2 = 60;
    FVV = 'B00061.vc7';
    FVVV = 'B[42:102].vc7';
elseif num == 1003
    FV = 'B[58:63].vc7';
    ImgNum = 38;
    Img1 = 58;
    Img2 = 75;
    FVV = 'B00075.vc7';
    FVVV = 'B[58:118].vc7';
elseif num == 15013
    FV = 'B[38:43].vc7';
    ImgNum = 34;
    Img1 = 38;
    Img2 = 70;
    FVV = 'B00070.vc7';
    FVVV = 'B[38:98].vc7';
elseif num == 15017
    FV = 'B[35:40].vc7';
    ImgNum = 21;
    Img1 = 35;
    Img2 = 55;
    FVV = 'B00055.vc7';
    FVVV = 'B[35:95].vc7';
end

% path = 'D:\MyProjects\Rising Droplet_May 16\201 (5-16-2017 3-19-17
PM)\Invert\ImgPreproc\PTV_TS_VectorCalc2D_04\';
% FV = 'B[42:52].vc7';

V = loadvec([path FV]);
% Zero matrix for storing velocity profiles at different locations
Vy = zeros(160,size(V,2));
ox = V.x;
oy = V.y;
ox = ox./3.2 - 0.23;
oy = oy./3;
% masking the velocity profile to just show the data in the range of
% -0.5<ox<0.5
```

```
j = 1;
% Determining the velocity profile at 3D/4 distance from the centre of the
% bubbles in each of images.
for i = 1:(size(Vy,2))

    % On each step, the velocity profile at y = 0 distance from center of bubble is derived
    y2 = data(i + 1 + Img1 - ImgNum, 2) + 0*AverageDiameter/4;
    x2 = data(i + 1 + Img1 - ImgNum, 1) + 0*AverageDiameter/4;

    % the location of velocity profile is subtracted from location in data
    sub_datay = abs(V(i).y - y2);
    sub_datax = abs(V(i).x - x2);

    % the nearest element to where the velocity profile should be found is derived here
    nearest_yLocation = find(sub_datay == min(sub_datay));
    nearest_xLocation = find(sub_datax == min(sub_datax));

    Vy(:,j) = V(i).vy(:,nearest_yLocation);

    % Determining the center of the bubble in the next image, based on
    j = j + 1;
end
% Average of velocity profiles at y=3D/4 location.
Vy_Ave = f.*mean(Vy,2);
```

Masking the center of the bubble to get rid of funny vectors around bubble center:

```
       Vy_Ave((nearest_xLocation - 7):(nearest_xLocation + 7),:) = NaN;
for i = -22:22
    if Vy_Ave(nearest_xLocation + i) == 0
        Vy_Ave(nearest_xLocation + i) = NaN;
    end
end
```

Velocity profile plot

```
       figure(1);
hold on
set(1,'pos',[70 70 1200 800]);
set(gca,'fontsize',font_size);
set(gcf,'color','w'); % Making plot background white

% Theoretical parabolic velocity profile for single phase flow
V_average = 1000*Q(1)/A * (1/3600); % Multiplied by 1000 to be in [mm/s]
r = -0.5:0.01:0.5;
V_Theory = (2*V_average).*(1 - (r.^2)./(0.5^2));
% ************************************************************************
```

```
plot(ox,Vy_Ave./(2*V_f/3),'-o','MarkerEdgeColor','k',...
    'MarkerFaceColor','b',...
    'MarkerSize',6);

ylabel('{\itV_{film}/q}','FontSize',font_size,'FontName', 'Times New Roman');
xlabel('{\itx/w}','FontSize',font_size,'FontName', 'Times New Roman');
axis equal
% grid minor
axis([-0.52 0.52 -0.6 4.6])

% ****************************************
```

Mapping the Cartesian coordinate to polar coordinate

```
       % Reading the images
VEC = loadvec([path FV]);
% Making the x, y, Vx and Vy of the velocity vector field the same size
for i = 1:size(VEC,2)
    VEC(i).x(145:160) = [];
    VEC(i).x(1:16) = [];
    VEC(i).vy(145:160,:) = [];
    VEC(i).vy(1:16,:) = [];
    VEC(i).vx(145:160,:) = [];
    VEC(i).vx(1:16,:) = [];
end

theta_Ave = zeros(128,128);

% Finding the origin of the bubble in each frame.
for i = 1:size(VEC,2)

    % (x2,y2) is the center of the bubble in the first frame:
    y2 = data(i + 2 + Img1 - ImgNum, 2);
    x2 = data(i + 2 + Img1- ImgNum, 1);

    % The location of bubble center is subtracted from the vector map image
    % to find the nearest point to bubble center
    sub_y = abs(VEC(i).y - y2);
    sub_x = abs(VEC(i).x - x2);

    % location of the center of the bubble in vector map images is found
    % here:
    y_center = find(sub_y == min(sub_y));
    x_center = find(sub_x == min(sub_x));

    % Shifting the origin of the images to the center of the bubble at each
    % individual frame
    y_dif = VEC(i).y(y_center) - VEC(i).y(find(abs(VEC(i).y) == min(abs(VEC(i).y))));
    x_dif = VEC(i).x(x_center) - VEC(i).x(find(abs(VEC(i).x) == min(abs(VEC(i).x))));
    VEC(i).y = VEC(i).y - y_dif;
```

```
    VEC(i).x = VEC(i).x - x_dif;

    for p = 1:128
        X(p,:) = VEC(i).x;
        Y(:,p) = VEC(i).y;
    end

    [theta,rho] = cart2pol(X,Y);
    theta = theta';
    theta(theta < -pi/2) = theta(theta < -pi/2) + 2*pi;
    %     rho = rho';
    V_r = VEC(i).vx.*cos(theta) + VEC(i).vy.*sin(theta);
    V_theta = VEC(i).vy.*cos(theta) - VEC(i).vx.*sin(theta);


    % Determining the bubble interface based on the bubble diameter and
    % r-component of polar coordinates
    rho_zero = find(rho == min(rho));
    [row, col] = find(rho>(0.5.*data(i + 2 + Img1- ImgNum,4)) & rho<(0.5.*data(i + 2 + Img1-
ImgNum,4) + 0.1));

    % Storing the information of theta around the bubble in each frame,
    % into a matrix:
    figure(2);
    hold on
    set(gcf,'pos',[70 70 1200 800]);
    set(gcf,'color','w');
    set(gca,'fontsize',font_size)
    for u = 1:size(col)
        V_theta(V_theta == 0) = NaN;
        h =
plot(theta(col(u),row(u))+pi/2,f.*V_theta(col(u),row(u)),'*','MarkerEdgeColor','k',...
            'MarkerSize',marker_size,'LineWidth',line_width_size,'Color','k');
        hold on
        ax = gca;
        ax.XTick = [ -2*pi -pi 0 pi 2*pi];                  % set x-axis ticks
        ax.XTickLabel = {'-2\pi','-\pi','0','\pi', '2\pi'};
        xlabel('{\it\theta}  (rad)','FontSize',font_size,'FontName', 'Times New Roman');
        ylabel('{\itV_{\theta}} (mm/s)','FontSize',font_size,'FontName', 'Times New Roman');
    end
end

% ************************************************************************
% Theoretical slip velocity
% Let us define a domain of -pi to pi for theta in theory
T = pi:0.01:3*pi;
% T = pi/2:0.01:2.5*pi;
% lambda is defined as the bubble diameter normalized to the hydraulic
% diameter of the mini-slot
lambda = AverageDiameter.*cos(T)./w;
V_slip = -(Bubble_Rising_Velocity - ((1 - lambda.^2).*V_f)).*0.5.*sin(T);

% ************************************************************************
% HIRAD'S METHOD
```

```
L = 0.2:0.003:2.085;
D = 3.*L;
V_Theta = -((V_f - Bubble_Rising_Velocity).*0.5.*sin(T) + ...
    (-5.*V_f.*((0.5.*AverageDiameter).^2)./9).*(sin(T)).^3) ...
    -(Bubble_Rising_Velocity).*sin(T);
V_R = -(8.*V_f.*(0.5.*AverageDiameter).^2./w^2.*(sin(T).^2).*cos(T) -
Bubble_Rising_Velocity.*cos(T));
V_R_center = -((V_f - Bubble_Rising_Velocity).*(1 - (0.5.*AverageDiameter)./D)) -
(Bubble_Rising_Velocity);
% ************************************************************************
l = plot(T-pi, V_Theta,'r-','MarkerEdgeColor','b',...
    'MarkerSize',5,'LineWidth',3);
axis([0 2*pi -3.2 3.2])
legend([h l],'Experimetal data','Theoretical {\itV_{\theta}} at {\itr = D_{e}/2}')
% ************************************************************************
```

Loading the Vector Field the FVV and path were defined according to the data set that was chosen at the beginning of this code. path = 'X:\01_Current_Students\HIRAD SOLTANI\Publicaitons_HS\Journal Papers\Paper 2\MATLAB & Figures\';

```
       V = loadvec([path FVV]);
V.vx = f.*V.vx;
V.vy = f.*V.vy;
% ************************************************************************
% Masking inside the bubble to eliminate invalid vectors in that region
% (x2,y2) is the center of the bubble in the first frame:
y2 = data(Img2 - ImgNum + 2, 2);
x2 = data(Img2 - ImgNum + 2, 1);

% The location of bubble center is subtracted from the vector map image
% to find the nearest point to bubble center
sub_y = abs(V.y - y2);
sub_x = abs(V.x - x2);

% location of the center of the bubble in vector map images is found
% here:
y_center = find(sub_y == min(sub_y));
x_center = find(sub_x == min(sub_x));

% determining the front and rear of the bubble
y2_front = data(Img2 - ImgNum + 2, 2) + 0.5.*data(Img2 - ImgNum + 2, 4);
y2_rear = data(Img2 - ImgNum + 2, 2) - 0.5.*data(Img2 - ImgNum + 2, 4);

sub_y_front = abs(V.y - y2_front);
sub_y_rear = abs(V.x - y2_rear);

y_center_front = find(sub_y_front == min(sub_y_front));
y_center_rear = find(sub_y_rear == min(sub_y_rear));
```

```
y_front = find(sub_y_front == min(sub_y_front));
y_rear = find(sub_y_rear == min(sub_y_rear));

% Masking out the center of the bubble
for i = (x_center - 4):(x_center + 4)
    for j = (y_center - 4):(y_center + 4)
        V.vx(i,j) = 0;
    end
    V.vx(i,j) = 0;
end
for i = (x_center - 4):(x_center + 4)
    for j = (y_center - 4):(y_center + 4)
        V.vy(i,j) = 0;
    end
    V.vy(i,j) = 0;
end
% End of masking
% ************************************************************************
% Positioning x-axis and y-axis and normalizing to slot width (w)
V.x = ((V.x) - Ox + 2.8/2)/w;
V.y = ((V.y) - Oy - 7/2)/w;
V = rotatef(V,0);
% % ************************************************************************
% VELOCITY VECTOR MAP
figure(3)
hold on
set(gca,'fontsize',font_size)
set(gcf,'pos',[70 70 800 800]);

% Get the mean velocity field
Vnorm = vec2scal(V,'norm');
vvv = Vnorm.w;

% Rotating and flipping the velocity vectors
vvv= imrotate(vvv,-90);
vvv = flipdim(vvv ,2);
% plotting the scalar field
h = imagesc(V.x,V.y,vvv);
colormap('hsv'); % Have a contoured color map
c = colorbar;
caxis([0,4.5]);
quiver(V.x(1:3:end),V.y(1:6:end)',V.vx(1:3:end,1:6:end)',V.vy(1:3:end,1:6:end)', ...
    'color','k', ...
    'AutoScaleFactor',0.8,'LineWidth',1.1);
hold off
axis equal;
axis([-0.5 0.5 -1.2 1.2]); %Normalized range

xlabel('{\itx/w }','FontSize',font_size,'FontName', 'Times New Roman');
ylabel('{\ity/w }','FontSize',font_size,'FontName', 'Times New Roman');
ylabel(c,'{\itV }{(mm/s)}','FontSize',font_size,'FontName', 'Times New Roman')
alphamap = zeros(size(vvv,1),size(vvv,2));
for i = 0:size(vvv,1)-1
    for j = 0:size(vvv,2)-1
```

```
        if(~(vvv(i+1,j+1) == 0))
            alphamap(i+1,j+1) = 1;
        end
    end
end

set(h, 'AlphaData', alphamap);
% ************************************************************************

% PLOTTING VORTICITY MAP
figure(4);
hold on
set(gca,'fontsize',font_size)
set(gcf,'color','w');
set(gcf,'pos',[70 70 800 800]);

vy_new = V.vy;
vx_new = V.vx;
vy_new(abs(vy_new) == 0) = inf;
vx_new(abs(vx_new) == 0) = inf;
% Calculating vorticity map
for i = 1:128
    dv_dx(:,i) = gradient(vy_new(:,i),V.x);
end
for j = 1:160
    du_dy(j,:) = gradient (vx_new(j,:),V.y);
end

vorticity = dv_dx - du_dy;
vorticity(vorticity == inf) = 0;
vorticity(vorticity == -inf) = 0;
vorticity (isnan(vorticity)) = 0;

% Flipping and rotating vorticity vectors
vorticity = imrotate(vorticity,-90);
vorticity = flipdim(vorticity,2);

% Plotting the vorticity map field
h_curl = imagesc(V.x,V.y,vorticity);
colormap('hsv');

quiver(V.x(1:3:end),V.y(1:6:end)',V.vx(1:3:end,1:6:end)',V.vy(1:3:end,1:6:end)', ...
    'color','k', ...
    'AutoScaleFactor',1,'LineWidth',1.1);
c = colorbar;
caxis([-25 25])
hold off

axis equal;
axis([-0.5 0.5 -1.2 1.2]); % Not normalized range
xlabel('{\itx/w}','FontSize',font_size,'FontName', 'Times New Roman');
ylabel('{\ity/w}','FontSize',font_size,'FontName', 'Times New Roman');
ylabel(c,'{\omega }{(1/s)}','FontSize',font_size,'FontName', 'Times New Roman');
```

```
alphamap = zeros(size(vorticity,1),size(vorticity,2));
for i = 0:size(vorticity,1)-1
    for j = 0:size(vorticity,2)-1
        if(~(vorticity(i+1,j+1) == 0))
            alphamap(i+1,j+1) = 1;
        end
    end
end
set(h_curl, 'AlphaData', alphamap);

% plotting velocity along a vertical line passing the bubble center
figure(5);
hold on
set(gca,'fontsize',font_size)
set(gcf,'color','w');
set(gcf,'pos',[70 70 800 800]);

% Ignoring zeros in the Vx and Vy:
V.vy(V.vy == 0) = NaN;
V.vx(V.vx == 0) = NaN;
h = plot(V.y(1:y_rear),sqrt(V.vy(x_center,1:y_rear).^2 + V.vx(x_center,1:y_rear).^2),'*',...
    'MarkerSize',marker_size,'LineWidth',line_width_size,'Color','k');
hold on
plot(V.y(y_front:end),sqrt(V.vy(x_center,y_front:end).^2 + V.vx(x_center,y_front:end).^2),'*',...
    'MarkerSize',marker_size,'LineWidth',line_width_size,'Color','k');
hold on
l = plot(D./3,-V_R_center,'r-','LineWidth',3)
hold on
plot(-D./3,-V_R_center,'r-','LineWidth',3)
annotation(gcf,'textarrow',[0.32375 0.205],[0.15775 0.15875],...
    'String',{'{\itg}'},'LineWidth',line_width_size, ...
    'FontSize',font_size,'FontName', 'Cambria');
xlabel('{\ity/w}','FontSize',font_size,'FontName', 'Times New Roman');
ylabel('{\itV_{y}}','FontSize',font_size,'FontName', 'Times New Roman');
axis([-2 2 0 4.8])
legend([h l],'Experimetal data','Theoretical {\itV_{r}}')
```

Mapping the Cartesian coordinate to polar coordinate

```
       % % Making the x, y, Vx and Vy of the velocity vector field the same size
% for i = 1:size(v,2)
%     v(i).x(2305:2560) = [];
%     v(i).x(1:256) = [];
%     v(i).vy(2305:2560,:) = [];
%     v(i).vy(1:256,:) = [];
%     v(i).vx(2305:2560,:) = [];
%     v(i).vx(1:256,:) = [];
% end

% Interpolation to convert a sparse PTV vector field into a regular grid
```

```
% Loading the TecPlot file containing particle information (ID number, x, y, Vx and Vy)
V_PTV = load(['PTV_Output_' name{1} '.mat']);

% V_PTV.C(:,4) = V_PTV.C(:,4).*f./281;
% V_PTV.C(:,5) = V_PTV.C(:,5).*f./281;

% Creating a meshgrid for PTV vector field
% [xq,yq] = meshgrid(1169:1:1999,0:1:2039); % for oil droplet
[xq,yq] = meshgrid(844:15:1727,0:15:2039); % for bubble
```

Interpolating on data field and scaling Vx and Vy

```
        frame1 = V_PTV.C(V_PTV.C(:,7) == Img2,:);
frame1(:,4) = frame1(:,4).*f./281;
frame1(:,5) = frame1(:,5).*f./281;
V_magnitude = sqrt(frame1(:,4).^2 + frame1(:,5).^2);
F = scatteredInterpolant(frame1(:,1),frame1(:,2),V_magnitude);
vq = F(xq,yq);
```

Scaling x and y for the regular grid

```
        vq = imrotate(vq,180);
% xx_map = (1/281).*(xq(1,1:end) + 1)./w - 1.87; % for oil droplet
% yy_map = (1/281).*(yq(1:end,1) + 1)./w - 1.21; % for oil droplet
xx_map = (1/281).*(xq(1,1:end) + 1)./w - 1.52; % for bubble
yy_map = (1/281).*(yq(1:end,1) + 1)./w - 1.21; % for bubble
```

Rescaling the shadowgraph data to have the same scale as PTV images

```
        data(2:end,1) = -(data(2:end,1)./w - 0.24);
data(2:end,2) = data(2:end,2)./w - 0.2;
```

```
        figure(6)
hold on
set(gca,'fontsize',font_size)
set(gcf, 'pos', [850 100 800 800]);
set(gcf,'color','w');
set(gca,'xdir','reverse')
h = imagesc(xx_map,yy_map,vq); % plot this scalar field
colormap('hsv'); % Have a contoured color map
```

```
c = colorbar;
caxis([0 4.5])
% ************************************************************************
% Scaling the x and y axes and putting zero at the center
xx_quiver = (1/281).*(frame1(:,1)-3180)./3 + 2.28; % for bubble
yy_quiver = (1/281).*(frame1(:,2)-2040)./3 + 1.21; % for bubble
% ************************************************************************
% rotating the vectors
g = hgtransform;
quiver(xx_quiver,yy_quiver,frame1(:,4),frame1(:,5),'color','k', ...
    'LineWidth',1,'AutoScaleFactor',1.5,'parent',g);
set(g,'Matrix',makehgtform('zrotate',pi))
xlabel('{\itx/w}','FontSize',font_size,'FontName', 'Times New Roman');
ylabel('{\ity/w}','FontSize',font_size,'FontName', 'Times New Roman');
ylabel(c,'{\itV }{(mm/s)}','FontSize',font_size,'FontName', 'Times New Roman');
axis equal
axis([-0.5 0.5 -1.2 1.2])
```

The centerline velocity at front and rear of the bubble

```
       % finding the center of the bubble
y2 = data(2 + Img2- ImgNum, 2);
x2 = data(2 + Img2- ImgNum, 1);

sub_y = abs(yy_map - y2);
sub_x = abs(xx_map - x2);

% location of the center of the bubble in vector map images is found
% here:
y_center = find(sub_y == min(sub_y));
x_center = find(sub_x == min(sub_x));

% Finding the front and rear of the bubble
y2_front = data(2 + Img2- ImgNum, 2) + 0.5.*data(2 + Img2- ImgNum, 4)./3;
sub_y_front = abs(yy_map - y2_front);
y_front = find(sub_y_front == min(sub_y_front));

y2_rear = data(2 + Img2- ImgNum, 2) - 0.5.*data(2 + Img2- ImgNum, 4)./3;
sub_y_rear = abs(yy_map - y2_rear);
y_rear = find(sub_y_rear == min(sub_y_rear));

figure(7)
hold on
set(gca,'fontsize',font_size)
set(gcf, 'pos', [850 100 800 800]);
set(gcf,'color','w');

h = plot(yy_map(y_front:end),vq(y_front:end,x_center),'*',...
    'MarkerSize',marker_size,'LineWidth',line_width_size,'Color','k');
```

```
hold on
plot(yy_map(1:y_rear),vq(1:y_rear,x_center),'*',...
    'MarkerSize',marker_size,'LineWidth',line_width_size,'Color','k');
hold on
l = plot(D./3,-V_R_center,'r-','LineWidth',3)
hold on
plot(-D./3,-V_R_center,'r-','LineWidth',3)
hold on
annotation(gcf,'textarrow',[0.32375 0.205],[0.15775 0.15875],...
    'String',{'{\itg}'},'LineWidth',line_width_size, ...
    'FontSize',font_size,'FontName', 'Cambria');
xlabel('{\ity/w}','FontSize',font_size,'FontName', 'Times New Roman');
ylabel('{\itV_{y}}','FontSize',font_size,'FontName', 'Times New Roman');
legend([h l],'Experimetal data','Theoretical {\itV_{r}}')
axis([-2 2 0 4.8])
```

Calculating the tangential velocity at bubble interface

```
        % Finding the origin of the bubble in each frame. we are picking 5 frames
% only
for i = 1:5
```

```
            % Interpolation of the sparse field
    frame1 = V_PTV.C(V_PTV.C(:,7) == i+Img1-1,:);
    [xq,yq] = meshgrid(844:15:1727,0:15:2039); % for bubble
    frame1(:,4) = frame1(:,4).*f./281;
    frame1(:,5) = frame1(:,5).*f./281;
    V_magnitude = sqrt(frame1(:,4).^2 + frame1(:,5).^2);
    Fx = scatteredInterpolant(frame1(:,1),frame1(:,2),frame1(:,4));
    Fy = scatteredInterpolant(frame1(:,1),frame1(:,2),frame1(:,5));
    F = scatteredInterpolant(frame1(:,1),frame1(:,2),V_magnitude);
    vq_x = Fx(xq,yq);
    vq_y = Fy(xq,yq);
    vq = F(xq,yq);
```

Scaling x and y for the regular grid

```
            vq = imrotate(vq,180);
    vq_y = imrotate(vq_y,180);
    vq_x = imrotate(vq_x,180);
%     set(gca,'xdir','reverse')
    xx_grid = (1/281).*(xq(1,1:end) + 1)./w - 1.55; % for bubble
    yy_grid = (1/281).*(yq(1:end,1) + 1)./w - 1.21; % for bubble
    % (x2,y2) is the center of the bubble in the first frame:
    y2 = data(i + 1 + Img1- ImgNum, 2);
    x2 = data(i + 1 + Img1- ImgNum, 1);

    % The location of bubble center is subtracted from the vector map image
```

```
    % to find the nearest point to bubble center
    sub_y = abs(yy_grid - y2);
    sub_x = abs(xx_grid - x2);

    % location of the center of the bubble in vector map images is found
    % here:
    y_center = find(sub_y == min(sub_y));
    x_center = find(sub_x == min(sub_x));

    % Shifting the origin of the images to the center of the bubble at each
    % individual frame
    y_dif = yy_grid(y_center) - yy_grid(find(abs(yy_grid) == min(abs(yy_grid))));
    x_dif = xx_grid(x_center) - xx_grid(find(abs(xx_grid) == min(abs(xx_grid))));
    yy_grid = yy_grid - y_dif;
    xx_grid = xx_grid - x_dif;

    % ************************************************************************
    % Interpolating data to convert PTV vector filed into a regular grid
    % ************************************************************************

    [theta,rho] = cart2pol(xx_grid,yy_grid);
    %     theta = theta';
    theta(theta < -pi/2) = theta(theta < -pi/2) + 2*pi;
    V_r_PTV = vq_x.*cos(theta) + vq_y.*sin(theta);
    V_theta_PTV = vq_y.*cos(theta) - vq_x.*sin(theta);
    % V_theta_PTV = (V_theta_PTV')';
    % ************************************************************************

    % Determining the bubble interface based on the bubble diameter and
    % r-component of polar coordinates
    rho_zero = find(rho == min(rho));
    [row, col] = find(rho>(0.5.*data(i + 1 + Img1- ImgNum,4)./w) & rho<(0.5.*data(i + 1 + Img1-
ImgNum,4)+0.1)./w);
    % Storing the information of theta around the bubble in each frame,
    % into a matrix:
    figure(8);
    hold on
    set(gcf,'pos',[70 70 1200 800]);
    set(gcf,'color','w');
    set(gca,'fontsize',font_size)

    for u = 1:size(col)
        V_theta_PTV(V_theta_PTV == 0) = NaN;
        % Since Davis does not export calibration of Vy and Vx along with
        % the PTV processed images, we need to deivde the tangential
        % velocity by 281 (1mm = 281 pixels in the collected images)
        h = plot(theta(row(u),col(u))+ pi/2,-V_theta_PTV(row(u),col(u)),'*',...
            'MarkerSize',marker_size,'LineWidth',line_width_size,'Color','k');

        hold on
        ax = gca;
        ax.XTick = [-2*pi -pi 0 pi 2*pi];                    % set x-axis ticks
        ax.XTickLabel = {'-2\pi','-\pi','0','\pi','2\pi'};
        xlabel('{\it\theta}  (rad)','FontSize',font_size,'FontName', 'Times New Roman');
```

```
        ylabel('{\itV_{\theta}} (mm/s)','FontSize',font_size,'FontName', 'Times New Roman');
    end
        end
l = plot(T-pi, V_Theta,'r-','MarkerEdgeColor','b',...
    'MarkerSize',5,'LineWidth',3);
axis([0 2*pi -3.2 3.2])
legend([h l],'Experimetal data','Theoretical {\itV_{\theta}} at {\itr = D_{e}/2}')
```

Published with MATLAB® R2016b

A-5. Post-processing code to plot the velocity field around and inside oil droplets rising through the rectangular confinement

```
%%%%%%%%%%%%%%%%%%%%%%%%%%%%%%%%%%%%%%%%%%%%%%%%%%%%%%%%%%%%%%%%%%%%%%%%%%%%%%%
% This code has been developed to derive velocity vector and vorticity map
% around/inside oil droplets rising through a rectangular confinement
% time_stamp should be defined first for velocity measurement.
% August, 2016
% hsoltani@ualberta.ca
%%%%%%%%%%%%%%%%%%%%%%%%%%%%%%%%%%%%%%%%%%%%%%%%%%%%%%%%%%%%%%%%%%%%%%%%%%%%%%%
%clearing all variables
clear all;
%closing all figures
close all;
%clearing the command area
clc;
warning('off')
```

Set default fonts

```
set(0, 'DefaultAxesFontName', 'Times New Roman');
set(0, 'DefaultUIControlFontName', 'Times New Roman');
set(0, 'defaultUitableFontName', 'Times New Roman');
set(0, 'defaultTextFontName', 'Times New Roman');
set(0, 'defaultUipanelFontName', 'Times New Roman');
font_size = 26;
line_width_size=2;
marker_size = 7;
Viscosity = 0.4; % Glycerol/water solution viscosity
% Parameters for slot geometry
w = 3; % Slot/Flow cell width, mm
A = 5.842 * w;   % mm2
Dh = 4*5.842*w/(2*(w + 5.842));% , [mm]
ttt = 3.62; % droplet velocity to be subtracted from the field
% ************************************************************************
```

```
% Set Parameters
Ox = 2.2; % offset for x-axis
Oy = -3;  % offset for y-axis
w = 3; % Slot/Flow cell width, mm
A = 5.842 * w;   % mm2

% Maximum velocity through the mini-slot (in [mm/s])
V_max20_Slot = 0.503;
V_max40_Slot = 1.008;
V_max60_Slot = 1.598;
V_max100_Slot = 2.67;
V_max150_Slot = 3.966;
```

Plotting the results of PIV processing

Loading velocity vector field for all images containing the bubble Pop up window to select the name of data file Img1: The first image that we want to read FVV and Img2: The image that is used to plot the instantaneous velocity vector and vorticity maps f: camera frequency

```
        prompt = {'Enter the data name:'};
name = inputdlg(prompt);
num = str2num(name{1});
if num == 201
    f = 30;
    Img2 = 283;
    FVV = 'B00283.vc7';
elseif num == 202
    f = 30;
    Img2 = 317;
    FVV = 'B00317.vc7';
elseif num == 401
    f = 45;
    Img2 = 317;
    FVV = 'B00317.vc7';
elseif num == 402
    f = 45;
    Img2 = 320;
    FVV = 'B00320.vc7';
elseif num == 601
    f = 70;
    Img2 = 290;
    FVV = 'B00290.vc7';
elseif num == 602
    f = 70;
    Img2 = 358;
    FVV = 'B00358.vc7';
```

```
elseif num == 1001
    f = 90;
    Img2 = 163;
    FVV = 'B00163.vc7';
elseif num == 1002
    f = 90;
    Img2 = 125;
    FVV = 'B00125.vc7';
elseif num == 1501
    f = 90;
    Img2 = 70;
    FVV = 'B00070.vc7';
elseif num == 1502
    f = 90;
    Img2 = 104;
    FVV = 'B00104.vc7';
end
path = ['D:\MyProjects\Rising Droplet_May 16\' name{1} '\TR_PIV_MP(1x64x64_75%ov)\'];
%
% V = loadvec([path FV]);
% % Zero matrix for storing velocity profiles at different locations
% Vy = zeros(160,size(V,2));
% ox = V.x;
% oy = V.y;
% ox = ox./3.2 - 0.23;
% oy = oy./3;
```

Loading the Vecotr Field the FVV and path were defined according to the data set that was chosen at the beginnning of this code. path = 'X:\01_Current_Students\HIRAD SOLTANI\Publicaitons_HS\Journal Papers\Paper 2\MATLAB & Figures\';

```
       V = loadvec([path FVV]);
V.vx = f.*V.vx;
V.vy = f.*V.vy-ttt;

% ************************************************************************
% Positioning x-axis and y-axis and normalizing to slot width (w)
V.x = ((V.x) - Ox + 0.3)/w;
V.y = ((V.y) - Oy - 7/2)/w;
V = rotatef(V,0);
% % ************************************************************************
% VELOCITY VECTOR MAP
figure(1)
hold on
set(gca,'fontsize',font_size)
set(gcf,'pos',[70 70 800 800]);
```

```
% Get the mean velocity field
Vnorm = vec2scal(V,'norm');
vvv = Vnorm.w;

% Rotating and flipping the velocity vectors
vvv= imrotate(vvv,-90);
vvv = flipdim(vvv ,2);
% plotting the scalar field
h = imagesc(V.x,V.y,vvv);
colormap('hsv'); % Have a contoured color map
c = colorbar;
caxis([0,4.5]);
%%%%%%%%%%%%%%%%%%%%%%%%%%%%%%%%%%%%%%%%%%%%%%%%%%%%%%%%%%%%%%%%%%%%%%%%%%%
% % Streamlines
% startx = -0.5:0.2:0.5;
% starty = ones(size(startx));
% [sx sy] = meshgrid(-0.5:0.05:0.5,-1.2:0.15:1.2);
quiver(V.x(1:3:end),V.y(1:6:end)',V.vx(1:3:end,1:6:end)',V.vy(1:3:end,1:6:end)', ...
    'color','k', ...
    'AutoScaleFactor',1,'LineWidth',1.1);
% g = streamline(V.x,V.y',V.vx',V.vy'-0.976,sx(:),sy(:));
% set(g,'color','r')
%%%%%%%%%%%%%%%%%%%%%%%%%%%%%%%%%%%%%%%%%%%%%%%%%%%%%%%%%%%%%%%%%%%%%%%%%%%
hold off
axis equal;
axis([-0.5 0.5 -1.2 1.2]); %Normalized range

xlabel('{\itx/w }','FontSize',font_size,'FontName', 'Times New Roman');
ylabel('{\ity/w }','FontSize',font_size,'FontName', 'Times New Roman');
ylabel(c,'{\itV }{(mm/s)}','FontSize',font_size,'FontName', 'Times New Roman')
alphamap = zeros(size(vvv,1),size(vvv,2));
for i = 0:size(vvv,1)-1
    for j = 0:size(vvv,2)-1
        if(~(vvv(i+1,j+1) == 0))
            alphamap(i+1,j+1) = 1;
        end
    end
end

set(h, 'AlphaData', alphamap);
% ************************************************************************

% PLOTTING VORTICITY MAP
figure(2);
hold on
set(gca,'fontsize',font_size)
set(gcf,'color','w');
set(gcf,'pos',[70 70 800 800]);

vy_new = V.vy;
vx_new = V.vx;
vy_new(abs(vy_new) == 0) = inf;
vx_new(abs(vx_new) == 0) = inf;
```

```
% Calculating vorticity map
for i = 1:128
    dv_dx(:,i) = gradient(vy_new(:,i),V.x);
end
for j = 1:160
    du_dy(j,:) = gradient (vx_new(j,:),V.y);
end

vorticity = dv_dx - du_dy;
vorticity(vorticity == inf) = 0;
vorticity(vorticity == -inf) = 0;
vorticity (isnan(vorticity)) = 0;

% Flipping and rotating vorticity vectors
vorticity = imrotate(vorticity,-90);
vorticity = flipdim(vorticity,2);

% Plotting the vorticity map field
h_curl = imagesc(V.x,V.y,vorticity);
colormap('hsv');

quiver(V.x(1:3:end),V.y(1:6:end)',V.vx(1:3:end,1:6:end)',V.vy(1:3:end,1:6:end)', ...
    'color','k', ...
    'AutoScaleFactor',1,'LineWidth',1.1);
c = colorbar;
caxis([-25 25])
hold off

axis equal;
axis([-0.5 0.5 -1.2 1.2]); % Not normalized range
xlabel('{\itx/w}','FontSize',font_size,'FontName', 'Times New Roman');
ylabel('{\ity/w}','FontSize',font_size,'FontName', 'Times New Roman');
ylabel(c,'{\omega }{(1/s)}','FontSize',font_size,'FontName', 'Times New Roman');

alphamap = zeros(size(vorticity,1),size(vorticity,2));
for i = 0:size(vorticity,1)-1
    for j = 0:size(vorticity,2)-1
        if(~(vorticity(i+1,j+1) == 0))
            alphamap(i+1,j+1) = 1;
        end
    end
end
set(h_curl, 'AlphaData', alphamap);
```

Plotting the PTV processing results

Interpolation to convert a sparse PTV vector field into a regular grid

```
        % Loading the TecPlot file containing particle information (ID number, x, y, Vx and Vy)
V_PTV = load(['PTV_Output_Oil_' name{1} '.mat']);

% V_PTV.C(:,4) = V_PTV.C(:,4).*f./281;
% V_PTV.C(:,5) = V_PTV.C(:,5).*f./281;
```

Creating a meshgrid for PTV vector field

```
        [xq,yq] = meshgrid(1169:1:1999,0:1:2039); % for oil droplet
% [xq,yq] = meshgrid(844:15:1727,0:15:2039); % for bubble
```

Interpolating on data field and scaling Vx and Vy

```
        frame1 = V_PTV.C(V_PTV.C(:,7) == Img2,:);
frame1(:,4) = frame1(:,4).*f./281;
frame1(:,5) = frame1(:,5).*f./281+ttt;
V_magnitude = sqrt(frame1(:,4).^2 + frame1(:,5).^2);
F = scatteredInterpolant(frame1(:,1),frame1(:,2),V_magnitude);
vq = F(xq,yq);
```

Scaling x and y for the regular grid

```
        vq = imrotate(vq,180);
xx_map = (1/281).*(xq(1,1:end) + 1)./w - 1.87; % for oil droplet
yy_map = (1/281).*(yq(1:end,1) + 1)./w - 1.21; % for oil droplet
% xx_map = (1/281).*(xq(1,1:end) + 1)./w - 1.52; % for bubble
% yy_map = (1/281).*(yq(1:end,1) + 1)./w - 1.21; % for bubble
```

```
        figure(3)
hold on
set(gca,'fontsize',font_size)
set(gcf, 'pos', [850 100 800 800]);
set(gcf,'color','w');
set(gca,'xdir','reverse')
h = imagesc(xx_map,yy_map,vq); % plot this scalar field
colormap('hsv'); % Have a contoured color map

c = colorbar;
caxis([0 4.5])
% ************************************************************************
% Scaling the x and y axes and putting zero at the center
xx_quiver = (1/281).*(frame1(:,1)-3180)./3 + 1.87; % for oil droplet
yy_quiver = (1/281).*(frame1(:,2)-2040)./3 + 1.21; % for oil droplet
% ************************************************************************
% rotating the vectors
```

```
g = hgtransform;
quiver(xx_quiver,yy_quiver,frame1(:,4),frame1(:,5),'color','k', ...
    'LineWidth',1,'AutoScaleFactor',1.5,'parent',g);
set(g,'Matrix',makehgtform('zrotate',pi))
xlabel('{\itx/w}','FontSize',font_size,'FontName', 'Times New Roman');
ylabel('{\ity/w}','FontSize',font_size,'FontName', 'Times New Roman');
ylabel(c,'{\itV }{(mm/s)}','FontSize',font_size,'FontName', 'Times New Roman');
axis equal
axis([-0.5 0.5 -1.2 1.2])
```

Published with MATLAB® R2016b

A-6. Post-processing code to plot the bubble characteristics

```
       % This code has been developed to derive air bubble characteristics from
% *.CSV files obtained from image processing in DaVis
% The resulted data are storred in array: final_data
% List of variables in each column
% 1='X/mm',2='Y/mm',3='Centricity',4='Diameter/mm',5='Minimal diameter/mm',
% 6='Maximal diameter/mm',7='Speed/mm/s',8='Horizontal speed/mm/s',
% 9='Vertical speed/mm/s',10='Volume/mm³,,,,,,,,,,'}

% time_stamp should be defined first for velocity measurement.
% November, 2016
% hsoltani@ualberta.ca
%%%%%%%%%%%%%%%%%%%%%%%%%%%%%%%%%%%%%%%%%%%%%%%%%%%%%%%%%%%%%%%%%%%%%%%%%%%%%%%
% DEVELOPED BY: HIRAD SOLTANI
%%%%%%%%%%%%%%%%%%%%%%%%%%%%%%%%%%%%%%%%%%%%%%%%%%%%%%%%%%%%%%%%%%%%%%%%%%%%%%%
clear all;
close all;
clc;
warning('off')
set(0, 'DefaultAxesFontName', 'Times New Roman');
set(0, 'DefaultUIControlFontName', 'Times New Roman');
set(0, 'defaultUitableFontName', 'Times New Roman');
set(0, 'defaultTextFontName', 'Times New Roman');
set(0, 'defaultUipanelFontName', 'Times New Roman');
set(0, 'defaulttextinterpreter', 'tex');

% set default font size, line width and marker size
font_size = 24;
line_width_size = 2;
marker_size = 12;
line_style = {'-','--','-.',':','-.'};
marker_style = {'*','o','<','s','d','+','x','^','>'};
style = {'-*','-o','-<','-+','-s','-d','-x','->','-^','-h','-p'};
% Pop up window to select marker style and color
% prompt = {'Enter the flow rate(Q):','Enter marker style 1:','Enter color:', 'enter line
style:'};
% dlg_title = 'Input';
```

```
% num_lines = 1;
% defaultans = {'20','s','r','-'};
% style = inputdlg(prompt,dlg_title,num_lines,defaultans);.
%
% Parameters for mathematical modeling of rising
% velocity through the slot
density_particle = 1.225;  % kg/m3
density_fluid = 1245.9;   % kg/m3
g = 9.807;
density_Ratio = density_fluid/density_particle;
viscosity_particle = 1.81e-5;  % [kg/ms]
viscosity_fluid = 0.4;  % [kg/ms]
sigma = viscosity_fluid/viscosity_particle;
R = 0:0.01:2.2;  % Diameter of the particle, [mm]
sigma = viscosity_fluid/viscosity_particle;
```

Q_2 data

```
       % Q = 40 ml/hr Flow Rate
Q = 0.09;
w = 22; % Slot/Flow cell width, mm
A = 5.842 * w;   % mm2
V_average = Q/A * (1/3600);
V_max = 0.001008*3/22;   % Maximum velocity in a laminar flow, [m/s]
Dh = 5.842;% 4*5.842*w/(2*(w + 5.842)), [mm]
% Dh = 2*(22 + 5.842)/pi;
b = Dh/2;  % b is equal to half diameter of the tube. Here, we assume that
% we have a hydrolic diameter and suppose "b" is half of that
lambda = R./b;
% Wall correction factors: k_1 and k_2:
% Wall correction factors for spheres within a circle, when particle is stationary
%
k_1 = ((1 - 0.75857.*(1 - sigma)./(1 + (2/3).*sigma)*lambda.^5))./ ...
    (1 - 2.1050.*(1 + (2/3).*sigma)./(1 + sigma).*lambda + ...
    2.0865.*(1./(1 + sigma).*lambda.^3)- ...
    1.7068.*((1 - (2/3).*sigma)./(1 + sigma).*lambda.^5)...
    + 0.72603.*(1 - sigma)./(1 + sigma).*lambda.^6);


% Wall correction factor for spheres within a circle, when there is a bulk flow
%
k_2 = (1 - (2/3).*(1./(1 + 2/3.*sigma)).*lambda.^2 - ...
    0.20217.*((1 - sigma)./(1 + 2/3.*sigma).*lambda.^5))./...
    (1 - 2.1050.*(1 + (2/3).*sigma)./(1 + sigma).*lambda + ...
    2.0865.*(1./(1 + sigma).*lambda.^3)- ...
    1.7068.*((1 - (2/3).*sigma)./(1 + sigma).*lambda.^5)...
    + 0.72603.*(1 - sigma)./(1 + sigma).*lambda.^6);

% ************************************************************************
% Correction factors for rise of air bubbles between two parallel plates
```

```
k_w1Hirad = (1 + 2.*(sigma + 3/2)./(sigma + 1).*lambda.*1.338);
U_Infinity = (((2/3).*((R.*0.001).^2.*g.*(density_fluid - density_particle).*(1 + 1./sigma) ...
    ./(viscosity_fluid.*(2 + 3./sigma))))).*1000;
% ************************************************************************

%Reading the data file
%begin
%%%%%%%%%%%%%%%%%%%  Define Folders in which data files are  %%%%%%%%%%%%%%%%
% myFolder{1} = uigetdir;
myFolder{2} = 'X:\01_Current_Students\HIRAD SOLTANI\Publicaitons_HS\Journal Papers\Paper 1\Bubble
Zoomout_February 23\Q40\';

for RunFolder_counter = 2
    if ~isdir(myFolder{RunFolder_counter})
        errorMessage = sprintf('Error: The following folder does not exist:\n%s',
myFolder{RunFolder_counter});
        uiwait(warndlg(errorMessage));
        return;
    end
    filePattern = fullfile(myFolder{RunFolder_counter}, '*.csv');
    logFiles = dir(filePattern);

    for k = 1:length(logFiles)

        baseFileName = logFiles(k).name;
        fullFileName = fullfile(myFolder{RunFolder_counter}, baseFileName);
        fileID = fopen(fullFileName);
        column_headers  = regexp(fgetl(fileID ),';','split');

        counter =1;
        while (~feof(fileID))
            [data,position] = textscan(fileID,'%s',10,'delimiter', ';');
            real_data{counter,:} = data;
            counter = counter + 1;
        end
        counter = counter - 2;
        fclose(fileID);
        for row_number = 1 : counter
            subcounter = 1;
            temp = real_data{row_number,1}{1,1};
            for column_number = 1 : 10
                data(row_number,subcounter) = temp(column_number);
                final_data_cell{row_number+1,subcounter} = temp(column_number);

                subcounter = subcounter + 1;
            end
        end
        final_data_cell = cellfun( @(x) str2double(strrep(x, ',', '.')), final_data_cell,
'uniformoutput', false);
        data = cell2mat(final_data_cell);
        final_data_cell(1,:) = column_headers;
        [r,c] = size(data);
        % define time interval between every two frames
        time_stamp = 1/8;
```

```
        % ********************************************************************
% Since some of the data are collected in another experiment, they
% should be consistent with other data. So the x and y information
% of all images (calibration) are tried to be the same in this
% section
if isequal(baseFileName,'ParticleList4042.csv')
    data(:,2) = data(:,2) + 4;
    data(:,1) = data(:,1) -3.8;
end
% ********************************************************************
data (4:r,7)= (data (4:r,1)-data (2:r-2,1))/(2*time_stamp);
data (4:r,8)= (data (4:r,2)-data (2:r-2,2))/(2*time_stamp);
data (4:r,9)= sqrt(data (4:r,7).^2 + data (4:r,8).^2);

% Uncertainty and averaging the risintg velocity and bubble diameter
% Before the slot region
p = max(find(data(:,2) < -12));
RisingVelocity1 = nanmean(data(1:p,9));
AverageDiameter1 = nanmean(data(1:p,4));
Centricity1 = nanmean(data(1:p,3));
std_Velocity1 = nanstd(data(1:p,9));
std_Centricity1 = nanstd(data(1:p,3));
std_Diameter1 = nanstd(data(1:p,4));

% After the slot region
m = min(find(data(:,2) > 17));
RisingVelocity2 = nanmean(data(m:end,9));
AverageDiameter2 = nanmean(data(m:end,4));
Centricity2 = nanmean(data(m:end,3));
std_Velocity2 = nanstd(data(m:end,9));
std_Centricity2 = nanstd(data(m:end,3));
std_Diameter2 = nanstd(data(m:end,4));

% The average data for before and after the slot regions
RisingVelocity(k) = (p*RisingVelocity1 + m*RisingVelocity2)/(m + p);
AverageDiameter(k) = (p*AverageDiameter1 + m*AverageDiameter2)/(m + p);
Centricity(k) = (p*Centricity1 + m*Centricity2)/(m + p);
std_Velocity(k) = (p*std_Velocity1 + m*std_Velocity2)/(m + p);
std_Centricity(k) = (p*std_Centricity1 + m*std_Centricity2)/(m + p);
std_Diameter(k) = (p*std_Diameter1 + m*std_Diameter2)/(m + p);

% In the slot region
s1 = min(find(data(:,2) > -2));
s2 = max(find(data(:,2) < 8.7));
RisingVelocity_Slot(k) = nanmean(data(s1:s2,9));
Centricity_Slot(k) = nanmean(data(s1:s2,3));
std_Velocity_Slot(k) = nanstd(data(s1:s2,9));
std_Centricity_Slot(k) = nanstd(data(s1:s2,3));
std_Diameter_Slot(k) = nanstd(data(s1:s2,4));

% X position of center of the bubble
Bubble_Center(k) = nanmean(data(s1:s2,1));

% Maximum velocity in the regions before and after the slot
```

```
        v_max_BeforeAfter(k) = max([data(m:end,9);data(1:p,9)]);
        % Maximum velocity through the slot
        v_max_Slot(k) = max(data(s1:s2,9));
        %*************************************************************************
        % Uncertainty of rising velocity in before and after the slot regions

        sortedVelocity(1:p,1) = data(1:p,9);
        sortedVelocity(p+1:size(data,1)-m+p+1,1) = data(m:end,9);
        Sx = 0;
        a = find(isnan(sortedVelocity(:,:)));
        sortedVelocity(a) = [];
        for i = 1:size(sortedVelocity,1)
            Sx = (sortedVelocity(i,1) - RisingVelocity(k)).^2./(length(logFiles)-1) + Sx;
        end
        Sx = Sx^0.5;
        P_xbar(k) = 2*Sx/length(logFiles)^0.5;
        %*************************************************************************
        % Uncertainty through the slot
        sortedVelocity_Slot = data(s1:s2,9);
        Sx_Slot = 0;
        b = find(isnan(sortedVelocity_Slot(:,:)));
        sortedVelocity_Slot(b) = [];
        for i = 1:size(sortedVelocity_Slot,1)
            Sx_Slot = (sortedVelocity_Slot(i,1) -
RisingVelocity_Slot(k)).^2./(size(sortedVelocity_Slot,1)) + Sx_Slot;
        end
        Sx_Slot = Sx_Slot^0.5;
        P_xbar_Slot(k) = 2*Sx_Slot/(size(sortedVelocity_Slot,1)^0.5);

        % For the 3D plot of instantaneous rising velocity, the data of all flow
        % rates should be stored (Rising velocity and Diameter data)
        if AverageDiameter(k) < 0.9
            Velocity_3D_40_min = data(:,9);
            Diameter_3D_40_min = data(:,2)/15 - 0.25;
        end
        if AverageDiameter(k) > 2.6
            Velocity_3D_40_max = data(:,9);
            Diameter_3D_40_max = data(:,2)/15 - 0.25;
        end
        % End of reading data file for RUN 1
    end
end
% Organizing the dimeter and velocity data.
AverageDiameter3 = sort(AverageDiameter);
[r,c] = size(AverageDiameter);
RisingVelocity3 = zeros(r,c);
RisingVelocity_Slot3 = zeros(r,c);
Centricity3 = zeros(r,c);
Centricity_Slot3 = zeros(r,c);
std_Velocity3 = zeros(r,c);
std_Velocity_Slot3 = zeros(r,c);
std_Centricity3 = zeros(r,c);
std_Centricity_Slot3 = zeros(r,c);
v_max_BeforeAfter3 = zeros(r,c);
```

```
v_max_Slot3 = zeros(r,c);
Bubble_Center3 = zeros(r,c);
std_Diameter3 = zeros(r,c);
std_Diameter_Slot3 = zeros(r,c);
i = 1;
for i = 1:c
    j = find(AverageDiameter3 == AverageDiameter(1,i));
    RisingVelocity3(1,j) = RisingVelocity(1,i);
    RisingVelocity_Slot3(1,j) = RisingVelocity_Slot(1,i);
    Centricity3(1,j) = Centricity(1,i);
    Centricity_Slot3(1,j) = Centricity_Slot(1,i);
    std_Velocity3(1,j) = std_Velocity(1,i);
    std_Velocity_Slot3(1,j) = std_Velocity_Slot(1,i);
    std_Centricity3(1,j) = std_Centricity(1,i);
    std_Centricity_Slot3(1,j) = std_Centricity_Slot(1,i);
    std_Diameter3(1,j) = std_Diameter(1,i);
    std_Diameter_Slot3(1,j) = std_Diameter_Slot(1,i);
    v_max_BeforeAfter3(1,j) = v_max_BeforeAfter(1,i);
    v_max_Slot3(1,j) = v_max_Slot(1,i);
    Bubble_Center3(1,j) = Bubble_Center(1,i);
    i = i + 1;
end

% Reynolds number for each bubble
Re = ((density_fluid.*((0.001.*RisingVelocity3) -
V_max)).*(0.001.*AverageDiameter3))./viscosity_fluid;
Re_Slot = ((density_fluid.*((0.001.*RisingVelocity_Slot3) -
V_max*22/3)).*(0.001.*AverageDiameter3))./viscosity_fluid;
% The terminal velocity through the slot
% the purpose of this section is to check how close the rising velocity is
% to theoretical terminal velocity
figure(1);
hold on
set(1,'pos',[70 70 1200 800]);
set(gcf,'color','w');
set(gca,'fontsize',font_size)
U = (((2/9).*((R.*0.001).^2.*g.*(density_fluid - density_particle).*(1 + sigma) ...
    ./(viscosity_fluid.*k_w1Hirad.*(1 + (2/3).*sigma))))).*1000; % Terminal rising velocity,
[mm/s]

plot(AverageDiameter3./5.842, RisingVelocity3 - 1000*V_max,'s','MarkerEdgeColor','r',...
    'MarkerFaceColor','r',...
    'MarkerSize',7);
hold on
plot(R./(5.842/2), U_Infinity,'k--','MarkerEdgeColor','b',...
    'MarkerFaceColor','b',...
    'MarkerSize',5,'LineWidth',2);
% grid minor
hold on
plot(R./(5.842/2), U,'b','MarkerEdgeColor','b',...
    'MarkerFaceColor','b',...
    'MarkerSize',5,'LineWidth',2);
% errorbar(AverageDiameter3./5.842, RisingVelocity3 -
1000*V_max,std_Velocity3,'s','MarkerEdgeColor','r',...
```

```
%     'MarkerFaceColor','r',...
%     'MarkerSize',7,'LineWidth',line_width_size,'Color','k');
xlabel('{\itD_{e}/t}','FontSize',font_size,'FontName', 'Times New Roman');
ylabel('{\itV_{b} - V_{f}} [mm/s]','FontSize',font_size,'FontName', 'Times New Roman');%
figure(2);
legend('Theoretical results for parallel plates (Shapira and Haber 1988)', ...
    'Theoretical results for infinite medium',strcat(['Current experimental data for {\itq =
}',num2str(Q)]))
% Saving the current figure in TIFF and EPS format

% saveas(gcf,'Rising Velocity_Not Modified_Q40.eps')
saveas(gcf,'Rising Velocity_Not Modified_Q40.fig')
% ********************************************
figure(2);
hold on
% grid minor
set(2,'pos',[70 70 1200 800]);
set(gcf,'color','w');
set(gca,'fontsize',font_size)
Cd = (4/3*g*(density_fluid - density_particle)/density_fluid) ...
    .*(0.001.*AverageDiameter3)./((0.001.*RisingVelocity3 - V_max).^2);
Cd_Infinity = 8*(2 + 3/sigma)/(1 + 1/sigma)./Re;
Cd_Theory = viscosity_fluid.*(2 + 3/sigma)...
    /(1 + 1/sigma).*(4./((density_fluid*0.001.*R).*((k_1*0.001).*U - k_2.*V_max)));

plot(AverageDiameter3./5.842,Cd,'s','MarkerEdgeColor','r',...
    'MarkerFaceColor','r',...
    'MarkerSize',7);
hold on
plot(R./(5.842/2),Cd_Theory,'b','MarkerEdgeColor','b',...
    'MarkerFaceColor','b',...
    'MarkerSize',5,'LineWidth',2);

xlabel('{\itD/t}','FontSize',font_size, 'FontName', 'Times New Roman');
ylabel('{\itC_{D}}','FontSize',font_size, 'FontName', 'Times New Roman');
legend(strcat(['Current experimental data for {\itq = }',num2str(Q)]),'Theoretical results for
circular tube')

% Saving the current figure in TIFF and EPS format

% saveas(gcf,'Drag Coefficient_Q40.eps')
saveas(gcf,'Drag Coefficient_Q40.fig')
% axis([-2 2 0 11]);
% ********************************************
% CENTRICITY PLOT BEFORE AND AFTER THE SLOT REGION
figure(3)
hold on
% grid minor
set(3,'pos',[70 70 1200 800]);
set(gcf,'color','w');
set(gca,'fontsize',font_size);
errorbar(AverageDiameter3./5.84,Centricity3,std_Centricity3,'s','MarkerEdgeColor','r',...
    'MarkerFaceColor','r',...
    'MarkerSize',7,'LineWidth',line_width_size,'Color','k');
```

```
xlabel('{\itD_{e}/t}','FontSize',font_size, 'FontName', 'Times New Roman');
ylabel('Centricity, {\itC}','FontSize',font_size, 'FontName', 'Times New Roman');
legend(strcat(['Current experimental data for {\itq = }',num2str(Q)]))

% Saving the current figure in TIFF
saveas(gcf,'Centricity_Q40.fig')
% ************************************************************************
% RE NUMBER PLOT FOR BEFORE AND AFTER THE SLOT REGIONS
figure(4);
hold on
% grid minor;
set(4,'pos',[70 70 1200 800]);
set(gcf,'color','w');
set(gca,'fontsize',font_size);
plot(AverageDiameter3./5.84,Re,'s','MarkerEdgeColor','r',...
    'MarkerFaceColor','r',...
    'MarkerSize',7);
xlabel('{\itD_{e}/w}','FontSize',font_size, 'FontName', 'Times New Roman');
ylabel('{\itRe}','FontSize',font_size, 'FontName', 'Times New Roman');
legend(strcat(['Current experimental data for {\itq = }',num2str(Q)]))

% Saving the current figure in TIFF
saveas(gcf,'Re_Q40.fig')

% ********************************************
% Calculating the parameters through the slot
Q = 0.67; % Flux (V/A)
w = 3; % Slot/Flow cell width, mm
A = 5.842 * w;   % mm2
V_average = Q/A * (1/3600);
V_max = 0.001008;   % Maximum velocity in a laminar flow, [m/s]
Dh =  4*5.842*w/(2*(w + 5.842)); % [mm]
b = Dh/2;  % b is equal to half diameter of the tube. Here, we assume that
% we have a hydrolic diameter and suppose "b" is half of that
lambda = R./b;

% ************************************************

% Wall correction factors: k_1 and k_2:
% Wall correction factors for spheres within a circle, when particle is stationary
%
k_1 = ((1 - 0.75857.*(1 - sigma)./(1 + (2/3).*sigma)*lambda.^5))./ ...
    (1 - 2.1050.*(1 + (2/3).*sigma)./(1 + sigma).*lambda + ...
    2.0865.*(1./(1 + sigma).*lambda.^3)- ...
    1.7068.*((1 - (2/3).*sigma)./(1 + sigma).*lambda.^5)...
    + 0.72603.*(1 - sigma)./(1 + sigma).*lambda.^6);


% Wall correction factor for spheres within a circle, when there is a bulk flow
%
k_2 = (1 - (2/3).*(1./(1 + 2/3.*sigma)).*lambda.^2 - ...
    0.20217.*((1 - sigma)./(1 + 2/3.*sigma).*lambda.^5))./...
    (1 - 2.1050.*(1 + (2/3).*sigma)./(1 + sigma).*lambda + ...
    2.0865.*(1./(1 + sigma).*lambda.^3)- ...
```

```
    1.7068.*((1 - (2/3).*sigma)./(1 + sigma).*lambda.^5)...
    + 0.72603.*(1 - sigma)./(1 + sigma).*lambda.^6);

% ************************************************************************
% Correction factor for rise of air bubbles between two parallel plates
b = 3/2;
lambda = R./b;
k_w1Hirad = (1 + 2.*(sigma + 3/2)./(sigma + 1).*lambda.*1.338);

b = 5.842/2;
lambda = R./b;
k_w2Hirad = (1 + 2.*(sigma + 3/2)./(sigma + 1).*lambda.*1.338);

U = (((2/9).*((R.*0.001).^2.*g.*(density_fluid - density_particle).*(1 + sigma) ...
    ./(viscosity_fluid.*(k_w1Hirad.*k_w2Hirad).*(1 + (2/3).*sigma))))).*1000; % Terminal rising
velocity, [mm/s]
U_Haberman = (((2/9).*((R.*0.001).^2.*g.*(density_fluid - density_particle).*(1 + sigma) ...
    ./(viscosity_fluid.*(k_1).*(1 + (2/3).*sigma)))) + V_max.*k_2./(k_1)).*1000; % Terminal
rising velocity, [mm/s]
% ************************************************************************
% CENTRICITY PLOT THROUGH THE SLOT REGION
figure(5)
hold on
% grid minor
set(5,'pos',[70 70 1200 800]);
set(gcf,'color','w');
set(gca,'fontsize',font_size);
errorbar(AverageDiameter3./w,Centricity_Slot3,std_Centricity_Slot3,'s','MarkerEdgeColor','r',...
    'MarkerFaceColor','r',...
    'MarkerSize',7,'LineWidth',line_width_size,'Color','k');
xlabel('{\itD_{e}/w}','FontSize',font_size, 'FontName', 'Times New Roman');
ylabel('Centricity, {\itC}','FontSize',font_size, 'FontName', 'Times New Roman');
legend(strcat(['Current experimental data for {\itq = }',num2str(Q)]))

% Saving the current figure in TIFF
saveas(gcf,'Centricity_Slot_Q40.fig')

% RE NUMBER PLOT FOR THROUGH THE SLOT REGIONS
figure(6);
hold on
% grid minor;
set(6,'pos',[70 70 1200 800]);
set(gcf,'color','w');
set(gca,'fontsize',font_size);
plot(AverageDiameter3./w,Re_Slot,'s','MarkerEdgeColor','r',...
    'MarkerFaceColor','r',...
    'MarkerSize',7);
xlabel('{\itD_{e}/w}','FontSize',font_size, 'FontName', 'Times New Roman');
ylabel('{\itRe}','FontSize',font_size, 'FontName', 'Times New Roman');
legend(strcat(['Current experimental data for {\itq = }',num2str(Q)]))

% Saving the current figure in TIFF

saveas(gcf,'Re_Slot_Q40.fig')
```

```
% AVERAGED RISING VELOCITY THROUGH THE SLOT
figure(7);
hold on
set(7,'pos',[70 70 1200 800]);
set(gcf,'color','w');
set(gca,'fontsize',font_size)
plot(AverageDiameter3./w, RisingVelocity_Slot3 - V_max*1000,'s','MarkerEdgeColor','r',...
    'MarkerFaceColor','r',...
    'MarkerSize',7);
hold on
plot(R./(w/2), U_Infinity,'k--','MarkerEdgeColor','k',...
    'MarkerFaceColor','k',...
    'MarkerSize',5,'LineWidth',2);
hold on
plot(R./(w/2), U,'b','MarkerEdgeColor','k',...
    'MarkerFaceColor','k',...
    'MarkerSize',5,'LineWidth',2);
% grid minor

xlabel('{\itD_{e}/w}','FontSize',font_size,'FontName', 'Times New Roman');
ylabel('{\it V_{b-Slot} - V_{f-Slot}} [mm/s]','FontSize',font_size,'FontName', 'Times New
Roman');% figure(2);
legend(strcat(['Current experimental data for {\itq = }',num2str(Q)]), 'Theoretical results for
infinite medium', ...
    'Theoretical results for parallel plates (Shapira and Haber 1988)')
saveas(gcf,'Rising Velocity_Not Modified_Slot_Q40.fig')
% ********************************************

% PLOTTING THE DRAG FORCE
figure(8);
hold on
% grid minor
set(8,'pos',[70 70 1200 800]);
set(gcf,'color','w');
set(gca,'fontsize',font_size)
Cd_Infinity = (4/3*g*(density_fluid - density_particle)/density_fluid) ...
    .*(0.001.*AverageDiameter3)./((0.001.*RisingVelocity_Slot3 - V_max).^2);
Cd = 8*(2 + 3/sigma)/(1 + 1/sigma)./Re_Slot;
Cd_Theory = viscosity_fluid.*(2 + 3/sigma)...
    /(1 + 1/sigma).*(4./((density_fluid*0.001.*R).*((k_1*0.001).*U - k_2.*V_max)));

plot(AverageDiameter3./w,Cd,'s','MarkerEdgeColor','r',...
    'MarkerFaceColor','r',...
    'MarkerSize',7);
hold on
plot(R./(w/2),Cd_Theory,'b','MarkerEdgeColor','b',...
    'MarkerFaceColor','b',...
    'MarkerSize',5,'LineWidth',2);

xlabel('{\itD/w}','FontSize',font_size, 'FontName', 'Times New Roman');
ylabel('{\itC_{D}}','FontSize',font_size, 'FontName', 'Times New Roman');
legend(strcat(['Current experimental data for {\itq = }',num2str(Q)]),'Theoretical results for
circular tube')
```

```
saveas(gcf,'Drag Coefficient_Slot_Q40.fig')
% axis([-2 2 0 11]);
% ************************************************************************
% Bubble rising velocity in infinity (no confinement)
U_Infinity = (((2/3).*((0.5.*AverageDiameter3.*0.001).^2.*g.*(density_fluid -
density_particle).*(1 + 1./sigma) ...
    ./(viscosity_fluid.*(2 + 3./sigma)))) + V_max).*1000;
```

Saving data files separately for each flow rate, and plotting all of data in one figure

```
       save('data40.mat','AverageDiameter3','RisingVelocity_Slot3','RisingVelocity3', ...
    'Centricity3','Centricity_Slot3','std_Velocity3','std_Velocity_Slot3' ...
    ,'std_Centricity3','std_Centricity_Slot3',
'U_Infinity','v_max_Slot3','v_max_BeforeAfter3','Bubble_Center3', ...
    'std_Diameter_Slot3','std_Diameter3')
close all
clear data
```

Q_5 data

```
       % Plotting for Q = 150
% Parameter for the regions before and after the slot

Q = 0.36; % Flux (Q/A)
w = 22; % Slot/Flow cell width, mm
A = 5.842 * w;   % mm2
V_average = Q/A * (1/3600);
V_max = 0.003966*3/22;   % Maximum velocity in a laminar flow, [m/s]
Dh = 5.842;% 4*5.842*w/(2*(w + 5.842)), [mm]
% Dh = 2*(22 + 5.842)/pi;
b = Dh/2;  % b is equal to half diameter of the tube. Here, we assume that
% we have a hydrolic diameter and suppose "b" is half of that
lambda = R./b;
% Wall correction factors: k_1 and k_2:
% k_1: Wall correction factors for spheres within a circle when there is
% wall effect

k_1 = ((1 - 0.75857.*(1 - sigma)./(1 + (2/3).*sigma)*lambda.^5))./ ...
    (1 - 2.1050.*(1 + (2/3).*sigma)./(1 + sigma).*lambda + ...
    2.0865.*(1./(1 + sigma).*lambda.^3)- ...
```

```
    1.7068.*((1 - (2/3).*sigma)./(1 + sigma).*lambda.^5)...
    + 0.72603.*(1 - sigma)./(1 + sigma).*lambda.^6);

% Wall correction factor for spheres within a circle, when there is a bulk flow

k_2 = (1 - (2/3).*(1./(1 + 2/3.*sigma)).*lambda.^2 - ...
    0.20217.*((1 - sigma)./(1 + 2/3.*sigma).*lambda.^5))./...
    (1 - 2.1050.*(1 + (2/3).*sigma)./(1 + sigma).*lambda + ...
    2.0865.*(1./(1 + sigma).*lambda.^3)- ...
    1.7068.*((1 - (2/3).*sigma)./(1 + sigma).*lambda.^5)...
    + 0.72603.*(1 - sigma)./(1 + sigma).*lambda.^6);
% ************************************************************************
% Correction factors for rise of air bubbles between two parallel plates
k_w1Hirad = (1 + 2.*(sigma + 3/2)./(sigma + 1).*lambda.*1.338);
U_Infinity = (((2/3).*((R.*0.001).^2.*g.*(density_fluid - density_particle).*(1 + 1./sigma) ...
    ./(viscosity_fluid.*(2 + 3./sigma))))).*1000;
% ************************************************************************
% Reading the data file
% begin
%%%%%%%%%%%%%%%%%%  Define Folders in which data files are  %%%%%%%%%%%%%%%%
% myFolder{1} = uigetdir;
myFolder{5} = 'X:\01_Current_Students\HIRAD SOLTANI\Publicaitons_HS\Journal Papers\Paper 1\Bubble
Zoomout_February 23\Q150\';

for RunFolder_counter = 5
    if ~isdir(myFolder{RunFolder_counter})
        errorMessage = sprintf('Error: The following folder does not exist:\n%s',
myFolder{RunFolder_counter});
        uiwait(warndlg(errorMessage));
        return;
    end
    filePattern = fullfile(myFolder{RunFolder_counter}, '*.csv');
    logFiles = dir(filePattern);

    for k = 1:length(logFiles)

        baseFileName = logFiles(k).name;
        fullFileName = fullfile(myFolder{RunFolder_counter}, baseFileName);
        %fprintf(1, 'Now reading %s\n', fullFileName);
        fileID = fopen(fullFileName);
        %   date_time = textscan(fileID,'Date %s Time %s','HeaderLines',1);
        %   column_headers = textscan(fileID,'%s',41,'delimiter', '\t');
        column_headers  = regexp(fgetl(fileID ),';','split');

        counter =1;
        while (~feof(fileID))
            [data,position] = textscan(fileID,'%s',10,'delimiter', ';');
            real_data{counter,:} = data;
            counter = counter + 1;
        end
        counter = counter - 2;
        fclose(fileID);
        for row_number = 1 : counter
            subcounter = 1;
```

```
            temp = real_data{row_number,1}{1,1};
            for column_number = 1 : 10
                %             if  (~isnan(temp(column_number)))
                data(row_number,subcounter) = temp(column_number);
                final_data_cell{row_number+1,subcounter} = temp(column_number);

                subcounter = subcounter + 1;
                %             end
            end
        end
        final_data_cell = cellfun( @(x) str2double(strrep(x, ',', '.')), final_data_cell,
'uniformoutput', false);
        data = cell2mat(final_data_cell);
        final_data_cell(1,:) = column_headers;
        [r,c] = size(data);
        % define time interval between every two frames
        time_stamp = 1/8;
        % ********************************************************************
        % Since some of the data are collected in another experiment, they
        % should be consistent with other data. So the x and y information
        % of all images (calibration) are tried to be the same in this
        % section
        if isequal(baseFileName,'ParticleList15012.csv')
            data(:,2) = data(:,2) + 4;
            data(:,1) = data(:,1) -3.8;
        end
        if isequal(baseFileName,'ParticleList15010.csv')
            data(:,2) = data(:,2) + 4;
            data(:,1) = data(:,1) -3.8;
        end
        % ********************************************************************
        data (4:r,7)= (data (4:r,1)-data (2:r-2,1))/(2*time_stamp);
        data (4:r,8)= (data (4:r,2)-data (2:r-2,2))/(2*time_stamp);
        data (4:r,9)= sqrt(data (4:r,7).^2 + data (4:r,8).^2);


        % For the 3D plot of instantaneous rising velocity, the data of all flow
        % rates should be stored (Rising velocity and Diameter data)
        if data(10,4) < 1.3
            Velocity_3D_150 = data(:,9);
            Diameter_3D_150 = data(:,2)/15 - 0.25;
        end
        % Uncertainty and averaging the risintg velocity and bubble
        % diameter through before and after the slot regions

        % Before the slot region:
        p = max(find(data(:,2) < -12));
        RisingVelocity1 = nanmean(data(1:p,9));
        AverageDiameter1 = nanmean(data(1:p,4));
        Centricity1 = nanmean(data(1:p,3));
        std_Velocity1 = nanstd(data(1:p,9));
        std_Centricity1 = nanstd(data(1:p,3));
        std_Diameter1 = nanstd(data(1:p,4));
```

```
        % After the slot region
        m = min(find(data(:,2) > 17));
        RisingVelocity2 = nanmean(data(m:end,9));
        AverageDiameter2 = nanmean(data(m:end,4));
        Centricity2 = nanmean(data(m:end,3));
        std_Velocity2 = nanstd(data(m:end,9));
        std_Centricity2 = nanstd(data(m:end,3));
        std_Diameter2 = nanstd(data(m:end,4));

        % The average data for before and after the slot regions
        RisingVelocity(k) = (p*RisingVelocity1 + m*RisingVelocity2)/(m + p);
        AverageDiameter(k) = (p*AverageDiameter1 + m*AverageDiameter2)/(m + p);
        Centricity(k) = (p*Centricity1 + m*Centricity2)/(m + p);
        std_Velocity(k) = (p*std_Velocity1 + m*std_Velocity2)/(m + p);
        std_Centricity(k) = (p*std_Centricity1 + m*std_Centricity2)/(m + p);
        std_Diameter(k) = (p*std_Diameter1 + m*std_Diameter2)/(m + p);


        % In the slot region
        s1 = min(find(data(:,2) > -2));
        s2 = max(find(data(:,2) < 8.7));
        RisingVelocity_Slot(k) = nanmean(data(s1:s2,9));
        Centricity_Slot(k) = nanmean(data(s1:s2,3));
        std_Velocity_Slot(k) = nanstd(data(s1:s2,9));
        std_Centricity_Slot(k) = nanstd(data(s1:s2,3));
        std_Diameter_Slot(k) = nanstd(data(s1:s2,4));

        % X position of center of the bubble
        Bubble_Center(k) = nanmean(data(s1:s2,1));

        % Maximum velocity in the regions before and after the slot
        v_max_BeforeAfter(k) = max([data(m:end,9);data(1:p,9)]);
        % Maximum velocity through the slot
        v_max_Slot(k) = max(data(s1:s2,9));
        % ********************************************************************
        % Uncertainty of rising velocity in before and after the slot regions

        sortedVelocity(1:p,1) = data(1:p,9);
        sortedVelocity(p+1:size(data,1)-m+p+1,1) = data(m:end,9);
        Sx = 0;
        a = find(isnan(sortedVelocity(:,:)));
        sortedVelocity(a) = [];
        for i = 1:size(sortedVelocity,1)
            Sx = (sortedVelocity(i,1) - RisingVelocity(k)).^2./(length(logFiles)-1) + Sx;
        end
        Sx = Sx^0.5;
        P_xbar(k) = 2*Sx/length(logFiles)^0.5;
        %*************************************************************************
        % Uncertainty through the slot
        sortedVelocity_Slot = data(s1:s2,9);
        Sx_Slot = 0;
        b = find(isnan(sortedVelocity_Slot(:,:)));
        sortedVelocity_Slot(b) = [];
        for i = 1:size(sortedVelocity_Slot,1)
```

```
            Sx_Slot = (sortedVelocity_Slot(i,1) -
RisingVelocity_Slot(k)).^2./(size(sortedVelocity_Slot,1)) + Sx_Slot;
        end
        Sx_Slot = Sx_Slot^0.5;
        P_xbar_Slot(k) = 2*Sx_Slot/(size(sortedVelocity_Slot,1)^0.5);

        % For the 3D plot of instantaneous rising velocity, the data of all flow
        % rates should be stored (Rising velocity and Diameter data)
        if AverageDiameter(k) < 1.1
            Velocity_3D_150_min = data(:,9);
            Diameter_3D_150_min = data(:,2)/15 - 0.25;
        end
        if AverageDiameter(k) > 2.9
            Velocity_3D_150_max = data(:,9);
            Diameter_3D_150_max = data(:,2)/15 - 0.25;
        end
        % End of reading data file for RUN 1
    end
end
% Organizing the dimeter, rising velocity, centricity and standard
% deviation data:
AverageDiameter3 = sort(AverageDiameter);
[r,c] = size(AverageDiameter);
RisingVelocity3 = zeros(r,c);
RisingVelocity_Slot3 = zeros(r,c);
Centricity3 = zeros(r,c);
Centricity_Slot3 = zeros(r,c);
std_Velocity3 = zeros(r,c);
std_Velocity_Slot3 = zeros(r,c);
std_Centricity3 = zeros(r,c);
std_Centricity_Slot3 = zeros(r,c);
v_max_BeforeAfter3 = zeros(r,c);
v_max_Slot3 = zeros(r,c);
Bubble_Center3 = zeros(r,c);
std_Diameter3 = zeros(r,c);
std_Diameter_Slot3 = zeros(r,c);
i = 1;
for i = 1:c
    j = find(AverageDiameter3 == AverageDiameter(1,i));
    RisingVelocity3(1,j) = RisingVelocity(1,i);
    RisingVelocity_Slot3(1,j) = RisingVelocity_Slot(1,i);
    Centricity3(1,j) = Centricity(1,i);
    Centricity_Slot3(1,j) = Centricity_Slot(1,i);
    std_Velocity3(1,j) = std_Velocity(1,i);
    std_Velocity_Slot3(1,j) = std_Velocity_Slot(1,i);
    std_Centricity3(1,j) = std_Centricity(1,i);
    std_Centricity_Slot3(1,j) = std_Centricity_Slot(1,i);
    std_Diameter3(1,j) = std_Diameter(1,i);
    std_Diameter_Slot3(1,j) = std_Diameter_Slot(1,i);
    v_max_BeforeAfter3(1,j) = v_max_BeforeAfter(1,i);
    v_max_Slot3(1,j) = v_max_Slot(1,i);
    Bubble_Center3(1,j) = Bubble_Center(1,i);
    i = i + 1;
end
```

```
% Reynolds number for each bubble:
Re = ((density_fluid.*((0.001.*RisingVelocity3) -
V_max)).*(0.001.*AverageDiameter3))./viscosity_fluid;
Re_Slot = ((density_fluid.*((0.001.*RisingVelocity_Slot3) -
V_max*22/3)).*(0.001.*AverageDiameter3))./viscosity_fluid;
% ************************************************************************
% Drag force calculation for the regions before and after the slot
lambda_bubble = AverageDiameter3./(Dh);
k_w = ((1 - 0.75857.*(1 - sigma)./(1 + (2/3).*sigma)*lambda_bubble.^5))./ ...
    (1 - 2.1050.*(1 + (2/3).*sigma)./(1 + sigma).*lambda_bubble + ...
    2.0865.*(1./(1 + sigma).*lambda_bubble.^3)- ...
    1.7068.*((1 - (2/3).*sigma)./(1 + sigma).*lambda_bubble.^5)...
    + 0.72603.*(1 - sigma)./(1 + sigma).*lambda_bubble.^6);
k_f = (1 - (2/3).*(1./(1 + 2/3.*sigma)).*lambda_bubble.^2 - ...
    0.20217.*((1 - sigma)./(1 + 2/3.*sigma).*lambda_bubble.^5))./...
    (1 - 2.1050.*(1 + (2/3).*sigma)./(1 + sigma).*lambda_bubble + ...
    2.0865.*(1./(1 + sigma).*lambda_bubble.^3)- ...
    1.7068.*((1 - (2/3).*sigma)./(1 + sigma).*lambda_bubble.^5)...
    + 0.72603.*(1 - sigma)./(1 + sigma).*lambda_bubble.^6);
% Plotting the data and validating with Haberman and Sayre correlation:

% PLOTTING THE RISING VELOCITY VERSUS EQUIVALENT DIAMETER
figure(1);
hold on
set(1,'pos',[70 70 1200 800]);
set(gcf,'color','w');
set(gca,'fontsize',font_size)
U = (((2/9).*((R.*0.001).^2.*g.*(density_fluid - density_particle).*(1 + sigma) ...
    ./(viscosity_fluid.*(k_w1Hirad).*(1 + (2/3).*sigma))))).*1000; % Terminal rising velocity,
[mm/s]
plot(R./(5.842/2), U,'b','MarkerEdgeColor','b',...
    'MarkerFaceColor','b',...
    'MarkerSize',5,'LineWidth',2);
% grid minor
hold on
errorbar(AverageDiameter3./5.842, RisingVelocity3  -
1000*V_max,std_Velocity3,'s','MarkerEdgeColor','r',...
    'MarkerFaceColor','r',...
    'MarkerSize',7,'LineWidth',line_width_size,'Color','k');
xlabel('{\itD_{e}/t}','FontSize',font_size,'FontName', 'Times New Roman');
ylabel('{\itV_{ave}} [mm/s]','FontSize',font_size,'FontName', 'Times New Roman');% figure(2);
legend('Theoretical results for circular tube',strcat(['Current experimental data for {\itq =
}',num2str(Q)]),...
    'Theoretical results for infinite medium')

saveas(gcf,'Rising Velocity_Not Modified_Q150.fig')
% ********************************************

% PLOTTING THE DRAG FORCE
figure(2);
hold on
% grid minor
set(2,'pos',[70 70 1200 800]);
```

```
set(gcf,'color','w');
set(gca,'fontsize',font_size)
Cd = (4/3*g*(density_fluid - density_particle)/density_fluid) ...
    .*(0.001.*AverageDiameter3)./((0.001.*RisingVelocity3 - V_max).^2);
Cd_Infinity = 8*(2 + 3/sigma)/(1 + 1/sigma)./Re;
Cd_Theory = viscosity_fluid.*(2 + 3/sigma)...
    /(1 + 1/sigma).*(4./((density_fluid*0.001.*R).*((k_1*0.001).*U - k_2.*V_max)));

plot(AverageDiameter3./5.842,Cd,'s','MarkerEdgeColor','r',...
    'MarkerFaceColor','r',...
    'MarkerSize',7);
hold on
plot(R./(5.842/2),Cd_Theory,'b','MarkerEdgeColor','b',...
    'MarkerFaceColor','b',...
    'MarkerSize',5,'LineWidth',2);

xlabel('{\itD/t}','FontSize',font_size, 'FontName', 'Times New Roman');
ylabel('{\itC_{D}}','FontSize',font_size, 'FontName', 'Times New Roman');
legend(strcat(['Current experimental data for {\itq = }',num2str(Q)]),'Theoretical results for
circular tube')

saveas(gcf,'Drag Coefficient_Q150.fig')
% axis([-2 2 0 11]);
% ********************************************
% CENTRICITY PLOT BEFORE AND AFTER THE SLOT REGION
figure(3)
hold on
% grid minor
set(3,'pos',[70 70 1200 800]);
set(gcf,'color','w');
set(gca,'fontsize',font_size);
errorbar(AverageDiameter3./5.84,Centricity3,std_Centricity3,'s','MarkerEdgeColor','r',...
    'MarkerFaceColor','r',...
    'MarkerSize',7,'LineWidth',line_width_size,'Color','k');
xlabel('{\itD_{e}/t}','FontSize',font_size, 'FontName', 'Times New Roman');
ylabel('Centricity, {\itC}','FontSize',font_size, 'FontName', 'Times New Roman');
legend(strcat(['Current experimental data for {\itq = }',num2str(Q)]))

% Saving the current figure in TIFF

saveas(gcf,'Centricity_Q150.fig')
% RE NUMBER PLOT FOR BEFORE AND AFTER THE SLOT REGIONS
figure(4);
hold on
% grid minor;
set(4,'pos',[70 70 1200 800]);
set(gcf,'color','w');
set(gca,'fontsize',font_size);
plot(AverageDiameter3./5.84,Re,'s','MarkerEdgeColor','r',...
    'MarkerFaceColor','r',...
    'MarkerSize',7);
xlabel('{\itD_{e}/w}','FontSize',font_size, 'FontName', 'Times New Roman');
ylabel('{\itRe}','FontSize',font_size, 'FontName', 'Times New Roman');
legend(strcat(['Current experimental data for {\itq = }',num2str(Q)]))
```

```
% Saving the current figure in TIFF

saveas(gcf,'Re_Q150.fig')
% ********************************************

% The parametrs for through the lsot region:
Q = 2.64; % Flux (V/A)
w = 3; % Slot/Flow cell width, mm
A = 5.842 * w;   % mm2
V_average = Q/A * (1/3600);
V_max = 0.003966;   % Maximum velocity in a laminar flow, [m/s]
Dh =  4*5.842*w/(2*(w + 5.842)); % [mm]

% b is equal to half diameter of the tube. Here, we assume that
% we have a hydrolic diameter and suppose "b" is half of that
b = Dh/2;
lambda = R./b;

% ************************************************

% Wall correction factors: k_1 and k_2:

% k_1: Wall correction factors for spheres within a circle condidering th wall
% effect
k_1 = ((1 - 0.75857.*(1 - sigma)./(1 + (2/3).*sigma)*lambda.^5))./ ...
    (1 - 2.1050.*(1 + (2/3).*sigma)./(1 + sigma).*lambda + ...
    2.0865.*(1./(1 + sigma).*lambda.^3)- ...
    1.7068.*((1 - (2/3).*sigma)./(1 + sigma).*lambda.^5)...
    + 0.72603.*(1 - sigma)./(1 + sigma).*lambda.^6);

% k_2: Wall correction factor for spheres within a circle, when there is a bulk flow

k_2 = (1 - (2/3).*(1./(1 + 2/3.*sigma)).*lambda.^2 - ...
    0.20217.*((1 - sigma)./(1 + 2/3.*sigma).*lambda.^5))./...
    (1 - 2.1050.*(1 + (2/3).*sigma)./(1 + sigma).*lambda + ...
    2.0865.*(1./(1 + sigma).*lambda.^3)- ...
    1.7068.*((1 - (2/3).*sigma)./(1 + sigma).*lambda.^5)...
    + 0.72603.*(1 - sigma)./(1 + sigma).*lambda.^6);
b = 3/2;
lambda = R./b;
k_w1Hirad = 1 + 2.*(sigma + 3/2)./(sigma + 1).*lambda.*1.338;

b = 5.842/2;
lambda = R./b;
k_w2Hirad = 1 + 2.*(sigma + 3/2)./(sigma + 1).*lambda.*1.338;

U = (((2/9).*((R.*0.001).^2.*g.*(density_fluid - density_particle).*(1 + sigma) ...
    ./(viscosity_fluid.*(k_w1Hirad.*k_w2Hirad).*(1 + (2/3).*sigma))))).*1000; % Terminal rising
velocity, [mm/s]
U_Haberman = (((2/9).*((R.*0.001).^2.*g.*(density_fluid - density_particle).*(1 + sigma) ...
    ./(viscosity_fluid.*(k_1).*(1 + (2/3).*sigma)))) + V_max.*k_2./(k_1)).*1000; % Terminal
rising velocity, [mm/s]
% Drag force calculation for the slot region
```

```
lambda_bubble = AverageDiameter3./Dh;
k_w = ((1 - 0.75857.*(1 - sigma)./(1 + (2/3).*sigma)*lambda_bubble.^5))./ ...
    (1 - 2.1050.*(1 + (2/3).*sigma)./(1 + sigma).*lambda_bubble + ...
    2.0865.*(1./(1 + sigma).*lambda_bubble.^3)- ...
    1.7068.*((1 - (2/3).*sigma)./(1 + sigma).*lambda_bubble.^5)...
    + 0.72603.*(1 - sigma)./(1 + sigma).*lambda_bubble.^6);
k_f = (1 - (2/3).*(1./(1 + 2/3.*sigma)).*lambda_bubble.^2 - ...
    0.20217.*((1 - sigma)./(1 + 2/3.*sigma).*lambda_bubble.^5))./...
    (1 - 2.1050.*(1 + (2/3).*sigma)./(1 + sigma).*lambda_bubble + ...
    2.0865.*(1./(1 + sigma).*lambda_bubble.^3)- ...
    1.7068.*((1 - (2/3).*sigma)./(1 + sigma).*lambda_bubble.^5)...
    + 0.72603.*(1 - sigma)./(1 + sigma).*lambda_bubble.^6);
Fd_Slot = pi.*g.*(0.001.*AverageDiameter3).^3.*(density_fluid - density_particle)/6;
Fd_Infinity_Slot = pi.*viscosity_fluid.*(0.001.*k_w.*RisingVelocity_Slot3-k_f.*V_max) ...
    .*(0.001.*AverageDiameter3).*(2 + 3/sigma)/(1 + 1/sigma);
Fd_Theory_Slot = 2.*pi.*viscosity_fluid.*(0.001.*R).*((2 + 3./sigma) ...
    ./(1 + 1./sigma)).*(0.001.*k_1.*U - k_2.*V_max);

% CENTRICITY PLOT THROUGH THE SLOT REGION
figure(5)
hold on
% grid minor
set(5,'pos',[70 70 1200 800]);
set(gcf,'color','w');
set(gca,'fontsize',font_size);
errorbar(AverageDiameter3./w,Centricity_Slot3,std_Centricity_Slot3,'s','MarkerEdgeColor','r',...
    'MarkerFaceColor','r',...
    'MarkerSize',7,'LineWidth',line_width_size,'Color','k');
xlabel('{\itD_{e}/w}','FontSize',font_size, 'FontName', 'Times New Roman');
ylabel('Centricity, {\itC}','FontSize',font_size, 'FontName', 'Times New Roman');
legend(strcat(['Current experimental data for {\itq = }',num2str(Q)]))

% Saving the current figure in TIFF

saveas(gcf,'Centricity_Slot_Q150.fig')
% ************************************************************************
% RE NUMBER PLOT FOR THROUGH THE SLOT REGIONS
figure(6);
hold on
set(6,'pos',[70 70 1200 800]);
set(gcf,'color','w');
set(gca,'fontsize',font_size);
plot(AverageDiameter3./w,Re_Slot,'s','MarkerEdgeColor','r',...
    'MarkerFaceColor','r',...
    'MarkerSize',7);
xlabel('{\itD_{e}/w}','FontSize',font_size, 'FontName', 'Times New Roman');
ylabel('{\itRe}','FontSize',font_size, 'FontName', 'Times New Roman');
legend(strcat(['Current experimental data for {\itq = }',num2str(Q)]))

% Saving the current figure in TIFF

saveas(gcf,'Re_Slot_Q150.fig')
% ************************************************************************
% AVERAGED RISING VELOCITY THROUGH THE SLOT
```

```
figure(7);
hold on
set(7,'pos',[70 70 1200 800]);
set(gcf,'color','w');
set(gca,'fontsize',font_size)
errorbar(AverageDiameter3./w, RisingVelocity_Slot3 -
V_max*1000,std_Velocity_Slot3,'s','MarkerEdgeColor','r',...
    'MarkerFaceColor','r',...
    'MarkerSize',7,'LineWidth',line_width_size,'Color','k');
hold on
plot(R./(w/2), U,'b','MarkerEdgeColor','k',...
    'MarkerFaceColor','k',...
    'MarkerSize',5,'LineWidth',2);
% grid minor
hold on

xlabel('{\itD_{e}/w}','FontSize',font_size,'FontName', 'Times New Roman');
ylabel('{\it V_{ave}} [mm/s]','FontSize',font_size,'FontName', 'Times New Roman');% figure(2);
legend(strcat(['Current experimental data for {\itq = }',num2str(Q)]),'Theoretical results for
circular tube (Haberman & Sayre 1958)')

% Saving the current figure in TIFF

saveas(gcf,'Rising Velocity_Not Modified_Slot_Q150.fig')
% ********************************************

% PLOTTING THE DRAG FORCE
figure(8);
hold on
% grid minor
set(8,'pos',[70 70 1200 800]);
set(gcf,'color','w');
set(gca,'fontsize',font_size)
Cd = (4/3*g*(density_fluid - density_particle)/density_fluid) ...
    .*(0.001.*AverageDiameter3)./((0.001.*RisingVelocity_Slot3 - V_max).^2);
Cd_Infinity = 8*(2 + 3/sigma)/(1 + 1/sigma)./Re_Slot;
Cd_Theory = viscosity_fluid.*(2 + 3/sigma)...
    /(1 + 1/sigma).*(4./((density_fluid*0.001.*R).*((k_1*0.001).*U - k_2.*V_max)));

plot(AverageDiameter3./w,Cd,'s','MarkerEdgeColor','r',...
    'MarkerFaceColor','r',...
    'MarkerSize',7);
hold on
plot(R./(w/2),Cd_Theory,'b','MarkerEdgeColor','b',...
    'MarkerFaceColor','b',...
    'MarkerSize',5,'LineWidth',2);

xlabel('{\itD/w}','FontSize',font_size, 'FontName', 'Times New Roman');
ylabel('{\itC_{D}}','FontSize',font_size, 'FontName', 'Times New Roman');
legend(strcat(['Current experimental data for {\itq = }',num2str(Q)]),'Theoretical results for
circular tube')

% Saving the current figure in TIFF
```

```
saveas(gcf,'Drag Coefficient_Slot_Q150.fig')

% Bubble rising velocity in infinity (no confinement)
U_Infinity = (((2/3).*((0.5.*AverageDiameter3.*0.001).^2.*g.*(density_fluid -
density_particle).*(1 + 1./sigma) ...
    ./(viscosity_fluid.*(2 + 3./sigma)))) + V_max).*1000;
```

Saving data files separately for each flow rate, and plotting all of data in one figure

```
       save('data150.mat','AverageDiameter3','RisingVelocity_Slot3','RisingVelocity3', ...
    'Centricity3','Centricity_Slot3','std_Velocity3','std_Velocity_Slot3', ...

'std_Centricity3','std_Centricity_Slot3','U_Infinity','v_max_Slot3','v_max_BeforeAfter3','Bubble_
Center3', ...
    'std_Diameter_Slot3','std_Diameter3')
close all
clear data
```

Q_1 data

```
       % Q = 20 ml/hr Flow Rate
Q = 0.05;
w = 22; % Slot/Flow cell width, mm
A = 5.842 * w;   % mm2
V_average = Q/A * (1/3600);
V_max = 0.000503*3/22;   % Maximum velocity in a laminar flow, [m/s]
Dh = 5.842;% 4*5.842*w/(2*(w + 5.842)), [mm]
% Dh = 2*(22 + 5.842)/pi;
b = Dh/2;  % b is equal to half diameter of the tube. Here, we assume that
% we have a hydrolic diameter and suppose "b" is half of that
lambda = R./b;
% Wall correction factors: k_1 and k_2:
% Wall correction factors for spheres within a circle, when particle is stationary
%
k_1 = ((1 - 0.75857.*(1 - sigma)./(1 + (2/3).*sigma)*lambda.^5))./ ...
    (1 - 2.1050.*(1 + (2/3).*sigma)./(1 + sigma).*lambda + ...
    2.0865.*(1./(1 + sigma).*lambda.^3)- ...
    1.7068.*((1 - (2/3).*sigma)./(1 + sigma).*lambda.^5)...
    + 0.72603.*(1 - sigma)./(1 + sigma).*lambda.^6);
```

```
% Wall correction factor for spheres within a circle, when there is a bulk flow
%
k_2 = (1 - (2/3).*(1./(1 + 2/3.*sigma)).*lambda.^2 - ...
    0.20217.*((1 - sigma)./(1 + 2/3.*sigma).*lambda.^5))./...
    (1 - 2.1050.*(1 + (2/3).*sigma)./(1 + sigma).*lambda + ...
    2.0865.*(1./(1 + sigma).*lambda.^3)- ...
    1.7068.*((1 - (2/3).*sigma)./(1 + sigma).*lambda.^5)...
    + 0.72603.*(1 - sigma)./(1 + sigma).*lambda.^6);

% ************************************************************************
% Correction factors for rise of air bubbles between two parallel plates
k_w1Hirad = (1 + 2.*(sigma + 3/2)./(sigma + 1).*lambda.*1.338);
U_Infinity = (((2/3).*((R.*0.001).^2.*g.*(density_fluid - density_particle).*(1 + 1./sigma) ...
    ./(viscosity_fluid.*(2 + 3./sigma))))).*1000;
% ************************************************************************

%Reading the data file
%begin
%%%%%%%%%%%%%%%%%%  Define Folders in which data files are  %%%%%%%%%%%%%%%%
% myFolder{1} = uigetdir;
myFolder{1} = 'X:\01_Current_Students\HIRAD SOLTANI\Publicaitons_HS\Journal Papers\Paper 1\Bubble
Zoomout_February 23\Q20\';

for RunFolder_counter = 1:1;
    if ~isdir(myFolder{RunFolder_counter})
        errorMessage = sprintf('Error: The following folder does not exist:\n%s',
myFolder{RunFolder_counter});
        uiwait(warndlg(errorMessage));
        return;
    end
    filePattern = fullfile(myFolder{RunFolder_counter}, '*.csv');
    logFiles = dir(filePattern);

    for k = 1:length(logFiles)

        baseFileName = logFiles(k).name;
        fullFileName = fullfile(myFolder{RunFolder_counter}, baseFileName);
        %fprintf(1, 'Now reading %s\n', fullFileName);
        fileID = fopen(fullFileName);
        %   date_time = textscan(fileID,'Date %s Time %s','HeaderLines',1);
        %   column_headers = textscan(fileID,'%s',41,'delimiter', '\t');
        column_headers  = regexp(fgetl(fileID ),';','split');

        counter =1;
        while (~feof(fileID))
            [data,position] = textscan(fileID,'%s',10,'delimiter', ';');
            real_data{counter,:} = data;
            counter = counter + 1;
        end
        counter = counter - 2;
        fclose(fileID);
        for row_number = 1 : counter
            subcounter = 1;
            temp = real_data{row_number,1}{1,1};
```

```
            for column_number = 1 : 10
                %             if  (~isnan(temp(column_number)))
                data(row_number,subcounter) = temp(column_number);
                final_data_cell{row_number+1,subcounter} = temp(column_number);

                subcounter = subcounter + 1;
                %             end
            end
        end
        final_data_cell = cellfun( @(x) str2double(strrep(x, ',', '.')), final_data_cell,
'uniformoutput', false);
        data = cell2mat(final_data_cell);
        final_data_cell(1,:) = column_headers;
        [r,c] = size(data);
        % define time interval between every two frames
        time_stamp = 1/8;
                % ********************************************************************
        % Since some of the data are collected in another experiment, they
        % should be consistent with other data. So the x and y information
        % of all images (calibration) are tried to be the same in this
        % section
        if isequal(baseFileName,'ParticleList2027.csv')
            data(:,2) = data(:,2) + 4;
            data(:,1) = data(:,1) -3.8;
        end
        if isequal(baseFileName,'ParticleList2026.csv')
            data(:,2) = data(:,2) + 4;
            data(:,1) = data(:,1) -3.8;
            data(128:297,1) = 13.0598;
            data(128:297,2) = data(128:297,2) - 0.1;
        end
        % ********************************************************************
        data (4:r,7)= (data (4:r,1)-data (2:r-2,1))/(2*time_stamp);
        data (4:r,8)= (data (4:r,2)-data (2:r-2,2))/(2*time_stamp);
        data (4:r,9)= sqrt(data (4:r,7).^2 + data (4:r,8).^2);

        % Uncertainty and averaging the risintg velocity and bubble diameter

        % Before the slot region:
        p = max(find(data(:,2) < -12));
        RisingVelocity1 = nanmean(data(1:p,9));
        AverageDiameter1 = nanmean(data(1:p,4));
        Centricity1 = nanmean(data(1:p,3));
        std_Velocity1 = nanstd(data(1:p,9));
        std_Centricity1 = nanstd(data(1:p,3));
        std_Diameter1 = nanstd(data(1:p,4));

        % After the slot region
        m = min(find(data(:,2) > 17));
        RisingVelocity2 = nanmean(data(m:end,9));
        AverageDiameter2 = nanmean(data(m:end,4));
        Centricity2 = nanmean(data(m:end,3));
        std_Velocity2 = nanstd(data(m:end,9));
        std_Centricity2 = nanstd(data(m:end,3));
```

```
        std_Diameter2 = nanstd(data(m:end,4));

        % The average data for before and after the slot regions
        RisingVelocity(k) = (p*RisingVelocity1 + m*RisingVelocity2)/(m + p);
        AverageDiameter(k) = (p*AverageDiameter1 + m*AverageDiameter2)/(m + p);
        Centricity(k) = (p*Centricity1 + m*Centricity2)/(m + p);
        std_Velocity(k) = (p*std_Velocity1 + m*std_Velocity2)/(m + p);
        std_Centricity(k) = (p*std_Centricity1 + m*std_Centricity2)/(m + p);
        std_Diameter(k) = (p*std_Diameter1 + m*std_Diameter2)/(m + p);

        % In the slot region
        s1 = find(data(:,2) > -2, 1 );
        s2 = max(find(data(:,2) < 8.7));
        RisingVelocity_Slot(k) = nanmean(data(s1:s2,9));
        Centricity_Slot(k) = nanmean(data(s1:s2,3));
        std_Velocity_Slot(k) = nanstd(data(s1:s2,9));
        std_Centricity_Slot(k) = nanstd(data(s1:s2,3));
        std_Diameter_Slot(k) = nanstd(data(s1:s2,3));

        % X position of center of the bubble
        Bubble_Center(k) = nanmean(data(s1:s2,1));

        % Maximum velocity in the regions before and after the slot
        v_max_BeforeAfter(k) = max([data(m:end,9);data(1:p,9)]);
        % Maximum velocity through the slot
        v_max_Slot(k) = max(data(s1:s2,9));
        %*************************************************************************
        % Uncertainty of rising velocity in before and after the slot regions

        sortedVelocity(1:p,1) = data(1:p,9);
        sortedVelocity(p+1:size(data,1)-m+p+1,1) = data(m:end,9);
        Sx = 0;
        a = find(isnan(sortedVelocity(:,:)));
        sortedVelocity(a) = [];
        for i = 1:size(sortedVelocity,1)
            Sx = (sortedVelocity(i,1) - RisingVelocity(k)).^2./(length(logFiles)-1) + Sx;
        end
        Sx = Sx^0.5;
        P_xbar(k) = 2*Sx/length(logFiles)^0.5;
        %*************************************************************************
        % Uncertainty through the slot
        sortedVelocity_Slot = data(s1:s2,9);
        Sx_Slot = 0;
        b = find(isnan(sortedVelocity_Slot(:,:)));
        sortedVelocity_Slot(b) = [];
        for i = 1:size(sortedVelocity_Slot,1)
            Sx_Slot = (sortedVelocity_Slot(i,1) -
RisingVelocity_Slot(k)).^2./(size(sortedVelocity_Slot,1)) + Sx_Slot;
        end
        Sx_Slot = Sx_Slot^0.5;
        P_xbar_Slot(k) = 2*Sx_Slot/(size(sortedVelocity_Slot,1)^0.5);


        % For the 3D plot of instantaneous rising velocity, the data of all flow
```

```
        % rates should be stored (Rising velocity and Diameter data)
        if AverageDiameter(k) < 0.9
            Velocity_3D_20_min = data(:,9);
            Diameter_3D_20_min = data(:,2)/15 - 0.25;
        end
        if AverageDiameter(k) > 2.8
            Velocity_3D_20_max = data(:,9);
            Diameter_3D_20_max = data(:,2)/15 - 0.25;
        end

    end
end
% Organizing the dimeter and velocity data.
AverageDiameter3 = sort(AverageDiameter);
[r,c] = size(AverageDiameter);
RisingVelocity3 = zeros(r,c);
RisingVelocity_Slot3 = zeros(r,c);
Centricity3 = zeros(r,c);
Centricity_Slot3 = zeros(r,c);
std_Velocity3 = zeros(r,c);
std_Velocity_Slot3 = zeros(r,c);
std_Centricity3 = zeros(r,c);
std_Centricity_Slot3 = zeros(r,c);
v_max_BeforeAfter3 = zeros(r,c);
v_max_Slot3 = zeros(r,c);
Bubble_Center3 = zeros(r,c);
std_Diameter3 = zeros(r,c);
std_Diameter_Slot3 = zeros(r,c);
i = 1;
for i = 1:c
    j = find(AverageDiameter3 == AverageDiameter(1,i));
    RisingVelocity3(1,j) = RisingVelocity(1,i);
    RisingVelocity_Slot3(1,j) = RisingVelocity_Slot(1,i);
    Centricity3(1,j) = Centricity(1,i);
    Centricity_Slot3(1,j) = Centricity_Slot(1,i);
    std_Velocity3(1,j) = std_Velocity(1,i);
    std_Velocity_Slot3(1,j) = std_Velocity_Slot(1,i);
    std_Centricity3(1,j) = std_Centricity(1,i);
    std_Centricity_Slot3(1,j) = std_Centricity_Slot(1,i);
    std_Diameter3(1,j) = std_Diameter(1,i);
    std_Diameter_Slot3(1,j) = std_Diameter_Slot(1,i);
    v_max_BeforeAfter3(1,j) = v_max_BeforeAfter(1,i);
    v_max_Slot3(1,j) = v_max_Slot(1,i);
    Bubble_Center3(1,j) = Bubble_Center(1,i);
    i = i + 1;
end

% Reynolds number for each bubble
Re = ((density_fluid.*((0.001.*RisingVelocity3) -
V_max)).*(0.001.*AverageDiameter3))./viscosity_fluid;
Re_Slot = ((density_fluid.*((0.001.*RisingVelocity_Slot3) -
V_max*22/3)).*(0.001.*AverageDiameter3))./viscosity_fluid;
% The terminal velocity through the slot
% the purpose of this section is to check how close the rising velocity is
```

```
% to theoretical terminal velocity
figure(1);
hold on
set(1,'pos',[70 70 1200 800]);
set(gcf,'color','w');
set(gca,'fontsize',font_size)
U = (((2/9).*((R.*0.001).^2.*g.*(density_fluid - density_particle).*(1 + sigma) ...
    ./(viscosity_fluid.*k_w1Hirad.*(1 + (2/3).*sigma))))).*1000; % Terminal rising velocity,
[mm/s]

plot(AverageDiameter3./5.842, RisingVelocity3 - 1000*V_max,'s','MarkerEdgeColor','r',...
    'MarkerFaceColor','r',...
    'MarkerSize',7);
hold on
plot(R./(5.842/2), U_Infinity,'k--','MarkerEdgeColor','b',...
    'MarkerFaceColor','b',...
    'MarkerSize',5,'LineWidth',2);
% grid minor
hold on
plot(R./(5.842/2), U,'b','MarkerEdgeColor','b',...
    'MarkerFaceColor','b',...
    'MarkerSize',5,'LineWidth',2);
% errorbar(AverageDiameter3./5.842, RisingVelocity3 -
1000*V_max,std_Velocity3,'s','MarkerEdgeColor','r',...
%     'MarkerFaceColor','r',...
%     'MarkerSize',7,'LineWidth',line_width_size,'Color','k');
xlabel('{\itD_{e}/t}','FontSize',font_size,'FontName', 'Times New Roman');
ylabel('{\itV_{b} - V_{f}} [mm/s]','FontSize',font_size,'FontName', 'Times New Roman');%
figure(2);
legend('Theoretical results for parallel plates (Shapira and Haber 1988)', ...
    'Theoretical results for infinite medium',strcat(['Current experimental data for {\itq =
}',num2str(Q)]))
%  [lgd, icons, plots, txt] = legend('Theoretical results for parallel plates (Shapira and Haber
1988)', ...
%      'Theoretical results for infinite medium','Current experimental data')

% Saving the current figure in TIFF and EPS format

% saveas(gcf,'Rising Velocity_Not Modified_Q20.eps')
saveas(gcf,'Rising Velocity_Not Modified_Q20.fig')
% ***********************************************
figure(2);
hold on
% grid minor
set(2,'pos',[70 70 1200 800]);
set(gcf,'color','w');
set(gca,'fontsize',font_size)
Cd = (4/3*g*(density_fluid - density_particle)/density_fluid) ...
    .*(0.001.*AverageDiameter3)./((0.001.*RisingVelocity3 - V_max).^2);
Cd_Infinity = 8*(2 + 3/sigma)/(1 + 1/sigma)./Re;
Cd_Theory = viscosity_fluid.*(2 + 3/sigma)...
    /(1 + 1/sigma).*(4./((density_fluid*0.001.*R).*((k_1*0.001).*U - k_2.*V_max)));

plot(AverageDiameter3./5.842,Cd,'s','MarkerEdgeColor','r',...
```

```
    'MarkerFaceColor','r',...
    'MarkerSize',7);
hold on
plot(R./(5.842/2),Cd_Theory,'b','MarkerEdgeColor','b',...
    'MarkerFaceColor','b',...
    'MarkerSize',5,'LineWidth',2);

xlabel('{\itD/t}','FontSize',font_size, 'FontName', 'Times New Roman');
ylabel('{\itC_{D}}','FontSize',font_size, 'FontName', 'Times New Roman');
legend(strcat(['Current experimental data for {\itq = }',num2str(Q)]),'Theoretical results for
circular tube')

% Saving the current figure in TIFF and EPS format
% saveas(gcf,'Drag Coefficient_Q20.eps')
saveas(gcf,'Drag Coefficient_Q20.fig')
% axis([-2 2 0 11]);
% ******************************************
% CENTRICITY PLOT BEFORE AND AFTER THE SLOT REGION
figure(3)
hold on
% grid minor
set(3,'pos',[70 70 1200 800]);
set(gcf,'color','w');
set(gca,'fontsize',font_size);
errorbar(AverageDiameter3./5.84,Centricity3,std_Centricity3,'s','MarkerEdgeColor','r',...
    'MarkerFaceColor','r',...
    'MarkerSize',7,'LineWidth',line_width_size,'Color','k');
xlabel('{\itD_{e}/t}','FontSize',font_size, 'FontName', 'Times New Roman');
ylabel('Centricity, {\itC}','FontSize',font_size, 'FontName', 'Times New Roman');
legend(strcat(['Current experimental data for {\itq = }',num2str(Q)]))

% Saving the current figure in TIFF and EPS format

% saveas(gcf,'Centricity_Q20.eps')
saveas(gcf,'Centricity_Q20.fig')

% RE NUMBER PLOT FOR BEFORE AND AFTER THE SLOT REGIONS
figure(4);
hold on
% grid minor;
set(4,'pos',[70 70 1200 800]);
set(gcf,'color','w');
set(gca,'fontsize',font_size);
plot(AverageDiameter3./5.84,Re,'s','MarkerEdgeColor','r',...
    'MarkerFaceColor','r',...
    'MarkerSize',7);
xlabel('{\itD_{e}/w}','FontSize',font_size, 'FontName', 'Times New Roman');
ylabel('{\itRe}','FontSize',font_size, 'FontName', 'Times New Roman');
legend(strcat(['Current experimental data for {\itq = }',num2str(Q)]))

% Saving the current figure in TIFF and EPS format

% saveas(gcf,'Re_Q20.eps')
saveas(gcf,'Re_Q20.fig')
```

```
% ******************************************
% Calculating the parameters through the slot
Q = 0.34; % Flux (V/A)
w = 3; % Slot/Flow cell width, mm
A = 5.842 * w;   % mm2
V_average = Q/A * (1/3600);
V_max = 0.000503;   % Maximum velocity in a laminar flow, [m/s]
Dh =  4*5.842*w/(2*(w + 5.842)); % [mm]
b = Dh/2;  % b is equal to half diameter of the tube. Here, we assume that
% we have a hydrolic diameter and suppose "b" is half of that
lambda = R./b;

% ************************************************

% Wall correction factors: k_1 and k_2:
% Wall correction factors for spheres within a circle, when particle is stationary
%
k_1 = ((1 - 0.75857.*(1 - sigma)./(1 + (2/3).*sigma)*lambda.^5))./ ...
    (1 - 2.1050.*(1 + (2/3).*sigma)./(1 + sigma).*lambda + ...
    2.0865.*(1./(1 + sigma).*lambda.^3)- ...
    1.7068.*((1 - (2/3).*sigma)./(1 + sigma).*lambda.^5)...
    + 0.72603.*(1 - sigma)./(1 + sigma).*lambda.^6);


% Wall correction factor for spheres within a circle, when there is a bulk flow
%
k_2 = (1 - (2/3).*(1./(1 + 2/3.*sigma)).*lambda.^2 - ...
    0.20217.*((1 - sigma)./(1 + 2/3.*sigma).*lambda.^5))./...
    (1 - 2.1050.*(1 + (2/3).*sigma)./(1 + sigma).*lambda + ...
    2.0865.*(1./(1 + sigma).*lambda.^3)- ...
    1.7068.*((1 - (2/3).*sigma)./(1 + sigma).*lambda.^5)...
    + 0.72603.*(1 - sigma)./(1 + sigma).*lambda.^6);
b = 3/2;
lambda = R./b;
k_w1Hirad = (1 + 2.*(sigma + 3/2)./(sigma + 1).*lambda.*1.338);

b = 5.842/2;
lambda = R./b;
k_w2Hirad = (1 + 2.*(sigma + 3/2)./(sigma + 1).*lambda.*1.338);

U = (((2/9).*((R.*0.001).^2.*g.*(density_fluid - density_particle).*(1 + sigma) ...
    ./(viscosity_fluid.*(k_w1Hirad.*k_w2Hirad).*(1 + (2/3).*sigma))))).*1000; % Terminal rising
velocity, [mm/s]
U_Haberman = (((2/9).*((R.*0.001).^2.*g.*(density_fluid - density_particle).*(1 + sigma) ...
    ./(viscosity_fluid.*(k_1).*(1 + (2/3).*sigma)))) + V_max.*k_2./(k_1)).*1000; % Terminal
rising velocity, [mm/s]
% U = (((2/9).*((R.*0.001).^2.*g.*(density_fluid - density_particle).*(1 + sigma) ...
%     ./(viscosity_fluid.*k_1.*(1 + (2/3).*sigma)))) + V_max.*k_2./k_1).*1000; % Terminal rising
velocity, [mm/s]
% CENTRICITY PLOT THROUGH THE SLOT REGION
figure(5)
hold on
% grid minor
```

```
set(5,'pos',[70 70 1200 800]);
set(gcf,'color','w');
set(gca,'fontsize',font_size);
errorbar(AverageDiameter3./w,Centricity_Slot3,std_Centricity_Slot3,'s','MarkerEdgeColor','r',...
    'MarkerFaceColor','r',...
    'MarkerSize',7,'LineWidth',line_width_size,'Color','k');
xlabel('{\itD_{e}/w}','FontSize',font_size, 'FontName', 'Times New Roman');
ylabel('Centricity, {\itC}','FontSize',font_size, 'FontName', 'Times New Roman');
legend(strcat(['Current experimental data for {\itq = }',num2str(Q)]))

% Saving the current figure in TIFF and EPS format

% saveas(gcf,'Centricity_Slot_Q20.eps')
saveas(gcf,'Centricity_Slot_Q20.fig')
% RE NUMBER PLOT FOR THROUGH THE SLOT REGIONS
figure(6);
hold on
% grid minor;
set(6,'pos',[70 70 1200 800]);
set(gcf,'color','w');
set(gca,'fontsize',font_size);
plot(AverageDiameter3./w,Re_Slot,'s','MarkerEdgeColor','r',...
    'MarkerFaceColor','r',...
    'MarkerSize',7);
xlabel('{\itD_{e}/w}','FontSize',font_size, 'FontName', 'Times New Roman');
ylabel('{\itRe}','FontSize',font_size, 'FontName', 'Times New Roman');
legend(strcat(['Current experimental data for {\itq = }',num2str(Q)]))

% Saving the current figure in TIFF and EPS format

% saveas(gcf,'Re_Slot_Q20.eps')
saveas(gcf,'Re_Slot_Q20.fig')
% AVERAGED RISING VELOCITY THROUGH THE SLOT
figure(7);
hold on
set(7,'pos',[70 70 1200 800]);
set(gcf,'color','w');
set(gca,'fontsize',font_size)
% errorbar(AverageDiameter3./w, RisingVelocity_Slot3 -
V_max*1000,std_Velocity_Slot3,'s','MarkerEdgeColor','r',...
%     'MarkerFaceColor','r',...
%     'MarkerSize',7,'LineWidth',line_width_size,'Color','k');
plot(AverageDiameter3./w, RisingVelocity_Slot3 - V_max*1000,'s','MarkerEdgeColor','r',...
    'MarkerFaceColor','r',...
    'MarkerSize',7);
hold on
plot(R./(w/2), U_Infinity,'k--','MarkerEdgeColor','k',...
    'MarkerFaceColor','k',...
    'MarkerSize',5,'LineWidth',2);
hold on
plot(R./(w/2), U,'b','MarkerEdgeColor','k',...
    'MarkerFaceColor','k',...
    'MarkerSize',5,'LineWidth',2);
% grid minor
```

```
xlabel('{\itD_{e}/w}','FontSize',font_size,'FontName', 'Times New Roman');
ylabel('{\it V_{b-Slot} - V_{f-Slot}} [mm/s]','FontSize',font_size,'FontName', 'Times New
Roman');% figure(2);
legend(strcat(['Current experimental data for {\itq = }',num2str(Q)]), 'Theoretical results for
infinite medium', ...
    'Theoretical results for parallel plates (Shapira and Haber 1988)')

% Saving the current figure in TIFF and EPS format

% saveas(gcf,'Rising Velocity_Not Modified_Slot_Q20.eps')
saveas(gcf,'Rising Velocity_Not Modified_Slot_Q20.fig')
% ********************************************

% PLOTTING THE DRAG FORCE
figure(8);
hold on
% grid minor
set(8,'pos',[70 70 1200 800]);
set(gcf,'color','w');
set(gca,'fontsize',font_size)
Cd = (4/3*g*(density_fluid - density_particle)/density_fluid) ...
    .*(0.001.*AverageDiameter3)./((0.001.*RisingVelocity_Slot3 - V_max).^2);
Cd_Infinity = 8*(2 + 3/sigma)/(1 + 1/sigma)./Re_Slot;
Cd_Theory = viscosity_fluid.*(2 + 3/sigma)...
    /(1 + 1/sigma).*(4./((density_fluid*0.001.*R).*((k_1*0.001).*U - k_2.*V_max)));

plot(AverageDiameter3./w,Cd,'s','MarkerEdgeColor','r',...
    'MarkerFaceColor','r',...
    'MarkerSize',7);
hold on
plot(R./(w/2),Cd_Theory,'b','MarkerEdgeColor','b',...
    'MarkerFaceColor','b',...
    'MarkerSize',5,'LineWidth',2);

xlabel('{\itD/w}','FontSize',font_size, 'FontName', 'Times New Roman');
ylabel('{\itC_{D}}','FontSize',font_size, 'FontName', 'Times New Roman');
legend(strcat(['Current experimental data for {\itq = }',num2str(Q)]),'Theoretical results for
circular tube')

% Saving the current figure in TIFF and EPS format

% saveas(gcf,'Drag Coefficient_Slot_Q20.eps')
saveas(gcf,'Drag Coefficient_Slot_Q20.fig')
% axis([-2 2 0 11]);
% ************************************************************************
figure(9);
hold on
% grid minor
set(gcf,'pos',[70 70 1200 800]);
set(gcf,'color','w');
set(gca,'fontsize',font_size)

% Distance between the center of bubble to the closest slot wall
```

```
h = ((w/2) - abs(Bubble_Center3 - 12.5));
plot(AverageDiameter3./w,(h./w),'s','MarkerEdgeColor','r',...
    'MarkerFaceColor','r',...
    'MarkerSize',7);
xlabel('{\itD_{e}/w}','FontSize',font_size, 'FontName', 'Times New Roman');
ylabel('{\ith/w}','FontSize',font_size, 'FontName', 'Times New Roman');
legend(strcat(['Current experimental data for {\itq = }',num2str(Q)]));
axis([0.2 1.5 0 0.5])
saveas(gcf,'Bubble Center_Q20.fig')
% ************************************************************************
% Bubble rising velocity in infinity (no confinement)
U_Infinity = (((2/3).*((0.5.*AverageDiameter3.*0.001).^2.*g.*(density_fluid -
density_particle).*(1 + 1./sigma) ...
    ./(viscosity_fluid.*(2 + 3./sigma)))) + V_max).*1000;
```

Saving data files separately for each flow rate, and plotting all of data in one figure

```
       save('data20.mat','AverageDiameter3','RisingVelocity_Slot3','RisingVelocity3', ...
    'Centricity3','Centricity_Slot3','std_Velocity3','std_Velocity_Slot3' ...

,'std_Centricity3','std_Centricity_Slot3','U_Infinity','v_max_Slot3','v_max_BeforeAfter3','Bubble
_Center3', ...
    'std_Diameter_Slot3','std_Diameter3')
close all
clear data
```

Q_4 data

```
       Q = 0.24;
w = 22; % Slot/Flow cell width, mm
A = 5.842 * w;   % mm2
V_average = Q/A * (1/3600);
V_max = 0.00267*3/22;   % Maximum velocity in a laminar flow, [m/s]
Dh = 5.842;% 4*5.842*w/(2*(w + 5.842)), [mm]
% Dh = 2*(22 + 5.842)/pi;
b = Dh/2;  % b is equal to half diameter of the tube. Here, we assume that
% we have a hydrolic diameter and suppose "b" is half of that
lambda = R./b;
% Wall correction factors: k_1 and k_2:
% Wall correction factors for spheres within a circle, when particle is stationary
```

```
%
k_1 = ((1 - 0.75857.*(1 - sigma)./(1 + (2/3).*sigma)*lambda.^5))./ ...
    (1 - 2.1050.*(1 + (2/3).*sigma)./(1 + sigma).*lambda + ...
    2.0865.*(1./(1 + sigma).*lambda.^3)- ...
    1.7068.*((1 - (2/3).*sigma)./(1 + sigma).*lambda.^5)...
    + 0.72603.*(1 - sigma)./(1 + sigma).*lambda.^6);


% Wall correction factor for spheres within a circle, when there is a bulk flow
%
k_2 = (1 - (2/3).*(1./(1 + 2/3.*sigma)).*lambda.^2 - ...
    0.20217.*((1 - sigma)./(1 + 2/3.*sigma).*lambda.^5))./...
    (1 - 2.1050.*(1 + (2/3).*sigma)./(1 + sigma).*lambda + ...
    2.0865.*(1./(1 + sigma).*lambda.^3)- ...
    1.7068.*((1 - (2/3).*sigma)./(1 + sigma).*lambda.^5)...
    + 0.72603.*(1 - sigma)./(1 + sigma).*lambda.^6);
% ************************************************************************
% Correction factors for rise of air bubbles between two parallel plates
k_w1Hirad = (1 + 2.*(sigma + 3/2)./(sigma + 1).*lambda.*1.338);
U_Infinity = (((2/3).*((R.*0.001).^2.*g.*(density_fluid - density_particle).*(1 + 1./sigma) ...
    ./(viscosity_fluid.*(2 + 3./sigma))))).*1000;
% ************************************************************************

% Reading the data file
%begin
%%%%%%%%%%%%%%%%%%%  Define Folders in which data files are  %%%%%%%%%%%%%%%%%
% myFolder{1} = uigetdir;
myFolder{4} = 'X:\01_Current_Students\HIRAD SOLTANI\Publicaitons_HS\Journal Papers\Paper 1\Bubble
Zoomout_February 23\Q100\';

for RunFolder_counter = 4;
    if ~isdir(myFolder{RunFolder_counter})
        errorMessage = sprintf('Error: The following folder does not exist:\n%s',
myFolder{RunFolder_counter});
        uiwait(warndlg(errorMessage));
        return;
    end
    filePattern = fullfile(myFolder{RunFolder_counter}, '*.csv');
    logFiles = dir(filePattern);

    for k = 1:length(logFiles)

        baseFileName = logFiles(k).name;
        fullFileName = fullfile(myFolder{RunFolder_counter}, baseFileName);
        %fprintf(1, 'Now reading %s\n', fullFileName);
        fileID = fopen(fullFileName);
        %   date_time = textscan(fileID,'Date %s Time %s','HeaderLines',1);
        %   column_headers = textscan(fileID,'%s',41,'delimiter', '\t');
        column_headers  = regexp(fgetl(fileID ),';','split');

        counter =1;
        while (~feof(fileID))
            [data,position] = textscan(fileID,'%s',10,'delimiter', ';');
            real_data{counter,:} = data;
```

```
            counter = counter + 1;
        end
        counter = counter - 2;
        fclose(fileID);
        for row_number = 1 : counter
            subcounter = 1;
            temp = real_data{row_number,1}{1,1};
            for column_number = 1 : 10
                %             if  (~isnan(temp(column_number)))
                data(row_number,subcounter) = temp(column_number);
                final_data_cell{row_number+1,subcounter} = temp(column_number);

                subcounter = subcounter + 1;
                %             end
            end
        end
        final_data_cell = cellfun( @(x) str2double(strrep(x, ',', '.')), final_data_cell,
'uniformoutput', false);
        data = cell2mat(final_data_cell);
        final_data_cell(1,:) = column_headers;
        [r,c] = size(data);
        % define time interval between every two frames
        time_stamp = 1/8;

        data (4:r,7)= (data (4:r,1)-data (2:r-2,1))/(2*time_stamp);
        data (4:r,8)= (data (4:r,2)-data (2:r-2,2))/(2*time_stamp);
        data (4:r,9)= sqrt(data (4:r,7).^2 + data (4:r,8).^2);

%         % For the 3D plot of instantaneous rising velocity, the data of all flow
%         % rates should be stored (Rising velocity and Diameter data)
%         if data(10,4) < 1.3
%             Velocity_3D_100 = data(:,9);
%             Diameter_3D_100 = data(:,2)/15 - 0.25;
%         end


        % Uncertainty and averaging the risintg velocity and bubble diameter
        % Before the slot region
        p = max(find(data(:,2) < -12));
        RisingVelocity1 = nanmean(data(1:p,9));
        AverageDiameter1 = nanmean(data(1:p,4));
        Centricity1 = nanmean(data(1:p,3));
        std_Velocity1 = nanstd(data(1:p,9));
        std_Centricity1 = nanstd(data(1:p,3));
        std_Diameter1 = nanstd(data(1:p,4));

        % After the slot region
        m = min(find(data(:,2) > 17));
        RisingVelocity2 = nanmean(data(m:end,9));
        AverageDiameter2 = nanmean(data(m:end,4));
        Centricity2 = nanmean(data(m:end,3));
        std_Velocity2 = nanstd(data(m:end,9));
        std_Centricity2 = nanstd(data(m:end,3));
        std_Diameter2 = nanstd(data(m:end,4));
```

```
        % The average data for before and after the slot regions
        RisingVelocity(k) = (p*RisingVelocity1 + m*RisingVelocity2)/(m + p);
        AverageDiameter(k) = (p*AverageDiameter1 + m*AverageDiameter2)/(m + p);
        Centricity(k) = (p*Centricity1 + m*Centricity2)/(m + p);
        std_Velocity(k) = (p*std_Velocity1 + m*std_Velocity2)/(m + p);
        std_Centricity(k) = (p*std_Centricity1 + m*std_Centricity2)/(m + p);
        std_Diameter(k) = (p*std_Diameter1 + m*std_Diameter2)/(m + p);

        % In the slot region
        s1 = min(find(data(:,2) > -2));
        s2 = max(find(data(:,2) < 8.7));
        RisingVelocity_Slot(k) = nanmean(data(s1:s2,9));
        Centricity_Slot(k) = nanmean(data(s1:s2,3));
        std_Velocity_Slot(k) = nanstd(data(s1:s2,9));
        std_Centricity_Slot(k) = nanstd(data(s1:s2,3));
        std_Diameter_Slot(k) = nanstd(data(s1:s2,3));

        % X position of center of the bubble
        Bubble_Center(k) = nanmean(data(s1:s2,1));

        % Maximum velocity in the regions before and after the slot
        v_max_BeforeAfter(k) = max([data(m:end,9);data(1:p,9)]);
        % Maximum velocity through the slot
        v_max_Slot(k) = max(data(s1:s2,9));
        %*************************************************************************
        % Uncertainty of rising velocity in before and after the slot regions

        sortedVelocity(1:p,1) = data(1:p,9);
        sortedVelocity(p+1:size(data,1)-m+p+1,1) = data(m:end,9);
        Sx = 0;
        a = find(isnan(sortedVelocity(:,:)));
        sortedVelocity(a) = [];
        for i = 1:size(sortedVelocity,1)
            Sx = (sortedVelocity(i,1) - RisingVelocity(k)).^2./(length(logFiles)-1) + Sx;
        end
        Sx = Sx^0.5;
        P_xbar(k) = 2*Sx/length(logFiles)^0.5;
        %*************************************************************************
        % Uncertainty through the slot
        sortedVelocity_Slot = data(s1:s2,9);
        Sx_Slot = 0;
        b = find(isnan(sortedVelocity_Slot(:,:)));
        sortedVelocity_Slot(b) = [];
        for i = 1:size(sortedVelocity_Slot,1)
            Sx_Slot = (sortedVelocity_Slot(i,1) -
RisingVelocity_Slot(k)).^2./(size(sortedVelocity_Slot,1)) + Sx_Slot;
        end
        Sx_Slot = Sx_Slot^0.5;
        P_xbar_Slot(k) = 2*Sx_Slot/(size(sortedVelocity_Slot,1)^0.5);
        % End of reading data file for RUN 1

                % For the 3D plot of instantaneous rising velocity, the data of all flow
        % rates should be stored (Rising velocity and Diameter data)
```

```
        if AverageDiameter(k) < 1.2
            Velocity_3D_100_min = data(:,9);
            Diameter_3D_100_min = data(:,2)/15 - 0.25;
        end
        if AverageDiameter(k) > 3
            Velocity_3D_100_max = data(:,9);
            Diameter_3D_100_max = data(:,2)/15 - 0.25;
        end
    end
end
% Organizing the dimeter and velocity data.
AverageDiameter3 = sort(AverageDiameter);
[r,c] = size(AverageDiameter);
RisingVelocity3 = zeros(r,c);
RisingVelocity_Slot3 = zeros(r,c);
Centricity3 = zeros(r,c);
Centricity_Slot3 = zeros(r,c);
std_Velocity3 = zeros(r,c);
std_Velocity_Slot3 = zeros(r,c);
std_Centricity3 = zeros(r,c);
std_Centricity_Slot3 = zeros(r,c);
v_max_BeforeAfter3 = zeros(r,c);
v_max_Slot3 = zeros(r,c);
Bubble_Center3 = zeros(r,c);
std_Diameter3 = zeros(r,c);
std_Diameter_Slot3 = zeros(r,c);
i = 1;
for i = 1:c
    j = find(AverageDiameter3 == AverageDiameter(1,i));
    RisingVelocity3(1,j) = RisingVelocity(1,i);
    RisingVelocity_Slot3(1,j) = RisingVelocity_Slot(1,i);
    Centricity3(1,j) = Centricity(1,i);
    Centricity_Slot3(1,j) = Centricity_Slot(1,i);
    std_Velocity3(1,j) = std_Velocity(1,i);
    std_Velocity_Slot3(1,j) = std_Velocity_Slot(1,i);
    std_Centricity3(1,j) = std_Centricity(1,i);
    std_Centricity_Slot3(1,j) = std_Centricity_Slot(1,i);
    std_Diameter3(1,j) = std_Diameter(1,i);
    std_Diameter_Slot3(1,j) = std_Diameter_Slot(1,i);
    v_max_BeforeAfter3(1,j) = v_max_BeforeAfter(1,i);
    v_max_Slot3(1,j) = v_max_Slot(1,i);
    Bubble_Center3(1,j) = Bubble_Center(1,i);
    i = i + 1;
end

% Reynolds number for each bubble
Re = ((density_fluid.*((0.001.*RisingVelocity3) -
V_max)).*(0.001.*AverageDiameter3))./viscosity_fluid;
Re_Slot = ((density_fluid.*((0.001.*RisingVelocity_Slot3) -
V_max*22/3)).*(0.001.*AverageDiameter3))./viscosity_fluid;
% The terminal velocity through the slot
% the purpose of this section is to check how close the rising velocity is
% to theoretical terminal velocity
figure(1);
```

```
hold on
set(1,'pos',[70 70 1200 800]);
set(gcf,'color','w');
set(gca,'fontsize',font_size)
U = (((2/9).*((R.*0.001).^2.*g.*(density_fluid - density_particle).*(1 + sigma) ...
    ./(viscosity_fluid.*k_w1Hirad.*(1 + (2/3).*sigma))))).*1000; % Terminal rising velocity,
[mm/s]

plot(AverageDiameter3./5.842, RisingVelocity3 - 1000*V_max,'s','MarkerEdgeColor','r',...
    'MarkerFaceColor','r',...
    'MarkerSize',7);
hold on
plot(R./(5.842/2), U_Infinity,'k--','MarkerEdgeColor','b',...
    'MarkerFaceColor','b',...
    'MarkerSize',5,'LineWidth',2);
% grid minor
hold on
plot(R./(5.842/2), U,'b','MarkerEdgeColor','b',...
    'MarkerFaceColor','b',...
    'MarkerSize',5,'LineWidth',2);
% errorbar(AverageDiameter3./5.842, RisingVelocity3 -
1000*V_max,std_Velocity3,'s','MarkerEdgeColor','r',...
%     'MarkerFaceColor','r',...
%     'MarkerSize',7,'LineWidth',line_width_size,'Color','k');
xlabel('{\itD_{e}/t}','FontSize',font_size,'FontName', 'Times New Roman');
ylabel('{\itV_{b} - V_{f}} [mm/s]','FontSize',font_size,'FontName', 'Times New Roman');%
figure(2);
legend('Theoretical results for parallel plates (Shapira and Haber 1988)', ...
    'Theoretical results for infinite medium',strcat(['Current experimental data for {\itq =
}',num2str(Q)]))

% Saving the current figure in TIFF and EPS format

% saveas(gcf,'Rising Velocity_Not Modified_Q100.eps')
saveas(gcf,'Rising Velocity_Not Modified_Q100.fig')
% ********************************************
figure(2);
hold on
% grid minor
set(2,'pos',[70 70 1200 800]);
set(gcf,'color','w');
set(gca,'fontsize',font_size)
Cd = (4/3*g*(density_fluid - density_particle)/density_fluid) ...
    .*(0.001.*AverageDiameter3)./((0.001.*RisingVelocity3 - V_max).^2);
Cd_Infinity = 8*(2 + 3/sigma)/(1 + 1/sigma)./Re;
Cd_Theory = viscosity_fluid.*(2 + 3/sigma)...
    /(1 + 1/sigma).*(4./((density_fluid*0.001.*R).*((k_1*0.001).*U - k_2.*V_max)));

plot(AverageDiameter3./5.842,Cd,'s','MarkerEdgeColor','r',...
    'MarkerFaceColor','r',...
    'MarkerSize',7);
hold on
plot(R./(5.842/2),Cd_Theory,'b','MarkerEdgeColor','b',...
    'MarkerFaceColor','b',...
```

```
    'MarkerSize',5,'LineWidth',2);

xlabel('{\itD/t}','FontSize',font_size, 'FontName', 'Times New Roman');
ylabel('{\itC_{D}}','FontSize',font_size, 'FontName', 'Times New Roman');
legend(strcat(['Current experimental data for {\itq = }',num2str(Q)]),'Theoretical results for
circular tube')

% Saving the current figure in TIFF and EPS format

% saveas(gcf,'Drag Coefficient_Q100.eps')
saveas(gcf,'Drag Coefficient_Q100.fig')
% axis([-2 2 0 11]);
% ********************************************
% CENTRICITY PLOT BEFORE AND AFTER THE SLOT REGION
figure(3)
hold on
% grid minor
set(3,'pos',[70 70 1200 800]);
set(gcf,'color','w');
set(gca,'fontsize',font_size);
errorbar(AverageDiameter3./5.84,Centricity3,std_Centricity3,'s','MarkerEdgeColor','r',...
    'MarkerFaceColor','r',...
    'MarkerSize',7,'LineWidth',line_width_size,'Color','k');
xlabel('{\itD_{e}/t}','FontSize',font_size, 'FontName', 'Times New Roman');
ylabel('Centricity, {\itC}','FontSize',font_size, 'FontName', 'Times New Roman');
legend(strcat(['Current experimental data for {\itq = }',num2str(Q)]))

% Saving the current figure in TIFF and EPS format

% saveas(gcf,'Centricity_Q100.eps')
saveas(gcf,'Centricity_Q100.fig')
% RE NUMBER PLOT FOR BEFORE AND AFTER THE SLOT REGIONS
figure(4);
hold on
% grid minor;
set(4,'pos',[70 70 1200 800]);
set(gcf,'color','w');
set(gca,'fontsize',font_size);
plot(AverageDiameter3./5.84,Re,'s','MarkerEdgeColor','r',...
    'MarkerFaceColor','r',...
    'MarkerSize',7);
xlabel('{\itD_{e}/w}','FontSize',font_size, 'FontName', 'Times New Roman');
ylabel('{\itRe}','FontSize',font_size, 'FontName', 'Times New Roman');
legend(strcat(['Current experimental data for {\itq = }',num2str(Q)]))

% Saving the current figure in TIFF and EPS format

% saveas(gcf,'Re_Q100.eps')
saveas(gcf,'Re_Q100.fig')

% ********************************************
% Calculating the parameters through the slot
Q = 1.78; % Flux (V/A)
w = 3; % Slot/Flow cell width, mm
```

```
A = 5.842 * w;   % mm2
V_average = Q/A * (1/3600);
V_max = 0.00267;   % Maximum velocity in a laminar flow, [m/s]
Dh =  4*5.842*w/(2*(w + 5.842)); % [mm]
b = Dh/2;  % b is equal to half diameter of the tube. Here, we assume that
% we have a hydrolic diameter and suppose "b" is half of that
lambda = R./b;

% ************************************************

% Wall correction factors: k_1 and k_2:
% Wall correction factors for spheres within a circle, when particle is stationary
%
k_1 = ((1 - 0.75857.*(1 - sigma)./(1 + (2/3).*sigma)*lambda.^5))./ ...
    (1 - 2.1050.*(1 + (2/3).*sigma)./(1 + sigma).*lambda + ...
    2.0865.*(1./(1 + sigma).*lambda.^3)- ...
    1.7068.*((1 - (2/3).*sigma)./(1 + sigma).*lambda.^5)...
    + 0.72603.*(1 - sigma)./(1 + sigma).*lambda.^6);


% Wall correction factor for spheres within a circle, when there is a bulk flow
%
k_2 = (1 - (2/3).*(1./(1 + 2/3.*sigma)).*lambda.^2 - ...
    0.20217.*((1 - sigma)./(1 + 2/3.*sigma).*lambda.^5))./...
    (1 - 2.1050.*(1 + (2/3).*sigma)./(1 + sigma).*lambda + ...
    2.0865.*(1./(1 + sigma).*lambda.^3)- ...
    1.7068.*((1 - (2/3).*sigma)./(1 + sigma).*lambda.^5)...
    + 0.72603.*(1 - sigma)./(1 + sigma).*lambda.^6);
% ************************************************************************
% Correction factor for rise of air bubbles between two parallel plates
b = 3/2;
lambda = R./b;
k_w1Hirad = (1 + 2.*(sigma + 3/2)./(sigma + 1).*lambda.*1.338);

b = 5.842/2;
lambda = R./b;
k_w2Hirad = (1 + 2.*(sigma + 3/2)./(sigma + 1).*lambda.*1.338);

U = (((2/9).*((R.*0.001).^2.*g.*(density_fluid - density_particle).*(1 + sigma) ...
    ./(viscosity_fluid.*(k_w1Hirad.*k_w2Hirad).*(1 + (2/3).*sigma))))).*1000; % Terminal rising
velocity, [mm/s]
U_Haberman = (((2/9).*((R.*0.001).^2.*g.*(density_fluid - density_particle).*(1 + sigma) ...
    ./(viscosity_fluid.*(k_1).*(1 + (2/3).*sigma)))) + V_max.*k_2./(k_1)).*1000; % Terminal
rising velocity, [mm/s]
% ************************************************************************
% CENTRICITY PLOT THROUGH THE SLOT REGION
figure(5)
hold on
% grid minor
set(5,'pos',[70 70 1200 800]);
set(gcf,'color','w');
set(gca,'fontsize',font_size);
errorbar(AverageDiameter3./w,Centricity_Slot3,std_Centricity_Slot3,'s','MarkerEdgeColor','r',...
    'MarkerFaceColor','r',...
```

```
    'MarkerSize',7,'LineWidth',line_width_size,'Color','k');
xlabel('{\itD_{e}/w}','FontSize',font_size, 'FontName', 'Times New Roman');
ylabel('Centricity, {\itC}','FontSize',font_size, 'FontName', 'Times New Roman');
legend(strcat(['Current experimental data for {\itq = }',num2str(Q)]))

% Saving the current figure in TIFF and EPS format

% saveas(gcf,'Centricity_Slot_Q100.eps')
saveas(gcf,'Centricity_Slot_Q100.fig')
% RE NUMBER PLOT FOR THROUGH THE SLOT REGIONS
figure(6);
hold on
% grid minor;
set(6,'pos',[70 70 1200 800]);
set(gcf,'color','w');
set(gca,'fontsize',font_size);
plot(AverageDiameter3./w,Re_Slot,'s','MarkerEdgeColor','r',...
    'MarkerFaceColor','r',...
    'MarkerSize',7);
xlabel('{\itD_{e}/w}','FontSize',font_size, 'FontName', 'Times New Roman');
ylabel('{\itRe}','FontSize',font_size, 'FontName', 'Times New Roman');
legend(strcat(['Current experimental data for {\itq = }',num2str(Q)]))

% Saving the current figure in TIFF and EPS format

% saveas(gcf,'Re_Slot_Q100.eps')
saveas(gcf,'Re_Slot_Q100.fig')
% AVERAGED RISING VELOCITY THROUGH THE SLOT
figure(7);
hold on
set(7,'pos',[70 70 1200 800]);
set(gcf,'color','w');
set(gca,'fontsize',font_size)
% errorbar(AverageDiameter3./w, RisingVelocity_Slot3 -
V_max*1000,std_Velocity_Slot3,'s','MarkerEdgeColor','r',...
%     'MarkerFaceColor','r',...
%     'MarkerSize',7,'LineWidth',line_width_size,'Color','k');
plot(AverageDiameter3./w, RisingVelocity_Slot3 - V_max*1000,'s','MarkerEdgeColor','r',...
    'MarkerFaceColor','r',...
    'MarkerSize',7);
hold on
plot(R./(w/2), U_Infinity,'k--','MarkerEdgeColor','k',...
    'MarkerFaceColor','k',...
    'MarkerSize',5,'LineWidth',2);
hold on
plot(R./(w/2), U,'b','MarkerEdgeColor','k',...
    'MarkerFaceColor','k',...
    'MarkerSize',5,'LineWidth',2);
% grid minor

xlabel('{\itD_{e}/w}','FontSize',font_size,'FontName', 'Times New Roman');
ylabel('{\it V_{b-Slot} - V_{f-Slot}} [mm/s]','FontSize',font_size,'FontName', 'Times New
Roman');% figure(2);
legend(strcat(['Current experimental data for {\itq = }',num2str(Q)]), 'Theoretical results for
```

```
infinite medium', ...
    'Theoretical results for parallel plates (Shapira and Haber 1988)')

% Saving the current figure in TIFF and EPS format

% saveas(gcf,'Rising Velocity_Not Modified_Slot_Q100.eps')
saveas(gcf,'Rising Velocity_Not Modified_Slot_Q100.fig')
% ************************************************************************
% ******************************************

% PLOTTING THE DRAG FORCE
figure(8);
hold on
% grid minor
set(8,'pos',[70 70 1200 800]);
set(gcf,'color','w');
set(gca,'fontsize',font_size)
Cd = (4/3*g*(density_fluid - density_particle)/density_fluid) ...
    .*(0.001.*AverageDiameter3)./((0.001.*RisingVelocity_Slot3 - V_max).^2);
Cd_Infinity = 8*(2 + 3/sigma)/(1 + 1/sigma)./Re_Slot;
Cd_Theory = viscosity_fluid.*(2 + 3/sigma)...
    /(1 + 1/sigma).*(4./((density_fluid*0.001.*R).*((k_1*0.001).*U - k_2.*V_max)));

plot(AverageDiameter3./w,Cd,'s','MarkerEdgeColor','r',...
    'MarkerFaceColor','r',...
    'MarkerSize',7);
hold on
plot(R./(w/2),Cd_Theory,'b','MarkerEdgeColor','b',...
    'MarkerFaceColor','b',...
    'MarkerSize',5,'LineWidth',2);

xlabel('{\itD/w}','FontSize',font_size, 'FontName', 'Times New Roman');
ylabel('{\itC_{D}}','FontSize',font_size, 'FontName', 'Times New Roman');
legend(strcat(['Current experimental data for {\itq = }',num2str(Q)]),'Theoretical results for
circular tube')

% Saving the current figure in TIFF and EPS format

% saveas(gcf,'Drag Coefficient_Slot_Q100.eps')
saveas(gcf,'Drag Coefficient_Slot_Q100.fig')
% axis([-2 2 0 11]);
% ************************************************************************
% Bubble rising velocity in infinity (no confinement)
U_Infinity = (((2/3).*((0.5.*AverageDiameter3.*0.001).^2.*g.*(density_fluid -
density_particle).*(1 + 1./sigma) ...
    ./(viscosity_fluid.*(2 + 3./sigma)))) + V_max).*1000;
```

Saving data files separately for each flow rate, and plotting all of data in one figure

```
       save('data100.mat','AverageDiameter3','RisingVelocity_Slot3','RisingVelocity3', ...
    'Centricity3','Centricity_Slot3','std_Velocity3','std_Velocity_Slot3' ...
    ,'std_Centricity3','std_Centricity_Slot3',
'U_Infinity','v_max_Slot3','v_max_BeforeAfter3','Bubble_Center3', ...
    'std_Diameter_Slot3','std_Diameter3')
close all
clear data
```

Q_3 data

```
       Q = 0.15;
w = 22; % Slot/Flow cell width, mm
A = 5.842 * w;   % mm2
V_average = Q/A * (1/3600);
V_max = 0.001598*3/22;   % Maximum velocity in a laminar flow, [m/s]
Dh = 5.842;% 4*5.842*w/(2*(w + 5.842)), [mm]
% Dh = 2*(22 + 5.842)/pi;
b = Dh/2;  % b is equal to half diameter of the tube. Here, we assume that
% we have a hydrolic diameter and suppose "b" is half of that
lambda = R./b;
% Wall correction factors: k_1 and k_2:
% Wall correction factors for spheres within a circle, when particle is stationary
%
k_1 = ((1 - 0.75857.*(1 - sigma)./(1 + (2/3).*sigma)*lambda.^5))./ ...
    (1 - 2.1050.*(1 + (2/3).*sigma)./(1 + sigma).*lambda + ...
    2.0865.*(1./(1 + sigma).*lambda.^3)- ...
    1.7068.*((1 - (2/3).*sigma)./(1 + sigma).*lambda.^5)...
    + 0.72603.*(1 - sigma)./(1 + sigma).*lambda.^6);


% Wall correction factor for spheres within a circle, when there is a bulk flow
%
k_2 = (1 - (2/3).*(1./(1 + 2/3.*sigma)).*lambda.^2 - ...
    0.20217.*((1 - sigma)./(1 + 2/3.*sigma).*lambda.^5))./...
    (1 - 2.1050.*(1 + (2/3).*sigma)./(1 + sigma).*lambda + ...
    2.0865.*(1./(1 + sigma).*lambda.^3)- ...
    1.7068.*((1 - (2/3).*sigma)./(1 + sigma).*lambda.^5)...
    + 0.72603.*(1 - sigma)./(1 + sigma).*lambda.^6);

% ************************************************************************
% Correction factors for rise of air bubbles between two parallel plates
k_w1Hirad = (1 + 2.*(sigma + 3/2)./(sigma + 1).*lambda.*1.338);
```

```
U_Infinity = (((2/3).*((R.*0.001).^2.*g.*(density_fluid - density_particle).*(1 + 1./sigma) ...
    ./(viscosity_fluid.*(2 + 3./sigma))))).*1000;
% ************************************************************************

% Reading the data file
%begin
%%%%%%%%%%%%%%%%%%%  Define Folders in which data files are  %%%%%%%%%%%%%%%%
% myFolder{1} = uigetdir;
myFolder{3} = 'X:\01_Current_Students\HIRAD SOLTANI\Publicaitons_HS\Journal Papers\Paper 1\Bubble
Zoomout_February 23\Q60\';

for RunFolder_counter = 3
    if ~isdir(myFolder{RunFolder_counter})
        errorMessage = sprintf('Error: The following folder does not exist:\n%s',
myFolder{RunFolder_counter});
        uiwait(warndlg(errorMessage));
        return;
    end
    filePattern = fullfile(myFolder{RunFolder_counter}, '*.csv');
    logFiles = dir(filePattern);

    for k = 1:length(logFiles)

        baseFileName = logFiles(k).name;
        fullFileName = fullfile(myFolder{RunFolder_counter}, baseFileName);
        %fprintf(1, 'Now reading %s\n', fullFileName);
        fileID = fopen(fullFileName);
        %   date_time = textscan(fileID,'Date %s Time %s','HeaderLines',1);
        %   column_headers = textscan(fileID,'%s',41,'delimiter', '\t');
        column_headers  = regexp(fgetl(fileID ),';','split');

        counter =1;
        while (~feof(fileID))
            [data,position] = textscan(fileID,'%s',10,'delimiter', ';');
            real_data{counter,:} = data;
            counter = counter + 1;
        end
        counter = counter - 2;
        fclose(fileID);
        for row_number = 1 : counter
            subcounter = 1;
            temp = real_data{row_number,1}{1,1};
            for column_number = 1 : 10
                %             if  (~isnan(temp(column_number)))
                data(row_number,subcounter) = temp(column_number);
                final_data_cell{row_number+1,subcounter} = temp(column_number);

                subcounter = subcounter + 1;
                %             end
            end
        end
        final_data_cell = cellfun( @(x) str2double(strrep(x, ',', '.')), final_data_cell,
'uniformoutput', false);
        data = cell2mat(final_data_cell);
```

```
        final_data_cell(1,:) = column_headers;
        [r,c] = size(data);
        % define time interval between every two frames
        time_stamp = 1/8;
                % ********************************************************************
        % Since some of the data are collected in another experiment, they
        % should be consistent with other data. So the x and y information
        % of all images (calibration) are tried to be the same in this
        % section
        if isequal(baseFileName,'ParticleList6024.csv')
            data(:,2) = data(:,2) + 4;
            data(:,1) = data(:,1) -3.8;
        end
        if isequal(baseFileName,'ParticleList6025.csv')
            data(:,2) = data(:,2) + 4;
            data(:,1) = data(:,1) -3.8;
        end
        if isequal(baseFileName,'ParticleList6026.csv')
            data(:,2) = data(:,2) + 4;
            data(:,1) = data(:,1) -3.8;
        end
        % ********************************************************************
        data (4:r,7)= (data (4:r,1)-data (2:r-2,1))/(2*time_stamp);
        data (4:r,8)= (data (4:r,2)-data (2:r-2,2))/(2*time_stamp);
        data (4:r,9)= sqrt(data (4:r,7).^2 + data (4:r,8).^2);

%         % For the 3D plot of instantaneous rising velocity, the data of all flow
%         % rates should be stored (Rising velocity and Diameter data)
%         if data(10,4) < 1
%             Velocity_3D_60 = data(:,9);
%             Diameter_3D_60 = data(:,2)/15 - 0.25;
%         end
%

        % Uncertainty and averaging the risintg velocity and bubble diameter
        % Before the slot region
        p = max(find(data(:,2) < -12));
        RisingVelocity1 = nanmean(data(1:p,9));
        AverageDiameter1 = nanmean(data(1:p,4));
        Centricity1 = nanmean(data(1:p,3));
        std_Velocity1 = nanstd(data(1:p,9));
        std_Centricity1 = nanstd(data(1:p,3));
        std_Diameter1 = nanstd(data(1:p,4));

        % After the slot region
        m = min(find(data(:,2) > 17));
        RisingVelocity2 = nanmean(data(m:end,9));
        AverageDiameter2 = nanmean(data(m:end,4));
        Centricity2 = nanmean(data(m:end,3));
        std_Velocity2 = nanstd(data(m:end,9));
        std_Centricity2 = nanstd(data(m:end,3));
        std_Diameter2 = nanstd(data(m:end,4));

        % The average data for before and after the slot regions
```

```
        RisingVelocity(k) = (p*RisingVelocity1 + m*RisingVelocity2)/(m + p);
        AverageDiameter(k) = (p*AverageDiameter1 + m*AverageDiameter2)/(m + p);
        Centricity(k) = (p*Centricity1 + m*Centricity2)/(m + p);
        std_Velocity(k) = (p*std_Velocity1 + m*std_Velocity2)/(m + p);
        std_Centricity(k) = (p*std_Centricity1 + m*std_Centricity2)/(m + p);
        std_Diameter(k) = (p*std_Diameter1 + m*std_Diameter2)/(m + p);

        % In the slot region
        s1 = min(find(data(:,2) > -2));
        s2 = max(find(data(:,2) < 8.7));
        RisingVelocity_Slot(k) = nanmean(data(s1:s2,9));
        Centricity_Slot(k) = nanmean(data(s1:s2,3));
        std_Velocity_Slot(k) = nanstd(data(s1:s2,9));
        std_Centricity_Slot(k) = nanstd(data(s1:s2,3));
        std_Diameter_Slot(k) = nanstd(data(s1:s2,3));

        % X position of center of the bubble
        Bubble_Center(k) = nanmean(data(s1:s2,1));

        % Maximum velocity in the regions before and after the slot
        v_max_BeforeAfter(k) = max([data(m:end,9);data(1:p,9)]);
        % Maximum velocity through the slot
        v_max_Slot(k) = max(data(s1:s2,9));
        %*************************************************************************
        % Uncertainty of rising velocity in before and after the slot regions

        sortedVelocity(1:p,1) = data(1:p,9);
        sortedVelocity(p+1:size(data,1)-m+p+1,1) = data(m:end,9);
        Sx = 0;
        a = find(isnan(sortedVelocity(:,:)));
        sortedVelocity(a) = [];
        for i = 1:size(sortedVelocity,1)
            Sx = (sortedVelocity(i,1) - RisingVelocity(k)).^2./(length(logFiles)-1) + Sx;
        end
        Sx = Sx^0.5;
        P_xbar(k) = 2*Sx/length(logFiles)^0.5;
        %*************************************************************************
        % Uncertainty through the slot
        sortedVelocity_Slot = data(s1:s2,9);
        Sx_Slot = 0;
        b = find(isnan(sortedVelocity_Slot(:,:)));
        sortedVelocity_Slot(b) = [];
        for i = 1:size(sortedVelocity_Slot,1)
            Sx_Slot = (sortedVelocity_Slot(i,1) -
RisingVelocity_Slot(k)).^2./(size(sortedVelocity_Slot,1)) + Sx_Slot;
        end
        Sx_Slot = Sx_Slot^0.5;
        P_xbar_Slot(k) = 2*Sx_Slot/(size(sortedVelocity_Slot,1)^0.5);

        % For the 3D plot of instantaneous rising velocity, the data of all flow
        % rates should be stored (Rising velocity and Diameter data)
        if AverageDiameter(k) < 0.9
            Velocity_3D_60_min = data(:,9);
            Diameter_3D_60_min = data(:,2)/15 - 0.25;
```

```
        end
        if AverageDiameter(k) > 3
            Velocity_3D_60_max = data(:,9);
            Diameter_3D_60_max = data(:,2)/15 - 0.25;
        end
        % End of reading data file for RUN 1
    end
end
% Organizing the dimeter and velocity data.
AverageDiameter3 = sort(AverageDiameter);
[r,c] = size(AverageDiameter);
RisingVelocity3 = zeros(r,c);
RisingVelocity_Slot3 = zeros(r,c);
Centricity3 = zeros(r,c);
Centricity_Slot3 = zeros(r,c);
std_Velocity3 = zeros(r,c);
std_Velocity_Slot3 = zeros(r,c);
std_Centricity3 = zeros(r,c);
std_Centricity_Slot3 = zeros(r,c);
v_max_BeforeAfter3 = zeros(r,c);
v_max_Slot3 = zeros(r,c);
Bubble_Center3 = zeros(r,c);
std_Diameter3 = zeros(r,c);
std_Diameter_Slot3 = zeros(r,c);
i = 1;
for i = 1:c
    j = find(AverageDiameter3 == AverageDiameter(1,i));
    RisingVelocity3(1,j) = RisingVelocity(1,i);
    RisingVelocity_Slot3(1,j) = RisingVelocity_Slot(1,i);
    Centricity3(1,j) = Centricity(1,i);
    Centricity_Slot3(1,j) = Centricity_Slot(1,i);
    std_Velocity3(1,j) = std_Velocity(1,i);
    std_Velocity_Slot3(1,j) = std_Velocity_Slot(1,i);
    std_Centricity3(1,j) = std_Centricity(1,i);
    std_Centricity_Slot3(1,j) = std_Centricity_Slot(1,i);
    std_Diameter3(1,j) = std_Diameter(1,i);
    std_Diameter_Slot3(1,j) = std_Diameter_Slot(1,i);
    v_max_BeforeAfter3(1,j) = v_max_BeforeAfter(1,i);
    v_max_Slot3(1,j) = v_max_Slot(1,i);
    Bubble_Center3(1,j) = Bubble_Center(1,i);
    i = i + 1;
end

% Reynolds number for each bubble
Re = ((density_fluid.*((0.001.*RisingVelocity3) -
V_max)).*(0.001.*AverageDiameter3))./viscosity_fluid;
Re_Slot = ((density_fluid.*((0.001.*RisingVelocity_Slot3) -
V_max*22/3)).*(0.001.*AverageDiameter3))./viscosity_fluid;
% The terminal velocity through the slot
% the purpose of this section is to check how close the rising velocity is
% to theoretical terminal velocity
figure(1);
hold on
set(1,'pos',[70 70 1200 800]);
```

```
set(gcf,'color','w');
set(gca,'fontsize',font_size)
U = (((2/9).*((R.*0.001).^2.*g.*(density_fluid - density_particle).*(1 + sigma) ...
    ./(viscosity_fluid.*k_w1Hirad.*(1 + (2/3).*sigma))))).*1000; % Terminal rising velocity,
[mm/s]

plot(AverageDiameter3./5.842, RisingVelocity3 - 1000*V_max,'s','MarkerEdgeColor','r',...
    'MarkerFaceColor','r',...
    'MarkerSize',7);
hold on
plot(R./(5.842/2), U_Infinity,'k--','MarkerEdgeColor','b',...
    'MarkerFaceColor','b',...
    'MarkerSize',5,'LineWidth',2);
% grid minor
hold on
plot(R./(5.842/2), U,'b','MarkerEdgeColor','b',...
    'MarkerFaceColor','b',...
    'MarkerSize',5,'LineWidth',2);
% errorbar(AverageDiameter3./5.842, RisingVelocity3 -
1000*V_max,std_Velocity3,'s','MarkerEdgeColor','r',...
%     'MarkerFaceColor','r',...
%     'MarkerSize',7,'LineWidth',line_width_size,'Color','k');
xlabel('{\itD_{e}/t}','FontSize',font_size,'FontName', 'Times New Roman');
ylabel('{\itV_{b} - V_{f}} [mm/s]','FontSize',font_size,'FontName', 'Times New Roman');%
figure(2);
legend('Theoretical results for parallel plates (Shapira and Haber 1988)', ...
    'Theoretical results for infinite medium',strcat(['Current experimental data for {\itq =
}',num2str(Q)]))

% Saving the current figure in TIFF and EPS format

% saveas(gcf,'Rising Velocity_Not Modified_Q60.eps')
saveas(gcf,'Rising Velocity_Not Modified_Q60.fig')
% ************************************************
figure(2);
hold on
% grid minor
set(2,'pos',[70 70 1200 800]);
set(gcf,'color','w');
set(gca,'fontsize',font_size)
Cd = (4/3*g*(density_fluid - density_particle)/density_fluid) ...
    .*(0.001.*AverageDiameter3)./((0.001.*RisingVelocity3 - V_max).^2);
Cd_Infinity = 8*(2 + 3/sigma)/(1 + 1/sigma)./Re;
Cd_Theory = viscosity_fluid.*(2 + 3/sigma)...
    /(1 + 1/sigma).*(4./((density_fluid*0.001.*R).*((k_1*0.001).*U - k_2.*V_max)));

plot(AverageDiameter3./5.842,Cd,'s','MarkerEdgeColor','r',...
    'MarkerFaceColor','r',...
    'MarkerSize',7);
hold on
plot(R./(5.842/2),Cd_Theory,'b','MarkerEdgeColor','b',...
    'MarkerFaceColor','b',...
    'MarkerSize',5,'LineWidth',2);
```

```
xlabel('{\itD/t}','FontSize',font_size, 'FontName', 'Times New Roman');
ylabel('{\itC_{D}}','FontSize',font_size, 'FontName', 'Times New Roman');
legend(strcat(['Current experimental data for {\itq = }',num2str(Q)]),'Theoretical results for
circular tube')

% Saving the current figure in TIFF and EPS format

% saveas(gcf,'Drag Coefficient_Q60.eps')
saveas(gcf,'Drag Coefficient_Q60.fig')
% axis([-2 2 0 11]);
% ******************************************
% CENTRICITY PLOT BEFORE AND AFTER THE SLOT REGION
figure(3)
hold on
% grid minor
set(3,'pos',[70 70 1200 800]);
set(gcf,'color','w');
set(gca,'fontsize',font_size);
errorbar(AverageDiameter3./5.84,Centricity3,std_Centricity3,'s','MarkerEdgeColor','r',...
    'MarkerFaceColor','r',...
    'MarkerSize',7,'LineWidth',line_width_size,'Color','k');
xlabel('{\itD_{e}/t}','FontSize',font_size, 'FontName', 'Times New Roman');
ylabel('Centricity, {\itC}','FontSize',font_size, 'FontName', 'Times New Roman');
legend(strcat(['Current experimental data for {\itq = }',num2str(Q)]))

% Saving the current figure in TIFF and EPS format

% saveas(gcf,'Centricity_Q60.eps')
saveas(gcf,'Centricity_Q60.fig')
% RE NUMBER PLOT FOR BEFORE AND AFTER THE SLOT REGIONS
figure(4);
hold on
% grid minor;
set(4,'pos',[70 70 1200 800]);
set(gcf,'color','w');
set(gca,'fontsize',font_size);
plot(AverageDiameter3./5.84,Re,'s','MarkerEdgeColor','r',...
    'MarkerFaceColor','r',...
    'MarkerSize',7);
xlabel('{\itD_{e}/w}','FontSize',font_size, 'FontName', 'Times New Roman');
ylabel('{\itRe}','FontSize',font_size, 'FontName', 'Times New Roman');
legend(strcat(['Current experimental data for {\itq = }',num2str(Q)]))

% Saving the current figure in TIFF and EPS format

% saveas(gcf,'Re_Q60.eps')
saveas(gcf,'Re_Q60.fig')
% ******************************************
% Calculating the parameters through the slot
Q = 1.07; % Flux (V/A)
w = 3; % Slot/Flow cell width, mm
A = 5.842 * w;   % mm2
V_average = Q/A * (1/3600);
V_max = 0.001598;   % Maximum velocity in a laminar flow, [m/s]
```

```
Dh =  4*5.842*w/(2*(w + 5.842)); % [mm]
b = Dh/2;  % b is equal to half diameter of the tube. Here, we assume that
% we have a hydrolic diameter and suppose "b" is half of that
lambda = R./b;

% ************************************************

% Wall correction factors: k_1 and k_2:
% Wall correction factors for spheres within a circle, when particle is stationary
%
k_1 = ((1 - 0.75857.*(1 - sigma)./(1 + (2/3).*sigma)*lambda.^5))./ ...
    (1 - 2.1050.*(1 + (2/3).*sigma)./(1 + sigma).*lambda + ...
    2.0865.*(1./(1 + sigma).*lambda.^3)- ...
    1.7068.*((1 - (2/3).*sigma)./(1 + sigma).*lambda.^5)...
    + 0.72603.*(1 - sigma)./(1 + sigma).*lambda.^6);


% Wall correction factor for spheres within a circle, when there is a bulk flow
%
k_2 = (1 - (2/3).*(1./(1 + 2/3.*sigma)).*lambda.^2 - ...
    0.20217.*((1 - sigma)./(1 + 2/3.*sigma).*lambda.^5))./...
    (1 - 2.1050.*(1 + (2/3).*sigma)./(1 + sigma).*lambda + ...
    2.0865.*(1./(1 + sigma).*lambda.^3)- ...
    1.7068.*((1 - (2/3).*sigma)./(1 + sigma).*lambda.^5)...
    + 0.72603.*(1 - sigma)./(1 + sigma).*lambda.^6);

% ************************************************************************
% Correction factor for rise of air bubbles between two parallel plates
b = 3/2;
lambda = R./b;
k_w1Hirad = (1 + 2.*(sigma + 3/2)./(sigma + 1).*lambda.*1.338);

b = 5.842/2;
lambda = R./b;
k_w2Hirad = (1 + 2.*(sigma + 3/2)./(sigma + 1).*lambda.*1.338);

U = (((2/9).*((R.*0.001).^2.*g.*(density_fluid - density_particle).*(1 + sigma) ...
    ./(viscosity_fluid.*(k_w1Hirad.*k_w2Hirad).*(1 + (2/3).*sigma))))).*1000; % Terminal rising
velocity, [mm/s]
U_Haberman = (((2/9).*((R.*0.001).^2.*g.*(density_fluid - density_particle).*(1 + sigma) ...
    ./(viscosity_fluid.*(k_1).*(1 + (2/3).*sigma)))) + V_max.*k_2./(k_1)).*1000; % Terminal
rising velocity, [mm/s]
% ************************************************************************
% CENTRICITY PLOT THROUGH THE SLOT REGION
figure(5)
hold on
% grid minor
set(5,'pos',[70 70 1200 800]);
set(gcf,'color','w');
set(gca,'fontsize',font_size);
errorbar(AverageDiameter3./w,Centricity_Slot3,std_Centricity_Slot3,'s','MarkerEdgeColor','r',...
    'MarkerFaceColor','r',...
    'MarkerSize',7,'LineWidth',line_width_size,'Color','k');
xlabel('{\itD_{e}/w}','FontSize',font_size, 'FontName', 'Times New Roman');
```

```
ylabel('Centricity, {\itC}','FontSize',font_size, 'FontName', 'Times New Roman');
legend(strcat(['Current experimental data for {\itq = }',num2str(Q)]))

% Saving the current figure in TIFF and EPS format

% saveas(gcf,'Centricity_Slot_Q60.eps')
saveas(gcf,'Centricity_Slot_Q60.fig')
% RE NUMBER PLOT FOR THROUGH THE SLOT REGIONS
figure(6);
hold on
% grid minor;
set(6,'pos',[70 70 1200 800]);
set(gcf,'color','w');
set(gca,'fontsize',font_size);
plot(AverageDiameter3./w,Re_Slot,'s','MarkerEdgeColor','r',...
    'MarkerFaceColor','r',...
    'MarkerSize',7);
xlabel('{\itD_{e}/w}','FontSize',font_size, 'FontName', 'Times New Roman');
ylabel('{\itRe}','FontSize',font_size, 'FontName', 'Times New Roman');
legend(strcat(['Current experimental data for {\itq = }',num2str(Q)]))

% Saving the current figure in TIFF and EPS format

% saveas(gcf,'Re_Slot_Q60.eps')
saveas(gcf,'Re_Slot_Q60.fig')
% AVERAGED RISING VELOCITY THROUGH THE SLOT
figure(7);
hold on
set(7,'pos',[70 70 1200 800]);
set(gcf,'color','w');
set(gca,'fontsize',font_size)
% errorbar(AverageDiameter3./w, RisingVelocity_Slot3 -
V_max*1000,std_Velocity_Slot3,'s','MarkerEdgeColor','r',...
%     'MarkerFaceColor','r',...
%     'MarkerSize',7,'LineWidth',line_width_size,'Color','k');
plot(AverageDiameter3./w, RisingVelocity_Slot3 - V_max*1000,'s','MarkerEdgeColor','r',...
    'MarkerFaceColor','r',...
    'MarkerSize',7);
hold on
plot(R./(w/2), U_Infinity,'k--','MarkerEdgeColor','k',...
    'MarkerFaceColor','k',...
    'MarkerSize',5,'LineWidth',2);
hold on
plot(R./(w/2), U,'b','MarkerEdgeColor','k',...
    'MarkerFaceColor','k',...
    'MarkerSize',5,'LineWidth',2);
% grid minor

xlabel('{\itD_{e}/w}','FontSize',font_size,'FontName', 'Times New Roman');
ylabel('{\it V_{b-Slot} - V_{f-Slot}} [mm/s]','FontSize',font_size,'FontName', 'Times New
Roman');% figure(2);
legend(strcat(['Current experimental data for {\itq = }',num2str(Q)]), 'Theoretical results for
infinite medium', ...
    'Theoretical results for parallel plates (Shapira and Haber 1988)')
```

```
% Saving the current figure in TIFF and EPS format

% saveas(gcf,'Rising Velocity_Not Modified_Slot_Q60.eps')
saveas(gcf,'Rising Velocity_Not Modified_Slot_Q60.fig')
% ********************************************

% PLOTTING THE DRAG FORCE
figure(8);
hold on
% grid minor
set(8,'pos',[70 70 1200 800]);
set(gcf,'color','w');
set(gca,'fontsize',font_size)
Cd = (4/3*g*(density_fluid - density_particle)/density_fluid) ...
    .*(0.001.*AverageDiameter3)./((0.001.*RisingVelocity_Slot3 - V_max).^2);
Cd_Infinity = 8*(2 + 3/sigma)/(1 + 1/sigma)./Re_Slot;
Cd_Theory = viscosity_fluid.*(2 + 3/sigma)...
    /(1 + 1/sigma).*(4./((density_fluid*0.001.*R).*((k_1*0.001).*U - k_2.*V_max)));

plot(AverageDiameter3./w,Cd,'s','MarkerEdgeColor','r',...
    'MarkerFaceColor','r',...
    'MarkerSize',7);
hold on
plot(R./(w/2),Cd_Theory,'b','MarkerEdgeColor','b',...
    'MarkerFaceColor','b',...
    'MarkerSize',5,'LineWidth',2);

xlabel('{\itD/w}','FontSize',font_size, 'FontName', 'Times New Roman');
ylabel('{\itC_{D}}','FontSize',font_size, 'FontName', 'Times New Roman');
legend(strcat(['Current experimental data for {\itq = }',num2str(Q)]),'Theoretical results for
circular tube')

% Saving the current figure in TIFF and EPS format

% saveas(gcf,'Drag Coefficient_Slot_Q60.eps')
saveas(gcf,'Drag Coefficient_Slot_Q60.fig')
% axis([-2 2 0 11]);
% ************************************************************************
% Bubble rising velocity in infinity (no confinement)
U_Infinity = (((2/3).*((0.5.*AverageDiameter3.*0.001).^2.*g.*(density_fluid -
density_particle).*(1 + 1./sigma) ...
    ./(viscosity_fluid.*(2 + 3./sigma)))) + V_max).*1000;
```

Saving data files separately for each flow rate, and plotting all of data in one figure

```
        save('data60.mat','AverageDiameter3','RisingVelocity_Slot3','RisingVelocity3', ...
    'Centricity3','Centricity_Slot3','std_Velocity3','std_Velocity_Slot3' ...

,'std_Centricity3','std_Centricity_Slot3','U_Infinity','v_max_Slot3','v_max_BeforeAfter3','Bubble
_Center3', ...
    'std_Diameter_Slot3','std_Diameter3')
close all
clear data
```

Model modification

```
        % Loading the MAT files
data20 = load('data20.mat');
data40 = load('data40.mat');
data60 = load('data60.mat');
data100 = load('data100.mat');
data150 = load('data150.mat');


V_max20 = 0.000503;
V_max40 = 0.001008;
V_max60 = 0.001598;
V_max100 = 0.00267;
V_max150 = 0.003966;
% Flow rates
Q20 = [20 20 20 20 20 20 20].*1000.*V_max20./20;
Q40 = [40 40 40 40 40].*1000.*V_max40./40;
Q60 = [60 60 60 60 60 60 60 60 60 60].*1000.*V_max60./60;
Q100 = [100 100 100 100 100 100 100 100].*1000.*V_max100./100;
Q150 = [150 150 150 150 150 150].*1000.*V_max150./150;
%%%%%%%%%%%%%%%%%%%%%%%%%%%%%%%%%%%%%%%%%%%%%%%%%%%%%%%%%%%%%%%%%%%%%%%%%%%%%%%
% MODEL OF RISING VELOCITY THROUGH THE SLOT
%%%%%%%%%%%%%%%%%%%%%%%%%%%%%%%%%%%%%%%%%%%%%%%%%%%%%%%%%%%%%%%%%%%%%%%%%%%%%%%
w = 3; % Slot/Flow cell width, mm
A = 5.842 * w;   % mm2
V_average = Q/A * (1/3600);

V_max = V_average;   % Maximum velocity in a laminar flow, [m/s]
Dh =  2*5.842*w/(w + 5.842);%, [mm]
% Dh = 2*(22 + 5.842)/pi;

% b is equal to half diameter of the tube. Here, we assume that
% we have a hydrolic diameter and suppose "b" is half of that

D20 = data20.AverageDiameter3;
D40 = data40.AverageDiameter3;
D60 = data60.AverageDiameter3;
D100 = data100.AverageDiameter3;
D150 = data150.AverageDiameter3;
```

```
% lambda20 = 0.5.*D20./b;
% lambda40 = 0.5.*D40./b;
% lambda60 = 0.5.*D60./b;
% lambda100 = 0.5.*D100./b;
% lambda150 = 0.5.*D150./b;
% Defining parameters
Diameter_Slot20 = data20.AverageDiameter3./3;
Velocity_Slot20 = data20.RisingVelocity_Slot3;
std_Velocity_Slot20 = data20.std_Velocity_Slot3;

Diameter_Slot40 = data40.AverageDiameter3./3;
Velocity_Slot40 = data40.RisingVelocity_Slot3;
std_Velocity_Slot40 = data40.std_Velocity_Slot3;

Diameter_Slot60 = data60.AverageDiameter3./3;
Velocity_Slot60 = data60.RisingVelocity_Slot3;
std_Velocity_Slot60 = data60.std_Velocity_Slot3;

Diameter_Slot100 = data100.AverageDiameter3./3;
Velocity_Slot100 = data100.RisingVelocity_Slot3;
std_Velocity_Slot100 = data100.std_Velocity_Slot3;


Diameter_Slot150 = data150.AverageDiameter3./3;
Velocity_Slot150 = data150.RisingVelocity_Slot3;
std_Velocity_Slot150 = data150.std_Velocity_Slot3;

% Wall correction factors for parallel plate correlation
b = 5.842/2;
lambda20_w2 = 0.5.*D20./b;
lambda40_w2 = 0.5.*D40./b;
lambda60_w2 = 0.5.*D60./b;
lambda100_w2 = 0.5.*D100./b;
lambda150_w2 = 0.5.*D150./b;

k_w2_20 = (1 + 2.*(sigma + 3/2)./(sigma + 1).*lambda20_w2.*1.338);
k_w2_40 = (1 + 2.*(sigma + 3/2)./(sigma + 1).*lambda40_w2.*1.338);
k_w2_60 = (1 + 2.*(sigma + 3/2)./(sigma + 1).*lambda60_w2.*1.338);
k_w2_100 = (1 + 2.*(sigma + 3/2)./(sigma + 1).*lambda100_w2.*1.338);
k_w2_150 = (1 + 2.*(sigma + 3/2)./(sigma + 1).*lambda150_w2.*1.338);

b = 3/2;
lambda20_w1 = 0.5.*D20./b;
lambda40_w1 = 0.5.*D40./b;
lambda60_w1 = 0.5.*D60./b;
lambda100_w1 = 0.5.*D100./b;
lambda150_w1 = 0.5.*D150./b;

k_w1_20 = (1 + 2.*(sigma + 3/2)./(sigma + 1).*lambda20_w1.*1.338);
k_w1_40 = (1 + 2.*(sigma + 3/2)./(sigma + 1).*lambda40_w1.*1.338);
k_w1_60 = (1 + 2.*(sigma + 3/2)./(sigma + 1).*lambda60_w1.*1.338);
k_w1_100 = (1 + 2.*(sigma + 3/2)./(sigma + 1).*lambda100_w1.*1.338);
k_w1_150 = (1 + 2.*(sigma + 3/2)./(sigma + 1).*lambda150_w1.*1.338);
```

```
%%%%%%%%%%%%%%%%%%%%%%%%%%%%%%%%%%%%%%%%%%%%%%%%%%%%%%%%%%%%%%%%%%%%%%%%%%%%
U20 = (((2/9).*(((D20./2).*0.001).^2.*g.*(density_fluid - density_particle).*(1 + sigma) ...
    ./(viscosity_fluid.*(1 + (2/3).*sigma))))).*1000;
U40 = (((2/9).*(((D40./2).*0.001).^2.*g.*(density_fluid - density_particle).*(1 + sigma) ...
    ./(viscosity_fluid.*(1 + (2/3).*sigma))))).*1000;
U60 = (((2/9).*(((D60./2).*0.001).^2.*g.*(density_fluid - density_particle).*(1 + sigma) ...
    ./(viscosity_fluid.*(1 + (2/3).*sigma))))).*1000;
U100 = (((2/9).*(((D100./2).*0.001).^2.*g.*(density_fluid - density_particle).*(1 + sigma) ...
    ./(viscosity_fluid.*(1 + (2/3).*sigma))))).*1000;
U150 = (((2/9).*(((D150./2).*0.001).^2.*g.*(density_fluid - density_particle).*(1 + sigma) ...
    ./(viscosity_fluid.*(1 + (2/3).*sigma))))).*1000;
%%%%%%%%%%%%%%%%%%%%%%%%%%%%%%%%%%%%%%%%%%%%%%%%%%%%%%%%%%%%%%%%%%%%%%%%%%%%
b = Dh/2;

lambda20 = 0.5.*D20./b;
lambda40 = 0.5.*D40./b;
lambda60 = 0.5.*D60./b;
lambda100 = 0.5.*D100./b;
lambda150 = 0.5.*D150./b;


X = [U20', lambda20', Q20',k_w1_20',k_w2_20';U40', lambda40', Q40',k_w1_40',k_w2_40' ...
    ;U60', lambda60',Q60',k_w1_60',k_w2_60'; U100', lambda100', Q100',k_w1_100',k_w2_100'; ...
    U150', lambda150',Q150',k_w1_150',k_w2_150'];
Y = [data20.RisingVelocity_Slot3';data40.RisingVelocity_Slot3';data60.RisingVelocity_Slot3'; ...
    data100.RisingVelocity_Slot3';data150.RisingVelocity_Slot3'];


% modelfun = @(b,x) x(:,1).*b(1).*exp((x(:,2)-b(2)).^2);
% modelfun = @(b,x) x(:,1).*(b(1) + b(2).*cos(x(:,2)));
% modelfun = @(b,x) x(:,1).*(b(1).*exp(b(2).*x(:,2)));
% modelfun_Slot = @(b,x) x(:,1).*(b(1).*x(:,2).^2.*exp((b(2).*(x(:,2)-b(3)).^2)));
% modelfun = @(b,x) x(:,1).*(b(1).*exp(-(x(:,2) - b(2)).^2)) +
(b(3).*x(:,3).*x(4).*x(5)./x(:,2));
modelfun = @(b,x) x(:,1).*b(1).*exp(-(x(:,2) - b(2)).^2)./(x(:,4).*x(:,5)) + b(3).*(1 -
x(:,2).^2).*x(:,3);
beta0 = [1.52 0.0955 0.95];
% modelfun = @(b,x) x(:,1).*b(1) + 0.*x(:,2).*x(:,3).*x(:,4).*x(:,5);
% beta0 = [1];

AverageVelocityFitFunction = fitnlm(X , Y , modelfun , beta0)
[p,d] = dwtest(AverageVelocityFitFunction.Residuals.Raw , X);
lambda = R./b;

V_20 = 1000.*(V_max20 + zeros(size(lambda)));
V_40 = 1000.*(V_max40 + zeros(size(lambda)));
V_60 = 1000.*(V_max60 + zeros(size(lambda)));
V_100 = 1000.*(V_max100 + zeros(size(lambda)));
V_150 = 1000.*(V_max150 + zeros(size(lambda)));

U = (((2/9).*((R.*0.001).^2.*g.*(density_fluid - density_particle).*(1 + sigma) ...
    ./(viscosity_fluid.*(1 + (2/3).*sigma))))).*1000;
```

```
AverageVelocity_Corrected20 = feval(AverageVelocityFitFunction, U,
lambda,V_20,k_w1Hirad,k_w2Hirad);
% U = (((2/9).*((R.*0.001).^2.*g.*(density_fluid - density_particle).*(1 + sigma) ...
%     ./(viscosity_fluid.*k_w1Hirad.*k_w2Hirad.*(1 + (2/3).*sigma))))).*1000;
AverageVelocity_Corrected40 = feval(AverageVelocityFitFunction, U,
lambda,V_40,k_w1Hirad,k_w2Hirad);
% U = (((2/9).*((R.*0.001).^2.*g.*(density_fluid - density_particle).*(1 + sigma) ...
%     ./(viscosity_fluid.*k_w1Hirad.*k_w2Hirad.*(1 + (2/3).*sigma))))).*1000;
AverageVelocity_Corrected60 = feval(AverageVelocityFitFunction, U,
lambda,V_60,k_w1Hirad,k_w2Hirad);
% U = (((2/9).*((R.*0.001).^2.*g.*(density_fluid - density_particle).*(1 + sigma) ...
%     ./(viscosity_fluid.*k_w1Hirad.*k_w2Hirad.*(1 + (2/3).*sigma))))).*1000;
AverageVelocity_Corrected100 = feval(AverageVelocityFitFunction, U,
lambda,V_100,k_w1Hirad,k_w2Hirad);
% U = (((2/9).*((R.*0.001).^2.*g.*(density_fluid - density_particle).*(1 + sigma) ...
%     ./(viscosity_fluid.*k_w1Hirad.*k_w2Hirad.*(1 + (2/3).*sigma))))).*1000;
AverageVelocity_Corrected150 = feval(AverageVelocityFitFunction, U, lambda
,V_150,k_w1Hirad,k_w2Hirad);
%%%%%%%%%%%%%%%%%%%%%%%%%%%%%%%%%%%%%%%%%%%%%%%%%%%%%%%%%%%%%%%%%%%%%%%%%%%
% MODEL OF RISING VELOCITY THROUGH THE SLOT BASED ON CIRCULAR TUBE THEORY
%%%%%%%%%%%%%%%%%%%%%%%%%%%%%%%%%%%%%%%%%%%%%%%%%%%%%%%%%%%%%%%%%%%%%%%%%%%

w = 3; % Slot/Flow cell width, mm
A = 5.842 * w;   % mm2
V_average = Q/A*(1/3600);

V_max = V_average;   % Maximum velocity in a laminar flow, [m/s]
Dh = 2*5.842*w/(w + 5.842); % [mm]
% Dh = 2*(22 + 5.842)/pi;


b = Dh/2;

% Defining parameters
Diameter20 = data20.AverageDiameter3./5.84;
Velocity20 = data20.RisingVelocity3;
Velocity_Slot20 = data20.RisingVelocity_Slot3;
std_Velocity20 = data20.std_Velocity3;
std_Velocity_Slot20 = data20.std_Velocity_Slot3;
std_Centricity20 = data20.std_Centricity3;
std_Centricity_Slot20 = data20.std_Centricity_Slot3;

Diameter40 = data40.AverageDiameter3./5.84;
Velocity40 = data40.RisingVelocity3;
Velocity_Slot40 = data40.RisingVelocity_Slot3;
std_Velocity40 = data40.std_Velocity3;
std_Velocity_Slot40 = data40.std_Velocity_Slot3;
std_Centricity40 = data40.std_Centricity3;
std_Centricity_Slot40 = data40.std_Centricity_Slot3;

Diameter60 = data60.AverageDiameter3./5.84;
Velocity60 = data60.RisingVelocity3;
Velocity_Slot60 = data60.RisingVelocity_Slot3;
```

```
std_Velocity60 = data60.std_Velocity3;
std_Velocity_Slot60 = data60.std_Velocity_Slot3;
std_Centricity60 = data60.std_Centricity3;
std_Centricity_Slot60 = data60.std_Centricity_Slot3;

Diameter100 = data100.AverageDiameter3./5.84;
Velocity100 = data100.RisingVelocity3;
Velocity_Slot100 = data100.RisingVelocity_Slot3;
std_Velocity100 = data100.std_Velocity3;
std_Velocity_Slot100 = data100.std_Velocity_Slot3;
std_Centricity100 = data100.std_Centricity3;
std_Centricity_Slot100 = data100.std_Centricity_Slot3;

Diameter150 = data150.AverageDiameter3./5.84;
Velocity150 = data150.RisingVelocity3;
Velocity_Slot150 = data150.RisingVelocity_Slot3;
std_Velocity150 = data150.std_Velocity3;
std_Velocity_Slot150 = data150.std_Velocity_Slot3;
std_Centricity150 = data150.std_Centricity3;
std_Centricity_Slot150 = data150.std_Centricity_Slot3;

D20 = data20.AverageDiameter3;
D40 = data40.AverageDiameter3;
D60 = data60.AverageDiameter3;
D100 = data100.AverageDiameter3;
D150 = data150.AverageDiameter3;
V_max = Q./(w*5.842)./3600;
lambda20 = 0.5.*D20./b;
lambda40 = 0.5.*D40./b;
lambda60 = 0.5.*D60./b;
lambda100 = 0.5.*D100./b;
lambda150 = 0.5.*D150./b;

%%%%%%%%%%%%%%%%%%%%%%%%%%%%%%%%%%%%%%%%%%%%%%%%%%%%%%%%%%%%%%%%%%%%%%%%%%%%

k_1_20 = ((1 - 0.75857.*(1 - sigma)./(1 + (2/3).*sigma)*lambda20.^5))./ ...
    (1 - 2.1050.*(1 + (2/3).*sigma)./(1 + sigma).*lambda20 + ...
    2.0865.*(1./(1 + sigma).*lambda20.^3)- ...
    1.7068.*((1 - (2/3).*sigma)./(1 + sigma).*lambda20.^5)...
    + 0.72603.*(1 - sigma)./(1 + sigma).*lambda20.^6);
% Wall correction factor for spheres within a circle, when there is a bulk flow
k_2_20 = (1 - (2/3).*(1./(1 + 2/3.*sigma)).*lambda20.^2 - ...
    0.20217.*((1 - sigma)./(1 + 2/3.*sigma).*lambda20.^5))./...
    (1 - 2.1050.*(1 + (2/3).*sigma)./(1 + sigma).*lambda20 + ...
    2.0865.*(1./(1 + sigma).*lambda20.^3)- ...
    1.7068.*((1 - (2/3).*sigma)./(1 + sigma).*lambda20.^5)...
    + 0.72603.*(1 - sigma)./(1 + sigma).*lambda20.^6);
k_1_40 = ((1 - 0.75857.*(1 - sigma)./(1 + (2/3).*sigma)*lambda40.^5))./ ...
    (1 - 2.1050.*(1 + (2/3).*sigma)./(1 + sigma).*lambda40 + ...
    2.0865.*(1./(1 + sigma).*lambda40.^3)- ...
    1.7068.*((1 - (2/3).*sigma)./(1 + sigma).*lambda40.^5)...
    + 0.72603.*(1 - sigma)./(1 + sigma).*lambda40.^6);
% Wall correction factor for spheres within a circle, when there is a bulk flow
k_2_40 = (1 - (2/3).*(1./(1 + 2/3.*sigma)).*lambda40.^2 - ...
```

```
    0.20217.*((1 - sigma)./(1 + 2/3.*sigma).*lambda40.^5))./...
    (1 - 2.1050.*(1 + (2/3).*sigma)./(1 + sigma).*lambda40 + ...
    2.0865.*(1./(1 + sigma).*lambda40.^3)- ...
    1.7068.*((1 - (2/3).*sigma)./(1 + sigma).*lambda40.^5)...
    + 0.72603.*(1 - sigma)./(1 + sigma).*lambda40.^6);
k_1_60 = ((1 - 0.75857.*(1 - sigma)./(1 + (2/3).*sigma)*lambda60.^5))./ ...
    (1 - 2.1050.*(1 + (2/3).*sigma)./(1 + sigma).*lambda60 + ...
    2.0865.*(1./(1 + sigma).*lambda60.^3)- ...
    1.7068.*((1 - (2/3).*sigma)./(1 + sigma).*lambda60.^5)...
    + 0.72603.*(1 - sigma)./(1 + sigma).*lambda60.^6);
% Wall correction factor for spheres within a circle, when there is a bulk flow
k_2_60 = (1 - (2/3).*(1./(1 + 2/3.*sigma)).*lambda60.^2 - ...
    0.20217.*((1 - sigma)./(1 + 2/3.*sigma).*lambda60.^5))./...
    (1 - 2.1050.*(1 + (2/3).*sigma)./(1 + sigma).*lambda60 + ...
    2.0865.*(1./(1 + sigma).*lambda60.^3)- ...
    1.7068.*((1 - (2/3).*sigma)./(1 + sigma).*lambda60.^5)...
    + 0.72603.*(1 - sigma)./(1 + sigma).*lambda60.^6);
k_1_100 = ((1 - 0.75857.*(1 - sigma)./(1 + (2/3).*sigma)*lambda100.^5))./ ...
    (1 - 2.1050.*(1 + (2/3).*sigma)./(1 + sigma).*lambda100 + ...
    2.0865.*(1./(1 + sigma).*lambda100.^3)- ...
    1.7068.*((1 - (2/3).*sigma)./(1 + sigma).*lambda100.^5)...
    + 0.72603.*(1 - sigma)./(1 + sigma).*lambda100.^6);
% Wall correction factor for spheres within a circle, when there is a bulk flow
k_2_100 = (1 - (2/3).*(1./(1 + 2/3.*sigma)).*lambda100.^2 - ...
    0.20217.*((1 - sigma)./(1 + 2/3.*sigma).*lambda100.^5))./...
    (1 - 2.1050.*(1 + (2/3).*sigma)./(1 + sigma).*lambda100 + ...
    2.0865.*(1./(1 + sigma).*lambda100.^3)- ...
    1.7068.*((1 - (2/3).*sigma)./(1 + sigma).*lambda100.^5)...
    + 0.72603.*(1 - sigma)./(1 + sigma).*lambda100.^6);
k_1_150 = ((1 - 0.75857.*(1 - sigma)./(1 + (2/3).*sigma)*lambda150.^5))./ ...
    (1 - 2.1050.*(1 + (2/3).*sigma)./(1 + sigma).*lambda150 + ...
    2.0865.*(1./(1 + sigma).*lambda150.^3)- ...
    1.7068.*((1 - (2/3).*sigma)./(1 + sigma).*lambda150.^5)...
    + 0.72603.*(1 - sigma)./(1 + sigma).*lambda150.^6);
% Wall correction factor for spheres within a circle, when there is a bulk flow
k_2_150 = (1 - (2/3).*(1./(1 + 2/3.*sigma)).*lambda150.^2 - ...
    0.20217.*((1 - sigma)./(1 + 2/3.*sigma).*lambda150.^5))./...
    (1 - 2.1050.*(1 + (2/3).*sigma)./(1 + sigma).*lambda150 + ...
    2.0865.*(1./(1 + sigma).*lambda150.^3)- ...
    1.7068.*((1 - (2/3).*sigma)./(1 + sigma).*lambda150.^5)...
    + 0.72603.*(1 - sigma)./(1 + sigma).*lambda150.^6);
%%%%%%%%%%%%%%%%%%%%%%%%%%%%%%%%%%%%%%%%%%%%%%%%%%%%%%%%%%%%%%%%%%%%%%%%%%%%

U20 = (((2/9).*(((D20./2).*0.001).^2.*g.*(density_fluid - density_particle).*(1 + sigma) ...
    ./(viscosity_fluid.*k_1_20.*(1 + (2/3).*sigma)))) + V_max20.*k_2_20./k_1_20).*1000;
U40 = (((2/9).*(((D40./2).*0.001).^2.*g.*(density_fluid - density_particle).*(1 + sigma) ...
    ./(viscosity_fluid.*k_1_40.*(1 + (2/3).*sigma)))) + V_max40.*k_2_40./k_1_40).*1000;
U60 = (((2/9).*(((D60./2).*0.001).^2.*g.*(density_fluid - density_particle).*(1 + sigma) ...
    ./(viscosity_fluid.*k_1_60.*(1 + (2/3).*sigma)))) + V_max60.*k_2_60./k_1_60).*1000;
U100 = (((2/9).*(((D100./2).*0.001).^2.*g.*(density_fluid - density_particle).*(1 + sigma) ...
    ./(viscosity_fluid.*k_1_100.*(1 + (2/3).*sigma)))) + V_max100.*k_2_100./k_1_100).*1000;
U150 = (((2/9).*(((D150./2).*0.001).^2.*g.*(density_fluid - density_particle).*(1 + sigma) ...
    ./(viscosity_fluid.*k_1_150.*(1 + (2/3).*sigma)))) + V_max150.*k_2_150./k_1_150).*1000;
% X = [U', lambda'];
```

```
% Y = [data20.RisingVelocity_Slot3'];
% X = [lambda20';lambda40';lambda60';lambda100';lambda150'];
X = [U20';U40';U60';U100';U150'];
Y = [data20.RisingVelocity3';data40.RisingVelocity3';data60.RisingVelocity3'; ...
    data100.RisingVelocity3';data150.RisingVelocity3'];

% we have a model, and we need to find the STD of the data points and the
% model. Since we do not want the model to change, an "a" coefficient is
% multiplied to the model function and it is restricted by lower and upper
% bounds to remain 1.

fit_options = fitoptions('Method','NonlinearLeastSquares','Lower',[1],'Upper',[1.01]);
fit_type = fittype('a*x ','options',fit_options);
[equation,other] = fit(X,Y,fit_type);

%%%%%%%%%%%%%%%%%%%%%%%%%%%%%%%%%%%%%%%%%%%%%%%%%%%%%%%%%%%%%%%%%%%%%%%%%%%%

lambda = R./b;
k_1 = ((1 - 0.75857.*(1 - sigma)./(1 + (2/3).*sigma)*lambda.^5))./ ...
    (1 - 2.1050.*(1 + (2/3).*sigma)./(1 + sigma).*lambda + ...
    2.0865.*(1./(1 + sigma).*lambda.^3)- ...
    1.7068.*((1 - (2/3).*sigma)./(1 + sigma).*lambda.^5)...
    + 0.72603.*(1 - sigma)./(1 + sigma).*lambda.^6);
% Wall correction factor for spheres within a circle, when there is a bulk flow

k_2 = (1 - (2/3).*(1./(1 + 2/3.*sigma)).*lambda.^2 - ...
    0.20217.*((1 - sigma)./(1 + 2/3.*sigma).*lambda.^5))./...
    (1 - 2.1050.*(1 + (2/3).*sigma)./(1 + sigma).*lambda + ...
    2.0865.*(1./(1 + sigma).*lambda.^3)- ...
    1.7068.*((1 - (2/3).*sigma)./(1 + sigma).*lambda.^5)...
    + 0.72603.*(1 - sigma)./(1 + sigma).*lambda.^6);

%%%%%%%%%%%%%%%%%%%%%%%%%%%%%%%%%%%%%%%%%%%%%%%%%%%%%%%%%%%%%%%%%%%%%%%%%%%%
% RISING VELOCITY PLOT WITH CORRECTED MODEL (THROUGH THE SLOT)
close all
figure(1);
hold on
set(1,'pos',[70 70 1200 800]);
set(gcf,'color','w');
set(gca,'fontsize',font_size)

h1=errorbar(Diameter_Slot20, Velocity_Slot20,std_Velocity_Slot20,'s','MarkerEdgeColor','b',...
    'MarkerSize',marker_size,'LineWidth',line_width_size,'Color','k');

hold on
h2=plot(R./(w/2), AverageVelocity_Corrected20,'b-','MarkerEdgeColor','b',...
    'MarkerSize',5,'LineWidth',2);
hold on
h3=errorbar(Diameter_Slot40, Velocity_Slot40,std_Velocity_Slot40,'d','MarkerEdgeColor','k',...
    'MarkerSize',marker_size,'LineWidth',line_width_size,'Color','k');
hold on
h4=plot(R./(w/2), AverageVelocity_Corrected40,'k-.',...
    'MarkerSize',5,'LineWidth',2);
hold on
```

```
h5=errorbar(Diameter_Slot60, Velocity_Slot60,std_Velocity_Slot60,'o','MarkerEdgeColor','r',...
    'MarkerSize',marker_size,'LineWidth',line_width_size,'Color','k');
hold on
h6=plot(R./(w/2), AverageVelocity_Corrected60,'r:','MarkerEdgeColor','r',...
    'MarkerFaceColor','r',...
    'MarkerSize',5,'LineWidth',2);
hold on
h7=errorbar(Diameter_Slot100, Velocity_Slot100,std_Velocity_Slot100,'^','MarkerEdgeColor','b',...
    'MarkerSize',marker_size,'LineWidth',line_width_size,'Color','k');
hold on
h8=plot(R./(w/2), AverageVelocity_Corrected100,'b--',...
    'MarkerSize',5,'LineWidth',2);
hold on
h9=errorbar(Diameter_Slot150, Velocity_Slot150,std_Velocity_Slot150,'v','MarkerEdgeColor','k',...
    'MarkerSize',marker_size,'LineWidth',line_width_size,'Color','k');
hold on
h10=plot(R./(w/2), AverageVelocity_Corrected150,'k-',...
    'MarkerSize',5,'LineWidth',2);
% Inserting a star at the points representing the prediction of rising
% velocity as bubble diameter approaches zero
hold on
plot(0,0.4748,'r*','LineWidth',line_width_size,'MarkerSize',marker_size)
hold on
plot(0,0.9593,'r*','LineWidth',line_width_size,'MarkerSize',marker_size)
hold on
plot(0,1.521,'r*','LineWidth',line_width_size,'MarkerSize',marker_size)
hold on
plot(0,2.541,'r*','LineWidth',line_width_size,'MarkerSize',marker_size)
hold on
plot(0,3.775,'r*','LineWidth',line_width_size,'MarkerSize',marker_size)
hold on
xlabel('{\itD_{e}/w}','FontSize',font_size,'FontName', 'Times New Roman');
ylabel('{\it V_{t-RCSR}} (mm/s)','FontSize',font_size,'FontName', 'Times New Roman');
legendflex([h1,h2,h3,h4,h5],{'{\itq_{1-RCSR}} = 0.34 mm/s','Modified theory for {\itq_{1-RCSR}}',
...
   '{\itq_{2-RCSR}} = 0.67 mm/s','Modified theory for {\itq_{2-RCSR}}', ...
   '{\itq_{3-RCSR}} = 1.07 mm/s'}', ...
   'ref', gcf,'FontSize',19)
legendflex([h6,h7,h8,h9,h10],{'Modified theory for {\itq_{3-RCSR}}', ...
   '{\itq_{4-RCSR}} = 1.78 mm/s','Modified theory for {\itq_{4-RCSR}}', ...
   '{\itq_{5-RCSR}} = 2.64 mm/s','Modified theory for {\itq_{5-RCSR}}'}', ...
   'ref', gcf,'FontSize',19)
axis([0 1.1 0 5.5])
% saveas(gcf,'Rising Velocity Zoomin_Modified_QAll.fig')

% RE NUMBER
figure(2);
hold on
set(2,'pos',[70 70 1200 800]);
set(gcf,'color','w');
set(gca,'fontsize',font_size)

% Re number before and after the slot
Re20 = ((density_fluid.*((0.001.*data20.RisingVelocity3) -
```

```
V_max20.*3./22)).*(0.001.*data20.AverageDiameter3))./viscosity_fluid;
Re40 = ((density_fluid.*((0.001.*data40.RisingVelocity3) -
V_max40.*3./22)).*(0.001.*data40.AverageDiameter3))./viscosity_fluid;
Re60 = ((density_fluid.*((0.001.*data60.RisingVelocity3) -
V_max60.*3./22)).*(0.001.*data60.AverageDiameter3))./viscosity_fluid;
Re100 = ((density_fluid.*((0.001.*data100.RisingVelocity3) -
V_max100.*3./22)).*(0.001.*data100.AverageDiameter3))./viscosity_fluid;
Re150 = ((density_fluid.*((0.001.*data150.RisingVelocity3) -
V_max150.*3./22)).*(0.001.*data150.AverageDiameter3))./viscosity_fluid;

% Re number through the slot
Re_Slot20 = ((density_fluid.*((0.001.*data20.RisingVelocity_Slot3) -
V_max20)).*(0.001.*data20.AverageDiameter3))./viscosity_fluid;
Re_Slot40 = ((density_fluid.*((0.001.*data40.RisingVelocity_Slot3) -
V_max40)).*(0.001.*data40.AverageDiameter3))./viscosity_fluid;
Re_Slot60 = ((density_fluid.*((0.001.*data60.RisingVelocity_Slot3) -
V_max60)).*(0.001.*data60.AverageDiameter3))./viscosity_fluid;
Re_Slot100 = ((density_fluid.*((0.001.*data100.RisingVelocity_Slot3) -
V_max100)).*(0.001.*data100.AverageDiameter3))./viscosity_fluid;
Re_Slot150 = ((density_fluid.*((0.001.*data150.RisingVelocity_Slot3) -
V_max150)).*(0.001.*data150.AverageDiameter3))./viscosity_fluid;

% Calculating the STD for Re number based on STD of averaged rising
% velocity
std_Re20 = 0.001.*sqrt(data20.std_Velocity3.^2 + data20.std_Diameter3.^2);
std_Re40 = 0.001.*sqrt(data40.std_Velocity3.^2 + data40.std_Diameter3.^2);
std_Re60 = 0.001.*sqrt(data60.std_Velocity3.^2 + data60.std_Diameter3.^2);
std_Re100 = 0.001.*sqrt(data100.std_Velocity3.^2 + data100.std_Diameter3.^2);
std_Re150 = 0.001.*sqrt(data150.std_Velocity3.^2 + data150.std_Diameter3.^2);

std_Re_Slot20 = 0.001.*sqrt(data20.std_Velocity_Slot3.^2 + data20.std_Diameter_Slot3.^2);
std_Re_Slot40 = 0.001.*sqrt(data40.std_Velocity_Slot3.^2 + data40.std_Diameter_Slot3.^2);
std_Re_Slot60 = 0.001.*sqrt(data60.std_Velocity_Slot3.^2 + data60.std_Diameter_Slot3.^2);
std_Re_Slot100 = 0.001.*sqrt(data100.std_Velocity_Slot3.^2 + data100.std_Diameter_Slot3.^2);
std_Re_Slot150 = 0.001.*sqrt(data150.std_Velocity_Slot3.^2 + data150.std_Diameter_Slot3.^2);


errorbar(Diameter20, Re20,std_Re20,'s','MarkerEdgeColor','b',...
    'MarkerSize',marker_size,'LineWidth',line_width_size,'Color','k');
hold on

errorbar(Diameter40, Re40,std_Re40,'d','MarkerEdgeColor','k',...
    'MarkerSize',marker_size,'LineWidth',line_width_size,'Color','k');
hold on

errorbar(Diameter60, Re60,std_Re60,'o','MarkerEdgeColor','r',...
    'MarkerSize',marker_size,'LineWidth',line_width_size,'Color','k');
hold on

errorbar(Diameter100, Re100,std_Re100,'^','MarkerEdgeColor','b',...
    'MarkerSize',marker_size,'LineWidth',line_width_size,'Color','k');
hold on

errorbar(Diameter150, Re150,std_Re150,'v','MarkerEdgeColor','k',...
```

```
    'MarkerSize',marker_size,'LineWidth',line_width_size,'Color','k');

xlabel('{\itD_{e}/t}','FontSize',font_size,'FontName', 'Times New Roman');
ylabel('{\it Re_{PPR}}','FontSize',font_size,'FontName', 'Times New Roman');
legendflex({'{\itq_{1-PPR}} = 0.05 mm/s', ...
    '{\itq_{2-PPR}} = 0.09 mm/s', ...
    '{\itq_{3-PPR}} = 0.15 mm/s', ...
    '{\itq_{4-PPR}} = 0.24 mm/s', ...
    '{\itq_{5-PPR}} = 0.36 mm/s'})
% saveas(gcf,'Re_QAll.fig')
% The unmodified theory which predicts the rising velocity of
% air bubbles rising in circular tubes, is calculated inside the figure
% commands


figure(3);
hold on
set(3,'pos',[70 70 1200 800]);
set(gcf,'color','w');
set(gca,'fontsize',font_size)

errorbar(Diameter20, (Velocity20 - 1000*V_max20.*3./22), ...
    std_Velocity20,'s','MarkerEdgeColor','b',...
    'MarkerSize',marker_size,'LineWidth',line_width_size,'Color','k');
hold on

errorbar(Diameter40, (Velocity40 - 1000*V_max40.*3./22)...
    ,std_Velocity40,'d','MarkerEdgeColor','k',...
    'MarkerSize',marker_size,'LineWidth',line_width_size,'Color','k');
hold on

errorbar(Diameter60, (Velocity60 - 1000*V_max60.*3./22)...
    ,std_Velocity60,'o','MarkerEdgeColor','r',...
    'MarkerSize',marker_size,'LineWidth',line_width_size,'Color','k');
hold on

errorbar(Diameter100, (Velocity100 - 1000*V_max100.*3./22)...
    ,std_Velocity100,'^','MarkerEdgeColor','b',...
    'MarkerSize',marker_size,'LineWidth',line_width_size,'Color','k');
hold on

errorbar(Diameter150, (Velocity150 - 1000*V_max150.*3./22)...
    ,std_Velocity150,'v','MarkerEdgeColor','k',...
    'MarkerSize',marker_size,'LineWidth',line_width_size,'Color','k');
hold on
U_Inf = (((2/3).*((R.*0.001).^2.*g.*(density_fluid - density_particle).*(1 + 1./sigma) ...
    ./(viscosity_fluid.*(2 + 3./sigma))))).*1000;
% Theoretical rising velocity for parallel plates.
U = (((2/9).*((R.*0.001).^2.*g.*(density_fluid - density_particle).*(1 + sigma) ...
    ./(viscosity_fluid.*k_w2Hirad.*(1 + (2/3).*sigma))))).*1000; % Terminal rising velocity,
[mm/s]
plot(R./(5.84/2), U,'r-','MarkerEdgeColor','b',...
    'MarkerFaceColor','b',...
    'MarkerSize',5,'LineWidth',2);
```

```
% hold on
% plot(R./(5.84/2), U_Inf,'k--','MarkerEdgeColor','b',...
%     'MarkerFaceColor','b',...
%     'MarkerSize',5,'LineWidth',2);
xlabel('{\itD_{e}/t}','FontSize',font_size,'FontName', 'Times New Roman');
ylabel('{\itV_{t-PPR} - V_{f-PPR}} (mm/s)','FontSize',font_size,'FontName', 'Times New Roman');
legendflex({'{\itq_{1-PPR}} = 0.05 mm/s', ...
    '{\itq_{2-PPR}} = 0.09 mm/s', ...
    '{\itq_{3-PPR}} = 0.15 mm/s', ...
    '{\itq_{4-PPR}} = 0.24 mm/s', ...
    '{\itq_{5-PPR}} = 0.36 mm/s', ...
    'Theory of two parallel plates'})
axis([0 0.55 0 12])
saveas(gcf,'Zoomout Velocity_Plates_QAll.fig')

% ************************************************************************
figure(4);
hold on
set(4,'pos',[70 70 1200 800]);
set(gcf,'color','w');
set(gca,'fontsize',font_size)
errorbar(Diameter20, data20.Centricity3,std_Centricity20,'s','MarkerEdgeColor','b',...
    'MarkerSize',marker_size,'LineWidth',line_width_size,'Color','k');
hold on
errorbar(Diameter40, data40.Centricity3,std_Centricity40,'d','MarkerEdgeColor','k',...
    'MarkerSize',marker_size,'LineWidth',line_width_size,'Color','k');
hold on
errorbar(Diameter60, data60.Centricity3,std_Centricity60,'o','MarkerEdgeColor','r',...
    'MarkerSize',marker_size,'LineWidth',line_width_size,'Color','k');
hold on
errorbar(Diameter100, data100.Centricity3,std_Centricity100,'^','MarkerEdgeColor','b',...
    'MarkerSize',marker_size,'LineWidth',line_width_size,'Color','k');
hold on
errorbar(Diameter150, data150.Centricity3,std_Centricity150,'v','MarkerEdgeColor','k',...
    'MarkerSize',marker_size,'LineWidth',line_width_size,'Color','k');
% grid minor
hold on
% Plotting the second x-axis. In the images, 1 pixel is 0.031 mm.

axisH = gca;
addTopXAxis(axisH, 'expression', '5.842.*argu./0.031', 'xLabStr', '{\itD_{e}} (pixels)')
xlabel('{\itD_{e}/t}','FontSize',font_size,'FontName', 'Times New Roman');
ylabel('{\itC_{b-PPR}}','FontSize',font_size,'FontName', 'Times New Roman');
legendflex({'{\itq_{1-PPR}} = 0.05 mm/s', ...
    '{\itq_{2-PPR}} = 0.09 mm/s', ...
    '{\itq_{3-PPR}} = 0.15 mm/s', ...
    '{\itq_{4-PPR}} = 0.24 mm/s', ...
    '{\itq_{5-PPR}} = 0.36 mm/s'})
axis([0 0.55 0.75 1])
% saveas(gcf,'Centricity_QAll.fig')

% ************************************************************************
figure(5);
hold on
```

```
set(gcf,'pos',[70 70 1200 800]);
set(gcf,'color','w');
set(gca,'fontsize',font_size)

h1=errorbar(Diameter_Slot20, Velocity_Slot20 - 0.95.*(1 -
lambda20.^2).*Q20,std_Velocity_Slot20,'s','MarkerEdgeColor','b',...
    'MarkerSize',marker_size,'LineWidth',line_width_size,'Color','k');

hold on
h2=errorbar(Diameter_Slot40, Velocity_Slot40 - 0.95.*(1 -
lambda40.^2).*Q40,std_Velocity_Slot40,'d','MarkerEdgeColor','k',...
    'MarkerSize',marker_size,'LineWidth',line_width_size,'Color','k');
hold on
h3=errorbar(Diameter_Slot60, Velocity_Slot60 - 0.95.*(1 -
lambda60.^2).*Q60,std_Velocity_Slot60,'o','MarkerEdgeColor','r',...
    'MarkerSize',marker_size,'LineWidth',line_width_size,'Color','k');
hold on
h4=errorbar(Diameter_Slot100, Velocity_Slot100 - 0.95.*(1 -
lambda100.^2).*Q100,std_Velocity_Slot100,'^','MarkerEdgeColor','b',...
    'MarkerSize',marker_size,'LineWidth',line_width_size,'Color','k');
hold on
h5=errorbar(Diameter_Slot150, Velocity_Slot150 - 0.95.*(1 -
lambda150.^2).*Q150,std_Velocity_Slot150,'v','MarkerEdgeColor','k',...
    'MarkerSize',marker_size,'LineWidth',line_width_size,'Color','k');
hold on
h6=plot(R./(w/2), AverageVelocity_Corrected150 - 0.95.*(1 - lambda.^2).*Q150(1),'k-',...
    'MarkerSize',5,'LineWidth',2);
% Inserting a star at the points representing the prediction of rising
% velocity as bubble diameter approaches zero
hold on
xlabel('{\itD_{e}/w}','FontSize',font_size,'FontName', 'Times New Roman');
ylabel('{\it V_{t-RCSR} - 0.95{\it(1 - \lambda^2)V_{t-RCSR}}}
(mm/s)','FontSize',font_size,'FontName', 'Times New Roman');
legendflex([h1,h2,h3,h4,h5,h6],{'{\itq_{1-RCSR}} = 0.34 mm/s', ...
   '{\itq_{2-RCSR}} = 0.67 mm/s','{\itq_{3-RCSR}} = 1.07 mm/s', ...
   '{\itq_{4-RCSR}} = 1.78 mm/s','{\itq_{5-RCSR}} = 2.64 mm/s','Modified theory with {\itq}  =
0'}', ...
   'ref', gcf,'FontSize',19)
axis([0 1.1 0 3.5])
% saveas(gcf,'Rising Velocity Zoomin_Modified_QAll.fig')


% %%%%%%%%%%%%%%%%%%%%%%%%%%%%%%%%%%%%%%%%%%%%%%%%%%%%%%%%%%%%%%%%%%%%%%%%%%%%%%%

% RISING VELOCITY THROUGH THE SLOT REGION

%%%%%%%%%%%%%%%%%%%%%%%%%%%%%%%%%%%%%%%%%%%%%%%%%%%%%%%%%%%%%%%%%%%%%%%%%%%%%%%


w = 3; % Slot/Flow cell width, mm
A = 5.842 * w;   % mm2
V_average = Q/A * (1/3600);
V_max20_Slot = 0.000503;
V_max40_Slot = 0.001008;
```

```
V_max60_Slot = 0.001598;
V_max100_Slot = 0.00267;
V_max150_Slot = 0.003966;   % Maximum velocity in a laminar flow, [m/s]
Dh = 2*5.842*w/(w + 5.842);%, [mm]
b = Dh/2;  % b is equal to half diameter of the tube. Here, we assume that
% we have a hydrolic diameter and suppose "b" is half of that
lambda20 = 0.5.*D20./b;
lambda40 = 0.5.*D40./b;
lambda60 = 0.5.*D60./b;
lambda100 = 0.5.*D100./b;
lambda150 = 0.5.*D150./b;
lambda = R./b;
%%%%%%%%%%%%%%%%%%%%%%%%%%%%%%%%%%%%%%%%%%%%%%%%%%%%%%%%%%%%%%%%%%%%%%%%%%%%
k_1 = ((1 - 0.75857.*(1 - sigma)./(1 + (2/3).*sigma)*lambda.^5))./ ...
    (1 - 2.1050.*(1 + (2/3).*sigma)./(1 + sigma).*lambda + ...
    2.0865.*(1./(1 + sigma).*lambda.^3)- ...
    1.7068.*((1 - (2/3).*sigma)./(1 + sigma).*lambda.^5)...
    + 0.72603.*(1 - sigma)./(1 + sigma).*lambda.^6);
% Wall correction factor for spheres within a circle, when there is a bulk flow

k_2 = (1 - (2/3).*(1./(1 + 2/3.*sigma)).*lambda.^2 - ...
    0.20217.*((1 - sigma)./(1 + 2/3.*sigma).*lambda.^5))./...
    (1 - 2.1050.*(1 + (2/3).*sigma)./(1 + sigma).*lambda + ...
    2.0865.*(1./(1 + sigma).*lambda.^3)- ...
    1.7068.*((1 - (2/3).*sigma)./(1 + sigma).*lambda.^5)...
    + 0.72603.*(1 - sigma)./(1 + sigma).*lambda.^6);
k_1_20 = ((1 - 0.75857.*(1 - sigma)./(1 + (2/3).*sigma)*lambda20.^5))./ ...
    (1 - 2.1050.*(1 + (2/3).*sigma)./(1 + sigma).*lambda20 + ...
    2.0865.*(1./(1 + sigma).*lambda20.^3)- ...
    1.7068.*((1 - (2/3).*sigma)./(1 + sigma).*lambda20.^5)...
    + 0.72603.*(1 - sigma)./(1 + sigma).*lambda20.^6);
% Wall correction factor for spheres within a circle, when there is a bulk flow
k_2_20 = (1 - (2/3).*(1./(1 + 2/3.*sigma)).*lambda20.^2 - ...
    0.20217.*((1 - sigma)./(1 + 2/3.*sigma).*lambda20.^5))./...
    (1 - 2.1050.*(1 + (2/3).*sigma)./(1 + sigma).*lambda20 + ...
    2.0865.*(1./(1 + sigma).*lambda20.^3)- ...
    1.7068.*((1 - (2/3).*sigma)./(1 + sigma).*lambda20.^5)...
    + 0.72603.*(1 - sigma)./(1 + sigma).*lambda20.^6);
k_1_40 = ((1 - 0.75857.*(1 - sigma)./(1 + (2/3).*sigma)*lambda40.^5))./ ...
    (1 - 2.1050.*(1 + (2/3).*sigma)./(1 + sigma).*lambda40 + ...
    2.0865.*(1./(1 + sigma).*lambda40.^3)- ...
    1.7068.*((1 - (2/3).*sigma)./(1 + sigma).*lambda40.^5)...
    + 0.72603.*(1 - sigma)./(1 + sigma).*lambda40.^6);
% Wall correction factor for spheres within a circle, when there is a bulk flow
k_2_40 = (1 - (2/3).*(1./(1 + 2/3.*sigma)).*lambda40.^2 - ...
    0.20217.*((1 - sigma)./(1 + 2/3.*sigma).*lambda40.^5))./...
    (1 - 2.1050.*(1 + (2/3).*sigma)./(1 + sigma).*lambda40 + ...
    2.0865.*(1./(1 + sigma).*lambda40.^3)- ...
    1.7068.*((1 - (2/3).*sigma)./(1 + sigma).*lambda40.^5)...
    + 0.72603.*(1 - sigma)./(1 + sigma).*lambda40.^6);
k_1_60 = ((1 - 0.75857.*(1 - sigma)./(1 + (2/3).*sigma)*lambda60.^5))./ ...
    (1 - 2.1050.*(1 + (2/3).*sigma)./(1 + sigma).*lambda60 + ...
    2.0865.*(1./(1 + sigma).*lambda60.^3)- ...
    1.7068.*((1 - (2/3).*sigma)./(1 + sigma).*lambda60.^5)...
```

```
    + 0.72603.*(1 - sigma)./(1 + sigma).*lambda60.^6);
% Wall correction factor for spheres within a circle, when there is a bulk flow
k_2_60 = (1 - (2/3).*(1./(1 + 2/3.*sigma)).*lambda60.^2 - ...
    0.20217.*((1 - sigma)./(1 + 2/3.*sigma).*lambda60.^5))./...
    (1 - 2.1050.*(1 + (2/3).*sigma)./(1 + sigma).*lambda60 + ...
    2.0865.*(1./(1 + sigma).*lambda60.^3)- ...
    1.7068.*((1 - (2/3).*sigma)./(1 + sigma).*lambda60.^5)...
    + 0.72603.*(1 - sigma)./(1 + sigma).*lambda60.^6);
k_1_100 = ((1 - 0.75857.*(1 - sigma)./(1 + (2/3).*sigma)*lambda100.^5))./ ...
    (1 - 2.1050.*(1 + (2/3).*sigma)./(1 + sigma).*lambda100 + ...
    2.0865.*(1./(1 + sigma).*lambda100.^3)- ...
    1.7068.*((1 - (2/3).*sigma)./(1 + sigma).*lambda100.^5)...
    + 0.72603.*(1 - sigma)./(1 + sigma).*lambda100.^6);
% Wall correction factor for spheres within a circle, when there is a bulk flow
k_2_100 = (1 - (2/3).*(1./(1 + 2/3.*sigma)).*lambda100.^2 - ...
    0.20217.*((1 - sigma)./(1 + 2/3.*sigma).*lambda100.^5))./...
    (1 - 2.1050.*(1 + (2/3).*sigma)./(1 + sigma).*lambda100 + ...
    2.0865.*(1./(1 + sigma).*lambda100.^3)- ...
    1.7068.*((1 - (2/3).*sigma)./(1 + sigma).*lambda100.^5)...
    + 0.72603.*(1 - sigma)./(1 + sigma).*lambda100.^6);
k_1_150 = ((1 - 0.75857.*(1 - sigma)./(1 + (2/3).*sigma)*lambda150.^5))./ ...
    (1 - 2.1050.*(1 + (2/3).*sigma)./(1 + sigma).*lambda150 + ...
    2.0865.*(1./(1 + sigma).*lambda150.^3)- ...
    1.7068.*((1 - (2/3).*sigma)./(1 + sigma).*lambda150.^5)...
    + 0.72603.*(1 - sigma)./(1 + sigma).*lambda150.^6);
% Wall correction factor for spheres within a circle, when there is a bulk flow
k_2_150 = (1 - (2/3).*(1./(1 + 2/3.*sigma)).*lambda150.^2 - ...
    0.20217.*((1 - sigma)./(1 + 2/3.*sigma).*lambda150.^5))./...
    (1 - 2.1050.*(1 + (2/3).*sigma)./(1 + sigma).*lambda150 + ...
    2.0865.*(1./(1 + sigma).*lambda150.^3)- ...
    1.7068.*((1 - (2/3).*sigma)./(1 + sigma).*lambda150.^5)...
    + 0.72603.*(1 - sigma)./(1 + sigma).*lambda150.^6);
%%%%%%%%%%%%%%%%%%%%%%%%%%%%%%%%%%%%%%%%%%%%%%%%%%%%%%%%%%%%%%%%%%%%%%%%%%%%

% The MODIFIED theory which predicts the rising velocity of
% air bubbles rising in circular tubes, is calculated inside the figure
% commands

figure(6);
hold on
set(6,'pos',[70 70 1200 800]);
set(gcf,'color','w');
set(gca,'fontsize',font_size)
errorbar(Diameter_Slot20,Re_Slot20,std_Re_Slot20,'s','MarkerEdgeColor','b',...
    'MarkerSize',marker_size,'LineWidth',line_width_size,'Color','k');
hold on

errorbar(Diameter_Slot40,Re_Slot40,std_Re_Slot40,'d','MarkerEdgeColor','k',...
    'MarkerSize',marker_size,'LineWidth',line_width_size,'Color','k');
hold on

errorbar(Diameter_Slot60,Re_Slot60,std_Re_Slot60,'o','MarkerEdgeColor','r',...
    'MarkerSize',marker_size,'LineWidth',line_width_size,'Color','k');
hold on
```

```
errorbar(Diameter_Slot100,Re_Slot100,std_Re_Slot100,'^','MarkerEdgeColor','b',...
    'MarkerSize',marker_size,'LineWidth',line_width_size,'Color','k');
hold on

errorbar(Diameter_Slot150,Re_Slot150,std_Re_Slot150,'v','MarkerEdgeColor','k',...
    'MarkerSize',marker_size,'LineWidth',line_width_size,'Color','k');
hold on

xlabel('{\itD_{e}/w}','FontSize',font_size,'FontName', 'Times New Roman');
ylabel('{\it Re}','FontSize',font_size,'FontName', 'Times New Roman');
legendflex({'{\itq_{1-RCSR}} = 0.34 mm/s', ...
    '{\itq_{2-RCSR}} = 0.67 mm/s', ...
    '{\itq_{3-RCSR}} = 1.07 mm/s', ...
    '{\itq_{4-RCSR}} = 1.78 mm/s', ...
    '{\itq_{5-RCSR}} = 2.64 mm/s'});
% axis([0.2 1.2 0 5.5])
% saveas(gcf,'Re_Slot_QAll.fig')

figure(7);
hold on
set(7,'pos',[70 70 1200 800]);
set(gcf,'color','w');
set(gca,'fontsize',font_size)
errorbar(Diameter_Slot20, Velocity_Slot20,std_Velocity_Slot20,'s','MarkerEdgeColor','b',...
    'MarkerSize',marker_size,'LineWidth',line_width_size,'Color','k');
hold on
U = (((2/9).*((R.*0.001).^2.*g.*(density_fluid - density_particle).*(1 + sigma) ...
    ./(viscosity_fluid.*k_1.*(1 + (2/3).*sigma)))) + V_max20_Slot.*k_2./k_1).*1000;
plot(R./(w/2), U,'b-','MarkerEdgeColor','b',...
    'MarkerFaceColor','b',...
    'MarkerSize',5,'LineWidth',2);
hold on
errorbar(Diameter_Slot40, Velocity_Slot40,std_Velocity_Slot40,'d','MarkerEdgeColor','k',...
    'MarkerSize',marker_size,'LineWidth',line_width_size,'Color','k');
hold on
U = (((2/9).*((R.*0.001).^2.*g.*(density_fluid - density_particle).*(1 + sigma) ...
    ./(viscosity_fluid.*k_1.*(1 + (2/3).*sigma)))) + V_max40_Slot.*k_2./k_1).*1000;
plot(R./(w/2), U,'k-.',...
    'MarkerSize',5,'LineWidth',2);
hold on
errorbar(Diameter_Slot60, Velocity_Slot60,std_Velocity_Slot60,'o','MarkerEdgeColor','r',...
    'MarkerSize',marker_size,'LineWidth',line_width_size,'Color','k');
hold on
U = (((2/9).*((R.*0.001).^2.*g.*(density_fluid - density_particle).*(1 + sigma) ...
    ./(viscosity_fluid.*k_1.*(1 + (2/3).*sigma)))) + V_max60_Slot.*k_2./k_1).*1000;

plot(R./(w/2), U,'r:','MarkerEdgeColor','b',...
    'MarkerFaceColor','b',...
    'MarkerSize',5,'LineWidth',2);
hold on
errorbar(Diameter_Slot100, Velocity_Slot100,std_Velocity_Slot100,'^','MarkerEdgeColor','b',...
    'MarkerSize',marker_size,'LineWidth',line_width_size,'Color','k');
hold on
```

```
U = (((2/9).*((R.*0.001).^2.*g.*(density_fluid - density_particle).*(1 + sigma) ...
    ./(viscosity_fluid.*k_1.*(1 + (2/3).*sigma)))) + V_max100_Slot.*k_2./k_1).*1000;

plot(R./(w/2), U,'b--',...
    'MarkerSize',5,'LineWidth',2);
hold on
errorbar(Diameter_Slot150, Velocity_Slot150,std_Velocity_Slot150,'v','MarkerEdgeColor','k',...
    'MarkerSize',marker_size,'LineWidth',line_width_size,'Color','k');
hold on
U = (((2/9).*((R.*0.001).^2.*g.*(density_fluid - density_particle).*(1 + sigma) ...
    ./(viscosity_fluid.*k_1.*(1 + (2/3).*sigma)))) + V_max150_Slot.*k_2./k_1).*1000;
plot(R./(w/2), U,'k-','MarkerEdgeColor','b',...
    'MarkerFaceColor','b',...
    'MarkerSize',5,'LineWidth',2);
hold on

plot(0,0.503,'r*','LineWidth',line_width_size,'MarkerSize',marker_size)
hold on
plot(0,1.008,'r*','LineWidth',line_width_size,'MarkerSize',marker_size)
hold on
plot(0,1.598,'r*','LineWidth',line_width_size,'MarkerSize',marker_size)
hold on
plot(0,2.67,'r*','LineWidth',line_width_size,'MarkerSize',marker_size)
hold on
plot(0,3.966,'r*','LineWidth',line_width_size,'MarkerSize',marker_size)
hold on
xlabel('{\itD_{e}/w}','FontSize',font_size,'FontName', 'Times New Roman');
ylabel('{\it V_{ave}} (mm/s)','FontSize',font_size,'FontName', 'Times New Roman');% figure(2);
legendflex([h1,h2,h3,h4,h5],{'{\itq_{1-RCSR}} = 0.34 mm/s','Modified theory for {\itq_{1-RCSR}}',
...
   '{\itq_{2-RCSR}} = 0.67 mm/s','Modified theory for {\itq_{2-RCSR}}', ...
   '{\itq_{3-RCSR}} = 1.07 mm/s'}', ...
   'ref', gcf,'FontSize',17)
legendflex([h6,h7,h8,h9,h10],{'Modified theory for {\itq_{3-RCSR}}', ...
   '{\itq_{4-RCSR}} = 1.78 mm/s','Modified theory for {\itq_{4-RCSR}}', ...
   '{\itq_{5-RCSR}} = 2.64 mm/s','Modified theory for {\itq_{5-RCSR}}'}', ...
   'ref', gcf,'FontSize',17)
axis([0 1.1 0 7])
% saveas(gcf,'Zoomin Velocity_Tube_Unmodified_QAll.fig')


figure(8);
hold on
set(gcf,'pos',[70 70 1200 800]);
set(gcf,'color','w');
set(gca,'fontsize',font_size)
errorbar(Diameter_Slot20,
data20.Centricity_Slot3,std_Centricity_Slot20,'s','MarkerEdgeColor','b',...
    'MarkerSize',marker_size,'LineWidth',line_width_size,'Color','k');
hold on
errorbar(Diameter_Slot40,
data40.Centricity_Slot3,std_Centricity_Slot40,'d','MarkerEdgeColor','k',...
    'MarkerSize',marker_size,'LineWidth',line_width_size,'Color','k');
hold on
```

```
errorbar(Diameter_Slot60,
data60.Centricity_Slot3,std_Centricity_Slot60,'o','MarkerEdgeColor','r',...
    'MarkerSize',marker_size,'LineWidth',line_width_size,'Color','k');
hold on
errorbar(Diameter_Slot100,
data100.Centricity_Slot3,std_Centricity_Slot100,'^','MarkerEdgeColor','b',...
    'MarkerSize',marker_size,'LineWidth',line_width_size,'Color','k');
hold on
errorbar(Diameter_Slot150,
data150.Centricity_Slot3,std_Centricity_Slot150,'v','MarkerEdgeColor','k',...
    'MarkerSize',marker_size,'LineWidth',line_width_size,'Color','k');
hold on

% Plotting the second x-axis. In the images, 1 pixel is 0.031 mm.

axisH = gca;
addTopXAxis(axisH, 'expression', '3.*argu./0.031', 'xLabStr', '{\itD_{e}} (pixels)')
set(axisH,'fontsize',font_size)
xlabel('{\itD_{e}/w}','FontSize',font_size,'FontName', 'Times New Roman');
ylabel('{\itC_{b-RCSR}}','FontSize',font_size,'FontName', 'Times New Roman');
legendflex({'{\itq_{1-PRR}} = 0.34 mm/s', ...
    '{\itq_{2-PRR}} = 0.67 mm/s', ...
    '{\itq_{3-PRR}} = 1.07 mm/s', ...
    '{\itq_{4-PRR}} = 1.78 mm/s', ...
    '{\itq_{5-PRR}} = 2.64 mm/s'});
axis([0 1.1 0.75 1])
% saveas(gcf,'Centricity_Slot_QAll.fig')
% ************************************************************************
% THE RATIO OF RISING VELOCITY THROUGH THE SLOT TO THE RISING VELOCITY
% BEFORE AND AFTER THE SLOT

figure(9);
hold on
% grid minor
set(gcf,'pos',[70 70 1200 800]);
set(gcf,'color','w');
set(gca,'fontsize',font_size)
% ************************************************************************
% Finding the linear regression of the model
x_data = [data20.AverageDiameter3./w data40.AverageDiameter3./w ...
    data60.AverageDiameter3./w data100.AverageDiameter3./w ...
    data150.AverageDiameter3./w]';
y_data = [(data20.RisingVelocity_Slot3 - ...
    0.503)./ ...
    (data20.RisingVelocity3 - 0.503*3/22) ...
    (data40.RisingVelocity_Slot3 - ...
    1.008)./ ...
    (data40.RisingVelocity3 - 1.008*3/22) ...
    (data60.RisingVelocity_Slot3 - ...
    1.598)./ ...
    (data60.RisingVelocity3 - 1.598*3/22) ...
    (data100.RisingVelocity_Slot3 - ...
    2.67)./ ...
    (data100.RisingVelocity3 - 2.67*3/22) ...
```

```
    (data150.RisingVelocity_Slot3 - ...
    3.966)./ ...
    (data150.RisingVelocity3 - 3.966*3/22)]';
X_data = [ones(size(x_data)) x_data];

% Finding the linear regression
beta = regress(y_data, X_data)
% Finding the regression line
a = beta(1) + beta(2).*2.*R./w;

% Finding a nonlinear regression
modelfun = @(b,x) 1./(b(1) + b(2).*x);
beta0 = [1 1];

AverageVelocityFitFunction = fitnlm(x_data , y_data , modelfun , beta0)
[p,d] = dwtest(AverageVelocityFitFunction.Residuals.Raw , X);
% ************************************************************************
% ************************************************************************
% Model modification
kk_20 = ((data20.RisingVelocity_Slot3 - 0.503)./(data20.RisingVelocity3 - 0.503*3/22));
kk_40 = ((data40.RisingVelocity_Slot3 - 1.008)./(data40.RisingVelocity3 - 1.008*3/22));
kk_60 = ((data60.RisingVelocity_Slot3 - 1.598)./(data60.RisingVelocity3 - 1.598*3/22));
kk_100 = ((data100.RisingVelocity_Slot3 - 2.67)./(data100.RisingVelocity3 - 2.67*3/22));
kk_150 = ((data150.RisingVelocity_Slot3 - 3.966)./(data150.RisingVelocity3 - 3.966*3/22));

X = [1./k_w1_20', lambda20';1./k_w1_40', lambda40';1./k_w1_60', lambda60'; ...
    1./k_w1_100', lambda100'; 1./k_w1_150', lambda150'];
Y = [kk_20'; kk_40'; kk_60'; kk_100'; kk_150'];
modelfun = @(b,x) x(:,1).*b(1).*exp(-(x(:,2) - b(2)).^2);
beta0 = [1.7682 -0.3085 ];
AverageVelocityFitFunction = fitnlm(X , Y , modelfun , beta0)
[p,d] = dwtest(AverageVelocityFitFunction.Residuals.Raw , X);

% ************************************************************************
% Correction factor for rise of air bubbles between two parallel plates
b = 3/2;
lambda = R./b;
k_w1Hirad = (1 + 2.*(sigma + 3/2)./(sigma + 1).*lambda.*1.338);

b = 5.842/2;
lambda = R./b;
k_w2Hirad = (1 + 2.*(sigma + 3/2)./(sigma + 1).*lambda.*1.338);
corrected_WallFactor = feval(AverageVelocityFitFunction, 1./k_w1Hirad, lambda);

% ************************************************************************
% ************************************************************************
plot(data20.AverageDiameter3./w,(data20.RisingVelocity_Slot3 - ...
    0.503)./ ...
    (data20.RisingVelocity3 - 0.503*3/22) ,'s','MarkerEdgeColor','b',...
    'MarkerSize',marker_size,'LineWidth',line_width_size,'Color','k');
hold on
plot(data40.AverageDiameter3./w,(data40.RisingVelocity_Slot3 - ...
    1.008)./ ...
    (data40.RisingVelocity3 - 1.008*3/22),'d','MarkerEdgeColor','k',...
```

```
    'MarkerSize',marker_size,'LineWidth',line_width_size,'Color','k');
hold on
plot(data60.AverageDiameter3./w,(data60.RisingVelocity_Slot3 - ...
    1.598)./ ...
    (data60.RisingVelocity3 - 1.598*3/22) ,'o','MarkerEdgeColor','r',...
    'MarkerSize',marker_size,'LineWidth',line_width_size,'Color','k');
hold on
plot(data100.AverageDiameter3./w,(data100.RisingVelocity_Slot3 - ...
    2.67)./ ...
    (data100.RisingVelocity3 - 2.67*3/22),'^','MarkerEdgeColor','b',...
    'MarkerSize',marker_size,'LineWidth',line_width_size,'Color','k');
hold on
plot(data150.AverageDiameter3./w,(data150.RisingVelocity_Slot3 - ...
    3.966)./ ...
    (data150.RisingVelocity3 - 3.966*3/22),'v','MarkerEdgeColor','k',...
    'MarkerSize',marker_size,'LineWidth',line_width_size,'Color','k');
hold on
plot(R./(w/2), (1./(0.05 + 4.*2.*R./3)),'k-','MarkerEdgeColor','r',...
    'MarkerFaceColor','b',...
    'MarkerSize',5,'LineWidth',2);
hold on
% plot(R./(w/2), k_w2Hirad./sqrt(k_w1Hirad.^2 + k_w2Hirad.^2),'k--','MarkerEdgeColor','b',...
%     'MarkerFaceColor','b',...
%     'MarkerSize',5,'LineWidth',2);
% hold on
% plot(R./(w/2), 1./k_w1Hirad,'k-.','MarkerEdgeColor','b',...
%     'MarkerFaceColor','b',...
%     'MarkerSize',5,'LineWidth',2);
xlabel('{\itD_{e}/w}','FontSize',font_size, 'FontName', 'Times New Roman');
ylabel('{\it(V_{t-RCSR} - V_{f-RCSR} )/(V_{t-PPr} - V_{f-PPR} )}','FontSize',font_size,
'FontName', 'Times New Roman');
legendflex({'{\itq_{1-RCSR}} = 0.34 mm/s', ...
    '{\itq_{2-RCSR}} = 0.67 mm/s', ...
    '{\itq_{3-RCSR}} = 1.07 mm/s', ...
    '{\itq_{4-RCSR}} = 1.78 mm/s', ...
    '{\itq_{5-RCSR}} = 2.64 mm/s', ...
    '\it{k_{t}/f(k_{w},k_{t})}'});
axis([0 1.1 0 1.2])
% saveas(gcf,'Linear Plot_QAll.fig')


% ************************************************************************
figure(10);
hold on
% grid minor
set(gcf,'pos',[70 70 1200 800]);
set(gcf,'color','w');
set(gca,'fontsize',font_size)

% Distance between the center of bubble to the closest slot wall
h20 = ((w/2) - abs(data20.Bubble_Center3 - 12.5));
h40 = ((w/2) - abs(data40.Bubble_Center3 - 12.5));
h60 = ((w/2) - abs(data60.Bubble_Center3 - 12.5));
h100 = ((w/2) - abs(data100.Bubble_Center3 - 12.5));
```

```
h150 = ((w/2) - abs(data150.Bubble_Center3 - 12.5));
plot(data20.AverageDiameter3./w,(h20./w) ...
    ,'s','MarkerEdgeColor','b',...
    'MarkerSize',marker_size,'LineWidth',line_width_size,'Color','k');
hold on
plot(data40.AverageDiameter3./w,(h40./w) ...
    ,'d','MarkerEdgeColor','k',...
    'MarkerSize',marker_size,'LineWidth',line_width_size,'Color','k');
hold on
plot(data60.AverageDiameter3./w,(h60./w) ...
    ,'o','MarkerEdgeColor','r',...
    'MarkerSize',marker_size,'LineWidth',line_width_size,'Color','k');
hold on
plot(data100.AverageDiameter3./w,(h100./w)...
    ,'^','MarkerEdgeColor','b',...
    'MarkerSize',marker_size,'LineWidth',line_width_size,'Color','k');
hold on
plot(data150.AverageDiameter3./w,(h150./w) ...
    ,'v','MarkerEdgeColor','k',...
    'MarkerSize',marker_size,'LineWidth',line_width_size,'Color','k');
xlabel('{\itD_{e}/w}','FontSize',font_size, 'FontName', 'Times New Roman');
ylabel('{\ith/w}','FontSize',font_size, 'FontName', 'Times New Roman');
legendflex({'{\itq_{1-RCSR}} = 0.34 mm/s', ...
    '{\itq_{2-RCSR}} = 0.67 mm/s', ...
    '{\itq_{3-RCSR}} = 1.07 mm/s', ...
    '{\itq_{4-RCSR}} = 1.78 mm/s', ...
    '{\itq_{5-RCSR}} = 2.64 mm/s', ...
    '\it{k_{t}/f(k_{w},k_{t})}'});
axis([0 1.1 0 0.5])
% saveas(gcf,'Bubble Center_QAll.fig')
% % ************************************************************************
figure(11);
hold on
% grid minor
set(gcf,'pos',[70 70 1200 800]);
set(gcf,'color','w');
set(gca,'fontsize',font_size)

% ************************************************************************
errorbar(Diameter_Slot20, (Velocity_Slot20 - V_max20_Slot*1000) ...
    ,std_Velocity_Slot20,'s','MarkerEdgeColor','b',...
    'MarkerSize',marker_size,'LineWidth',line_width_size,'Color','k');
hold on
errorbar(Diameter_Slot40, (Velocity_Slot40 - V_max40_Slot*1000)...
    ,std_Velocity_Slot40,'d','MarkerEdgeColor','k',...
    'MarkerSize',marker_size,'LineWidth',line_width_size,'Color','k');
hold on
errorbar(Diameter_Slot60, (Velocity_Slot60 - V_max60_Slot*1000)...
    ,std_Velocity_Slot60,'o','MarkerEdgeColor','r',...
    'MarkerSize',marker_size,'LineWidth',line_width_size,'Color','k');
hold on
errorbar(Diameter_Slot100, (Velocity_Slot100 - V_max100_Slot*1000)...
    ,std_Velocity_Slot100,'^','MarkerEdgeColor','b',...
    'MarkerSize',marker_size,'LineWidth',line_width_size,'Color','k');
```

```
hold on
errorbar(Diameter_Slot150, (Velocity_Slot150 - V_max150_Slot*1000) ...
    ,std_Velocity_Slot150,'v','MarkerEdgeColor','k',...
    'MarkerSize',marker_size,'LineWidth',line_width_size,'Color','k');
% grid minor
hold on
U = (((2/9).*((R.*0.001).^2.*g.*(density_fluid - density_particle).*(1 + sigma) ...
    ./(viscosity_fluid.*k_w2Hirad.*(1 + (2/3).*sigma))))).*1000;
plot(R./(w/2), U,'r-','MarkerEdgeColor','b',...
    'MarkerFaceColor','b',...
    'MarkerSize',5,'LineWidth',2);
hold on
U = (((2/9).*((R.*0.001).^2.*g.*(density_fluid - density_particle).*(1 + sigma) ...
    ./(viscosity_fluid.*k_w1Hirad.*(1 + (2/3).*sigma))))).*1000;
plot(R./(w/2), U,'b--','MarkerEdgeColor','b',...
    'MarkerFaceColor','b',...
    'MarkerSize',5,'LineWidth',2);
xlabel('{\itD_{e}/w}','FontSize',font_size,'FontName', 'Times New Roman');
ylabel('{\it(V_{t-RCSR} - V_{f-RCSR}} ) (mm/s)','FontSize',font_size,'FontName', 'Times New
Roman');
legendflex({'{\itq_{1-RCSR}} = 0.34 mm/s', ...
    '{\itq_{2-RCSR}} = 0.67 mm/s', ...
    '{\itq_{3-RCSR}} = 1.07 mm/s', ...
    '{\itq_{4-RCSR}} = 1.78 mm/s', ...
    '{\itq_{5-RCSR}} = 2.64 mm/s', ...
    'Theory of parallel plates ({\itk_{t}})', ...
    'Theory of parallel plates ({\itk_{w}})'},'Fontsize',19);
% legend boxoff
axis([0 1.1 0 5])
% saveas(gcf,'Rising Velocity_Parallel Plates_QAll.fig')
% ************************************************************************
% 3D PLOT OF RISING VELOCITY FOR SMALLEST DIAMETERS OF EACH FLOW RATE

figure(12);
set(gcf,'pos',[70 70 1200 800]);
set(gcf,'color','w');
set(gca,'fontsize',font_size)
zMat = [[Velocity_3D_20_min./0.34 Velocity_3D_20_max./0.34]';[Velocity_3D_40_min./0.67
Velocity_3D_40_max./0.67]' ...
    ;[Velocity_3D_60_min./1.07 Velocity_3D_60_max./1.07]';[Velocity_3D_100_min./1.78
Velocity_3D_100_max./1.78]' ...
    ;[Velocity_3D_150_min./2.64 Velocity_3D_150_max./2.64]'];
yMat = [[Diameter_3D_20_min Diameter_3D_20_max] [Diameter_3D_40_min Diameter_3D_40_max] ...
    [Diameter_3D_60_min Diameter_3D_60_max] [Diameter_3D_100_min Diameter_3D_100_max]
[Diameter_3D_150_min Diameter_3D_150_max]];
xMat = [[repmat([0.34],numel(Diameter_3D_20_min),1) repmat([0.34],numel(Diameter_3D_20_max),1)]
...
    [repmat([0.67],numel(Diameter_3D_40_min),1) repmat([0.67],numel(Diameter_3D_40_max),1)] ...
    [repmat([1.07],numel(Diameter_3D_60_min),1) repmat([1.07],numel(Diameter_3D_60_max),1)] ...
    [repmat([1.78],numel(Diameter_3D_100_min),1) repmat([1.78],numel(Diameter_3D_100_max),1)] ...
    [repmat([2.64],numel(Diameter_3D_150_min),1) repmat([2.64],numel(Diameter_3D_150_max),1)]];
% zMat = [Velocity_3D_20_max';Velocity_3D_40_max' ...
%     ;Velocity_3D_60_max'; Velocity_3D_100_max' ...
%     ;Velocity_3D_150_max'];
```

```
% yMat = [Diameter_3D_20 Diameter_3D_40 Diameter_3D_60 Diameter_3D_100 Diameter_3D_150];
% xMat = [repmat([0.25],numel(Diameter_3D_20),1) repmat([0.50],numel(Diameter_3D_40),1) ...
%     repmat([0.80],numel(Diameter_3D_60),1) repmat([1.34],numel(Diameter_3D_100),1)
repmat([1.98],numel(Diameter_3D_150),1)];
plot3(xMat,yMat,zMat,style{k}, ...
    'MarkerSize',7)

ax = gca;
ax.XTick = [0.34 0.67 1.07 1.78 2.64];                  % set x-axis ticks
ax.XTickLabel = {'0.34','0.67','1.07','1.78','2.64'};
% columnlegend(['{\itq} = 0.25 mm/s', '{\itq} = 0.50 mm/s','{\itq} = 0.80 mm/s', ...
%     '{\itq} = 1.34 mm/s','{\itq} = 1.98 mm/s'],3)

% legend('{\itq} = 0.25 mm/s', '{\itq} = 0.50 mm/s','{\itq} = 0.80 mm/s','{\itq} = 1.34
mm/s','{\itq} = 1.98 mm/s')

ylabel('{\ity/l}','FontSize',font_size,'FontName', 'Times New Roman');
zlabel('{\itV_{r-inst}}','FontSize',font_size,'FontName', 'Times New Roman');
xlabel('{\it{q} (mm/s)}','FontSize',font_size,'FontName', 'Times New Roman');
% axis([0 2.8 -2 2 0 12])
% saveas(gcf,'3D_Velocity.fig')
```

Published with MATLAB® R2016b